MODELLING THE TWO-PHASE PLUME DYNAMICS OF CO_2 LEAKAGE INTO OPEN SHALLOW WATERS

Marius Dewar

Submitted for the degree of Doctor of Philosophy

Heriot-Watt University

Institute of Mechanical, Process and Energy Engineering

School of Engineering and Physical Sciences

March 2016

ABSTRACT

A numerical model of two-phase plume developments in a small scale turbulent ocean is proposed and designed as a fundamental study to predict the near field physicochemical impacts and biological risk to the marine ecosystem from CO_2 leakage from potential carbon storage locations around the North Sea.

New sub-models are developed for bubble formation and drag coefficients using in-situ measurements from videos of the Quantifying and monitoring potential ecosystem Impacts of geological Carbon Storage (QICS) experiment. Existing sub-models such as Sherwood numbers and plume interactions are also compared, verified and implemented into the new model. Observational data collected from the North Sea provides the ability to develop and verify a large eddy simulation turbulence model, limited to situations where the non-slip boundary wall may be neglected.

The model is then tested to assimilate the QICS experiment, before being applied to potential leakage scenarios around the North Sea with key marine impacts from pCO_2 and pH changes. The most serious leak is from a well blowout, with maximum pH changes of up to -2.7 and changes greater than -0.1 affecting areas up to 0.23 km^2. Other scenarios through geological structures would be challenging to detect with pH changes below -0.27.

DEDICATION

Dedicated to my two nieces, Aurora Dewar Craig born on the 5th June 2012 and Penelope Willow Craig born on the 11th May 2014, both enjoying the study of bubbles just as much as I do.

ACKNOWLEDGEMENTS

I would like to take this opportunity to express my deep and sincere gratitude to those that have supported and assisted me throughout my research and writing, without their help this thesis would simply not exist in any shape or form.

Greatest thanks to my supervisor, Dr Baixin Chen, for his endless support, guidance and encouragement. His openness to new ideas has allowed this project to mature from the onset, which has motivated me in wanting to explore what new methods and concepts could be used to develop the work, both now and in the future.

A special thanks to our engineering group and colleagues in the Institute of Mechanical, Process and Energy Engineering, especially Nazmi Sellami, Wei Wei, Sorush Khajepor, Stephanie Zihms, Marina Sousani, Boris Tapah, Tariq Chaudhary, Onne, Okpu and visiting Associate Professor Zhang Yi, for their technical advice and support throughout the project along with colleagues from the Centre for Innovation in Carbon Capture and Storage.

Thanks are also due to the School of Engineering and Physical Sciences (EPS) and IMPEE support staff, especially Rebecca Crawford and Mylene Honore-L'Hortalle for taking care of multiple amounts of paperwork allowing me to travel to various conferences and meetings, at times on very short notice.

I am extremely grateful to the Secure Project supported by the CLIMIT Program under the Research Council of Norway, for providing funding for the bulk of this project, along with the QICS project through the Natural Environment Research Council; and the ECO_2 project through the FP7 Cooperation Work Programme. The support from these projects and the work packages within has been invaluable, not just in aspects of funding, but also advice, guidance and collaborations within the projects.

Special appreciation is due to my close friends and to my parents and my two sisters, for their patience, encouragement, support, understanding and guidance. I cannot state how grateful I am to all that have helped me get to this stage in my academic career.

ACADEMIC REGISTRY
Research Thesis Submission

Name:	Marius Dewar		
School/PGI:	School of Engineering and Physical Sciences		
Version: *(i.e. First, Resubmission, Final)*	Final	Degree Sought (Award **and** Subject area)	PhD Mechanical Engineering

Declaration

In accordance with the appropriate regulations I hereby submit my thesis and I declare that:

1) the thesis embodies the results of my own work and has been composed by myself
2) where appropriate, I have made acknowledgement of the work of others and have made reference to work carried out in collaboration with other persons
3) the thesis is the correct version of the thesis for submission and is the same version as any electronic versions submitted*.
4) my thesis for the award referred to, deposited in the Heriot-Watt University Library, should be made available for loan or photocopying and be available via the Institutional Repository, subject to such conditions as the Librarian may require.
5) I understand that as a student of the University I am required to abide by the Regulations of the University and to conform to its discipline.

* *Please note that it is the responsibility of the candidate to ensure that the correct version of the thesis is submitted.*

Signature of Candidate*:*		Date:	

Submission

Submitted By *(name in capitals):*	MARIUS DEWAR
Signature of Individual Submitting:	
Date Submitted:	

For Completion in the Student Service Centre (SSC)

Received in the SSC by *(name in capitals):*			
Method of Submission *(Handed in to SSC; posted through internal/external mail):*			
E-thesis Submitted (***mandatory for final theses***)			
Signature:		Date:	

TABLE OF CONTENTS

LIST OF TABLES

LIST OF FIGURES

NOMENCLATURE

Scales and Units

Length

mm	Millimetre	10^{-3} m
cm	Centimetre	10^{-2} m
m	Meter	
km	Kilometre	10^{3} m

Mass

kg	Kilogram	
t	Tonne	10^{3} kg
Mt	Megatonne	10^{6} t
Gt	Gigatonne	10^{9} kg
Mol	Mole	

Time

s	Seconds	
mins	Minutes	60s
days	Days	1440 mins
yr	Year	365.25 days

Pressure

Pa	Pascals	kg/ms^2
bar	Bar	10^{5} Pa
atm	Atmospheres	~1 bar
ppm	Parts per million	(partial pressure)
ppb	Parts per billion	(partial pressure)

Temperature

°C	Degrees Celsius	
K	Kelvin	

Energy

J	Joules	kgm^2/s^2

Angle

rad	radians

Fluids and Measures of Fluids

CO_2	Carbon Dioxide, referred to as a gas, however also may be in liquid or hydrate form
CH_4	Methane, referred to as a gas, however also may be in supercritical or hydrate form
N_2O	Nitrous Oxide, referred to as a gas, however also may be in liquid or hydrate form
H_2	Hydrogen, referred to as a gas, however also may be in liquid or hydrate form
H_2O	Water, referred to as a vapour in its gas form, however often found in liquid form
pCO_2 (μatm, ppm, ppb)	Partial Pressure of Carbon Dioxide, a measure of dissolved carbon dioxide content
DIC (μMol/kg)	Dissolved Inorganic Carbon, a measure of dissolved carbon dioxide content
pH	Potential (or Power) of Hydrogen – a negative $\log_{10}$ of the concentration of hydrogen ions, commonly used to measure acidity

Subscripts

i, j	Representing the X, Y, Z coordinates of flow.
sw	Seawater
CO_2	Carbon dioxide
1, 2	Representing the two phases, 1 being the bubble or droplet plume, and 2 being the seawater and dissolved CO_2 solution
0	Initial values
ch	Channel
sed	Sediments
m	Specific mass
n	Number density

f	Drag force
c	Coalescence
b	Breakup
s	Scalar

Abbreviations

CCS	Carbon Capture and Storage (or Carbon Capture and Sequestration), the process of taking waste CO_2 and injecting it into a reservoir rather than allowing it to pollute the atmosphere
LES	Large Eddy Simulation – a method of simulating turbulence in the small scale through solving larger eddies and modelling smaller ones
ROV	Remotely Operated Vehicle
CCD	Charge-Coupled Device, a digital imaging sensor
CMOS	Complementary Metal–Oxide–Semiconductor, a digital imaging sensor
PIV	Particle Image Velocimeter, an imaging processing technique that can be used to measure the detailed variation in bubble characteristics
LDA	Laser Dropper Analysis is a method that significantly reduces the extraction of velocity data and allows the measurement of a bubble or droplet rise velocity, even in a high number density plume
LIF	Laser Induced Fluorescence, tracks bubble trajectories utilising photosensitive dyes, with the fluorescence highlighting the trajectory and dynamics of the bubble
fps	Frames per second, the rate at which images are collected during video samples.
HD	High Definition, the quality of digital image produced by the camera, with images of 1920 by 1080 pixels

Scientific Terms

$\frac{\partial}{\partial t}, \frac{\partial}{\partial x}$	Partial differential equation in terms of time, or distance
Ψ_k, φ_k	Dependant variable
d	Diameter, measured in m
Ø	Diameter of leakage zone, measured in m
d_{eq}	Equivalent diameter, from area or volume, measured in m
d_{mj}	Major axis dimension, measured in m
d_{mi}	Minor axis dimension, measured in m
r, R	Radius, measured in m
ρ	Density of fluid, measured in kg/m^3
u	Velocity, measured in m/s
u'	Turbulent velocity, measured in m/s
C	Speed of sound, measured in m/s
V	Volume, measured in m^3
$\dot{V}$	Volume flow rate, measured in m^3/s
A	Area, measured in m^2
α	Void fraction, ratio of the fluid volumes.
$\dot{q}_\varphi$	Source terms for differential equations, units vary
q̇	Heat flow, measured in either J/s, kgK/s, or J/m^3s
ẇ	Work rate, measured in J/m^3s
ṁ	Mass flow rate, measured in kg/s
Y	Mass fraction or Mass Concentration, measured in kg/kg_{sw} or $kg/m^3{}_{sw}$
F	Forces applied to fluids in calculating momentum, measured in N (kgm/s^2)
Fs_{ij}	Turbulent energy forcing, measured in kg/ms^2
Ds_{ij}	Turbulent energy dissipation, measured in kg/ms^2
J	Momentum, measured in kgm/s
g	Gravity, measured in m/s^2
p	Pressure, measured in Pa (kg/ms^2)
μ (Pa·s), ν (m^2/s)	Viscosity (dynamic μ, measured in kg/ms and kinematic ν, measured in m^2/s respectively)
T	Temperature, measured in °C

T_K	Temperature, measured in K
S	Salinity
k_t	Thermal conductivity, measured in J/mKs
k_m	Mass transfer coefficient, measured in m/s
c_p	Specific heat capacity, measured in J/kgK
n	Number density, measured in #/m^3
N	Number of bubbles / droplets
D_f	Diffusivity, measured in m^2/s
E	Energy, measured in J
E(k), E_k	Kinetic energy, measured in J
E_p	Potential energy, measured in J
σ	Interfacial tension, measured in N/m N (kg/s^2)
k	Wavenumber, measured in m^{-1}
ε	Energy dissipation rate, measured in J/s
F_2	Structure function of the local grid velocity, measured in m^2/s^2
ω	Angular frequency, measured in rad/s
f	Linear frequency, measured in Hertz, s^{-1}
γ_{co_2}	The isentropic exponent
f_f	Friction factor
ϕ	Porosity
τ_m	Breakup time, measured in s
ϑ_c	Coalescence frequency, measured in Hertz, s^{-1}
ϑ_b	Breakup frequency, measured in Hertz, s^{-1}
η	Efficiency
t_c	Time for film drainage, measured in s
τ_c	Contact time for bubbles, measured in s
$\overline{E}_B$	Energy to break a bubble, measured in J
$\overline{e}_B$	Energy from a single turbulent eddy, measured in J

Non-Dimensional Numbers

$$\mathrm{Re} = \frac{\rho u d}{\mu}$$

Reynolds number, analysing the ratio of the inertial against viscous forces to define a critical point where flow turns from laminar to turbulent.

$$We = \frac{\rho u^2 d}{\sigma}$$

Weber number, analysing the ratio of the inertial and viscous forces against tension forces to define maximum size characteristics.

$$Eo = Bo = \frac{\Delta\rho g d^2}{\sigma}$$

Eötvös (Bond) number, analysing the ratio of the buoyancy against tension forces to define shape characteristics.

$$Mo = \frac{g\mu^4 \Delta\rho}{\rho^2 \sigma^3}$$

Morton number, analysing the ratio of the inertial against tension forces to define shape characteristics.

$$c_d = \frac{F_d}{1/2\, \rho u^2 A}$$

Drag coefficient, analysing the ratio of the real flow including the drag force on the body from the viscous forces and shear stresses, with an ideal flow (the inertial force).

$$Sh = \frac{k_m d}{D_f}$$

Sherwood number, analysing the ratio of the convective mass transfer against the diffusive mass transfer.

$$Sc = \frac{\nu}{D_f}$$

Schmidt Number, the ratio of momentum and diffusive mass transfers

LIST OF PUBLICATIONS BY THE CANDIDATE

Journal Articles

N. Sellami, **M. Dewar**, H. Stahl, and B. Chen, "Dynamics of rising CO_2 bubble plumes in the QICS field experiment: Part 1 – The experiment," *Int. J. Greenhouse Gas Control*, March 2015, DOI 10.1016/J.IJGGC.2015.02.011.

S. Khajepor, **M. Dewar**, J. Wen, and B. Chen, "Consistent implementation of real fluid EOS in pseudopotential lattice Boltzmann models," *Proc. Appl. Math. Mech*, December 2014, DOI 10.1002/pamm.201410323.

M. Dewar, N. Sellami, and B. Chen, "Dynamics of rising CO_2 bubble plumes in the QICS field experiment: Part 2 – Modelling," *Int. J. Greenhouse Gas Control*, November 2014, DOI 10.1016/j.ijggc.2014.11.003.

M. Dewar, W. Wei, D. McNeil, and B. Chen, "Small-scale modelling of the physiochemical impacts of CO_2 leaked from sub-seabed reservoirs or pipelines within the North Sea and surrounding waters," *Marine Pollution Bulletin*, August 2013, DOI 10.1016/j.marpolbul.2013.03.005.

M. Dewar, W. Wei, D. McNeil, and B. Chen, "Simulation of the Near Field Physiochemical Impact of CO_2 Leakage into Shallow Water in the North Sea," *Energy Procedia*, August 2013, DOI 10.1016/j.egypro.2013.06.230.

Reports

K. Wallmann, M. Haeckel, P. Linke, L. Haffert, M. Schmidt, S. Buenz, R. James, C. Hauton, M. Tsimplis, S. Widdicombe, J. Blackford, A. M. Queiros, D. Connelly, A. Lichtschlag, **M. Dewar**, B. Chen, T. Baumberger, S. Beaubin, S. Vercelli, A. Proelss, T. Wildenborg, T. Mikunda, M. Nepveu, C. Maynard, S. Finnerty, T. Flach, N. Ahmed, A. Ulfsnes, L. Brooks, T. Moskeland, and M. Purcell, "Best Practice Guidance for Environmental Risk Assessment for offshore CO_2 geological storage," ECO_2 Deliverable, D14.1. , May 2015, DOI 10.3289/ECO_2_D14.1.

G. Alendal, **M. Dewar**, A. Ali, Y. Evgeniy, L. Vielstädte, H. Avlesen, and B. Chen, "Technical report on environmental conditions and possible leak scenarios in the North Sea" ECO_2 Deliverable, D3.4. , November 2014, DOI 10.3289/ECO_2_D3.4.

M. Dewar, B. Chen, Y. Evgeniy, H. Avlesen, G. Alendal, A. Ali, and L. Vielstädte, "Technical report on verified and validated application of droplet/bubble plume-, geochemical- and general flow- models" ECO_2 Deliverable, D3.3. , November 2013, DOI 10.3289/ECO_2_D3.3.

G. Alendal., A. Omar, A. R. Denny, T. Baumberger, S. E. Beaubien, L. Vielstädte, **M. Dewar,** B. Chen, R. B. Pedersen, C. De Vittor, and T. Johannessen, "Technical synthesis report on droplet/bubble dynamics, plume dynamics and modelling parameters, use of hydro-acoustics to quantify droplet/bubble fluxes, and carbonate system variable assessment" ECO_2 Deliverable, D3.1. , November 2013, DOI 10.3289/ECO_2_D3.1.

Chapter 1 – Introduction

1.1 Perspective

It is well recognised and documented that increasing greenhouse gas concentrations in the atmosphere, due to human activities, is a likely contributor to global warming (globally averaged temperatures increase since the mid-20th century) [1] and the fundamental factor influencing climate change [2]. Among the atmospheric greenhouse gasses, carbon dioxide, CO_2, is the second most abundant after water vapour [3]. With this high threat, investigations have been carried out since the 1970s [4] on mitigation methods for greenhouse gas release to the atmosphere [5].

One such method is Carbon Capture and Storage, CCS [6], a process where CO_2 is removed from industrial waste when burning fossil fuels, and rather than releasing it into the atmosphere, it is injected in porous rock reservoirs deep underground, protected by the impermeable rocks above, with the aim of storing the CO_2 from escape for tens of thousands of years or more [7]. Worldwide demonstration projects are already in operation or in the development phase [8], however, the potential impacts of stored CO_2 on geoformations, and the associated risks are major concerns for a full large scale operation.

The greatest concern is leakage from a storage site, where CO_2 may travel through the geoformations into the atmosphere (from on-shore storage), or the water column and atmosphere (from off-shore undersea bed storage) [6]. When selecting suitable CCS sites, multiple geological barriers should be present to seal the CO_2, reducing the likelihood of leakage [9]; while fractures due to interactions of CO_2 with cap-rocks and geological faults make leakages potentially possible. To further prevent any risk of leakage, CCS operators are required to test the storage capability of CCS reservoirs over 10,000 years through reservoir modelling [6]. Monitoring and modelling during and after CO_2 injection is also recommended to mitigate any potential leakages before they occur. However, there is still a lack of knowledge and understanding, especially on the impacts of a leak from an under seabed storage site on marine environments and ecosystems.

The acute impacts on marine biology from a leakage site occur within the near-field [10], which covers a scale of the seawater from meters to kilometres. Therefore small scale field and laboratory experiments are required, with the development of numerical models to understand the mechanisms of leakage from the seabed into the turbulent seawater to fill the gaps and uncertainties left, providing further data and a full risk assessment.

1.2 Research Hypothesis and Objectives

In this thesis a numerical model of two-phase plume developments in a small scale turbulent ocean is designed, with sub-models for CO_2 leakage, including bubble/droplet interaction and dynamics in a free rising plume. This model is designed, calibrated and validated through use of in-situ and laboratory observation and experimental data. An in-house experiment is designed to validate bubble flow rate and measurement techniques, which are then utilised on video data provided from the divers overseeing the QICS experiment. The data is then used to develop new correlations and sub-models to increase the accuracy of the simulations. This can then be applied to predict the potential impacts of leaked CO_2 within near-field ocean in the North Sea, including the dispersed CO_2 dynamics, dissolution, fate of the CO_2 (through either full dissolution or rising to the atmosphere) leaked in either liquid, gas or hydrate form, and the physicochemical impact on the marine environment, measured in terms of pCO_2 or pH changes.

1.3 Thesis Structure

The structure of the thesis is schematically described in Figure 1-1 to outline each chapter, with an overview and hypothesis of the thesis containing the main aims and objectives of the research in Chapter 1. Chapter 2 introduces a literature review into the fundamentals of climate change and mitigation, the geological storage mechanism in CCS, and a risk assessment of leakage with an up to date literature review into leakage analysis through experiments, field observations and numerical modelling techniques. Chapter 3 describes the theories and mechanisms of two phase flow (dispersed liquid/gas and seawater) for both in-situ analysis, and numerical modelling, including details of the reconstructed small scale turbulent ocean through literature review.

Chapter 4 discusses the bubble plume dynamics, developing new sub-models for the exchanges in mass, momentum and energy of the bubble/droplet with seawater, along with the bubble interactions using data from in-situ experiments and observations. The construction of the small-scale two-phase turbulent plume model is described in Chapter 5 for analysis of a leak into turbulent open waters. Chapter 6 describes the methodology and techniques to for solve the governing equations of the numerical model and Chapter 7 tests and validates the numerical model by simulating the QICS experiment, with a comparison of the findings between the numerical model and the in-situ experiment. The model is then calibrated to the North Sea and surrounding waters in Chapter 8 and applied in Chapter 9 to demonstrate predictions of the suggested leakage impacts through case studies and scenarios. Chapter 10 summarises the findings from the thesis, along with providing proposals for future work within this area to further develop the numerical model.

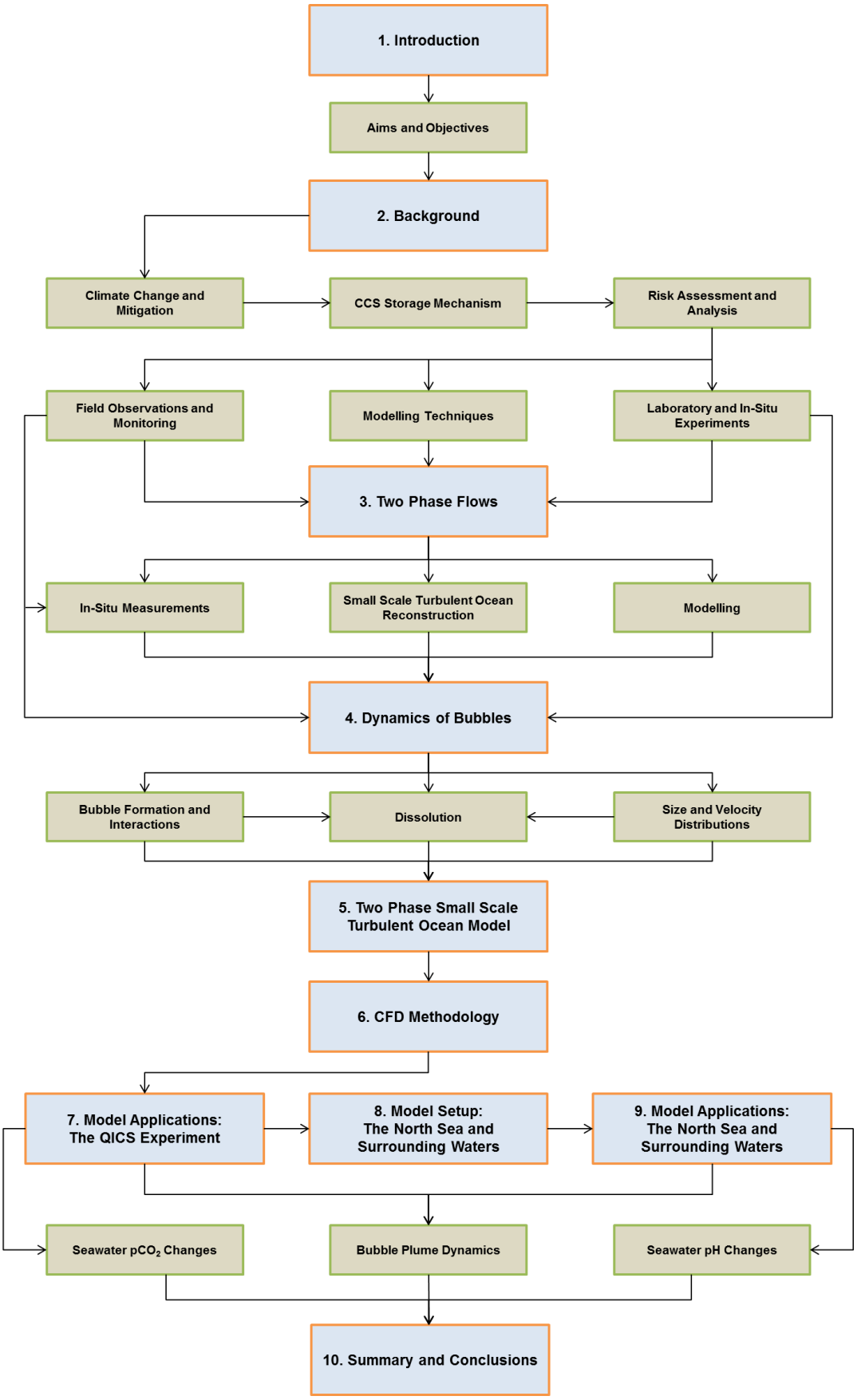

Figure 1-1 *– Thesis Structure.*

Chapter 2 – Background Review

2.1 Introduction

The work in this thesis is drawn from a range of research areas and topics. However, they all develop from the fundamental basis of global warming and mitigation methods of carbon dioxide emissions, especially Carbon Capture and Storage, CCS. A review of these topics are outlined and organized within this chapter. Section 2.2 describes the history of climate change, along with presenting a timeline for predicted risks, and the preventative measures to be taken. Section 2.3 focuses on a background into CCS, one of the mitigation methods, looking into the capture, transport and storage mechanisms to prevent the greenhouse gas from reaching the atmosphere. Section 2.4 presents a risk assessment for offshore CCS, including the causes of leakage and the local environmental impacts. Section 2.5 provides an up to date literature review into leakage analysis through experiments, field observations and numerical modelling techniques. Finally, Section 2.6 summarises the background and the need for this work to develop the risk assessment further.

2.2 Global Warming and Mitigation

Global warming is a serious risk to life and the ecosystem, from changing weather patterns, expanding deserts and increases of sea levels, all destroying natural habitats [11]. The Intergovernmental Panel on Climate Change, IPCC, formed in 1988 with the aim of providing access to the most recent scientific facts on climate change, investigating all aspects of potential impacts, risks and mitigation [12].

2.2.1 Global Warming

There are two definitions of planet weather patterns based on the time scale, climate change and global warming. Climate change is defined as the average weather over a period from centuries to millennia by the World Meteorological Organization [13]. From a range of measurements and data sets, as shown in Figure 2-1, the mean temperatures of the air, both at the surface of the earth and up to the troposphere increased by about 1°C from 1850 to 2009, with a dramatic increase in the gradient of change over the last century.

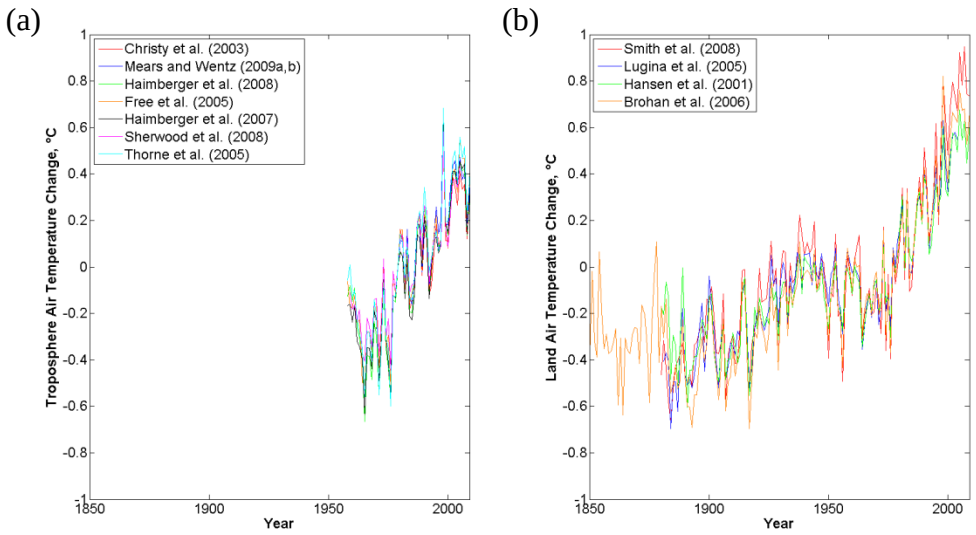

Figure 2-1 *– The change in temperature from the mean value taken from a range of data sets, courtesy of the Met Office Hadley Centre. (a) The temperature change of air high in the troposphere [14 – 21], left; (b) The temperature change of air at the surface of the earth [22 – 25], right.*

Infrared radiation reflected off the earth from the sun is absorbed by what is known as greenhouse gasses (water vapour, H_2O, carbon dioxide, CO_2, methane, CH_4, nitrous oxide, N_2O) and reflected in all directions, including back to the surface of the earth providing the greenhouse effect and global warming [26]. Observation data for atmospheric levels of CO_2, CH_4 and N_2O, such as those from the Mauna Loa Observatory, Hawaii and NOAA ESRL Global Monitoring Division [27], clearly indicate a trend of increasing greenhouse gas concentrations matching that of the temperature in Figure 2-1 (a). This shows evidence of the effect of human activities on global warming. Although at various rates, a steady annual increase of each gas can be identified, with the mean CO_2 concentration two orders of magnitude greater than that of CH_4 and N_2, and increasing by more than 1.7 ppm/yr as shown in Figure 2-2. Therefore the IPCC determines that the rise in levels of these gasses in the atmosphere is a contributory factor for the recorded global temperature increases [26], where the CO_2 contributes up to 26 % of the effect from greenhouse gases [28].

The IPCC predict that the mean land and sea surface temperatures increased by a linear trend of 0.85 ± 0.2 °C from 1880 to 2012 [26], where shorter term trends don't necessarily give an accurate prediction due to natural variability [26].

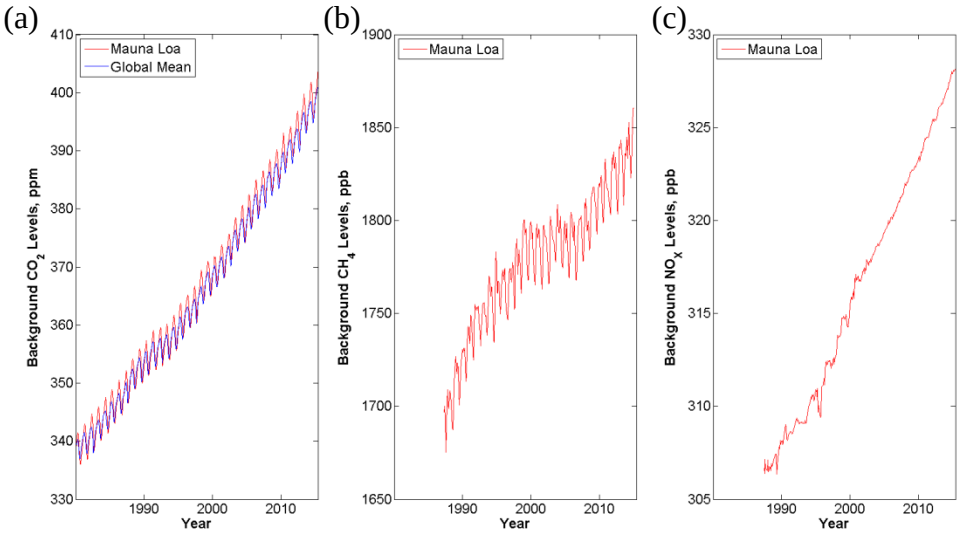

Figure 2-2 *– Atmospheric Levels of greenhouse gases, with Carbon Dioxide, Methane and Nitrous Oxide data from the NOAA/ESRL halocarbons in situ program [27] with data for comparison of each gas from Mauna Loa. (a) CO_2 in the atmosphere, Global mean (blue line) and Mauna Loa measurements (red line), left; (b) CH_4 in the atmosphere, Mauna Loa measurements, middle; (c) N_2O in the atmosphere, Mauna Loa measurements, right.*

Projections of future temperature rises are difficult due to various possible scenarios and natural variability, however, the IPCC predicted that the levels of CO_2 could increase up to 480 ppm by 2035 [26] in comparison to 200 - 280 ppm in the pre-industrial age [29], where temperatures could rise by 0.3 to 0.7 °C in the 2016 - 2035 period, relative to the 1986 - 2005 temperature, assuming that there are little changes in solar irradiance or volcanic eruptions [26]. These rising temperatures and CO_2 levels will have great consequences on the environment and ecosystem.

2.2.2 Consequences of Climate Change

There are both direct and indirect consequences of global warming. Direct consequences are a decrease in the size of the polar caps, with reduced glacier mass, and reduced snow cover shown in Figure 2-3 (a) caused by the increase in temperature forcing melting. The subsequent effect is increasing water and sea levels shown in Figure 2-3 (b). The other direct effect of temperature increases is the increase in desert size, taking over Mediterranean-like landscapes through heat and drought [11].

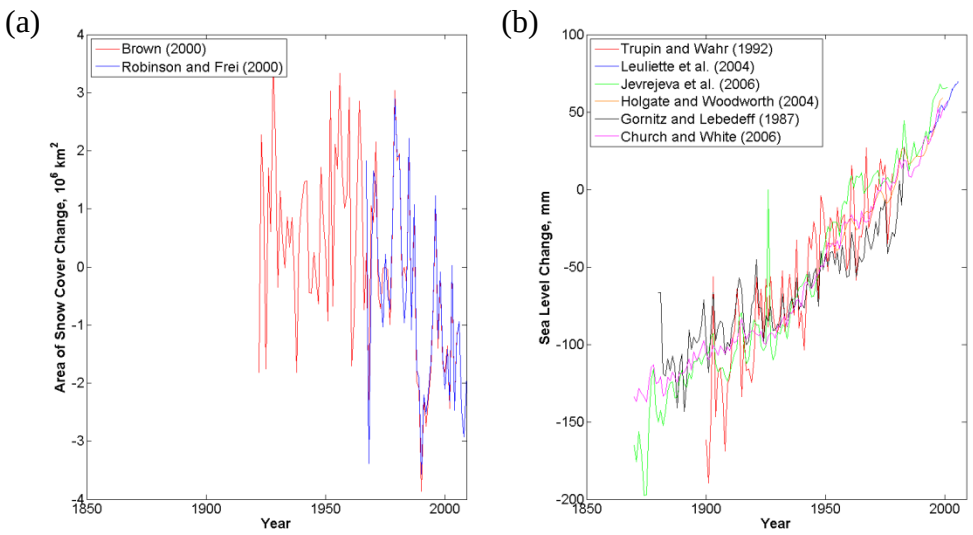

Figure 2-3 *– The consequences of climate change taken from a range of data sets, courtesy of the Met Office Hadley Centre. (a) The change in area of snow cover in the northern hemisphere compared to the mean [30, 31], left; (b) The change of the sea level compared to the mean [32 – 38], right.*

The indirect consequences can have an even more profound effect, such as ocean acidification, where CO_2 is absorbed by the ocean buffering the atmospheric effect [6, 26, 39]. The dissolved CO_2 breaks down into carbonic acid, therefore the ocean becomes more acidic with a decrease in pH that can affect the marine ecosystem [40]. There are further impacts, such as the melting of the polar ice caps causing a reconstruction of the global oceanic cycle and in turn, the global climate [41, 42], along with the destruction of polar habitats [43]. On land, similar destruction to habitats occurs, with extreme weather also providing droughts, floods and storms that can disrupt food production and water supplies in both developed and undeveloped countries [44].

2.2.3 Mitigation

Greenhouse gas emissions have increased, with global CO_2 emissions increasing from ~5 Gt/yr in 1900 to ~37 Gt/yr in 2010, with the majority from fossil fuels, cement and flaring [5]. The consumption of fossil fuels contributes to around 78 % of the emissions increase from 1970 to 2010 [5] and is expected to continue to be the main contributor, with 14.4 Gt/yr of CO_2 emissions in 2010 expected to be doubled or even tripled by 2050 [7]. To reduced CO_2 in the atmosphere, the EU countries planned to reduce greenhouse gas emissions for developed countries by 80 – 95 % of 1990 levels in 2050, although this plan is under constant review [45].

Mitigation methods have been proposed and assessed against energy demands investigating CO_2 mitigation potentials [7, 46, 47]. A full range of scenarios have been compiled to determine the measures required to prevent climate change [48] as shown in Figure 2-4, with the current trend showing that by 2050 the temperature will increase by 6 degrees compared to those of pre-industrial levels, with emissions of CO_2 reaching 56 Gt/yr

To reduce to a 2 degrees rise from pre-industrial levels requires a huge reduction to 14 Gt/yr, with possible contributions of this decrease from CCS (-6.46 Gt/yr), renewable energy (-12.62 Gt/yr), reduction in end use energy and electrical efficiency (-14.9 Gt/yr), end user fossil fuel switching (-4.42 Gt/yr), nuclear energy (-2.75 Gt/yr) and both power generation efficiency and fuel switching (-0.11 Gt/yr) by 2050 [49].

One mitigation method for emissions is with regards to consumption patterns, both in terms of energy (more efficient use and less wastage) and food waste [7]. However this, will only remove an estimated 20 % of the demand for energy in the short term [50] and typically 50 % of demand in the longer term [51, 52]. Therefore further measures are needed in the short and long term.

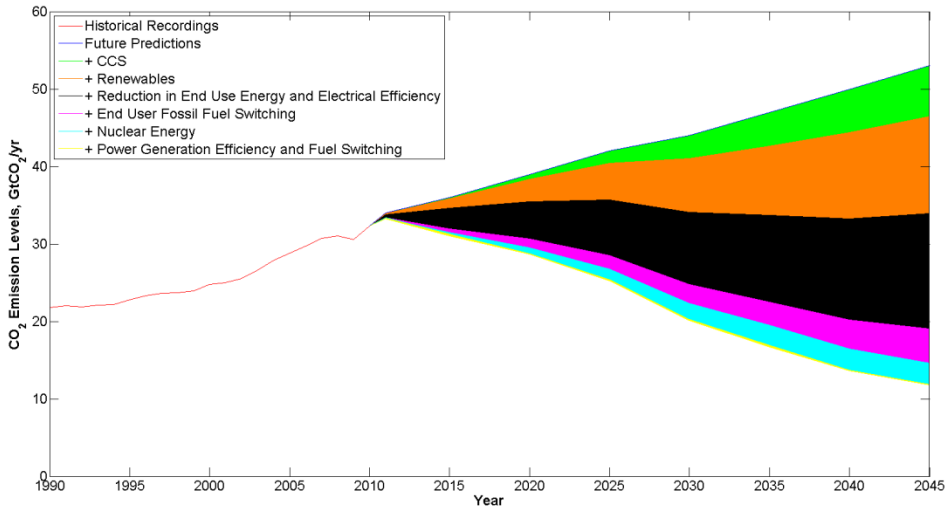

Figure 2-4 *– Yearly emissions of CO_2 (up to 2012, measured in $GtCO_2/yr$), along with possible emission reductions through mitigation techniques to approach the target of 14 $GtCO_2/yr$ (2 degrees rise in temperature from preindustrial level by 2050), data from the International Energy Agency [48].*

Decarbonisation, the use of non-carbon emitting energy sources, is clearly a way forward [53], where on average the worlds energy system has been in the process of decarbonizing since the 1970s through the increase in nuclear and renewable energies (wind, solar, geothermal, hydro, tidal and wave), along with low carbon fuels such as natural gas [7] and biomass. In 2012 the use of nuclear and renewables contributed to almost a third of global electricity generation, with the bulk of this energy coming from hydropower and nuclear (16.3 % and 11 % respectively) [7]. The problem with most of the current renewable energy sources is that they are all intermittent [54], where nuclear, biomass or fossil fuel power stations are required to cover periods of low energy generation.

Nuclear power is a non-carbon exothermic electric and heat energy source. As it is non-carbon, it has low greenhouse gas emissions rated at below 100 gCO_2eq per kWh [7], with the majority of estimates far lower, varying based greatly on the grade of uranium [55]. However there are other concerns for the environment, with two major accidents, Chernobyl in 1986, widely regarded as one of the worst accidents in recent history [56], and Fukushima in 2011, where Japan ceased all nuclear power operations in 2014 [57] until August 2015 [58]. In 2012 nuclear energy supplied an estimated 11 % of global energy, where at the peak in 1993 it was an estimated 17 % [7].

In addition to the proposed mitigation, natural mitigation exists. Biological carbon sinking, where the carbon dioxide in the atmosphere is absorbed by plants on land through photosynthesis, converting CO_2 into sugars and other carbohydrates is a natural storage mechanism of the gas from the atmosphere [59]. As estimated by IPCC, biological carbon sinking in vegetation within soils absorbs ~30 % of all anthropogenic CO_2 emissions [26], meanwhile deforestation is a major concern with the total emissions from forestry and other land use increased by 40 % from 1970 to 2011 [5].

The oceans also naturally sink CO_2, where the Dissolve Inorganic Carbon, DIC, in the surface layers, taken from the atmosphere dampening the greenhouse effect [60], is then transported through a biological/chemical carbon pump by photosynthesis of the upper ocean layer into the deep ocean [61]. Over the last 200 years, the total estimated anthropogenic emissions of CO_2 to the atmosphere are 1,300 Gt, with about 500 Gt

absorbed in the oceans [6]. Recent numbers (within the last 3 years), provide slightly lower estimates on ocean absorption with about ~30 % of all anthropogenic CO_2 emissions [26]. However, the effects on the ocean from this natural sink can be as bad as, or worse than in the atmosphere, with increased acidification damaging coral reefs, plankton and other marine habitats [62].

Another potential solution to prevent CO_2 releases into the atmosphere is the disposal of CO_2 waste in deep geoformations underground or in the ocean through Carbon Capture and Storage, CCS [63], enabling the continued use of fossil fuels; especially coal, the primary fuel use in electricity generation providing 43 % electricity emissions of CO_2 in 2010 [7]. Industrial scale CCS projects have been active since 1996, the first being Sleipner by Statoil, removing CO_2 from natural gas to meet the market specifications, and storing it ~1.0 km beneath the seabed, with ~0.9 Mt stored annually, and 12 Mt of CO_2 stored by 2010 that would have otherwise been released to the atmosphere [64].

According to the International Energy Agency, IEA [65], there have been 22 large scale CCS projects in operation or development as of November 2014, and a further 14 in advanced planning stage with final investment to be decided upon this year (2015). Conservative estimates give global offshore CO_2 geological storage capacities of 3,873 Gt and total global storage of 10,506 Gt [66], Therefore CCS is a vital and viable mechanism for mitigating emissions whilst allowing the continued use of fossil fuels in the short to medium term, shown in Figure 2-4 as vital to meet emissions and climate targets by 2050.

2.3 Carbon Capture and Storage

CCS is recognised as a vital step in reducing the effects of climate change caused by greenhouse gasses, it is a multi-stage process where the waste from fossil fuel or biomass burning in an electrical power plant, industrial site or other large point source of CO_2 emissions is separated, collected and compressed in a way that the CO_2 may be transported to a permanent storage reservoir as shown in Figure 2-5, with the aim of storing the CO_2 from escape for tens of thousands of years or more [7]. This enables the continuing use of fossil fuel, but reduces the emissions released to the atmosphere.

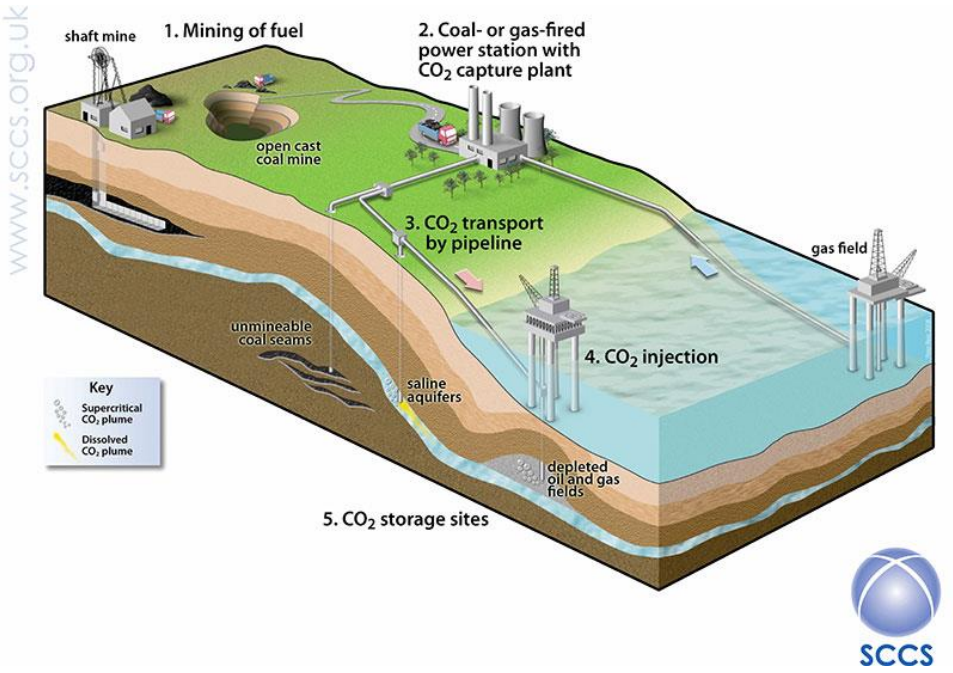

Figure 2-5 *– The Carbon Capture and Storage mechanism [67].*

However, there are major concerns with CCS, mainly how long it can be safely stored and the dangers of seepage to the air and ocean and its effects, with the unknown risk or likelihood of leakage from a pipeline or storage reservoir, and the effect this would have on the local environment and ecosystems. The worry has intensified further by oil and gas leaks in the petroleum industry including the oil and gas leak in the Gulf of Mexico in 2010 [68].

2.3.1 Carbon Capture and Storage Processes

2.3.1.1 Capture

There are a number of CCS capture technologies, known as post-combustion, pre combustion, or oxy-combustion [69]. Waste fumes from fossil fuel or biomass are collected rather than released to the atmosphere in post-combustion. Whereas pre-combustion processes the original fuel prior to burning, producing hydrogen, H_2, and CO_2 [70] where the H_2 may be burned as a carbon free gas. Oxy-combustion burns the fossil fuels or biomass in 95 – 99 % pure oxygen providing fumes consisting of mostly CO_2 and water vapour.

There have been recent laboratory and pilot scale developments in post-combustion [71], along with a commercial size project of 110MW operational since October 2014 [72] capturing 1.0 Mt/yr [73]. There are currently no pre-combustion demonstration power plants in operation, however one is due to start operation in March 2016, and two industrial applications are commercially active, with more due through 2015-2016 [74]. There has been one successful project of oxy-combustion (the Callide Oxyfuel Project) as a mini demonstration, however the White Rose Project is the last potential full scale project utilising this technology, with others put on hold or cancelled [75].

2.3.1.2 Transport

The captured CO_2 must be transported to the storage sites via pipelines, ships, trucks or trains. Pipes are commonly used in the oil and gas industry for extracting the crude oil and natural gases, with industries such as enhanced oil recovery, EOR, also using pipelines to transport CO_2 in supercritical or liquid form [76]. However, for overseas the shipping of liquid CO_2 may be more practical, especially for smaller scale quantities. Road and rail options are possible, however very uneconomical, with pipelines and ships providing the most cost effective methods with the least logistical challenges [77].

2.3.1.3 Storage

Two storage methods are possible, geological storage or deep ocean storage, proposed in the 1970s where the CO_2 is injected into the deep ocean [4], or seabed below 3000 m where a CO_2 lake would form of both dissolved and liquid CO_2 [78]. The choice of storage location depends on availability along with political, social and environmental factors that vary globally, with the London Dumping Convention, 1972, currently preventing direct ocean storage for member states [79], and features such as land faults and earthquakes making geological storage impractical in certain locations [9, 80].

As shown in Figure 2-5, geological storage may be considered onshore [81] or offshore [82]. Both comprise of the injection of CO_2 in a porous and permeable rock formation, deep below the earth's surface [6], with several layers of cap-rock and low permeability barriers preventing the CO_2 from rising back to the surface. Geological CO_2 storage may be conducted in saline aquifers containing reservoir fluids in permeable rocks, unmineable coal beds, with the option of coal mine methane recovery, along with either

active or depleted oil and gas reservoirs with the option of EOR, a technology that has utilised CO_2 for over 35 years in the US [76]. The injected CO_2 will either displace the reservoir fluids, dissolve into them, or most likely a combination of the two [6].

The injection utilises many technologies already used in oil and gas exploration and extraction, including drilling, reservoir monitoring and modelling techniques [83]. Injection is expected to occur at more than 800 m depth from the surface where the temperature and pressure maintains a high density liquid or supercritical state; where the supercritical CO_2 benefits from gas-like expansion and low viscosity allowing the CO_2 to travel through the permeable rock, but with a liquid like high density [84].

2.3.1.4 Trapping in geological storage

Various trapping mechanisms prevent CO_2 rising to the surface, water column and atmosphere. With an injection at ~800 m sediment depth, the density of the CO_2 is expected to be 50 – 80 % that of the brine formation waters, and geoformations at depths greater than 2000 meters will provide a negatively buoyant fluid [6]. Therefore, as a lighter fluid, the CO_2 is forced towards the surface by the reservoir fluids. As a primary trapping mechanism, well-sealed, low permeable cap-rocks are vital to trap the fluid in the reservoir as the first preventative measure of the rising CO_2 [85]. However, in coal beds, the CO_2 is absorbed in the coal as its primary trapping mechanism [86].

Secondary trapping mechanisms include capillary forces keeping the CO_2 in the pore spaces through inter-molecular forces between the solid rock particles in the reservoir, and the fluid, preventing CO_2 migration [87, 88]. Geochemical trapping is another mechanism, where the CO_2 dissolves in the formation waters creating a negatively buoyant solution [89, 90]. Chemical reactions then occur between the solution and the rocks creating carbonate minerals, further blocking the rock pores [91]. However, a recent study shows that the dissolved solution can also become positively buoyant under conditions in a reservoir with high salinity and temperatures [92], but will find an equilibrium density when the temperature and salinity decrease prior to reaching the sediment surface. Another secondary trapping mechanism is the formation of hydrate within low temperature sediment basins which could reduce or even stop the CO_2 release to the ocean through producing a hydrate layer or cap blocking pore spaces [93].

2.4 Risk Assessment

In terms of capture, categorising the risk is relatively straight forward using legislation of current industrial practices for health, safety and environmental control; where much of the capture technology is already in use for separating CO_2 in industries such as ammonia fertiliser and natural gas production [6].

As for the oil and gas industry, there are standards set for pipeline quality, which should be applied to that of CCS in transportation [6]. The quality of the CO_2 transported would also have to be regulated, for example, acceptable quantities of impurities such as hydrogen sulphide [77]. If moisture is present, CO_2 becomes highly corrosive [94] and therefore corrosion resistant alloys or internal pipeline coatings would be required as minimum protection. Even with all the preventative measures in place, accidents happen, however current CO_2 pipelines are reporting less than one accident per year and no injuries or fatalities [95]. This is on the same level as with oil and gas pipelines, with the impact of a CO_2 leak being no worse than that of natural gas [6]. A catastrophic leak would be detected very quickly due to the drop in pressure and rapid release, providing a potential large leakage into the atmosphere or ocean over a very small time period before rectified [40], however also dissipating very quickly, limiting the effects locally and globally.

In terms of shipping, hydrocarbon tankers are potentially dangerous due to the explosive nature of the gas, thus standards are implemented in the design to prevent this, with oil and gas shipping accidents being rare [6], Therefore CO_2 industrial standards should be met, again with corrosion protection measures.

The greatest concern on performing CCS storage in geological locations is the risk and impacts from any potential CO_2 leakage from the storage reservoirs into the shallow water column, marine environment and atmosphere [40]. It is therefore necessary to investigate the leakage possibility and the impacts any potential CO_2 leakage would have on the environment and on the marine life and ecosystems from offshore geological storage [9], the main storage method in consideration across Europe [82]. Although the trapping mechanisms in Section 2.3.1.4 provide multiple leak prevention measures, there is still risk from unforeseeable factors or missed geological anomalies.

The chance of leakage can be minimised utilising many technologies used in oil and gas exploration and extraction [96], including reservoir monitoring and modelling techniques, however if all trapping fails then the ultimate scenario is that the CO_2 will be released to the water column or the atmosphere.

In the global environment, the risk of leakage is very small based on a number of analysis techniques including monitoring of existing storage sites, natural leakage systems and modelling. Predictions show more than 99 % of the injected CO_2 is likely to remain within the reservoir for 100-1000 years, with longer periods decreasing the risk through developments in modelling, monitoring and rectifying techniques, along with further trapping mechanisms [6].

However, leakages may occur, with an effect on the local environment from two possible migration mechanisms for the gas to reach the surface. The most likely leakage scenario [97] may occur at the injection well, or a poorly plugged abandoned well, providing a large release of CO_2 in a short period of time (estimated 0.5 to 5 days from offshore US and North sea oil and gas averages [98]). Detection and rectification is expected to be very quick through mechanisms such as drops in pressure and the rapid release providing initial warnings [40], and blowout preventers preventing further release into the water column [99]. The effects of such a leak will be focused on the local environment, with a very rapid change in gas composition in the atmosphere, or pH in the water column [100] but over a very small area. This would be hazardous to workers in the vicinity of the leak, with gas concentrations of 7 – 10 % CO_2 in air becoming dangerous, and life threatening after 20 - 30 mins at more than 20 % [101], giving offshore CCS as the preferred storage method in Europe [82, 102]. The quantity likely to leak in terms of what is stored in the reservoir is considered very small, with required leak management techniques already tried, tested and in use within the oil and gas industry [96].

The other leakage scenario is migration of the CO_2 through fractures, chimneys, faults in the rock into the higher sediments, or through a leaky well by exceeding the cap-rock fracture pressure, allowing flow out the reservoir [91]. As the CO_2 dissolves in the formation, or around a poorly plugged wellbore, the dissolved solution may also travel

through high pressure out of the reservoir into the water column [103]. The permeability of a fault increases with pressure and can vary across the fault meaning that the leakage zone can be unpredictable, where a fault may be reactivated when the shear stress exceeds the normal strength of the formation, or hydraulic fracturing occurs [104]. These leakages are a lot lower than a well blowout in terms of the leakage flux [40] and may be spread over a far greater area with multiple bubbly pockmarks such as in the QICS experiment [105]. Therefore the leakage may occur over a long period of time due to delayed detection of the smaller leaks, and slower mitigation options of intercepting and removal of the CO_2, with re-injection elsewhere [6]. These leakage methods are summarised in Figure 2-6.

As has been highlighted through the leakage mechanisms, the interactions between leaked CO_2 and the water column is very important in terms of the detectability of leaks, and determining the largely unknown chemical, physical and biological effects on the marine ecosystem for both individual species and the ecosystem as a whole [106]. There are a number of uncertainties in determining these effects that require studies on both existing and potential reservoir modelling and monitoring, but also leakage analysis through both laboratory and in-situ experimental data, along with numerical modelling of various scenarios. These methods are detailed and reviewed in the following section.

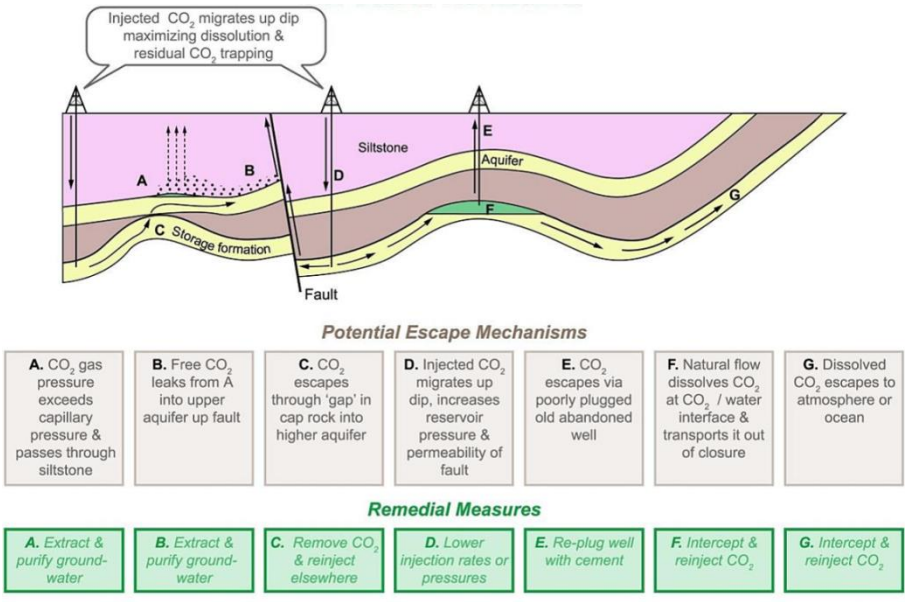

Figure 2-6 *– The potential routes for leakage, along with possible remediation techniques for CO_2 injected into storage formations [6].*

2.5 Review of Risk Analysis

To enable a full risk analysis, monitoring, laboratory and in-situ experiments have been carried out, along with numerical modelling in various recent UK, European and global projects. A common factor in these projects is the aim to better define the impact that a CO_2 leak would have on the marine environment and ecosystem. The ECO_2 [107] and QICS projects [108] describe further objectives of investigating the likelihood and probability of leakage, define monitoring tools and strategies, along with the development of numerical models.

The risk analysis covers a range of topics from geology, sediments and cap-rock integrity, assessing migration pathways [109], monitoring strategies with the likelihood of leakage into the sediments and the leakage flux into the water column through both in-situ experimental work [105, 110 – 116] and modelling [117 – 122]. In the water column, investigations continue on the fate of the CO_2 through in-situ experiments [105, 115, 116, 123 – 126], natural seeps [127 – 133], and numerical modelling [117, 118], 121, 122, 124, 129, 134 – 136] to help develop monitoring strategies, techniques and equipment [105, 110, 115, 125, 128 – 131, 133, 135, 137 – 144]. Biologists determine the impact this has on the marine ecosystem, looking at the consequences of leakage in the short, medium and long term [112, 116, 123, 145 – 158]. This all works towards a comprehensive risk assessment, utilising social, economic and legal studies to determine whether CCS is viable [159 – 163].

2.5.1 Likelihood of Leakage

One of the biggest challenges with the lack of large scale demonstration projects in CCS and the lack of leakages is how to predict the likelihood of leakage, and in turn, the risk to the environment and ecosystem.

Based on data from seepage from natural gas stores, EOR, existing CCS sites, numerical modelling of the physical, mechanical and chemical processes, along with both leakage and storage projects, a common assumption may be made that leakages of any size are extremely unlikely [160].

The likelihood and leakage rates for both high rate well failure, and low rate faults is a greatly debated topic [159]. With the ECO_2 best practice guide [9] and findings from the QICS experiment, it is determined that the best way to reduce the likelihood of leakage is with extensive baseline site and risk characterisation, monitoring and modelling studies to avoid geological structures that may promote leakage mechanisms and risk to the marine ecosystem [9, 137].

2.5.2 Effect on Marine Ecosystem

As the CO_2 dissolves, it creates a change in the acidity in the waters. This acidity adds to the effect of CO_2 on marine life through low pH levels [164], which in turn causes increased mortality rates, distress and narcosis. Long term, lower levels can also have an effect on the metabolism of marine organisms, and be detrimental to the activity, growth and reproduction of marine organisms, with fish being slightly less sensitive than marine invertebrates [6], posing the possibility of local extinctions of particular groups [145].

In the QICS experiment, a low level leak was produced over 37 days [105] where no measurable impact was witnessed on the behaviour of megafauna on the seabed or in the waters during or after the CO_2 release [123]. This was also true for invertebrates such as the common mussel and king scallop that were caged in the area [145]. However, non-caged invertebrates local to the bubble plumes were seen to decline in terms of diversity and numbers. However, a speedy recovery was also witnessed after 18 days [146] suggesting they may have relocated during the disturbance.

Benthic microbes were affected much more, with increases of numbers of microbial genes up to 25 m from the leak epicentre, and a decrease recorded at the epicentre [147]. Little effect on ammonia oxidation through microbial processes was also recorded. However, with higher concentrations of CO_2, ammonia oxidation would slow [148]. Observations of the sediments in the Yonaguni Knoll IV hydrothermal system in Japan also found that the number of microbes decreases sharply with increases in depth and concentrations of CO_2 [153].

Minerals such as phosphorus, calcium, iron, manganese and silicon may be released in the sediments from increased seawater acidity; however, minimal impacts from phosphorus were recorded during the QICS experiment [149], and increased concentrations of the metals were below safe limits [112]. Laboratory experiments show burrowing urchins further affect the water chemistry, giving a greater release of silicate and phosphate and NO_X from within the sediments [152].

Laboratory experiments in the ECO_2 project determine effects at greater pH changes. Larvae of the green sea urchin were witnessed to slow in development, with a reduced growth rate and increased mortality when exposed a pH of 7.0; with pH of 6.5, none of the larvae survived beyond 13 days [150] due to the reduced pH in their digestive system [151], along with a higher frequency of budding (division of cells) witnessed in larvae of the purple urchin [154]. In fully grown green sea urchin, an increase in pCO_2 caused decreased rates of cell and reproductive growth, although metabolic and mortality rates are not significantly affected [158].

The survival of juvenile starfish exposed to pCO_2 levels between 650 and 3500 µatm in 6 and 39 week experiments were not affected by the pCO_2. However, at higher rates the feeding and growth rates reduce due to the inability to acclimatise to the pCO_2 [155]. Brittle star are significantly affected when exposed to pCO_2 of up to 6000 µatm, with reduced metabolic and regeneration rates [156]. However, the acoel worm is found to be unaffected by pCO_2, except in the extreme case where seawater becomes saturated in CO_2 (270,000 µatm), at which point non-lethal bleaching can be seen to occur [157].

Clearly the presence of various species is a large factor in determining the effect and impact on the local marine ecosystem, with each species having a different reaction to increased levels of CO_2 and decreased levels of pH, varying with the size and duration of a leak, along with the distribution of the dissolved solution.

2.5.3 Monitoring

To minimise the risk of leakage and the associated effects, site specific monitoring strategies are required, initially to provide a baseline by logging the sites geological features and the presence of any ecologically or biologically protected or threatened

marine habitats that may be cause for concern prior to CO_2 injection. The baseline also allows predictions of storage capacity and efficiency [165, 166]. Once injection begins, monitoring is required to track the fluid plume movements in the reservoir to determine the direction and speed of the flow towards any geological leakage mechanisms. The water column also requires monitoring in terms of changes that may signify a leak occurring [9].

Comprehensive studies have been investigated at offshore storage facilities, such as Sleipner and Snøhvit, to predict possible pathways that CO_2 could leak through the cap-rock into the sediments [9]. Although no leakage was detected at both sites, a number of geological structures in the larger region of the storage sites were found, namely the Hugin fracture, 25 km north of Sleipner [167], but also further signs of natural fluid pockets, mud volcanoes, craters on the seabed and vertical fluid pathways above the cap-rock [168]. This has helped define new guidelines on baseline assessments of storage locations prior to CO_2 injection to evaluate the suitability for CCS [9].

2.5.3.1 Initial baseline assessment

For the baseline, it is recommended that the overburden, seabed, and the water column of potential storage locations are surveyed prior to CO_2 injection through 3D seismic analysis, high resolution bathymetry/backscatter mapping of the seabed and chemical analysis of any gas or water seeps. The presence of any pockmarks should also be recorded and analysed to determine whether they hinder the structural integrity of the reservoir [9, 137].

In the water column, recordings of the marine biota at the seabed along with the ecosystem above the selected reservoir, and the chemical composition of the seabed and local waters, including combinations of pCO_2, pH, alkalinity, DIC, salinity, phosphate and oxygen which are necessary to determine the waters natural state. Analysis of the water currents is also essential to determine any possible build-up of dissolved solution enhancing the localised risk [169, 170].

These baseline studies provide an outlook of the natural variability of the ecosystem surrounding a potential reservoir. due to seasonal variability, times series data covering at least one year is considered vital prior to drilling or injection [9].

2.5.3.2 CO_2 injection monitoring

Changes beyond the baseline and natural variability are an indication of leakage. Therefore during injection and after storage is complete, sites must be monitored on a regular basis to detect anomalies that present evidence of leakage, including chemical analysis of any emitted gas or fluids in the water column through geological structures to determine the origin [137].

Monitoring in the reservoir can be achieved through 3D seismic recordings, investigating the movement of fluids and the risk of travel through large geological structures [167, 171]. An example from Sleipner can be seen in Figure 2-7, with seismic recordings from the baseline and throughout injection [172]. However, leakages through small structures may only be detected through visual, hydro-acoustic, backscatter or chemical sensors that detect either bubble or droplets, dissolved solutions or reservoir fluids [114]. Once detected and responsibility assigned, the leakage needs to be quantified, determining the effect and impact on the marine environment [137] so that remedial action can be taken.

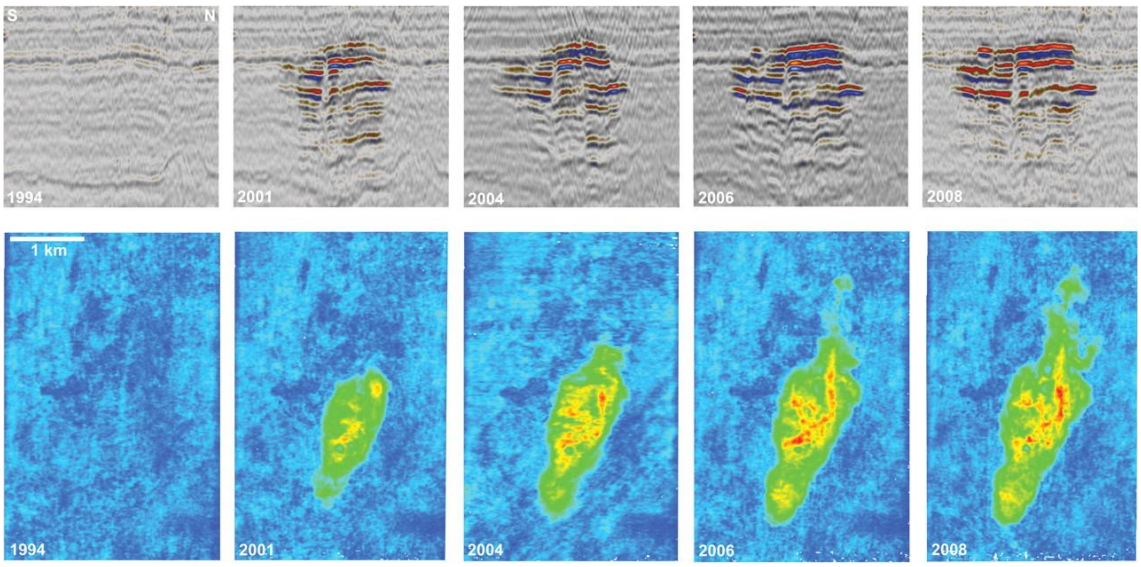

Figure 2-7 *– Time lapse seismic recordings of the Sleipner CO_2 plume, from the baseline in 1994, to 2008. Vertical cross sections, top; Horizontal plan, bottom [172].*

2.5.4 Experiments

To develop monitoring strategies, experimental data is required to provide vital information on signs of leakage including the presence of bubbles or droplets and changes in seawater chemistry. Studies on flow in porous media are common in the petroleum industry to determine hot spots for oil and gas extraction through core sample analysis [173]. Experimental studies of carbon storage structures are no different, with core samples used to determine the porosity and permeability of geological structures [174, 175], well cements [176] and sediments [114, 115] to determine leakage pathways and identify trapping mechanisms. However, as CO_2 is far more soluble than hydrocarbons in seawater [177], the solubility and dynamics of the dissolved solution also require analysis to determine the full storage capability of the reservoir.

In the water column, in-situ experimental studies have also been carried out in the oil and gas industry for well blowouts and leakages in both shallow [178] and deep waters [179]. Again, the solubility will play a greater role with mass transferred from the CO_2 bubble or droplet, and the dissolved solution reacting with the surrounding waters.

A number of experimental studies have been implemented, both in the laboratory, or in-situ, developing the work on two phase flow, CCS viability, along with the risk and effects of leakage.

2.5.4.1 Laboratory

In the water column, analysis of both individual bubble and droplet dynamics, including the presence of hydrate, have been extensively studied in the laboratory [180 – 196] with data sets from air [181 – 186], CH_4 [187 – 189, 197], or O_2 [180] in water, which can be applied to CO_2 through comparing fluid properties and parameters. The dynamics of the dissolved solution has also been investigated to determine the changes in density [92, 198, 199], along with the changes in pH of the water surrounding a droplet [200].

Bubbles and droplets interact through breakup, where larger bubbles break into two or more bubbles as they interact with the waters through tension and turbulent eddies;. meanwhile, coalescence of two or more bubbles also occurs when they collide [201 –

209]. The majority of experiments for interactions have been carried out in pipeline flow; however, models based on these experiments do not take into account the pipeline walls and therefore Hibiki and Ishii [202] predict that they may be suitable for open waters, although further experimental data is required to validate this.

2.5.4.2 In-situ

Laboratory studies which are conducted in ideal conditions, cannot provide the same data as in-situ due to varied fluid properties, natural oceanic conditions and varying currents controlled by both local [210] and global [211] ocean dynamics in the natural environment. It is also a challenge to investigate the fate of CO_2 bubbles and droplets in the laboratory due to the complex dynamics [212]. Therefore to accurately measure the plume dynamics and effect of rising gasses in the open waters, in-situ experiments are required to validate laboratory results.

In-situ experiments of rise velocity and dissolution of CO_2 droplets [212], CO_2 bubbles [105, 212, 213] and CH_4 bubbles [197] have been carried out in-situ over the past 15 years; along with analysis of the impact and effect on the marine ecosystem from a CO_2 droplet plume on the seawater pH [214]. The older bubble and droplet experiments [197, 212] involve the release and tracking of individual bubbles and droplets. However it has been shown that plume effects can modify the dynamics of the gas or liquid release [187, 215] and therefore larger release experiments [105, 213] have also been carried out.

In order to improve the understanding of the effects and impacts from a potential leak on the marine environment, the QICS project was launched in 2010 [105], where for the first time CO_2 was injected into shallow rock sediments to closely mimic leakage into the water column as shown in Figure 2-8; gaining valuable bubble plume data and determining the local fate of the leaked CO_2, changes in pCO_2 and the effect and impact on the marine environment and ecosystem [105].

These experiments are vital, providing essential bubble and droplet data. However, legal and political constraints and scrutiny [212] limit these experiments, despite the minimal long term impact on the area.

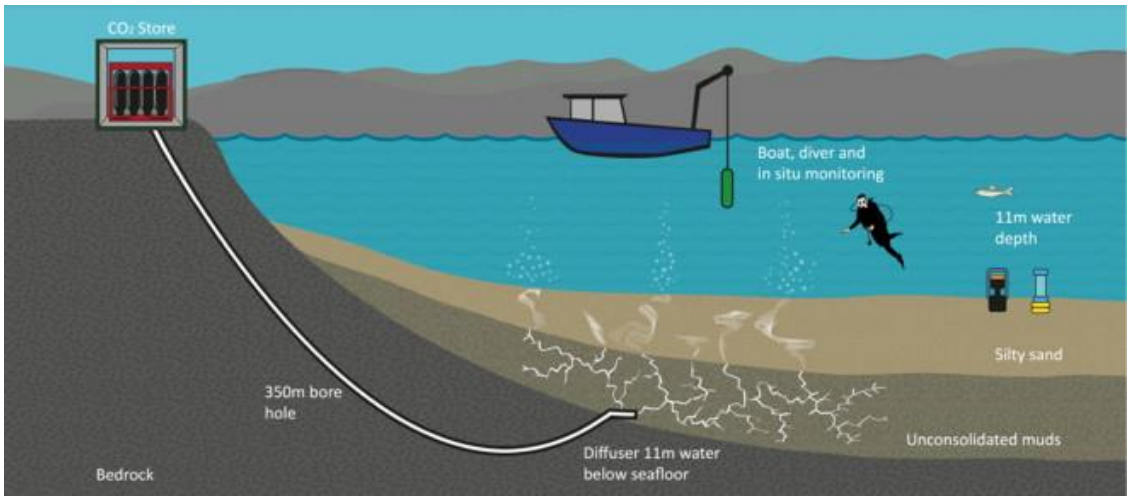

Figure 2-8 *– Schematic of the in-situ QICS experiment [115].*

2.5.5 Natural Seep Observations

Supplementing experimental data, field observations can provide an insight into CCS leakages into the ocean. Comprehensive studies have been performed at natural seepage sites, such as just off the volcanic island of Panarea, Italy, shown in Figure 2-9 [128 – 131, 216], near the Jan Mayen Island in the Norwegian-Greenland Sea [127], the Yonaguni Knoll IV hydrothermal system in Japan [132], the Kelud volcanic lake in Java, Indonesia [217], and in the southern German North Sea [218]. Measurements have been made for bubble size, distribution and dynamics [128, 129, 217], CO_2 concentrations in the water column [127 – 131, 218], along with testing monitoring equipment [128, 130, 131], and measurements of pH in the sediments [132].

Common findings with these CO_2 natural vents are that the bubbles found tend to be small, mostly less than 10mm in size [128, 129] and dissolve in ~10 m height [128, 129]. The velocity varies widely between 22.5 and 47 cm/s not necessarily dependant on bubble size, and linear dissolution rates for diameter with depth are witnessed [129]. The DIC and pCO_2 are found to increase in the water column local to the vents [127], where the pH decreases [128, 218], and further large changes recorded in the sediments [132].

Figure 2-9 *– Natural CO_2 seepage at the Panarea site in Italy [219]*

2.5.6 Modelling

Numerical simulations and modelling are useful tools in estimating leakage rates and predicting the environmental impact [9]; these also have a key role in filling the gaps in the experimental data and observations when determining the fate of CO_2 in the event of leakage from the storage reservoir into the sediments, water column and atmosphere.

2.5.6.1 Geological

Once the structures of the reservoir, cap-rock or sediments are known through core sampling and seismic data, they may be used in numerical models for determining storage capacity [6], potential leakage mechanisms, pathways and structures, along with leakage rates and highlighted risk zones [171, 220] with possible mitigation strategies. The pore scale investigates the fluid flow through rock, with pore interactions and dissolution into surrounding fluids. This can be up-scaled to predict flow rates in a reservoir, geological structures or sediments, which in turn may then be used in the larger scale reservoir modelling and site modelling of up to 1,000 km [221].

Predictions of the geological migration of injected CO_2 through the geological structure into the water column may be conducted through a system of interconnected models, with the migration and dispersion in the sub-surface affected by both geological features

and geochemical reactions [9]. Geological models interpret the geology of the area, highlighting fractures and faults and surrounding geochemical properties that may buffer pH changes and further block the release to the water column [9].

2.5.6.2 Water column

As with the geological models, there is a range of scale for numerical models in the water column. The global-scale models have sub-models for ocean current generation and dissipation between 250 and 600 km [222]. In terms of CCS leakage, these models are not likely to show any significant changes in seawater concentration of CO_2 or pH changes due to the smallest grid length typically of the order of 10^2 and the effects limited to the immediate vicinity [9].

Regional and meso-scale models also include ocean current generation and dissipation sub-models from 10.0 km to the order of 10^2 km [223]. Small-scale models use the ocean energy generated either from larger scale models or experimental data and simulate the sub-grid scale dissipation, showing data within 10.0 km [223]. Bubble and droplet dynamics models can predict the formation, dynamics and dissolution of bubbles and droplets giving the distribution, along with predicting the likelihood of the CO_2 reaching the atmosphere in a gas phase [224].

Each of the models may be coupled or linked together allowing the plume dynamics of the bubbles or droplets to be shown in the water column, analysing the chance of CO_2 reaching the atmosphere, and the effect of the seawater in terms of distribution of the dissolved solution determining the impact on the local environment [169, 225].

2.5.6.2.1 Direct injection

A number of two-phase small-scale simulations were investigated in terms of direct ocean storage [169, 170, 225, 226], either from stationary pipelines or moving ships, rather than leakage from a geological reservoir; these have validated against both laboratory and in-situ experimental data [188, 189, 212, 227]. The dissolution process and reactions between CO_2 and the localised waters is investigated by each of these models, including hydrate formation, through the dynamics of the leaked CO_2 and the

CO_2 enriched waters, with effects to the ecosystem shown by the distribution of dissolved CO_2 or pH changes of the waters.

Although research is continuing in this field [228, 229], progress has slowed with no new developments due to CO_2 direct injection being considered as ocean waste disposal, prohibited under the London protocol and the OSPAR conventions [71]. Following on from a suggestion by Brewer at al. [227] that some of the models and experimental data may also be valid for examining both natural vents and leakage from geological storage sites, a number of models [169, 225, 226] have been further developed so that they may be used in quantifying the risk and impact of leakage from geological structures into the water column.

2.5.6.2.2 Geological leakage

In geological leakage models, the main difference from the direct injection models are that the gas comes from the seabed, where the gas composition, depth, leakage rate, leakage area, and bubble / droplet size cannot be controlled and therefore must be estimated based on observational or experimental data, fluid and geological properties along with data from geological structure models.

If the parameters above can be predicted, then the models designed for direct injection may, through slight modification, be used at high depth leakages from CCS geological sites. Although injection is suggested at >1000 m below the geological surface [212], should leaks form and rise to the geological surface with a lower depth water column of < 500 m [224], leakage would be in the form of gas bubbles and as such the dynamics and dissolution rates are affected [189]. In the medium to deep oceans (>180 m) at a high pressure and low temperature, hydrate coatings form almost instantaneously on the interface between the CO_2 bubbles or droplets and the seawater [230] which affects the dynamics and reduces the dissolution rate [187, 231, 232]. Individual bubble models including hydrate formation have been developed for both CO_2 [224] and CH_4 [187] alongside the droplet plume models designed for direct injection at high depth. These models are based on experimental data for dissolution rates through mass transfer coefficients [233] and solubility [232, 234 – 236] with the dynamics through the velocity [183, 184, 237].

Although individual bubble models are useful in their own right, providing very fast estimations for rising velocities and height predictions based on initial bubble sizes (in the order of seconds for the model by Chen et al. [224]), they have a number of shortcomings. Firstly they do not predict the concentration and distribution of the dissolved solution, and thus cannot predict the impact on the marine ecosystem. They also do not take into account the ocean current which varies the dynamics of the bubbles. The initial bubble size must also be estimated and the simulations do not take into account any inter-bubble interactions. These models are also developed utilising laboratory data that can widely vary with that of in-situ conditions, where McGinnis et al. [187] suggest that two-phase plume effects have a role to play when multiple bubbles leak in close vicinity of one another, not experienced within the results.

To remove some of these assumptions, two-phase plume models bubble are required, such as those in the direct injection droplet models. These can show the dynamics of the bubbles and droplets, and are capable of showing the effect and impact that the leakage would have on the marine environment and ecosystem. However, the existing models contain a number of shortcomings. Prior to the work in this theis, a lack of two phase flow modelling existed for low depth bubbly flow in CO_2 leakage scenarios. There is also currently no two-phase small scale model designed for CO_2 leakage scenarios capable of simulating bubbles, droplets and hydrate formations in the same model, where the previous models simulate one phase or two at most.

The link between geological formations and the water column is also poor, where initial bubble size formation is estimated, instead of calculated [169, 170, 225, 226]; this is one of the most important parameters when determining the distribution of the dispersed and dissolved plumes [170, 225, 226]. There is also a lack of experimental data used to develop the models and sub-models, with no prior studies on interactions of bubbles or droplets as they rise in the water column. Prior interaction studies have only been conducted in pipelines [201 – 209] and only one further modelling study on the distribution from breakup of jet flow into bubbles or droplets in the oil and gas industry [238]. There is also a lack of available in-situ experimental data, where due to the currents, changing seawater conditions and natural variability, data collected from laboratory conditions cannot always accurately compare with oceanic waters.

2.6 Summary

The focus of this project is to investigate the risk and impact of a leak of CO_2 from under the seabed in a geological aquifer formation similar to that of Statoil's Sleipner Project into the water column. The dynamics, behaviour and dissolution of the leaked CO_2 bubbles and droplets will be analysed through the use of numerical simulations. The basis for this model is through the simulations created for direct injection into the ocean, including Alendal and Drange [170], Sato and Sato [226], Chen et al. [169, 225], but focussing on the model produced by Chen et al. [169, 225], which is a double plume model including sub-models of dissolution and movement in a turbulent flow ocean; where further developing the model enables the simulation of both bubble and droplet leakages.

From the literature review, it is clear that there are missing parameters from existing numerical models that are required for further development, such a numerical model capable of simulating the two-phase plume dynamics of CO_2 leakage into open shallow waters in and around the North Sea. Therefore further investigation is required into the two phase flow mechanism and dynamics of the turbulent waters with the effect this has on bubble and droplet formation in the water column from the sediments. This requires analysis of both new and existing sub-models along with new and existing collections of experimental data.

Chapter 3 – Review of the Two Phase Flow

3.1 Introduction

Two-phase or multi-phase flow is the study of exchanges in mass, momentum and energy through interactions between different fluids [184]. The term 'phase' refers to either the physical state of the fluid, such as gas, liquid or solid; or can refer to the chemical components of fluid, such as CO_2 or seawater. These exchanges are governed by the physical laws of conservation of mass, momentum and energy [239] affected by the physicochemical and interfacial properties, and interactions of each fluid.

The focus in this thesis is on geophysical and environmental two phase flows, with the flow of dispersed bubbles/droplets in an unrestricted continuous phase of turbulent seawater, with an investigation on the dynamics of the two-phase plumes. A review of these topics are outlined and organized within this chapter through the theories of two phase flow in Section 3.2 and interfacial interaction dynamics in Section 3.3. Section 3.4 presents an up to date review of the experimental measurements and analysis of two phase plumes. Modelling methods for the turbulent ocean are then described in Section 3.5, with Section 3.6 summarising the findings.

3.2 Conservation Equations for Two Phase Flow

Two phase flow can be categorised by the fluid interaction mechanism. Separated flows are two continuous components with a defined boundary which interact at the interface. Mixed flows are where the fluids are continuous, but also intertwined and mixed. Lastly, dispersed flows are where one fluid distributes and spreads into another fluid [239]. With this work, two of these flows are of interest, namely dispersed flow for the leaked bubbles or droplets into the water column, and mixed flow for the seawater and the dissolved CO_2 as it further disperses in the oceanic waters; note that the latter may be treated as a single phase of mixed fluid of seawater and the dissolved CO_2 solution [239].

The physics of the flow in nature is multi-scale [239], where the interactions at the interfacial layers affect the dynamics developed in the upper scales [240]. Therefore to analyse two-phase flow, these interactions must to be understood [239]. The scale and dynamics in the study of a CO_2 plume in the ocean are schematically described in

Figure 3-1. As the focus of this investigation is on the near-field impacts of leaked CO_2 from the seabed, the spatial scale is set within the order of kilometres; here the CO_2 bubble/droplet plume will develop and couple with the turbulent ocean. The CO_2 can leak from varied depths and areas which gives different leakage rates from the assorted types of sediment on the seabed. The CO_2 may also form as bubbles or droplets, with or without hydrate coatings depending on the depth, with the bubble/droplet size and shape also controlled by the structure of sediments. The bubbles/droplets may further develop to form a plume where collisions and interactions may occur through breakup or coalescence; meanwhile, the dissolute in the surrounding seawater forms another plume of CO_2 solution with a reduced pH.

Using continuum mechanics, the two-phase flow may be considered as two single phase fields with an exchangeable interface between the constituents [239]. Therefore a numerical model may be developed with sub-models to predict the transfer of mass, momentum and energy between each phase.

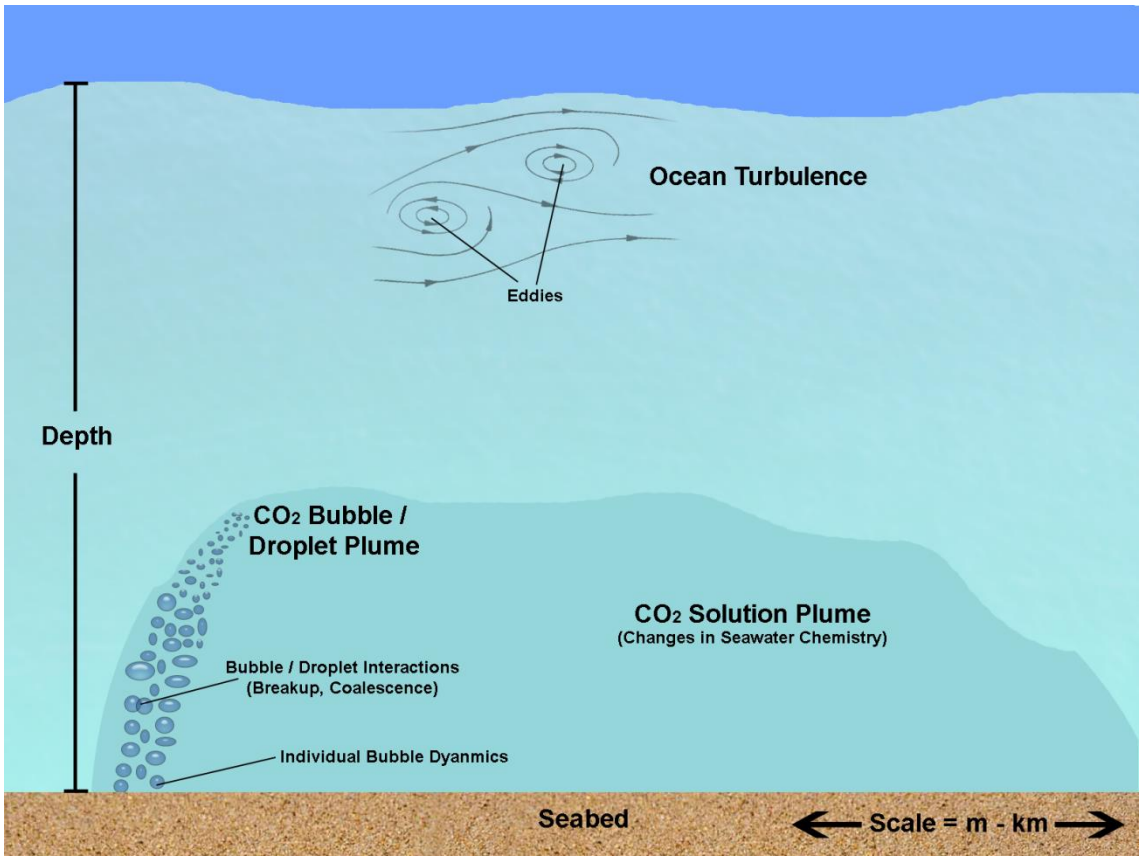

Figure 3-1 *– Schematic of CO_2 plume and dissolution process at a potential leakage site.*

The two phases can be defined as a dispersed phase for the CO_2 bubbles or droplets as subscript 1, and a continuous phase for the seawater as subscript 2, where the void fraction, α, of each fluid may be considered as

$$\alpha_1 + \alpha_2 = 1 \tag{3-1}$$

3.2.1 The Rate of Change of Fluid Properties

Consider a volume, *V*, as shown in Figure 3-2, through which the two fluid flows carry the properties of mass, momentum and energy, Ψ_k, for each phase, *k*, in a Cartesian coordinate system of *j* = x, y, z. The value for the property Ψ_k, of phase *k*, may be expressed through its rate of change within the volume from both changes with time, and changes due to flux across the surface area, *A*, along with any source or sink terms, $\dot{q}_k$.

$$\frac{\delta(\Psi_k)}{\delta t} = \frac{\partial}{\partial t}\int_v \alpha_k \varphi_k dV + \oint_A \alpha_k \varphi_k u_{k,j} dA \frac{\partial}{\partial t} - \int_v \dot{q}_{k,\Psi} dV \tag{3-2}$$

The surface integral in the second term on the right hand side of the equation may be converted to a volume integral by application of Stoke's theorem [241] in the vector field.

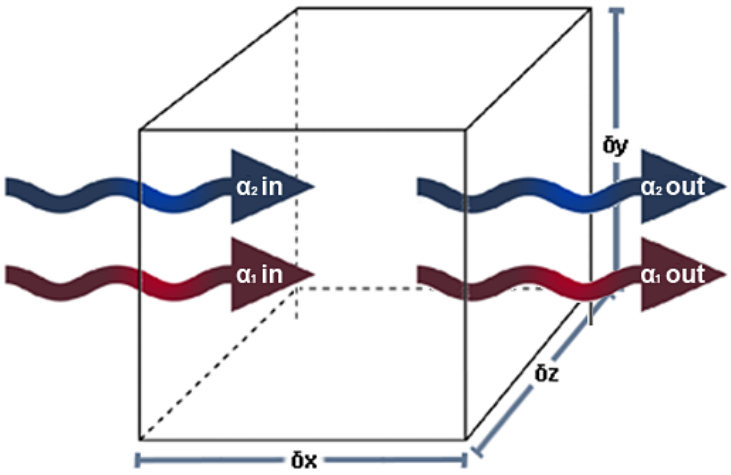

Figure 3-2 *– The volume into which the fluids flow, with an example of one dimensional flow in the X direction.*

$$\oint_A \alpha_k \varphi_k u_{k,j} dA = \int_v \frac{\partial \alpha_k \varphi_k u_{k,j}}{\partial x_j} dV \tag{3-3}$$

Substituting (3-3) into (3-2) yields the rate of change of the property in the considered volume,

$$\frac{\delta \Psi}{\delta t} = \int_v \left(\frac{\partial \alpha_k \varphi_k}{\partial t} + \frac{\partial \alpha_k \varphi_k u_{k,j}}{\partial x_j} - \dot{q}_{k,\Psi} \right) dV \tag{3-4}$$

and will be applied in the derivation of the governing equations for two-phase flow in the following sections.

3.2.2 Conservation of Mass

The continuity of mass is a physical law based on chemistry experiments from Mikhail Lomonosov and Antoine Lavoisier in the 18th century [242]. The concept is that mass remains constant with the absence of any sources or sinks. Considering a given volume of multi-phase fluid, this may be expressed in that the rate of change in mass of a fluid can only be due to the mass exchange between fluids. Applying Equation (3-4) with $m_k = \Psi_k$ and $\varphi_k = \rho_k$, we have,

$$\int_v \left(\frac{\partial \alpha_k \rho_k}{\partial t} + \frac{\partial \alpha_k \rho_k u_{k,j}}{\partial x_j} - \dot{q}_{k,m} \right) dV = 0 \tag{3-5}$$

where $\dot{q}_m$ is the specific mass exchange rate between the fluids, in this case through dissolution. Approaching the infinitesimal volume, *V*, this leads to the core integral

$$\frac{\partial \alpha_k \rho_k}{\partial t} + \frac{\partial \alpha_k \rho_k u_{k,j}}{\partial x_j} - \dot{q}_{k,m} = 0 \tag{3-6}$$

Finally, for each phase we have,

$$\frac{\partial \alpha_1 \rho_1}{\partial t} + \frac{\partial \alpha_1 \rho_1 u_{1,j}}{\partial x_j} = -\dot{q}_m \qquad \textit{and} \qquad \frac{\partial \alpha_2 \rho_2}{\partial t} + \frac{\partial \alpha_2 \rho_2 u_{2,j}}{\partial x_j} = \dot{q}_m \tag{3-7}$$

3.2.3 Conservation of Momentum

The momentum transfer of fluids is governed by Newton's second law, where the change in inertia is equal to the total applied forces [243]. Applied to two phase flow, the rate of change in momentum for phase, *k*, is balanced by forces that are applied to the fluid. The momentum of fluid *k* in the given volume is therefore calculated with $M_{k,i} = \Psi_k$ and $\varphi_k = \rho_k u_{k,i}$ through Equation (3-4),

$$\frac{\partial \alpha_k \rho_k u_{k,i}}{\partial t} + \frac{\partial \alpha_k \rho_k u_{k,i} u_{k,j}}{\partial x_j} - F_{b,k} - \frac{\partial F_{s,k}}{\partial x_j} - \dot{q}_f = 0 \tag{3-8}$$

with the source and sink term $\dot{q}_{k,\Psi}$ for momentum including body forces, F_b, with respect to the volume and surface forces, F_s, with respect to the surface area converted to a volume integral through Stoke's theorem, along with the momentum transfer occurring between the two fluids $\dot{q}_f$ [239].

Momentum transfers from fluid 1 to fluid 2, as the bubble or droplet plume acts on the seawater plume. Therefore, for each phase we have

$$\begin{aligned} &\frac{\partial \alpha_1 \rho_1 u_{1,i}}{\partial t} + \frac{\partial \alpha_1 \rho_1 u_{1,i} u_{1,j}}{\partial x_j} = F_{b,1} + \frac{\partial F_{s,1}}{\partial x_j} - \dot{q}_f \quad \textit{and} \\ &\frac{\partial \alpha_2 \rho_2 u_{2,i}}{\partial t} + \frac{\partial \alpha_2 \rho_2 u_{2,i} u_{2,j}}{\partial x_j} = -F_{b,2} - \frac{\partial F_{s,2}}{\partial x_j} + \dot{q}_f \end{aligned} \tag{3-9}$$

3.2.3.1 Forces

The applied forces can include surface forces and body forces [244], where body forces act on the inside the fluid itself. The most common body force in fluid flow is buoyancy through gravity, with negligible further electrostatic and electromagnetic forces [239].

$$F_g = -\Delta(\alpha\rho)g \tag{3-10}$$

Surface forces are those that are applied on an area of the fluid [245], this includes both pressure and shear forces, with the pressure acting on the area perpendicular to each surface.

$$F_s = - p + t_{ij} \tag{3-11}$$

In shear forces, t_{ij}, the velocity gradients due to viscosities act parallel to the surface as shown in Figure 3-3. The shear force, with viscosity resisting the motion [246], can be estimated by

$$t_{ij} = m\frac{\P u_i}{\P x_j} \tag{3-12}$$

3.2.3.2 Navier-Stokes and Euler equations

Applying the buoyancy, pressure and shear forces listed in Equations (3-10), (3-11) and (3-12) to the momentum balance in Equation (3-9), gives the Navier-Stokes equation [247, 248],

$$\frac{\partial \alpha_2 \rho_2 u_{2,i}}{\partial t} + \frac{\partial \alpha_2 \rho_2 u_{2,i} u_{2,j}}{\partial x_j} = -\frac{\partial p}{\partial x_i} + \frac{\partial}{\partial x_j}\left(\alpha_2 \mu \frac{\partial u_{2,i}}{\partial x_j}\right) - \alpha_2(\rho_2 - \rho_{sw})g + \dot{q}_f \tag{3-13}$$

where the buoyancy in the seawater (fluid 2) comes from the changes in the fluid density from both the temperature gradient, and the effect of the dissolved CO_2 solution.

If the viscosity term is ignored in an ideal flow setting, this would give Euler's equation which was developed ~100 years prior to the Navier Stokes equation [249]. This can be used to govern the momentum flow of the dispersed phase for bubble or droplet plumes given as,

$$\frac{\partial \alpha_1 \rho_1 u_{1,i}}{\partial t} + \frac{\partial \alpha_1 \rho_1 u_{1,i} u_{1,j}}{\partial x_j} = \alpha_1(\rho_2 - \rho_1)g - \dot{q}_f \tag{3-14}$$

where the shear and pressure forces in the dispersed bubble or droplet plume (fluid 1) are negligibly small in comparison to the buoyancy driving force.

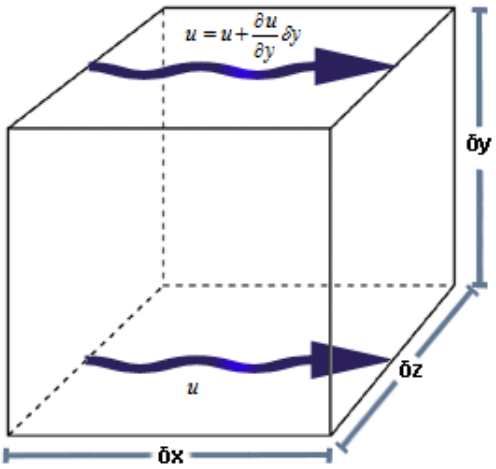

Figure 3-3 *– Changes in the X velocity from shear forces in the Y direction.*

3.2.4 Conservation of Energy

The energy equation is derived from the physical law of the conservation of energy in an open system within the given volume. For seawater, the total energy, E_2, includes both internal and kinetic energies, neglecting potential energy. Applying Equation (3-4), the rate of change of total energy comes from heat interactions and the work done on the system, with $E_2 = \Psi_k$ and $\varphi_k = \rho_2 h_2 = \rho_2 (E_2 + \frac{1}{2} u_{2,j}{}^2)$,

$$\int_v \left(\frac{\partial \alpha_2 \rho_2 h_2}{\partial t} + \frac{\partial \alpha_2 \rho_2 h_2 u_{2,j}}{\partial x_j}\right) dV = \oint_A (-\dot{q}_s + \dot{w}_s) dA + \int_v (\dot{q}_t + \dot{w}_b) dV \qquad (3\text{-}15)$$

where $\dot{q}_t$ and $\dot{w}_b$ are the heat transfer received from and work done by the dispersed phase respectively, and $\dot{q}_s$ is the heat flux out across the system surface, with $\dot{w}_s$ as the work done on the system by the surface forces. Utilising Stoke's theorem [241] on the right hand side of (3-15), we have

$$\oint_A (-q_s + w_s) dA = \int_v \frac{\partial}{\partial x_j} (-q_s + w_s) dV \qquad (3\text{-}16)$$

This gives the general energy equation of seawater by substituting (3-16) to (3-15), where the volume becomes infinitesimal,

$$\frac{\partial \alpha_2 \rho_2 h_2}{\partial t} + \frac{\partial \alpha_2 \rho_2 h_2 u_{2,j}}{\partial x_j} = -\frac{\partial (\dot{q}_s - \dot{w}_s)}{\partial x_j} + \dot{q}_t + \dot{w}_b \tag{3-17}$$

The heat flux may be predicted through Fourier's law [250], where the heat flux is equal to the fluid conductivity, K_t, multiplied by the negative of the local gradient of temperature,

$$\dot{q}_s = -\alpha_2 K_t \frac{\partial T_2}{\partial x_j} \tag{3-18}$$

The work done by surface forces normal to the system come from the pressure gradient and shear forces.

$$\dot{w}_s = -\left(p + \alpha_2 \tau_{ij}\right) \cdot u_{2,j} \tag{3-19}$$

Substituting Equations (3-16) - (3-19) to Equation (3-15) gives the full energy balance for seawater.

$$\frac{\partial \alpha_2 \rho_2 h_2}{\partial t} + \frac{\partial \alpha_2 \rho_2 h_2 u_{2,j}}{\partial x_j} = \frac{\partial}{\partial x_j}\left(\alpha_2 \rho_2 K_t \frac{\partial T_2}{\partial x_j} - \left(p + \alpha_2 \tau_{ij}\right) \cdot u_{2,j} \right) + \dot{q}_t + \dot{w}_b \tag{3-20}$$

To further simplify this equation, the momentum in Equation (3-8) may be converted to energy by multiplying by the velocity $u_{2,j}$.

$$\frac{\partial \alpha_2 \rho_2 \frac{1}{2} u^2_{2,j}}{\partial t} + \frac{\partial \alpha_2 \rho_2 u_{2,i} \frac{1}{2} u^2_{2,j}}{\partial x_j} = u_{2,j}\left[-\frac{\partial p}{\partial x_i} + \frac{\partial \alpha_2 \tau_{ij}}{\partial x_j} + \left(F_b - \dot{q}_f\right) \right] \tag{3-21}$$

Subtracting Equation (3-21) from Equation (3-20) gives the internal energy equation,

$$\frac{\partial \alpha_2 \rho_2 E_2}{\partial t} + \frac{\partial \alpha_2 \rho_2 E_2 u_{2,j}}{\partial x_j} = \frac{\partial}{\partial x_j}\left(\alpha_2 \rho_2 K_t \frac{\partial T_2}{\partial x_j} \right) + \alpha_2 \tau_{ij} \frac{\partial u_{2,j}}{\partial x_j} + \dot{q}_t \tag{3-22}$$

where the second term on the right hand side of the equation is the heat generated from the viscous dissipation of fluid flows that may be neglected for the energy balance in

this study. If the specific heat capacity of seawater, c_v, is considered as an constant, then the final version of the energy equation of seawater can be obtained and applied as,

$$\frac{\partial \alpha_2 \rho_2 T_2}{\partial t} + \frac{\partial \alpha_2 \rho_2 T_2 u_{2,j}}{\partial x_j} = \frac{\partial}{\partial x_j}\left(\alpha_2 \rho_2 K_t \frac{\partial T_2}{\partial x_j}\right) + \frac{\dot{q}_t}{c_v} \tag{3-23}$$

For the CO_2 bubble/droplet plume, there are two kinds of heat interaction; the formation and dissociation heat from CO_2 hydrates, along with the heat generated from CO_2 dissolution. As discussed by Chen et al. [225], the effect of these heat interactions on the dynamics of both phases of CO_2 and seawater will be negligibly small if the dispersed plume is the scale of a bubbly leakage rather than an eruption. This effect is therefore neglected by setting $\dot{q}_t = 0$. It is further assumed that a thermodynamic equilibrium state for CO_2 and seawater can be reached instantaneously because of the relatively large heat capacity of seawater, and the effective heat transfer enhanced by the convective flow across the bubbles/droplets, giving $T_1 = T_2$.

3.2.5 The Transport of Scalar Properties

In addition to the mass, momentum and energy, further properties of seawater and CO_2 are needed to model simulations of the plume dynamics. These include the bubble/droplet number density, salinity of the seawater, and concentration of the CO_2 solution. These are known as scalar properties, $\phi_s = (n_k, S, Y_{CO2})$, which share a transportation equation.

The flow of the scalar properties through a considered volume may be treated in the same manner to that of mass by the continuity equation. The the rate of change in each scalar is caused by the presence of any source terms, $\dot{q}_s$, such as dissolution for the dissolved CO_2 concentration, interactions for the bubble/droplet number density and with diffusion, D_s, across the volume surface for the salinity and CO_2 solution.

By applying Equation (3-4) and setting $\phi_s = \Psi_k$ and $\varphi_k = \phi_s$, the transportation equation of scalars can be derived as,

$$\int_v \left(\frac{\partial \alpha_k \rho_k \phi_s}{\partial t} + \frac{\partial \alpha_k \rho_k \phi_s u_{k,j}}{\partial x_j}\right) dV = \oint_A \rho_k D_s \frac{\partial \phi_s}{\partial x_j} dA + \int_v (\dot{q}_s) dV \tag{3-24}$$

Applying Stoke's theorem [241] to the first integral on the right hand side of the equation gives the equation for scalar transportation,

$$\frac{\partial \alpha_k \rho_k \phi_s}{\partial t} + \frac{\partial \alpha_k \rho_k \phi_s u_{k,j}}{\partial x_j} = \frac{\partial}{\partial x_j}\left[\alpha_k \rho_k D_s \frac{\partial \phi_s}{\partial x_j}\right] + \dot{q}_s \tag{3-25}$$

Both the density and the void fraction are set to 1.0 for the concentration of the dissolved solution, Y_{CO2}, and for the bubble/droplet number density, $n_{k,}$ respectively, with the diffusivity of the latter set to zero.

3.3 Two Phase Flow Interactions

The viscosity of the fluid defines the fluids internal resistance to changes in motion and flow through shear stress [246]. Ludwig Prandl showed that fluid flow past an object has two very distinct regions through both theory and experiments [251]. One region is a thin film close to and surrounding the object known as the boundary/interface layer where friction, shear stresses and viscosity take a large role. The second region is the remaining flow outside of this layer where effects may be greatly neglected [252]. Low viscosity flows such as air flow more freely at a distance away from the object in comparison to a high viscosity fluid such as oil at the same distance [252]. Therefore, this boundary/interface layer theory is important in two phase flow as interactions between each phase occurs within the boundary/interface layers, such as drag forces and heat or mass transfer [252]. To describe the flow characteristics of the boundary, mechanically similar flow properties must be defined, where similar boundaries and interactions are witnessed in the flow for different fluids, velocities, and dimensions based on dimensionless numbers including ratios of forces applied to the fluids [252].

3.3.1 Turbulence and the Reynolds Number

Boundary layer theory was originally developed in laminar flows of incompressible fluids, this theory is now fully developed [252]. Turbulent flow studies with boundary layer theory have also been advanced through Reynolds [253] highlighting the importance of turbulent stresses, and Prandtl [254] introducing theories of the Prandtl

mixing length. However, a theory for fully developed flows is yet to be accurately defined [252]. The point when flows transition from a laminar flow to a turbulent flow was investigated by both Reynolds in pipe flow [253] and Prandtl in flow around a sphere [254], where a non-dimensional number, named after Osbourne Reynolds as the Reynolds number, Re, is used to define mechanically similar flows for varied fluids, velocities and geometries [252], along with investigating the mechanically similar point where the inertial forces of the fluid largely overcome the viscous forces [253],

$$\mathrm{Re} = \frac{inertial\ force}{friction\ force} = \frac{\rho u \partial u/\partial x}{\mu \partial^2 u/\partial y^2} = \frac{\rho u L}{\mu} \qquad (3\text{-}26)$$

where L is a characteristic length scale which can be the diameter of a bubble or droplet flowing through liquid or the distance the flow travels across a surface. When Re exceeds a critical transitional number, regardless of the fluid, geometry or velocity, the laminar fluid flow changes to a flow with irregular movements of fluid parcels with eddies and circulation, where the fluctuating kinetic energy eventually dissipates into heat at a molecular level due to the viscosity [240], this is known as turbulent flow.

In a pipeline the critical Reynolds number to transition from laminar to turbulent is considered to be from 2,300 [255], however over a flat surface the transition to turbulent flow is much greater, upwards of 200,000 [256] dependant on the roughness of the surface, with a figure of 500,00 widely accepted [257]. To reach the critical Reynolds number usually requires a high velocity, however low velocity flows such as the ocean are turbulent due to the significant length of the surface of the seabed that the flow travels across, with a 10 cm/s flow reaching a Reynolds number of 500,000 over a distance of around 5 – 10 m.

3.3.2 Bubble/Droplet Breakup, Coalescence and the Weber Number

The Weber number is a measure of the bubble or droplet stability which analyses the ratio of the inertial against tension forces to define maximum size characteristics.

$$We = \frac{inertial\ force}{tension\ force} = \frac{\rho u^2 d}{\sigma} \quad (3\text{-}27)$$

The Weber number is most often used in bubble or droplet break-up where the inertial force exceeds the surface tension giving a critical size at which bubbles can form, or where larger bubbles break into smaller bubbles [258] as shown in Figure 3-4. The number density source term in Equation (3-25) may be predicted through bubble or droplet interactions, with a combination of coalescence and breakup terms, where the breakup and coalescence may be predicted by correlations such as those developed in pipe flow [201 – 209], with the breakup based on the critical Weber number and the coalescence based on the kinetic theory of ideal gas molecule interactions.

3.3.3 Bubble/Droplet Shape and the Morton and Eötvös Numbers

Further dimensionless numbers exist from interactions in the interfacial layer, allowing interactions to define geometrical patterns and mechanically similar properties in the bubble or droplets, such as shape and size. These patterns are controlled by the buoyancy, inertial and tension forces.

The Eötvös number, Eo, also known as the Bond Number, Bo, analyses the ratio of the buoyancy against tension forces [259] to define shape characteristics.

$$Eo = Bo = \frac{buoyancy\ force}{tension\ force} = \frac{\Delta\rho g V}{\sigma L} = \frac{\Delta\rho g d^2}{\sigma} \quad (3\text{-}28)$$

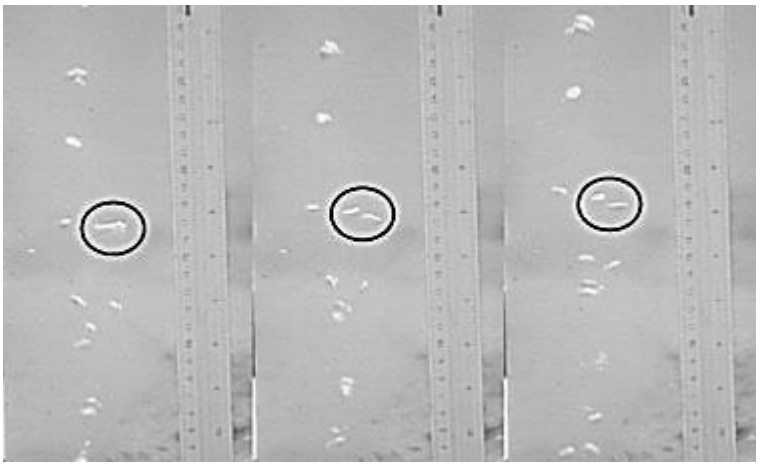

Figure 3-4 *– Photo montage of CO_2 bubble breakup.*

With a high number indicating a low surface tension, making a bubble or droplet more likely to deform [260]. This is often used in combination with the Morton number, Mo, utilising the inertial, buoyancy, tension and friction forces to describe shape characteristics [261] defined from fluid properties alone with no geometrical dimensions.

$$Mo = \frac{\left(\frac{inertial\ force}{tension\ force}\right)^3}{\left(\frac{inertial\ force}{friction\ force}\right)^4} \cdot \left(\frac{buoyancy\ force}{inertial\ force}\right) = \frac{We^3}{\mathrm{Re}^4} \cdot \frac{\Delta\rho g}{\rho u^2 / L}$$

$$Mo \quad \frac{g\mu^4 \Delta\rho}{\rho^2 \sigma^3} \tag{3-29}$$

3.3.4 Drag Force and the Drag Coefficient

Shear force or drag is generated by the viscous forces between fluids when a relative velocity is created at the interface. The drag force may be described through use of a drag coefficient, C_d, another dimensionless number, linking the drag force to the inertial force,

$$C_d = \frac{drag\ force}{inertial\ force} = \frac{F_d}{1/2\,\rho u^2 A} \tag{3-30}$$

As the drag force is a resisting force between a pair of mechanically similar fluids, the drag coefficient is a function of the Reynolds number, especially smaller bubbles that remain spherical due to low buoyancy forces. Many correlations have been proposed for the drag coefficient, with rising bubble and droplet flows researched experimentally [181 – 186, 188 – 190, 192, 262], and numerically. Stokes [263] defined the drag coefficient for spherical objects at low velocities as a function of the Reynolds number, C_d=24/Re. Larger bubbles and droplets have greater buoyancy and therefore start to deform from spherical to elongated, with cap like shapes, where further studies have focused on taking into account the aspect ratio of the deformed bubbles or droplets at larger sizes [169, 184, 225, 226, 237, 262, 264, 265]. To also take into account the

effect of shape deformation, dimensionless numbers including Weber, Morton and Eötvös numbers are used in some studies [189, 265, 266] and tested within many numerical models [188, 189, 266 – 269].

The drag force therefore provides the momentum exchange between the bubble or droplet and the seawater as shown in Figure 3-5. The mean surface area that the drag force acts upon is calculated in Equation (3-31), based on the volume fraction and number density, where the volume fraction is equal to the number density of the droplets multiplied by the individual bubble or droplet volume.

$$\alpha = nV = n\frac{\pi}{6}d^3 \qquad d = \left(\frac{\alpha}{n}\frac{6}{\pi}\right)^{1/3} \qquad A = \frac{\pi d^2}{4} = \frac{1}{4}\left(\frac{6\alpha}{n}\right)^{2/3} \tag{3-31}$$

The drag force source term for Equation (3-13) and (3-14) may then be modelled in terms of the drag coefficient, C_d, from Equation (3-30).

$$q_f = \frac{1}{8}\bar{\rho}_1(6\bar{\alpha})^{2/3}(\pi\bar{n})^{1/3}C_d\left|\bar{u}_{2j} - \bar{u}_{1j}\right|\left(\bar{u}_{2j} - \bar{u}_{1j}\right) \tag{3-32}$$

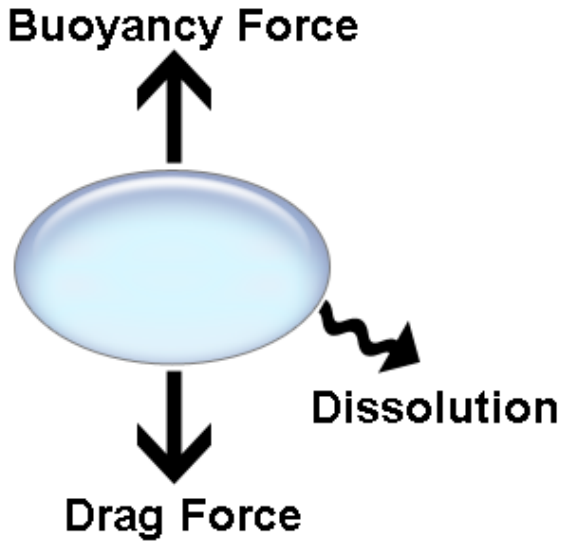

Figure 3-5 *– CO_2 rising bubble or droplet dynamics, with the drag force acting against the inertial force from the buoyancy force and dissolution through convective mas transfer.*

3.3.5 Mass Transfer and the Sherwood Number

Mass transfer through dissolution occurs in the interfacial layer through convection; a sum of the bulk mass transfer through the fluid flow (advection) and the natural mass transfer at the molecular level (diffusion) [270], shown in Figure 3-5.

To compare between the mass transfer by diffusion and convection, the dimensionless Sherwood number, Sh, is employed, defined as the ratio of convective mass transfer in real fluid flow, with that of pure diffusive mass transfer [271, 272].

$$Sh = \frac{Effective\ \ Mass\ Transfer}{Diffusive\ Mass\ Transfer} = \frac{k_m d}{D_f} \tag{3-33}$$

As another parameter for mechanically similar flows, Sh, should also be a function of the Reynolds number and other dimensionless parameters. Studies have been carried out by experiments [180, 181, 186, 190 – 193], where empirical correlations have been developed for mass transfer with bubbles [184, 187, 194, 233, 268] in terms of mass transfer coefficient, and droplets [169, 225, 231, 262, 269, 273, 274] in terms of Sherwood number.

As with the drag coefficient, modifications to this function are made to take into account the shape deformation and geometry, where for droplets [169, 195, 225, 262, 275, 276] deformation factors for the aspect ratio are often included along with additional dimensionless numbers to ensure the flow is mechanically similar such as the Schmidt number, Sc, that defines the ratio of momentum diffusivity (viscosity) and the diffusive mass transfer in the boundary layer [277] as shown in Equation (3-34).

$$Sc = \frac{Diffusive\ Momentum\ Transfer}{Diffusive\ Mass\ Transfer} = \frac{\nu}{D_f} \tag{3-34}$$

For bubbles, the mass transfer occurs at a lower rate [224] due to the smaller density, where the shape, especially for larger bubbles, can be far more deformed than a liquid counterpart. The effective mass transfer, k, is therefore predicted, not by Re, but by the size and relative velocity of the bubble directly in experimental correlations [183, 184, 233, 267, 278, 279], from which, the Sherwood number may be predicted.

The mass exchange source term in Equations (3-7) may be predicted through the CO_2 mass dissolution rate [184],

$$q_m = k_m A(C_s - C_0) \tag{3-35}$$

where C_s and C_0 are the solubility of the CO_2 and the background concentration of dissolved CO_2 concentration in seawater respectively, and A is the total interface area. The source term in the governing Equation (3-7) can then be calculated by,

$$q_m = (6\bar{\alpha})^{1/3}(\pi\bar{n})^{2/3} Sh D_f (C_s - C_0) \tag{3-36}$$

through converting the surface area using Equation (3-31) and the mass transfer coefficient using Equation (3-33).

3.4 Measurements of Two Phase Flow

As detailed in Section 2.5, two phase flow interaction experiments for bubble and droplets have been developed extensively in the laboratory, allowing numerical correlations to be developed, such as the drag coefficient, the mass transfer coefficient or Sherwood number, along with the coalescence and breakup interactions for a range of bubble and droplet shapes and sizes.

In-situ experiments and natural leakage analysis provide additional data to validate these correlations, where properties of the plume effects, ocean currents and the dynamics of turbulence are largely excluded from laboratory experiments due to the size of the apparatus required to simulate open water flow acting against the ability to focus on the micro-scale two phase interactions of individual bubbles or droplets. In-situ experiments may be at great depth where the instruments cannot be deployed or managed without Remotely Operated Vehicles, ROV, due to the harsh conditions, where the ROV also has the ability to travel quickly through the water column, tracking bubble or droplet dynamics and dissolution.

3.4.1 Imaging Techniques

Regarding the experimental measurements of bubble dynamics, rise velocity and dissolution, most previous in-situ or laboratory studies have gathered data using high

speed photography and imaging techniques [280] as shown in Figure 3-6, with recent studies utilising either CCD [197, 212, 281 – 284] or CMOS [285] sensors, and prior studies using analogue video cameras. The differences in the principles of CCD and CMOS sensors in digital cameras and camcorders is not discussed in detail as it goes well beyond the scope of this study. However, the specifications of each sensor in terms of application are briefly analysed.

The signal to noise ratio measures the amount of noise in the signal provided from the sensor, and the spatial standard deviation measures how varied the signal is recorded across the sensor. State of the art CCD sensors, such as in the PCO Sensicam, provide good image precision through a high signal to noise ratio, and a low spatial standard deviation at both high and low signal levels, compared to the CMOS sensor in the PCO 1200hs (with the same resolution and exposure time) that only has a high signal to noise ratio and low spatial standard deviation at high signal levels [286]. However, CMOS sensors often provide better data in time series images as they can be used at a higher frame rate without compromising on picture quality due to the shorter exposure time required; an example is the Photron APX CMOS sensor which has an exposure time of 50 μs compared to 2 ms with the PCO Sensicam CCD sensor [286].

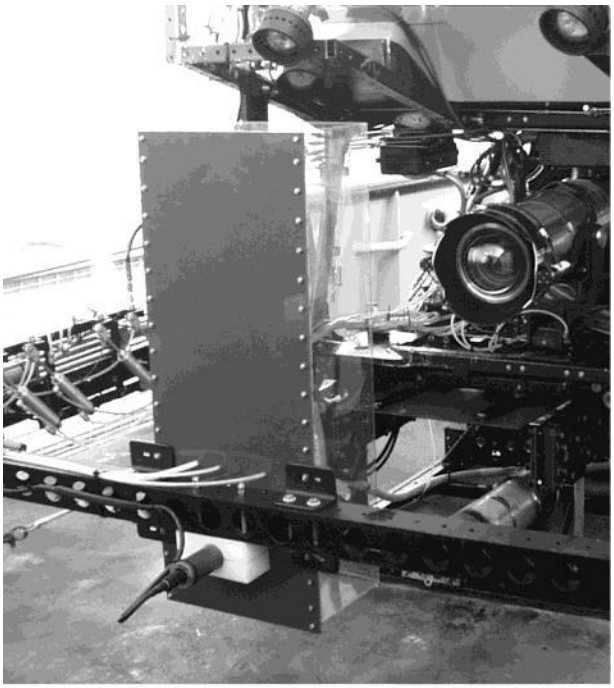

Figure 3-6 *– A CCD camera mounted on the front of an ROV, with an imaging box in front to prevent the bubble stream from travelling away from the camera [212].*

3.4.2 Enhanced Imaging and Laser Techniques

The bubble/droplet images recorded are often unsteady with unpredictable instantaneous dynamics. Therefore, Particle Image Velocimetry, PIV, can be used as an imaging processing technique to measure the detailed variation in bubble characteristics in a turbulent flow field [287], capable of tracking the size, shape, velocity, acceleration, and mass transfer of a bubble or droplet, whilst simultaneously measuring the fluid velocity field in 2 dimensions [280]. This is achieved through utilising both a camera and a laser/strobe to highlight tracer particles that are added to the fluid allowing the flow pattern to be recorded. Laser Induced Fluorescence, LIF, can however also help in tracking bubble trajectories utilising photosensitive dyes [280], with the fluorescence highlighting the trajectory and dynamics of the bubble interface including dissolution. Utilising a pH sensitive dye, pH changes from bubble or droplet dissolution may be established [200] as shown in Figure 3-7.

Imaging techniques and analysis for measurements is highly time intensive to obtain good data [280]. Laser Doppler Anemometry, LDA, is a method that significantly reduces the extraction time for the measurement of a bubble or droplet rise velocity, even in a high number density plume. However this technique is unable to detect other properties such as bubble shape or size [288]. The measurements are based on the analysis of a laser light at a set frequency that changes in proportion to the velocity of the bubble/droplet as it travels through a measuring location [289].

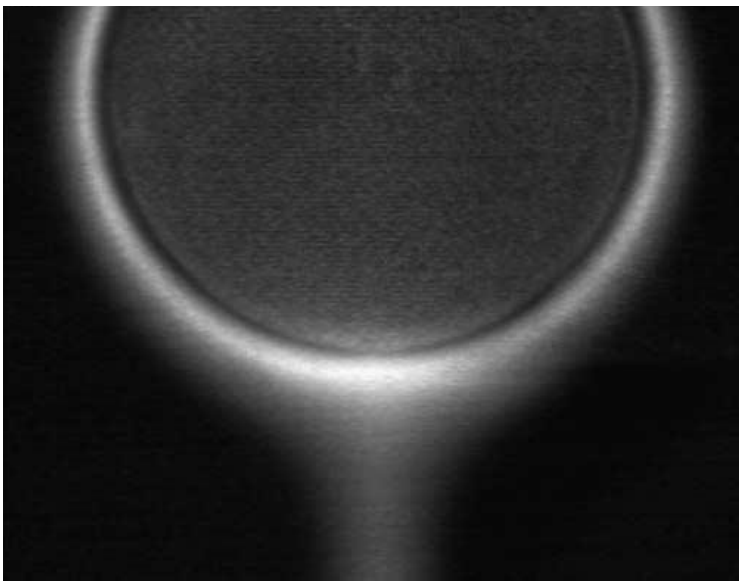

***Figure 3-7** – An image of CO_2 bubble dissolution, utilising LIF and a pH dependant dye [200].*

3.4.3 Acoustic Techniques

Acoustic techniques include both active and passive measurements. Passive techniques record the sound created by the bubbles themselves as they emerge from the sediments, and active techniques produce a sound wave and collect the reflected signal which allows a sonar image to be produced [290]. Both active and passive techniques have the potential to predict gas flux, however, for long term monitoring, passive systems are preferred, with active systems requiring greater power to produce the acoustic wave [126].

Studies on passive acoustic bubble sizing and distribution have shown that as a bubble breaks free from a surface, the bubble and surrounding fluid oscillate at a low amplitude to the bubbles natural frequency in simple harmonic motion. This property can be exploited, as suggested by Minnaert [291] to detect bubbles where the natural frequency of each bubble is inversely proportional to the bubble diameter. The benefits of this method to determine bubble sizes over optical or active acoustic measurements and gas collection systems are that the passive acoustic recording requests very low power [292], with a Canon EOS 5D Mark II CMOS camera requiring 24W [293] compared to a sonar active acoustic technique requiring about half of this at 12 W [294], and a hydrophone of less than 1W [295]. Therefore constant monitoring in the long term can be achieved, and the effects of rapid dissolution of gasses such as CO_2 [218] in collection and imaging measurements can be avoided [3]. Greene & Wilson [292] studied the passive acoustic technique to measure the flow rate of air in distilled water, and as with this study, the results were compared with optical methods. They also collected the gas to verify the results due to the low solubility of air [177]. In their study, small ($d_e \approx 2$mm) individual bubbles were released at frequencies between 0 and 10 bubbles per second from a single nozzle. The passive acoustic technique works well, where the authors suggest that this technique can likely provide an effective method in monitoring gas seeps of both individual and multiple bubble streams if the flow rate is sufficiently low. In-situ recordings have also been conducted at methane seeps in the natural environment with average frequencies of 25 bubbles per second which supports the application of this theory [296]. More recently Leighton and White [297] have successfully captured bubble size distribution in high flux leaks where bubble acoustics overlap through analysis of the acoustic energy of each bubble, utilising the assumption

that each bubble is excited once, allowing the contribution of each bubble to the overall acoustic spectrum to be predicted [126].

3.5 Reconstruction of the Small Scale Turbulent Ocean

Ocean turbulence is a nonlinear dynamic system of unsteady fluid motion. Its scale varies from global where energy is generated through interactions with atmosphere, solar system and moon to drive the ocean circulation at low frequencies [298], down to microscopic scales where kinetic energy dissipates through molecular viscosity into heat [240] as shown in Figure 3-8.

Atmospheric weather patterns and energy, such as kinetic energy in wind and thermal energy, are generated by the sun. When air is heated at ground level, absorbed and radiated by the earth from the sun, it rises due to the decrease in density. This displaces the cooler air above providing the dynamic energy to the air in the lower atmosphere [298].

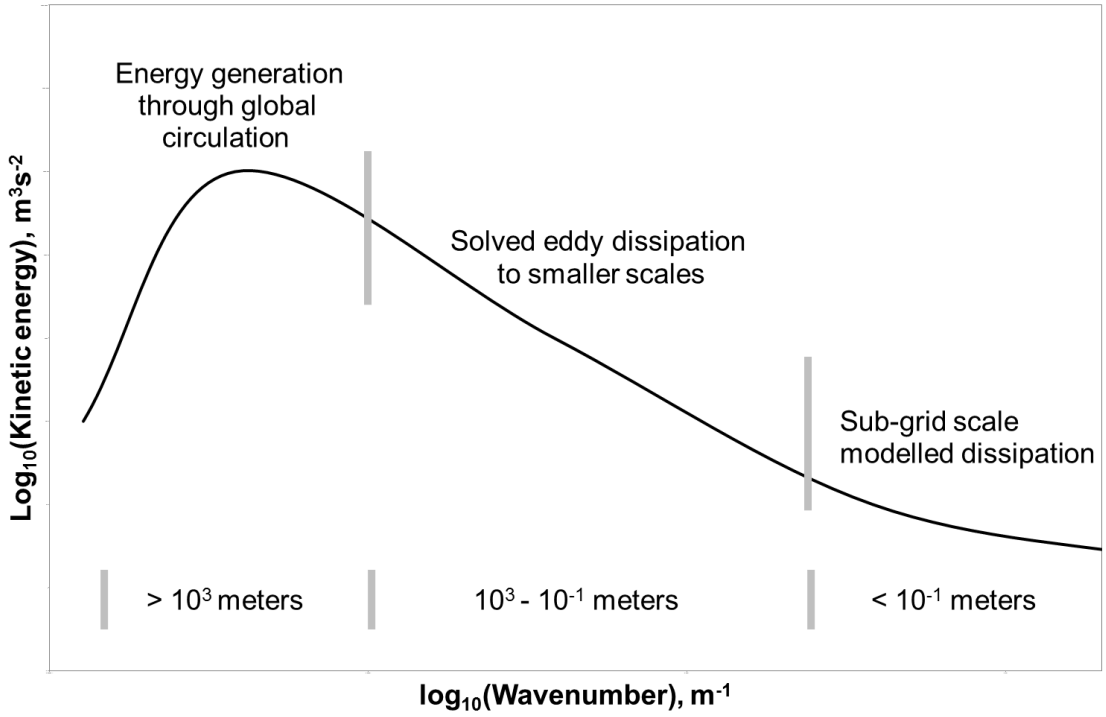

Figure 3-8 *– Sketch of a kinetic energy spectra (not to scale); showing the energy provided from global circulation to the small scale dissipation.*

In global scales, heating in the tropical regions, and cooling from higher latitudes providing upwards and downwards motions. Including the rotation of the earth, this generates circulation in the atmosphere as proposed by Halley [299] and Hadley [300]. In the same manner, kinetic energy and circulation is generated in ocean currents from solar radiation and the rotation of the earth, along with momentum transferred from atmospheric winds [298].

3.5.1 Modelling Turbulence

It is crucial to develop a small-scale turbulence model to predict pollution dispersion and impacts to the ocean. At the small scale, pollution cannot be considered as just a mass source to the ocean, but also a momentum source. Kinetic energy from buoyant bubbles is transferred to the local seawaters in bubbly gas leaks, providing upward motions. As gasses are soluble in seawater [177], the dissolved solution can also produce further buoyancy motion depending on the effect of the solution in terms of changes in density.

The interactions between the leaked bubble plume and the original turbulent ocean are investigated by the two-phase small-scale turbulent ocean model through kinetic energy spectrum analysis. A small-scale turbulent ocean is therefore reconstructed from the theories of a forced-dissipation mechanism for the ocean, from the meso to small scales. To understand the turbulence characteristics in the small scale, a set of time series current data observed from The North Sea [301] is collected as shown in Figure 3-9, with the mean current over 98.5 hours, along with the fluctuating mean over 10.0 and 1.0 hours.

Although turbulent flows are irregular and seemingly random and chaotic, it can be found that the flow has statistically regular characteristics [302]. This means that although flow is developing with unpredictable eddies at various velocities and scales, the time average or volume average of the flow over a set scale may be statistically predicted. This allows analysis of the fluctuating flow through kinetic energy spectra taken by a Fast Fourier Transform (FFT) of the current data as shown in Figure 3-10.

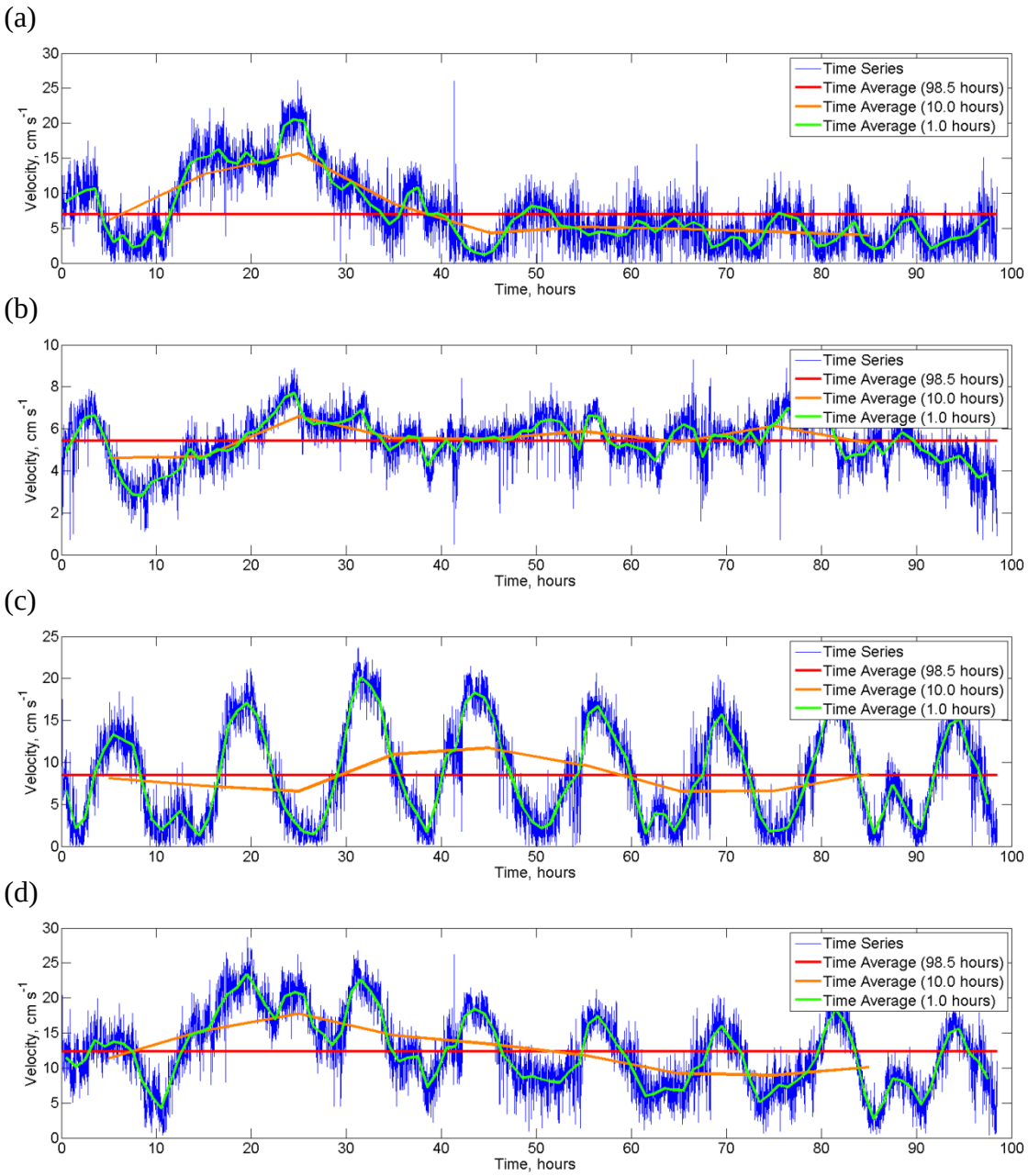

Figure 3-9 *– Time series current data (blue line) from 27th - 31st July 2012 in the central North Sea (58°24'23.11"N 2°1'25.33"E) [301], with the time average mean velocities (red line for 98.5 hours, orange line for 10.0 hours, green line for 1.0 hour). (a) X direction, top; (b) Y direction (vertical), middle top; (c) Z direction, middle bottom; (d) total magnitude, bottom.*

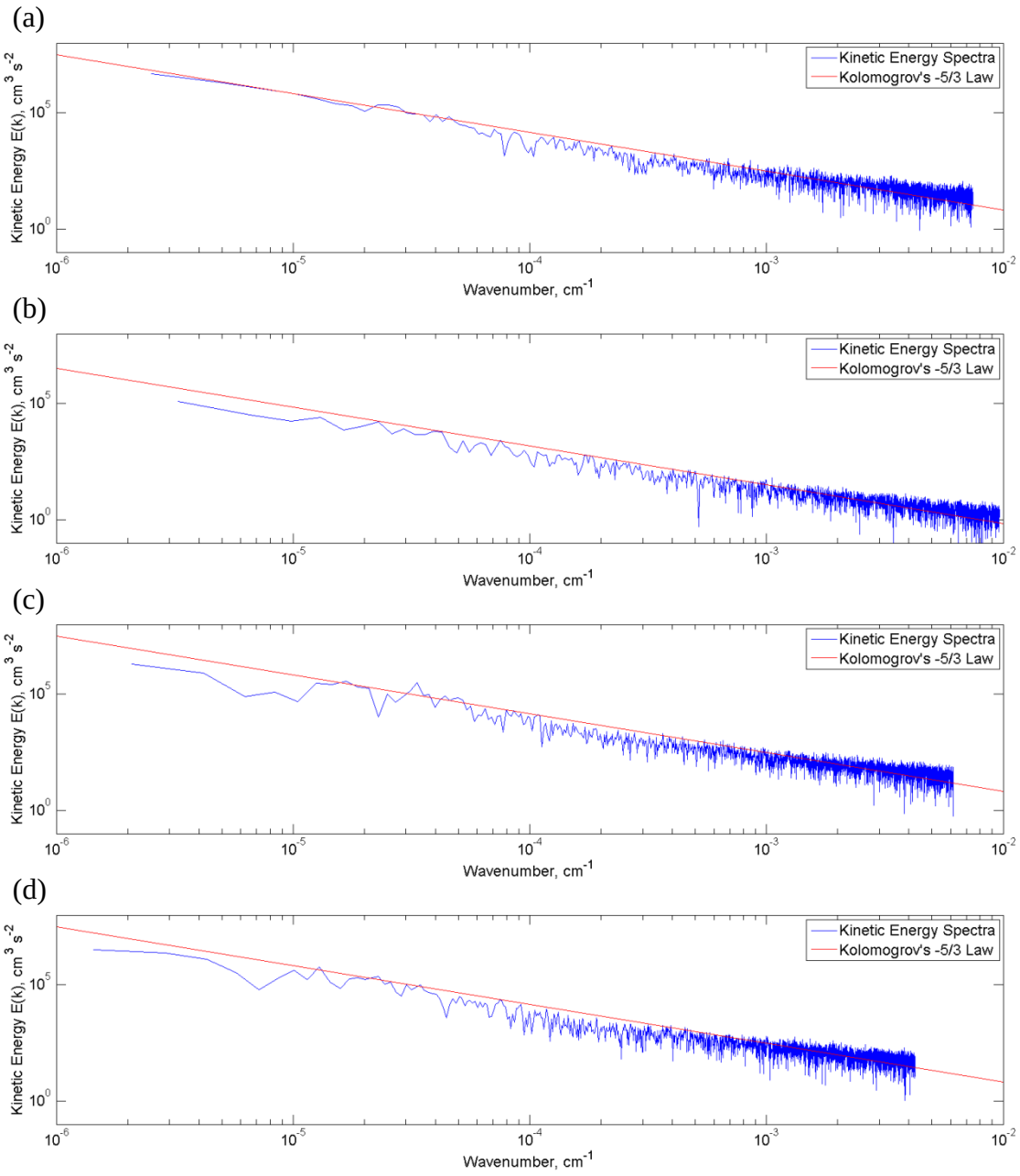

Figure 3-10 *– Fluctuating kinetic energy spectra (blue line) taken from data analysed from the central North Sea (58°24'23.11"N 2°1'25.33"E), compared with Kolmogorov's -5/3 gradient law [303] (red line). (a) X direction, top; (b) Y direction (vertical), middle top; (c) Z direction, middle bottom; (d) total magnitude, bottom.*

Kolmogorov [303] found through theoretical investigations that turbulence behaves with isotropic energy cascade characteristics at scales much smaller than the source of turbulent energy, but much larger than those where viscosity plays a role. Therefore the rate of transfer of turbulent kinetic energy from greater scales to smaller scales should be consistent. For the ocean, it has already been identified that the sources of turbulent kinetic energy are that of the larger regional and global scale; and dissipation through viscosity into heat occurs on the molecular scale. Therefore in the meso and small scales, the dissipation through breakup and decay of eddies from one scale to another will occur at a constant rate. In each of the directions, the rate of dissipation may be predicted in the logarithmic scale with a gradient of -5/3 through Kolmogorov's law [303],

$$E(k) = C_k \varepsilon^{\frac{2}{3}} k^{-\frac{5}{3}} \tag{3-37}$$

with C_k as a constant. A good agreement is found from the theory and that from the observation data from the North Sea, shown in Figure 3-10. The fluctuations may come from the limited range of experimental data, observational noise, and rounding errors in the FFT. The errors from the limited available data would reduce through the use of an increased data set increasing the statistical predictability of the fluid flow. However, the number of errors from rounding would increase with the larger data set [304].

The fluctuating kinetic energy from oceanic turbulence in the vertical direction, shown in Figure 3-10 (b), is at least one order lower than that of the horizontal plane, which demonstrates the effects of ocean stratification. The kinetic energy in the vertical direction is generated by thermal heat transfer, surface waves, and momentum transferred from the horizontal planes. This kinetic energy is dissipated at all scales through stratification due to the vertical density distribution.

Turbulence is arguably the most complex phenomenon in terms of fluid motion. However, it can be described in terms of the conservation of momentum; especially for simple liquid and gas flows. This is defined theoretically by the Navier-Stokes (N-S) equation [305]. Ideally, turbulent flows would be directly numerically simulated. This would require a powerful super computer to simulate the dynamics down to the smallest

scales, known as the Kolmogorov scale, $\eta = (\nu^3 / \varepsilon)^{1/4}$; in the range of 0.1 to 10 mm in oceanic flows [306]. However, with today's technology this is not possible. Without a powerful super computer, the turbulent stress term in the momentum transportation and the turbulent scalar transportation equations must be modelled for the smaller eddies.

The N-S equations for a single phase small-scale ocean can be derived from Equation (3-13) by removing the source term for two-phase flow,

$$\frac{\partial \rho_2 u_{2,i}}{\partial t} + \frac{\partial \rho_2 u_{2,i} u_{2,j}}{\partial x_j} = -\frac{\partial p}{\partial x_i} + \frac{\partial}{\partial x_j}\left(\mu \frac{\partial u_{2,i}}{\partial x_j}\right) - (\rho_2 - \rho_{sw})g + Fs_{ij} - \frac{\partial Ds_{ij}}{\partial x_j} \qquad (3\text{-}38a)$$

where, Fs_{ij} is the force transferred from the large-scale oceanic kinetic energy, while, Ds_{ij}, is the sub-grid scale turbulent stress, dissipating the kinetic energy to maintain the cascade dynamics of the ocean.

$$Ds_{ij} = \rho_2 \overline{u'_{2,i}\, u'_{2,j}} = \rho_2 \nu_t \frac{\partial u_{2,i}}{\partial x_j} \qquad (3\text{-}38b)$$

This technique is known as the force-dissipation mechanism, where modelling of the forcing and dissipation terms is discussed in the following sections.

3.5.1.1 Reynolds-Averaged Navier-Stokes

The first method for simulating turbulent flows is from Osbourne Reynolds [307], later known as Reynolds-averaged Navier-Stokes (RANS). In this technique the turbulent flow may be characterized from the time or distance average of the motion, along with the local fluctuation of the motion.

$$\rho u(x,t) = \rho \bar{u}(x,t) + \rho u'(x,t) \qquad (3\text{-}39)$$

The first such model introduced eddy viscosities to close the averaged Navier-Stokes equations [308]. Models developed can be categorized as mixing-length based one-equation models [309], k-e based two-equation models [310], and Reynolds stress models [311]. The benefits of RANS are that it has a small computational cost, with low requirements for computational power, memory and time. However, it is limited in that

the average flow may be solved, but the internal turbulent flow field itself is unable to be predicted [240].

3.5.1.2 Direct Numerical Simulation

Direct Numerical Simulation (DNS) is a numerical method where the Navier-Stokes equation is solved directly with no extra turbulence models required [312]. However, the grid must be to very fine to encounter the turbulent flow for all scales, including resolving each individual temporal and spatial fluctuation of the flow [240]. In most cases this in not feasible in terms of computational power, memory and timescale, except for the most simple of fluid flows that contain relatively low Reynolds numbers [313].

3.5.1.3 Large Eddy Simulation

Large Eddy Simulation (LES) is a concept where the larger scales of the turbulent fluid flow are explicitly solved, with the smaller unresolved turbulent flows included as an additional modelling term in the Navier-Stokes equation [314]. Low pass filtering is utilised to remove the fluctuations at the smaller scales [315], reducing the computational cost and allowing the flow to be calculated over a coarser field than in DNS. The turbulent characteristics at these unresolved smaller scales are modelled through a range of sub-grid scale models [314].

The larger scales are relevant in terms of the mixing and transport of the flow, with the smaller scales providing more of a universal isotropic dissipative flow, independent from the larger scales [303, 316]. The key difference between LES and RANS, is that the small scales are those in the same order or smaller than the grid size in LES, whereas RANS considers all but the largest eddy to be cut off, with the smaller scales averaged [314]. The suitability for LES can be seen in Figure 3-8, with the small scale numerical model fitting between the large scale energy generation at scales greater than those simulated, and the linear grid and sub-grid dissipation, with the latter numerically modelled.

3.5.2 Choice of Modelling Technique for the Small-Scale Turbulent Ocean

Although DNS, LES and RANS numerical models are valid modelling techniques for the small-scale turbulent ocean, the quality of results from the model can vary based on

the chosen technique. Figure 3-11 shows a sketch of arbitrary simulations of DNS, LES and RANS at a single point in a fully developed steady turbulent flow. DNS simulations cover all scales of the simulation, including the largest and smallest eddies showing the complete flow field. However, DNS is not practical in this case as previously discussed due to the size of grid required to cover all the scales. RANS by its definition gives a constant mean velocity fluctuation at a point in a steady flow, where LES fits between the two, giving a range of wavelengths, but smoother than DNS due to the filtered velocities [317].

Turbulent fluctuations occur in the ocean at scales from millimetres to hundreds of kilometres [318], therefore as the turbulent features across the grid scale (meters) are not numerically calculated in RANS, LES simulations are often considered more reliable and numerically suitable than RANS methods [314]. In other words, LES shows the fluctuations across the grid elements at all the wavelengths above its filter size, whereas RANS shows less detail by filtering out all but the top wavelength, giving the averaged fluctuating flow across the grid [317]. However, LES will only provide a better match to experimental data than RANS when a sufficiently fine grid is employed in wall bounded flows [319].

In the open ocean, when the grid size is sufficiently large as to ignore the wall effects, LES is suitable at lower resolutions in the small-scale region, within 10.0 km [223]. The energy is generated through a forcing term within the simulation [320, 321], and dissipates through the isotropic cascade characteristics predicted by Kolmogorov [303]. An increase in the number of grid points or the reduction of mesh size in LES will only increase the accuracy, approaching that of DNS.

LES also provides a far lower computational cost than DNS, allowing flows at relatively greater Reynolds numbers be simulated. However LES does require higher computational time and power than RANS methods [314]. Therefore LES is considered to provide a good medium between the extremes in terms of both computational use, and the ability to show the turbulent field accurately for the larger scale flows in non-wall bounded simulations.

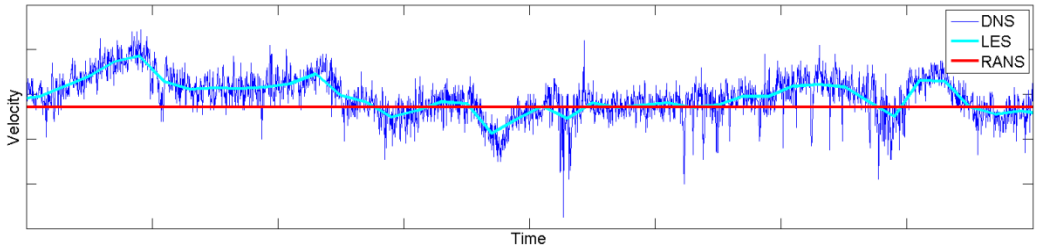

Figure 3-11 *– Sketch of the comparison between DNS, LES and RANS simulations at a single point in the grid from a fully developed steady turbulent flow.*

3.6 Summary

Two phase flow mechanisms are developed and a set of governing equations are derived to numerically predict the mass, momentum and energy transfers between each phase. A number of complex phenomenon in the interfacial boundary layers are investigated utilising sub-models to predict mechanically similar properties; this includes bubble stability and break-up through the We number, the bubble or droplet changes in shape through the Eo and Mo numbers analysing both geometrical and fluid properties, the drag force between the two phases through the drag coefficient and mass transfer through the Sh number.

Most of the correlations for these two phase dynamics are developed from laboratory experimental data, therefore there is a need to validate against in-situ experiments or natural seepage observations where there are far less controlled conditions providing a better indication off the two phase flow in turbulent waters and open water column.

The turbulent ocean must also be modelled, with the various options investigated and analysed in terms of DNS, RANS and LES, with a discussions on the applicability dependant on both the simulation resolution and grid size.

Chapter 4 – Dynamics of Bubbles: The QICS Experiment

4.1 Introduction

Sufficient understanding of the dynamics of dispersion and dissolution of CO_2 bubbles and droplets in both water and seawater are necessary and fundamental to the development of associated correlations for the drag coefficient and Sherwood number, key to the drag force and dissolution mechanisms, and required to close the momentum and continuity equations for two phase flow in the two phase model developed for this thesis. Further sub-models also require development to predict plume interactions including breakup and coalescence affecting the number density distributions, the source term of Equation (3-25). Bubble size distribution and the related velocity are key parameters to these sub models and correlations, along with the fluid properties and phase.

In Section 4.2 there is a discussion on the fluid phase, under which circumstances the CO_2 is in the gas or liquid state, along with the presence of a hydrate coating. Then Section 4.3 presents the new experimental observations made as part of this thesis, both in the laboratory and in-situ, enhancing the correlation sub-model development utilising both imaging and passive acoustic measurements to determine the bubble size, shape, interactions and velocity. Finally, Section 4.4 summarises the experimental findings for the dynamics of bubbles in the dispersed phase.

4.2 Physical State

The physical state of the CO_2 has a great effect on dissolution and dynamics of the fluid, mainly due to the differences in density and solubility. A plume of rising bubbles can be found at depths shallower than 400 meters [224], there is also the potential of the bubbles forming hydrate coats if the depth is more than 180 meters and the temperature is below ~4°C as shown in Figure 4-1 based on data from Sun and Duan [322]. As the density increases, a plume of rising droplets can be found at depths greater than 550 meters [224], these also have the potential to form hydrate coats when the temperature reduces below ~8°C [322]. The intermittent depths between 400 meters and 550 meters may provide bubbles or droplets dependant on the local temperature, as seen in Figure 4-1.

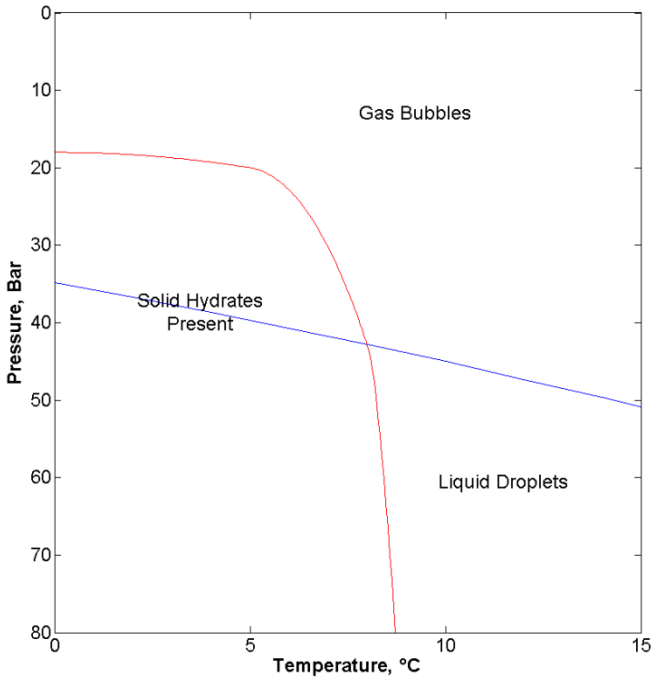

Figure 4-1 *- The phase change of CO_2 from liquid droplets, to gas bubbles (blue line); and the stability of hydrates (red line) based on pressure (1 bar ≈ 10 meters depth), and temperature [322].*

4.3 Experimental Observations

Experimental observations for the dynamics of bubbles and droplets in the seawater have been studied greatly in terms of oil and gas, with more recent observations on that of CO_2 droplets, in terms of dissolution [212] and dispersion [188, 189]. However there are few data sets for CO_2 bubbles at shallow ocean in terms of dispersion, with previous data sets based on either CH4 [187 – 189, 197] or air [181 – 186].

Therefore experiments have been designed for investigation on shallow bubble leakage, both in the laboratory (utilising air to validate the measurement techniques) and in-situ (with CO_2) to fill the gaps from the available data to simulate leakages within the North Sea.

4.3.1 Imaging Technique

The bubble size, shape, trajectories and interactions among gas bubbles are processed using image processing software [323]. The location and edges of each CO_2 bubble were determined as a result of manual image processing, where the evaluation of the

bubble size is characterised by the equivalent diameter, d_e, from the measured cross sectional area, A, against a scale.

$$d_e = \sqrt{\frac{4A}{\pi}} \tag{4-1}$$

The geometry of the larger CO_2 bubbles measured may be further characterised by two dimensions: the major axis dimension, d_{mj}, and the minor axis dimension, d_{mi}, of the bubble. Where an in-line scale was not possible, the measured dimensions are corrected for perspective through a geometrical calculation based upon the distance between the bubble plume and the scale, X, along with the focal length of the camera, L, as seen in Figure 4-2.

$$d_e = d_s\left(1 - X/L\right) \tag{4-2}$$

The velocity of CO_2 bubbles is also measured by comparing the vertical coordinate of each bubble centre between frames y_1 and y_2 respectively. With a time interval of $\Delta t = 1/30\,\text{s}$, the vertical velocity of the CO_2 bubble relative to the seafloor may be calculated.

$$V = \frac{\left(y_2 - y_1\right)}{\Delta t} \tag{4-3}$$

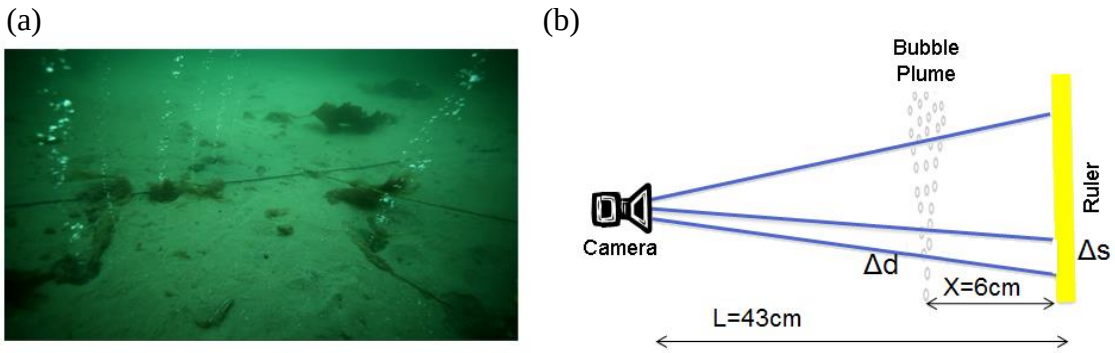

Figure 4-2 *– Experimental set up. (a) The observation field of bubble-plumes, left; (b) schematic view of the observation system, right.*

4.3.2 Passive Acoustic Technique

Through the digital audio signal spectrum, a passive acoustic method is also employed to investigate the size of the bubbles and the bubble distribution utilising the natural frequency of each individual bubble emitted from the sediments into the water column. This technique was developed by Minnaert [291] as applied by Leighton [290], to exploit the natural frequency of the bubble oscillation.

The general principle of the technique is a kinetic and internal energy balance of the bubble in simple harmonic motion where the fluctuating bubble radius may be described as $r = r_0 + r_\varepsilon(t) = r_0 - r_{\varepsilon 0} e^{i\omega_0 t}$. Assuming the bubble has a spherical surface, the kinetic energy of the water flow around the bubble may be calculated as

$$E_k = \frac{1}{2}\int_r^\infty \left(4\pi R^2 \rho \partial R\right)\dot{R}^2 \tag{4-4}$$

where the mass of the liquid flowing around the bubble skin is $m_{skin} = 4\pi R^2 \rho \partial R$, and the mass flow rate of liquid through a spherical surface around the bubble within time Δt is $\dot{m} = 4\pi R^2 \rho \dot{R} \Delta t$. If the surrounding liquid is considered to be incompressible, the mass flow rate is constant at any radius [290], providing the ratio

$$\dot{R}/\dot{r} = r^2/R^2 \tag{4-5}$$

Substituting Equation (4-5) into Equation (4-4) and conducting the integration provides the kinetic energy as

$$E_k = 2\pi r^3 \rho \dot{r}^2 \tag{4-6}$$

The maximum kinetic energy, $E_{k,\max}$, occurs when the bubble radius is at the equilibrium position $r = r_0$ and under simple harmonic motion $\dot{r} = i\omega_0 r_{\varepsilon 0} e^{i\omega_0 t}$ giving the solution

$$E_{k,\max} = 2\pi r_0^{\,3}\rho\left(r_{\varepsilon 0}\omega_0\right)^2 \tag{4-7}$$

The maximum bubble potential energy, $E_{p,\max}$, will occur when the bubble radius is furthest away from the equilibrium position $r = r_0 \pm r_{\varepsilon 0}$ and under simple harmonic motion $\dot{r} = 0$. Assuming the process is adiabatic and the work done to compress the bubble is $-\left(p - p_e\right)dV$

$$E_{p,\max} = -\int_{V_0}^{V_{\min}} \left(p - p_0\right)dV = -\int_{r_0}^{r_0 - r_{\varepsilon 0}} \left(p - p_0\right)4\pi R^2 \partial R \tag{4-8}$$

In addition, assuming the gas in the bubble is a perfect gas, experiencing an adiabatic process $pV^{\gamma} = k$ and $r_{\varepsilon} = r - r_0$ provides the relation

$$\frac{p}{p_0} = \left(1 + \frac{r_{\varepsilon}}{r_0}\right)^{-3\gamma} \tag{4-9}$$

Using a first order binomial series approximation this may be expanded to

$$p_0 - p = 3\gamma \frac{r_{\varepsilon}}{r_0} p_0 \tag{4-10}$$

Substituting Equation (4-10) into Equation (4-8), the maximum internal potential energy is

$$E_{p,\max} = \int_0^{r_{\varepsilon 0}} \left(3\gamma \frac{r_{\varepsilon}}{r_0} p_0\right) 4\pi r_0^{\,2} \partial r_{\varepsilon} = 6\pi\gamma p_0 r_0 r_{\varepsilon 0}^2 \tag{4-11}$$

By combining Equations (4-11) and (4-7), the equivalent diameter may then be related to the natural frequency of the bubble through $\omega_0 = 2\pi f_0$.

$$d_e = 2r_e = \frac{1}{\pi f_0}\sqrt{\frac{3\gamma p_e}{\rho_{sw}}} \tag{4-12}$$

The acoustic signal may first be filtered to remove sections of ambient noise, with Bergès et al. [126] suggesting the band for their experiment to be between 800 Hz and 8 kHz based on the mean acoustic signal. The filtered acoustic spectrum may then be split into short timeframe sections, where the section size must be approximately the same time frame as the rate at which each bubble is leaked. In principle, if more than one bubble is in the section, it will only be counted as one bubble, conversely if one bubble is in more than one section, it may be counted twice. Calculating the Fast Fourier Transform (FFT) of each section provides a range of frequencies with their amplitude. Selecting the highest amplitude frequency and applying Equation (4-12) allows the bubble diameter to be predicted and a cut off amplitude is also used to ensure that no bubble is recorded if no bubbles are released. The leakage rate may then be predicted by the summation of each bubble volume.

$$\dot{V} = \sum \frac{\pi d_e^{\,3}}{6} \tag{4-13}$$

4.3.3 Laboratory Observations

To test the passive acoustic technique for predicting bubble sizes, and in turn leakage rates, a laboratory experiment is designed using air as the gas to remove the effects of dissolution. The flow rate of the gas may be measured through a flow meter, and compared with the flow rate measured through acoustic bubble sizing to validate this method of predicting leakage rates. The aim of this laboratory experiment is to identify and validate the passive acoustic bubble size measurement technique, before applying it to the data analysis for the QICS field observations.

4.3.3.1 Design and performance

Apparatus was set up as shown in Figure 4-3, where compressed air at a range of leakage rates was released, through a flow meter and into a water tank through a nozzle. The first 40 cm of the tank is filled with 2 mm diameter glass beads as artificial sediments, giving an estimated porosity of between 0.36 and 0.47 [324] with a 110 cm

water column above at atmospheric pressure and temperature. The formation size of bubbles freely rising in the first 10 cm from the sediments into the water column are observed and tracked through filming video clips utilising a GoPro Hero 4 Silver camera situated on the artificial sediment basin, with a ruler as a reference dimension aligned with the bubble plume. The camera also recorded local audio allowing the comparison between both the passive acoustic techniques and the measured flow rate. The motions of the bubbles were captured with a frame rate 29 fps producing full HD 1080 digital images.

4.3.3.2 Laboratory plume experiment data

From the laboratory experiment, the dynamics of the leaked air bubbles released into the water are recorded through imaging and acoustic data, enabling the prediction of the initial bubble size distribution and leakage rate. The recordings of passive audio and images are simultaneous; therefore a direct comparison between findings can be made within these clips for the bubble size distribution and leakage rate. The imaging technique was found to be ineffective due to the unpredictability of the leakage position within the tank, along with the large distance ratio between the plume/ruler and the camera/ruler, giving a large, but unpredictable (XL) in Equation (4-2) as shown in Figure 4-4. Therefore only a direct comparison between the measured leakage rate and the acoustic data was made to validate the passive acoustic technique.

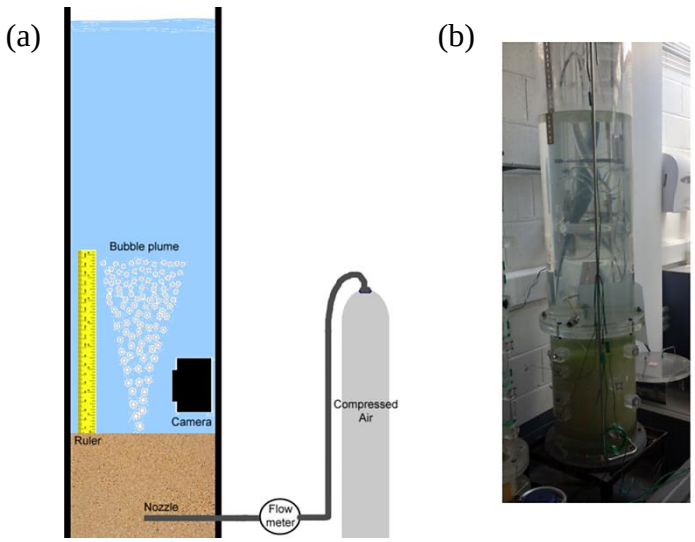

Figure 4-3 *– Laboratory experimental set up. (a) A schematic of the experimental apparatus, left; (b) a photograph of the tank used in the experiments, right.*

4.3.3.2.1 Initial bubble size distribution and leakage rate prediction

The raw data from the passive acoustic audio signal is plotted in Figure 4-5 (a). The FFT of the raw data in Figure 4-5 (b) is used to determine the regular background noise and interference frequencies and amplitude, where a high pass Butterworth filter is employed as a low frequency acoustic noise reduction mechanism [325], with a frequency of 500 Hz selected based on the high amplitude of the lower frequency noise and interference.

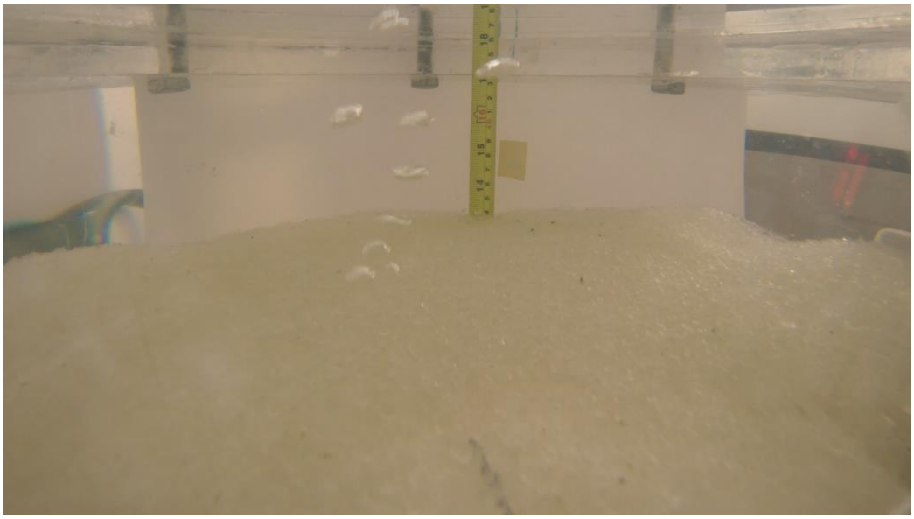

Figure 4-4 *– The observation of a bubble plume in the laboratory experiment.*

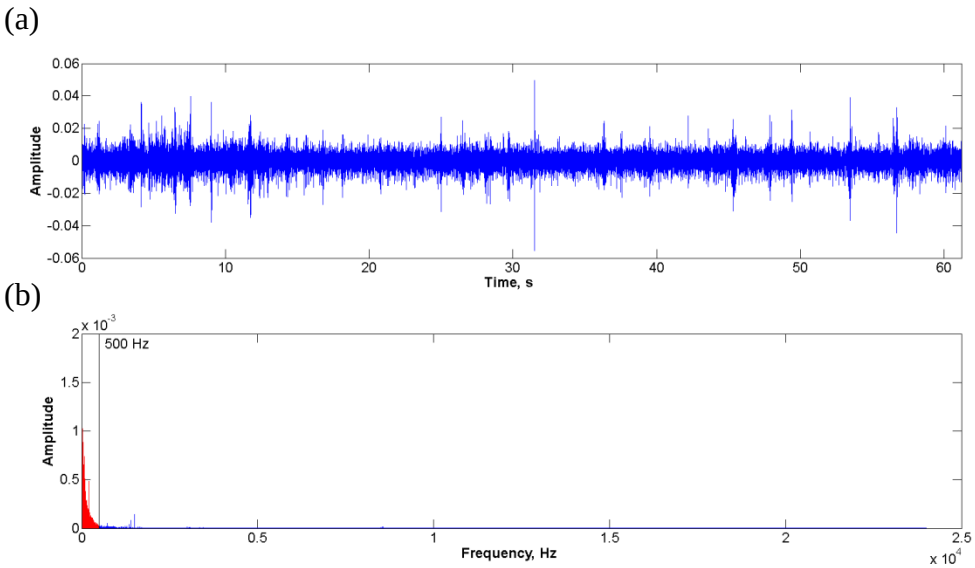

Figure 4-5 *– (a) Passive acoustic audio signal for the full data set at a sampling rate of 48.0 kHz, top; (b) FFT spectrum to determine ambient noise frequencies, with the red data (below 500 Hz) reduced through a Butterworth high pass filter before analysis, bottom.*

For multiple leakage rates in multiple 60 second recordings, the acoustic spectrum is analysed in 1/30th of a second segments, as described in Section 4.3.2, to determine the bubble size in each section. Figure 4-6 (a) shows an example case where the total number of bubbles of each size is calculated in Figure 4-6 (b). From the number of bubbles of each size, the volume flow rate may be established from Equation (4-13), where for the example case above, the flow rate is estimated as 19.99 ml/min, in comparison to that measured of 20 ml/min.

A number of experiments were carried out under the same conditions to verify the leakage rate prediction up to 680 l/min as shown in Figure 4-7. The experiment concluded that the passive acoustic technique is suitable for detecting the bubble size and flow rate, therefore this technique was applied in the data analysis for QICS field experiment.

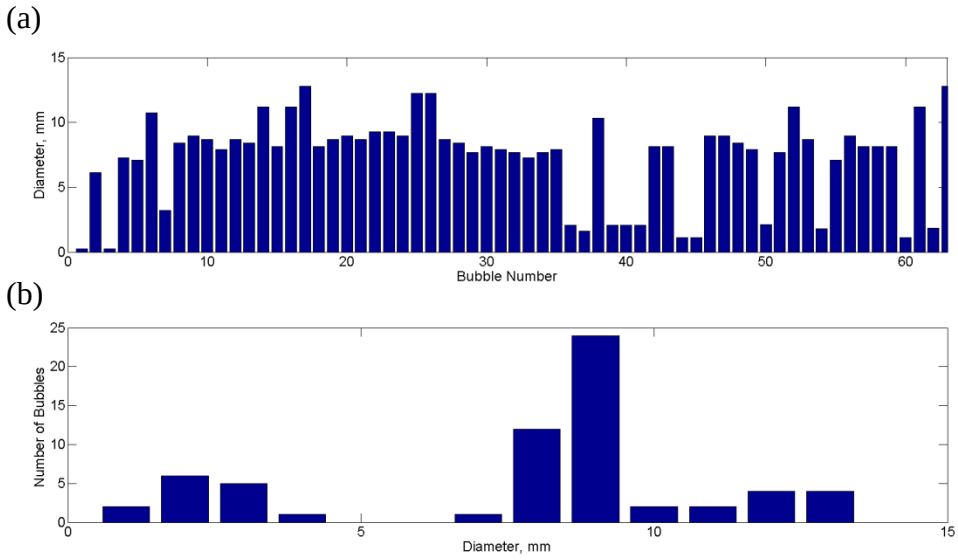

Figure 4-6 *– (a) An example of the predicted bubble size in each time section, top; (b) the total number of bubbles of each size, bottom.*

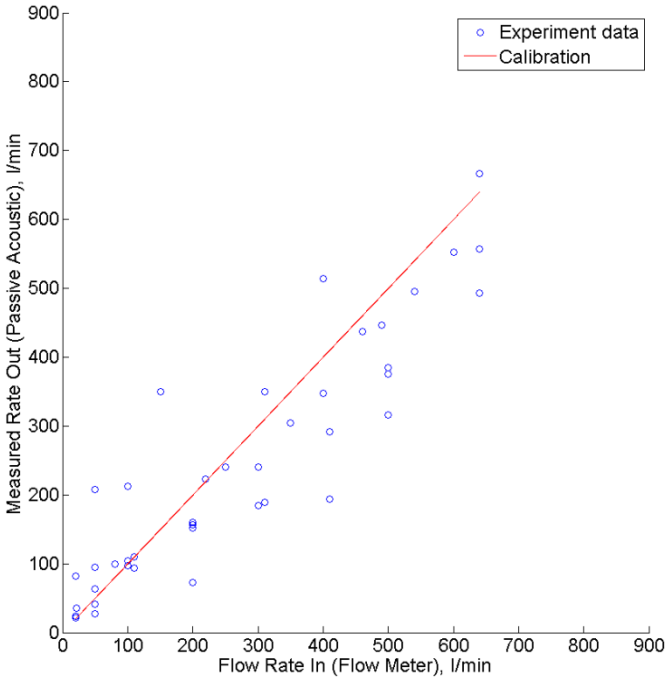

Figure 4-7 *– A comparison between the leakage rate measured acoustically, and that from the flow meter, with a calibration gradient of 1.0 to compare.*

4.3.4 QICS

The QICS experiment involved drilling a narrow borehole from land, terminating in unconsolidated sediments ~12 m below the sea floor approximately 350 meters offshore in a semi-enclosed bay in the Scottish waters (56 29.55 N, 05 25.71 W). CO_2 gas was released through May - June 2012 with a total of 4.2 tonnes of CO_2 over 37 days [105]. A borehole was drilled into the sandy mud sediments as illustrated in Figure 4-8, with the release of the CO_2 through the sediments controlled and monitored from a mobile laboratory at a nearby site. After migration through the sediments, the CO_2 reached the seabed and formed as gas bubble plumes in a water column of 9 - 12 metres depending on the tide.

Key data required to analyse the dynamics of the bubbles in the field experiment included the leakage parameters: bubble rising velocity, shape, shrinking rate, and interactions; with each of these parameters also related to the bubble size distribution. By measuring these bubble parameters, along with further data of the estimated leakage flux and area, the marine impact may be estimated in terms of the changes in DIC, pH, or pCO_2, as well as the reflections of these effects on marine organisms.

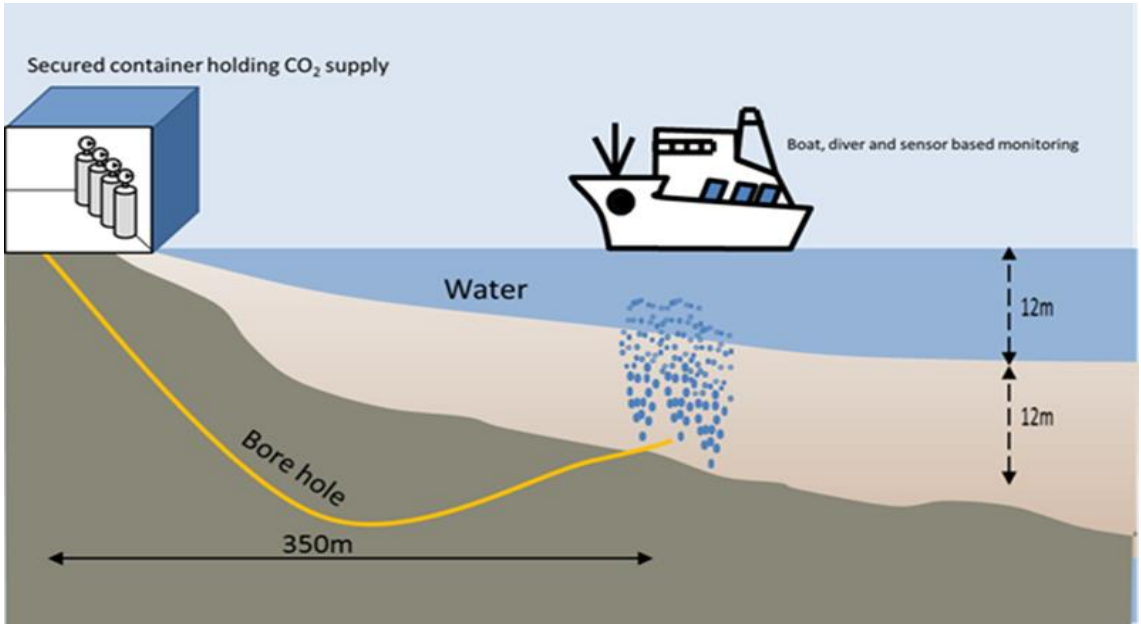

Figure 4-8 *– Schematic of QICS CO_2 release experiment [113].*

4.3.4.1 Design and performance

Leaked CO_2 bubbles freely rising in the first 30cm from the sediments into the water column are observed and tracked through video clips provided by the divers overseeing the QICS experiment, filmed from three select pockmarks locations utilising a Canon EOS 5D Mark II CMOS camera, elevated approximately 20 cm above the sea floor, with a ruler as a reference dimension aligned with the CO_2 bubble plume as seen in Figure 4-2. This limits the collected experimental data to the first 30cm in the water column. The camera also recorded local audio allowing the comparison between the imaging and passive acoustic techniques. The motions of the CO_2 bubbles were captured with a frame rate 30 fps producing full HD 1080 digital images, also providing mono passive acoustic recordings at a fixed frequency of 44.1 kHz. In the experiment, upwards of thirty five pockmarks were formed, however only three select locations were observed.

Measurements of the leakage rate showed that a mean of ~15 % of the injected gas was detectable in the water column using both acoustic [126] and physical collection measurement techniques [105]. This suggests that either some gas is dissolved prior to reaching the water column, is released as very small bubbles dissolving quickly, or it remains as a gas within the sediments. As the camera placement is close to individual

bubble plumes, passive acoustic recordings will be able to detect the smaller bubbles that may not be recorded by the camera. A combination of the passive acoustic and imaging methods from the camera are therefore utilised to compare and analyse the data providing a bubble size distribution.

4.3.4.2 In-situ plume experiment data

From the QICS experiment, the data recorded through imaging and acoustic techniques enable the prediction of the initial bubble size distribution, leakage rate, bubble shapes, velocity distribution, along with bubble interactions including break up or coalescence. The recordings of passive audio and images are simultaneous; therefore a direct comparison between findings can be made within these clips for analysing the bubble data and understanding the plume mechanisms.

Data such as the rise height of the bubbles is observational data, rather than quantitative, due to the limitations of the distance in which bubbles may be tracked by the camera. However, as an indication of the rise height, bubbles of an undistinguishable size (< 0.01 mm) were found to reach the seawater surface during low tide (9 meters water depth).

4.3.4.2.1 Initial bubble size distribution and leakage rate prediction

The size of the CO_2 bubbles and leakage rate are the key parameters for the analysing the dynamics of free rising bubbles, including the dispersion and dissolution. The larger the bubble, the further it will travel in the seawater and the longer it will take to dissolve. For this reason, the distribution of the initial bubble size is vital to predict the height travelled by the CO_2 bubbles in the water column before dissolving, as well as the leakage rate to determine the concentration of the dissolved solution in the plume and the related changes in pH of the seawater.

4.3.4.2.1.1 Imaging technique

The initial bubble size distribution and the leakage rate from the sediments into the water column are measured through analysis of the video clips, with the count of each equivalent diameter, d_e, presented in Figure 4-9 (a) and the summation of each bubble size shown in Figure 4-9 (b).

The number of bubbles at each size is then converted to a percentage distribution through Equation (4-14) and presented in Figure 4-10 (a). Greater than 50 % of the measured CO_2 bubbles are shown to have a diameter between 6.0 mm and 8.0 mm, compared to a low percentage (< 1.5 %) of the small (d_e < 4.0 mm) and large bubbles (d_e > 11.0 mm).

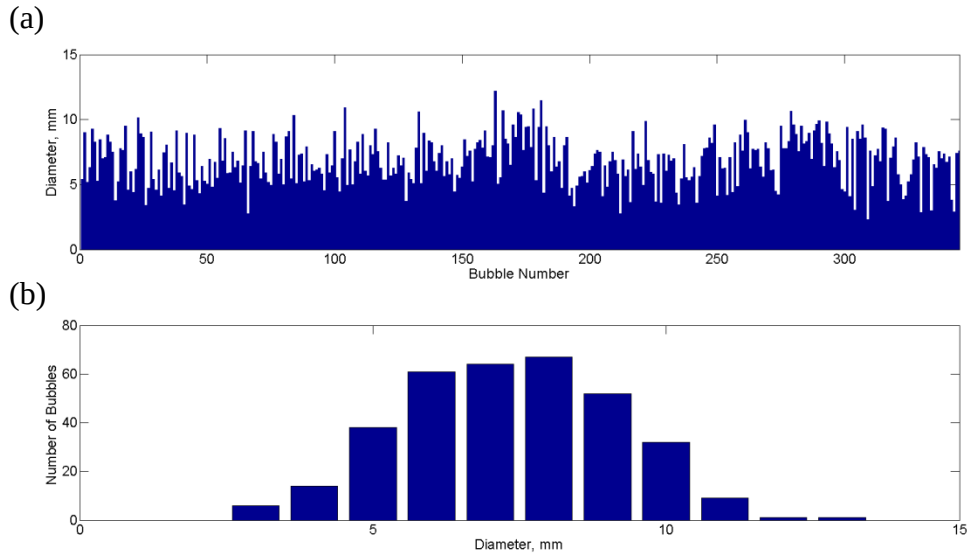

Figure 4-9 *– (a) Each measured bubble size, top; (b) the total number of bubbles of each size, bottom.*

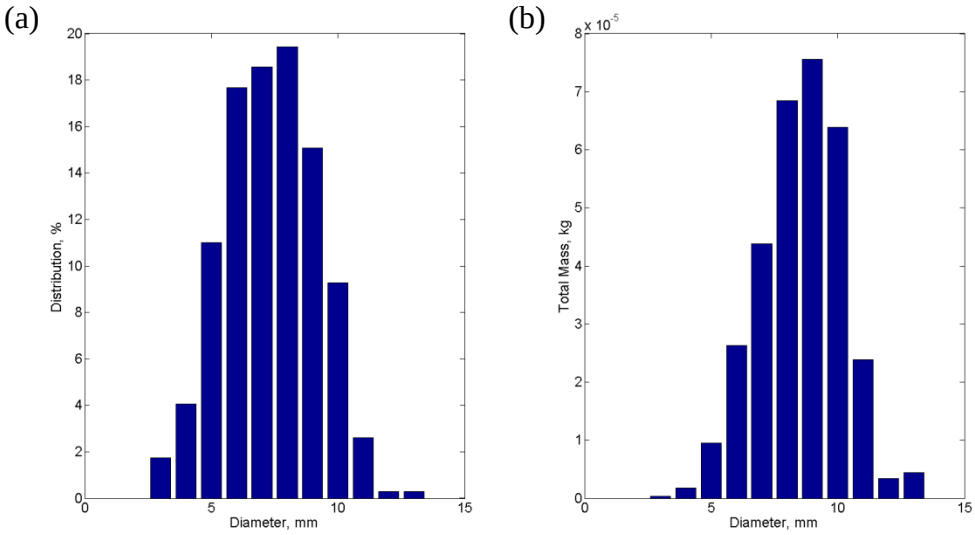

Figure 4-10 *– (a) The predicted bubble size distribution, left; (b) the total mass of each bubble size, right.*

From this data, the mass distribution of each bubble size may be calculated as shown in Figure 4-10 (b). The flow rate of a single pockmark is also predicted as 0.06 kg/day and extrapolating to 35 pockmarks gives an estimated leakage rate of 1.97 kg/day.

$$N_{i\%} = \frac{N_i}{\sum N} \times 100\% \qquad i = \mathrm{int}(d_e) \tag{4-14}$$

4.3.4.2.1.2 Acoustic technique

The formation size and distribution of the gas bubbles was also determined through a passive acoustic technique as a comparison. Sections of excessive noise and interference (diver movements and breathing apparatus) were removed from the video clips providing 72.76 seconds of data that may be analysed. The raw data from the passive acoustic audio signal is seen in Figure 4-11 (a). The FFT of the raw data in Figure 4-11 (b) is utalised to determine the regular background noise and interference frequencies and amplitude, where a high pass Butterworth filter is employed as a low frequency acoustic noise reduction mechanism [325], with a frequency of 950 Hz selected based on the high amplitude of the lower frequency noise and interference. This may be compared with the reduced noise of 500 Hz in Laboratory conditions in Figure 4-5 (b).

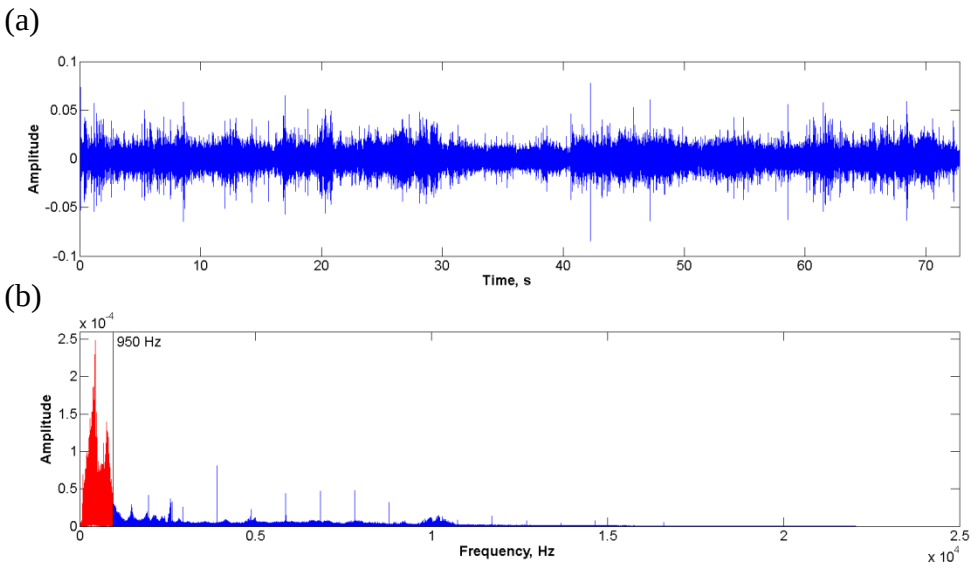

Figure 4-11 *– (a) Passive acoustic audio signal for the full data set at a sampling rate of 44.1 kHz, top; (b) FFT spectrum to determine ambient noise frequencies, with the red data (below 950 Hz) reduced through a Butterworth high pass filter before analysis, bottom.*

The acoustic spectrum is analysed in 1/30th of a second sections, as described in Section 4.3.2, to determine the bubble size in each section as shown in Figure 4-12 (a), where the total number of bubbles of each size is shown in Figure 4-12 (b). The number of bubbles of each size is then converted to a number distribution through Equation (4-14) as shown in Figure 4-13 (a).

It is found that greater than 50 % of the measured CO_2 bubbles have a diameter between 4.0 mm and 8.0 mm, with a slightly lower percentage (27%) of small bubbles (diameter < 2 mm) and a significantly lower percentage (7%) of large bubbles (diameter > 10 mm) respectively. From this data, the mass distribution of each bubble size may be calculated as shown in Figure 4-13 (b), with the flow rate of the single pockmark estimated as 1.07 kg/day which is extrapolated to 35 pockmarks to give a leakage rate of 37.5 kg/day. This is much larger than the value estimated by the image technique. Further discussion on the difference in the leakage rate measured by the two techniques is made in the modelling section.

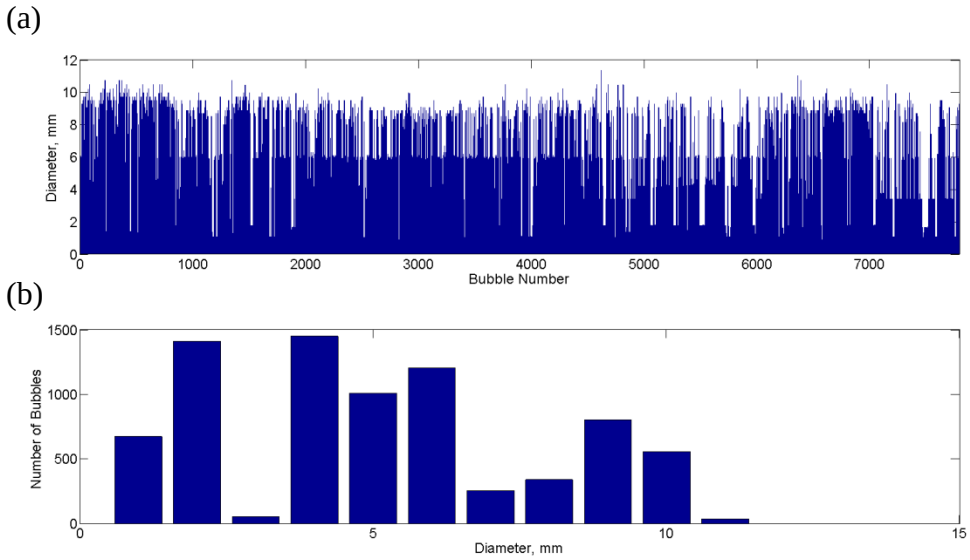

Figure 4-12 *– (a) The predicted bubble size in each time section, top; (b) the total number of bubbles of each size, bottom.*

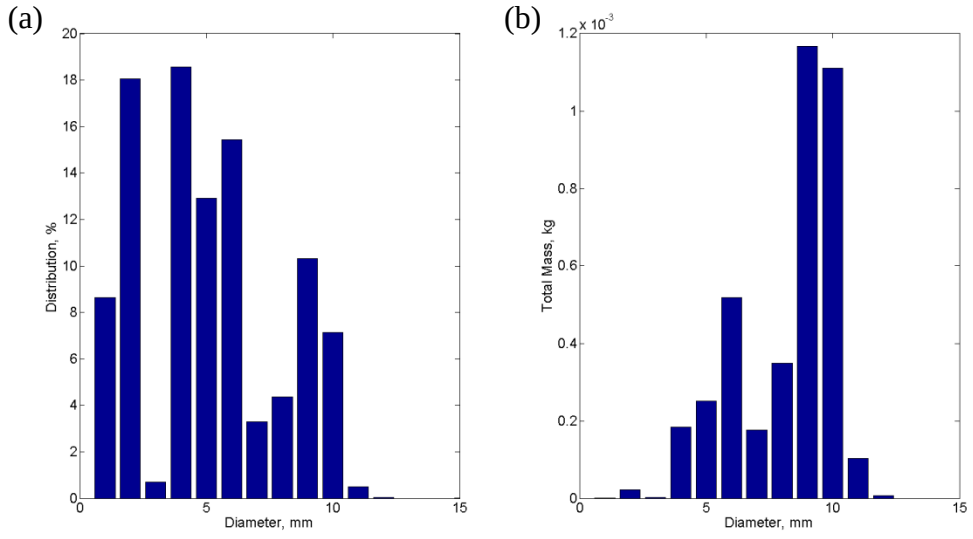

Figure 4-13 *– (a) The predicted bubble size distribution, left; (b) the total mass of each bubble size, right.*

4.3.4.2.2 Bubble shapes

It is also observed from the QICS experiment that the bubbles exist in a variety of shapes. The shape has important effects on bubble breakup, the drag force of the bubble along with the mass dissolution rate [184]. Therefore the geometric characterisation of the bubbles obtained from QICS experiment is analysed for CO_2 bubbles in the open seawater.

Figure 4-14 shows still images captured from six typical bubble shapes. Figure 4-14 (e) shows the moment of bubble breakup when the bubbles are about to divide, and Figure 4-14 (f) shows the moment after the bubbles break apart. The CO_2 bubble shapes can be categorised into types of spherical (small size), ellipsoidal and cap, along with wobbling shapes from the larger bubbles in the turbulent open waters, which makes measurements somewhat complex.

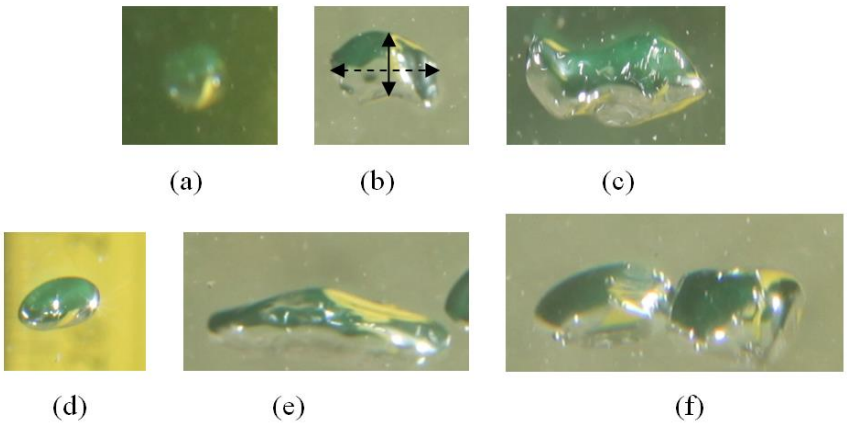

Figure 4-14 *– Shapes of the leaked CO_2 bubbles [113]: (a) Spherical; (b) Ellipsoidal; (c) Ellipsoidal wobbling; (d) Ellipsoidal; (e) Cap shape before breakup; (f) Breakup moment.*

These bubble deformation characteristics can be described mathematically through the Morton, Eötvös and Reynolds numbers. As the Morton number is based on fluid properties, the value will not change for different sizes or shapes of the same fluid under the same conditions. However, the Eötvös and Reynolds numbers will vary as they are based on the bubble dimensions and fluid properties. As shown in Figure 4-15, small CO_2 bubbles have spherical shapes at the low range (Eo < 2), at the mid-range (2 < Eo < 7) the CO_2 bubbles have ellipsoidal shapes, and the CO_2 bubbles have either cap or ellipsoidal wobbling shapes at the higher ranges (Eo > 7).

The experiment video shows that wobbling bubbles could potentially develop towards two possible shape situations; breaking into two or more smaller bubbles, or stabilising into an ellipsoidal shape after losing part of its volume through dissolution. As mentioned in Section 4.3.1, the geometry of larger CO_2 bubbles can be characterised by two further dimensions to the equivalent diameter, d_e; the major axis dimension, d_{mj}, and the minor axis dimension, d_{mi}. As seen in Figure 4-14, the CO_2 bubbles with the same equivalent diameter can have different major axis dimensions. However from the experiment data, a good liner relation is found between the equivalent diameter of the CO_2 bubbles and their major axis when d_e > 4.0 mm as shown in Figure 4-16.

$$d_{mj} = \begin{cases} d_e & \text{if } d_e \le 5.0mm \\ 1.82\ d_e - 4.0 & \text{if } d_e > 5.0mm \end{cases} \quad (4\text{-}15)$$

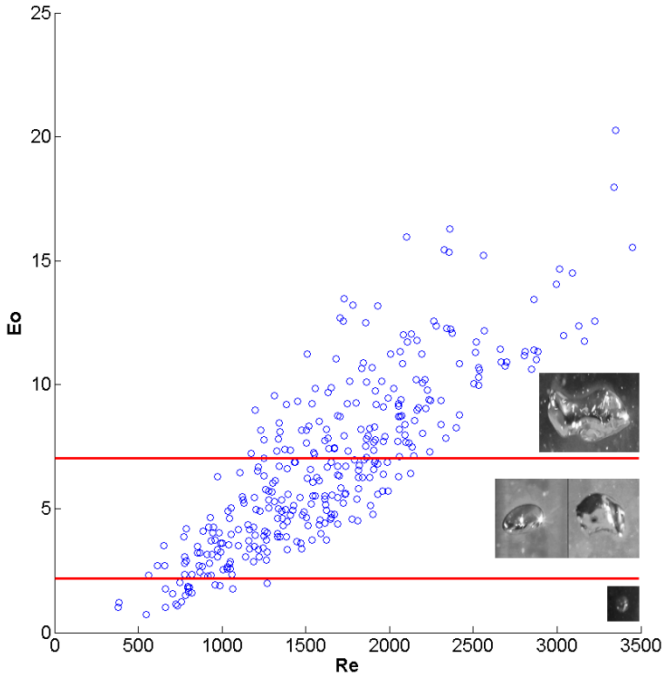

Figure 4-15 *- Characterisation of the CO_2 bubble shapes observed from QICS experiment through Eötvös and Reynolds numbers.*

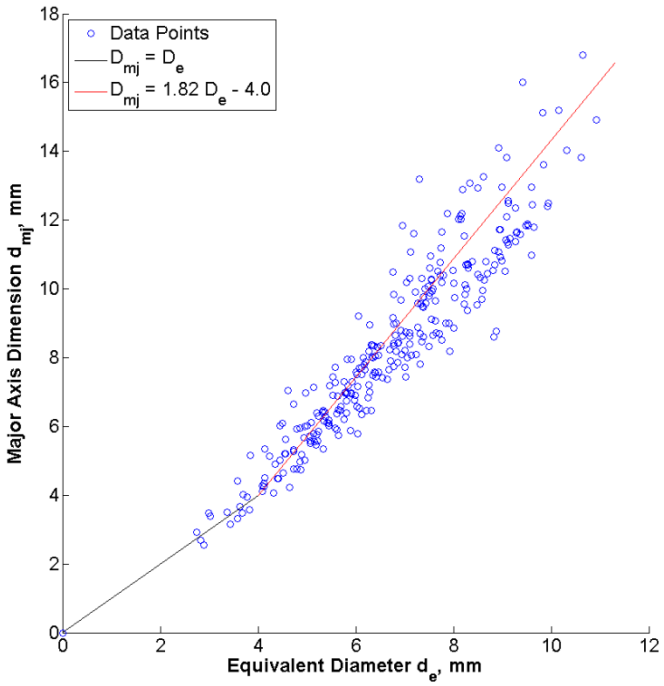

Figure 4-16 *– The relation between the major axis of the bubbles, d_{mj}, and the equivalent diameter, d_e, from the QICS experiment (data points) and the liner correlation for bubbles smaller than 4.0 mm (black line), and those larger than 4.0 mm (red line).*

From this result, the bubbles with an equivalent diameter larger than ~5 mm will deform to non-spherical bubbles. This correlation can be utilised to further distinguish the bubbles that may break up as discussed in Section 3.3.2 for bubble interactions.

4.3.4.2.3 Bubble Plume Rising Velocity

Another important parameter of the free rising CO_2 bubbles in the QICS experiment is the rising velocity. The raw data from the digital imaging of CO_2 bubble sizes and corresponding velocity taken through the imaging technique are presented in Figure 4-17 (a), where the size of the leaked CO_2 bubbles varies between 2 and 12.5 mm with a correspondent velocity varying between 20 cm/s and 45 cm/s.

The distribution of the leaked CO_2 bubble velocities was also calculated through the same method as Equation (4-14), as illustrated in Figure 4-17 (b), where most of the CO_2 bubbles (>75%) rise with a velocity between 25 cm/s and 40 cm/s.

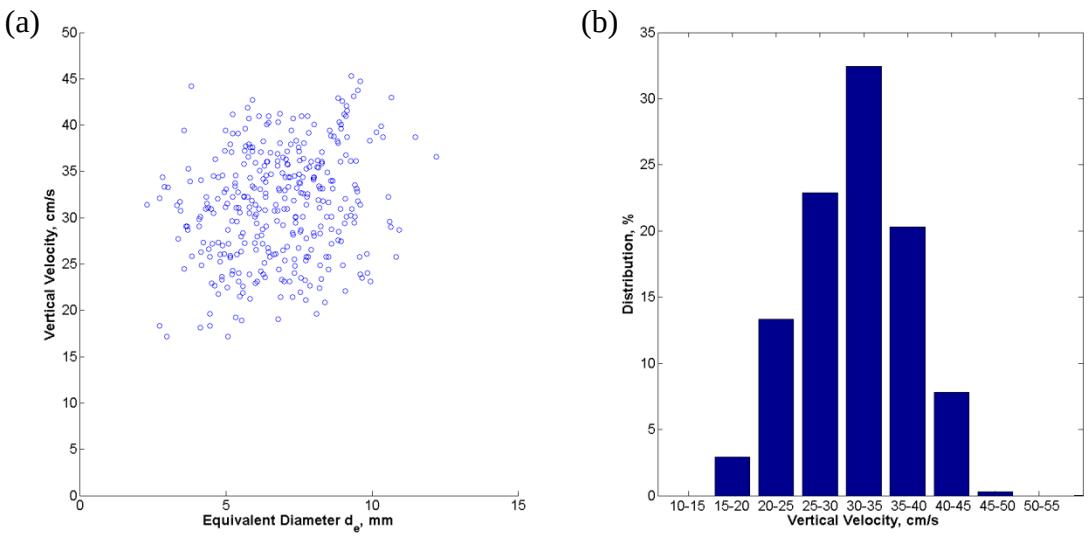

Figure 4-17 *– (a) The size and velocity of each of the individual CO_2 bubbles, left; (b) the velocity distribution of the CO_2 bubbles, right.*

4.3.4.2.4 Bubble interactions

Through processing the video recordings from the QICS experiment, interactions between the CO_2 bubbles are observed. Interactions occur as either a breakup of the larger CO_2 bubbles, increasing the number density while reducing bubble size, or coalescence between two or more neighbouring bubbles which gives birth to a larger bubble.

Breakup frequency is a parameter used to predict the dynamics of bubbles in a plume. As smaller bubbles break from a relatively large bubble, they will reduce in buoyancy, and dissolve far quicker which greatly affects the overall structure of both the bubble and the dissolved solution plumes. An example of bubble breakup is captured in the QICS experiment and shown in the Figure 3-4 photo montage. Figure 3-4 (a) shows a single CO_2 bubble with a wide d_{mj} which is circled before breaking into two bubbles shown in Figure 3-4 (b) and Figure 3-4 (c) at 1/30 and 1/15 seconds later respectively.

To further investigate the breakup characteristics of the CO_2 bubbles, an Eo – Re diagram is illustrated in Figure 4-18 as a classic bubble dynamic analysis method using the equivalent diameter of the bubbles, shown by circle symbols. The bubbles that break up are indicated by the red colour based on data just before breakup. It is found that although the bubbles experiencing break-up interactions are in the upper region of the Eötvös numbers, they are difficult to differentiate from the rest of the bubbles. It is therefore proposed that the Eötvös and Reynolds numbers are defined by the major dimension, d_{mj}, rather than the equivalent diameter, de. Through this definition, as shown by in Figure 4-18, the breaking bubbles can be clearly identified where the wider and faster moving large bubbles become unstable and break. It can be established that breakup occurs for the CO_2 bubbles when Eo > 20 (d_{mj}) and Re > 3500 (d_{mj}).

In addition to the bubble breakup, coalescence between bubbles is observed at a frequency of ~2.5 per second within the first 30 cm, with the greatest coalescence rate found at around 7 cm from the seabed.

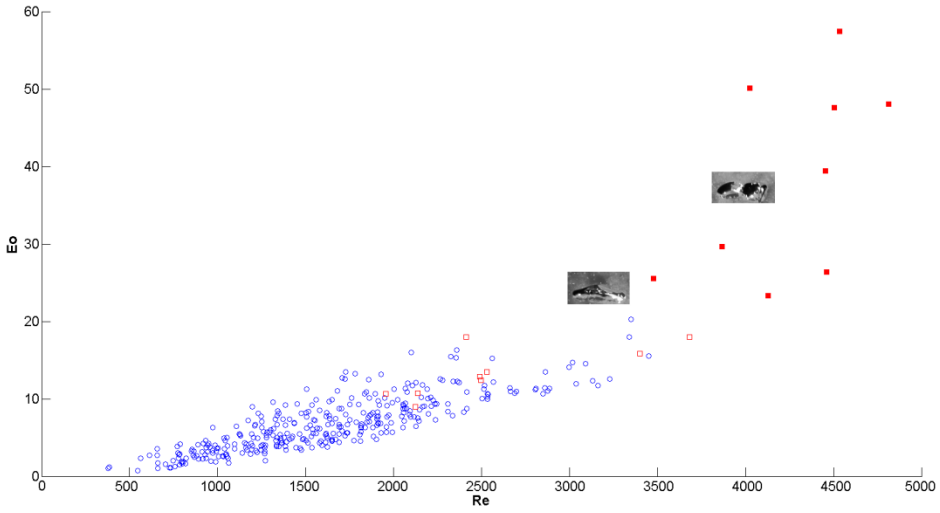

Figure 4-18 *– Eötvös and Reynolds diagram of CO_2 bubbles; data for non-breaking bubbles (blue points as shown in Figure 4-15), and data for breaking bubbles, measured by d_e (red squares) and by d_{mj} (filled red squares).*

4.3.5 Discussion on Data

4.3.5.1 Initial bubble size distribution and leakage rate prediction

With only three video samples, a limited amount of data is collected from three out of the thirty five pockmarks observed in the QICS experiment. This small proportion provides great uncertainty when predicting leakage rates through extrapolation. However the laboratory experiment shows that for individual plumes, the leakage rate may be predicted with good accuracy, even at leakage rates as high as 700 ml / min (~1.25 kg/ day), which is the same order as measured for an individual plume in the QICS experiment (1.07 kg/ day predicted acoustically).

Some uncertainties are generated by the nature of the QICS field experiment, such as the lack of measurements in three dimensions due to the use of a single camera, noise from particles in the seawater as seen in Figure 4-19 (a) and both focal and motion blur from the fast moving 3 dimensional bubbles as seen in Figure 4-19 (b). If the resolution is also taken into account on top of these uncertainties, an error of +/- 0.5 mm is estimated for the bubble size measurement.

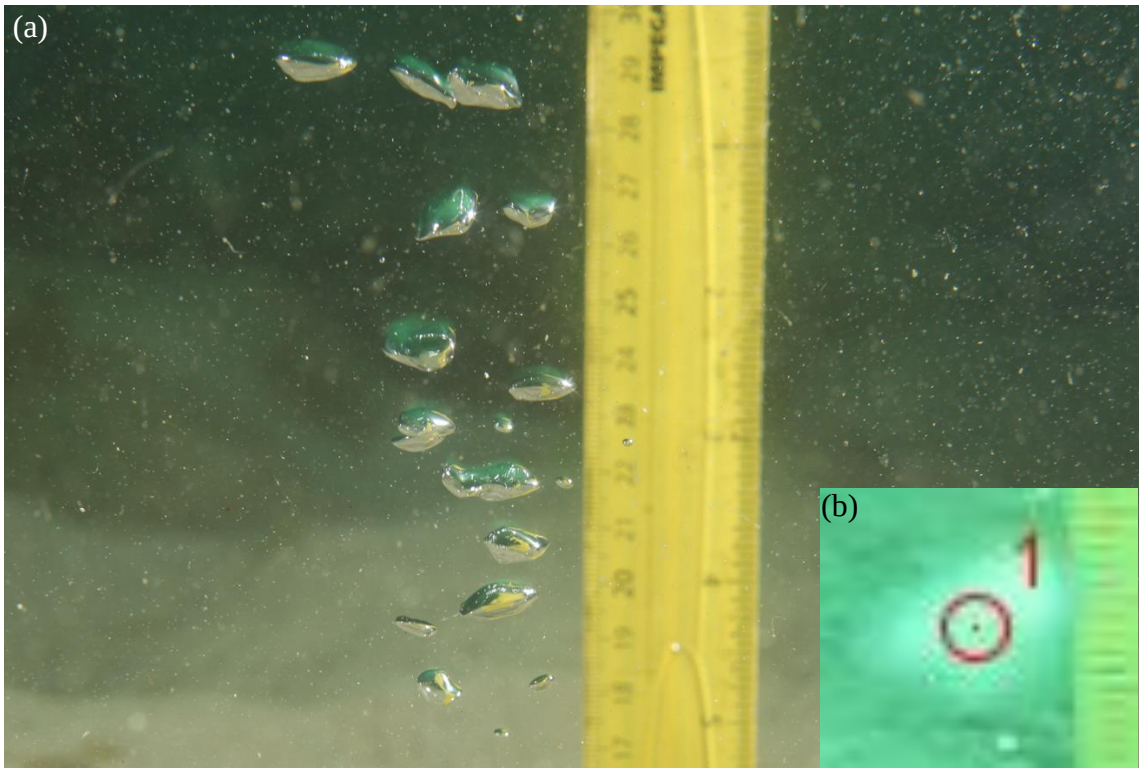

Figure 4-19 *– (a) A still image taken with the same camera as the video clips, utilising the camera flash to highlight the noise from the particles along with the possibility of tiny bubbles, left; (b) A frame from the video with motion and focal blur, bottom right corner.*

Taking the optical measurement of each bubble that was visible in the video frames forming at the surface, Figure 4-2 shows that the smaller bubbles were not able to be measured due to their size in comparison to the image resolution (~0.5 mm per pixel). Therefore the smallest bubbles that were measured were above 2 mm in size. Difficulties also occurred when measuring the larger bubbles due to the shape changes and the subsequent effect of blur between frames.

Greene and Wilson [292] suggest that an improvement on measuring the initial bubble distribution from imaging techniques may be made through the passive acoustic method. This method predicts initial bubble sizes with a greater accuracy compared to imaging methods and also measures the smaller bubbles. The total number of bubbles that could be measured using the imaging method was 345, which is 4.43 % of the 7793 bubbles that were predicted by the passive acoustic method, which further supports this idea. However, the passive acoustic technique provides no data on the bubble shapes, velocities or interactions, and comes with limitations such as inaccuracies from background noise and interference.

One of the largest difficulties in the passive acoustic technique is the use of a microphone rather than a hydrophone; this increases the interference and noise level as the sound must also travel through the waterproof casing of the camera which distorts the sound. Therefore a large low frequency filter is required to remove this distortion, where the noise interferes with the same frequencies as those from the larger bubbles. An example is the filter of frequencies below 950 Hz using Equation (4-12); this provides a bubble size of 6.5 mm meaning that bubbles above this size are lost within the noise. For this reason, a Butterworth filter was chosen in place of fully cutting the data below 950 Hz in the QICS experiment; this reduces the amplitude of the lower frequencies through a polynomial curve [326]. With lower noise and interference, a lower cut-off filter may be used, such as in the laboratory experiment that allowed a Butterworth filter of 500 Hz, without losing many of the bubble measurements. However, as can be seen in Figure 4-20 for the QICS experiment, lower cut-off frequency filters in combination with high noise and interference can distort the bubble count and therefore exaggerate the bubble sizes released as well as the leakage rate.

Due to the expansion of the lower bubble size data range using the passive acoustic technique, there is a decrease in the mean bubble size recorded to 4.6 mm from 6.8 mm in the imaged data. This is due to the number of small bubbles that are detected in the acoustic technique that were neglected in the imaging method.

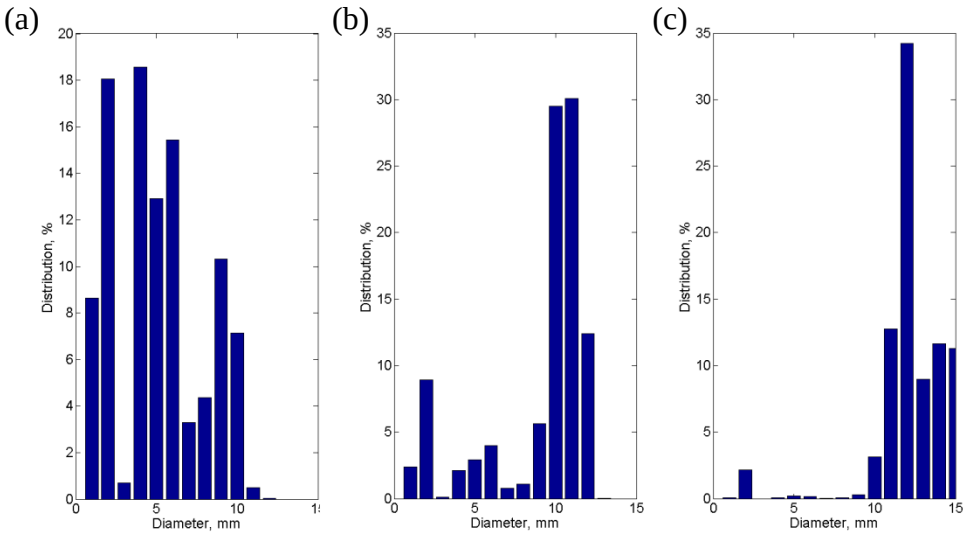

Figure 4-20 *– The predicted bubble size distribution testing various high-pass cut-off frequencies; (a) 950 Hz, left; (b) 800 Hz, middle; (c) 500 Hz, right.*

The distribution shape of the measured bubble distribution is different between the imaging and passive acoustic techniques, as seen in Figure 4-21, where although the largest percentage of bubbles are witnessed in the mid-range, between 4 and 8 mm, the acoustic technique predicts a lower percentage of bubbles at a diameter of 3, 7 and 8 mm.

A number of estimates have been compiled for the leakage rate during the QICS experiment. Samples of the leaked gas were collected during the high injection phase of 210 kg/day, giving a CO_2 leakage rate at the seabed of 31.8 kg/day [105]. This is in line with passive acoustic measurements made by a hydrophone throughout the later stages of the experiment which show the leakage rate varies significantly between almost 0 kg/day at high tide and up to 80 kg/day at low tide [126]. From our camera experimental data, the imaging predicted a leakage rate of 1.97 kg/day, and simultaneously the acoustic recordings, utilising a 950 Hz high pass filter, predict 37.5 kg/day. From this, it can be seen that the acoustic data from the camera is consistent with the hydrophone data, and data from the gas collection sample. If a lower frequency cut-off filter is used then, with the increased interference and noise, the leakage rate becomes less realistic with 151.7 kg/day and 385 kg/day calculated using an 800 Hz and 500Hz filter respectively.

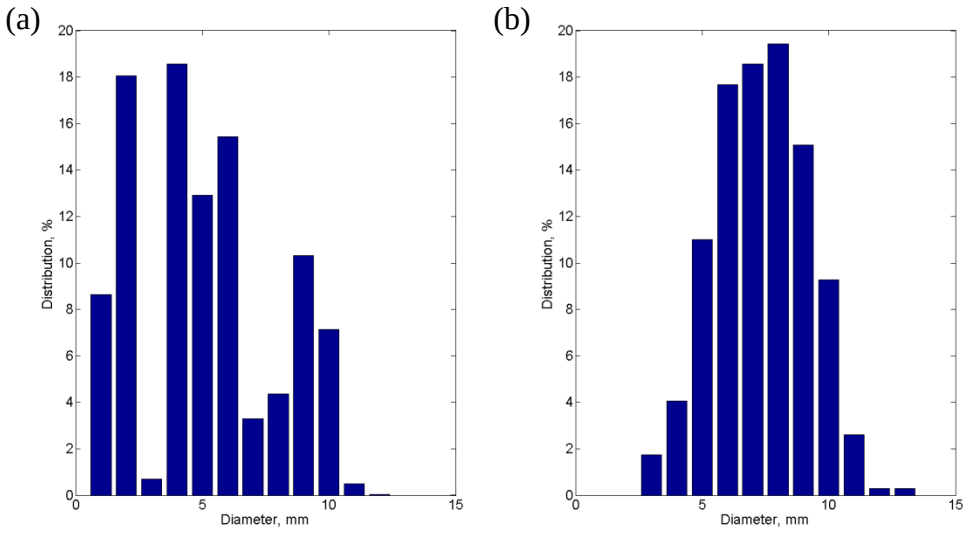

Figure 4-21 *– The predicted bubble size distribution; (a) Passive acoustic technique, left; (b) Imaging technique, right.*

4.3.5.1.1 pCO_2

Related to the leakage rate, measurements of pCO_2 are taken in the later stages of the QICS experiment at 30 cm above the seabed [105]. On day 30, at the injection rate of 170 kg/day, a mean pCO_2 of 390 - 400 µatm was measured during both high and low tide, rising from a background of 360 µatm. On days 32 to 36, where the injection rate was increased to the maximum of 208 kg/day, the pCO_2 measurements varied rising from 390 µatm to a peak of 1250 - 1500 µatm before settling at approximately 500 µatm [138].

4.3.5.2 Bubble shapes

The CO_2 bubble shape may also be characterised by the aspect ratio,

$$A_r = \frac{d_{mi}}{d_{mj}} \tag{4-16}$$

which is examined against the Eötvös number as illustrated in Figure 4-22, where the aspect ratio decreases with an increase in the Eötvös number as the larger buoyancy forces enhance the deformation of the bubbles. In comparison with laboratory experiment data and simulations presented by Bozzano and Dente [266], the QICS experimental results show a consistency which validates the use of Eo in characterising the shapes of the CO_2 bubbles.

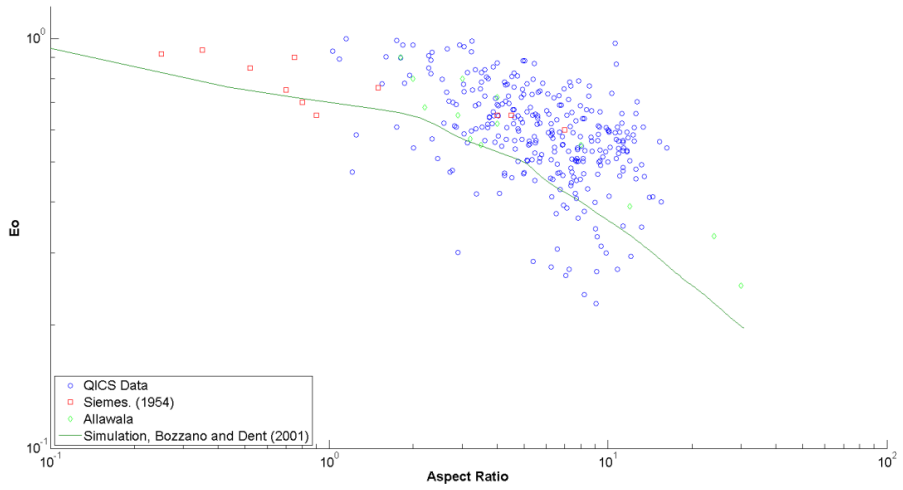

Figure 4-22 *– QICS CO_2 bubbles aspect ratio (blue circles), in comparison with experimental data (red squares and light green diamonds) and simulation data (green line) from Bozzano and Dent [266].*

4.3.5.3 Plume rising velocity and drag coefficient

In the QICs experiment, the bubble rising velocity is higher than experienced in laboratory and in-situ individual bubbles of equivalent size, with relative velocities ranging up to 25-30 cm/s for CH4 [187 – 189, 197], and air [181 – 186]. Where McGinnis et al. [187] suggests that two-phase plume effects have a role to play, not accounted for within their simulations.

There is a direct analytical relationship between the drag coefficient, C_d, and the CO_2 bubble velocity, where the drag coefficient from the leaked CO_2 bubbles is calculated for each bubble - assuming the rising velocity measured is the terminal velocity of the bubble with no vertical seawater currents present. For bubbles rising freely in the seawater, the vertical forces acting on each bubble are due to buoyancy and drag forces, shown in Equation (3-10) and Equation (3-30) respectively. If we assume no acceleration (the velocity has reached its terminal velocity), then the drag coefficient may be predicted from the experimental data through

$$C_d = \frac{4(\rho_{sw} - \rho_{CO_2})gd_e}{3\rho_{sw}u^2} \tag{4-17}$$

Using Equations (4-17) and Equation (3-26), the drag coefficient, C_d, and the Reynolds number, Re, are calculated for the measured CO_2 bubbles.

The relationship between the drag coefficient and the Reynolds number obtained from the raw QICS experiment data is shown in Figure 4-23, along with the drag coefficient results of gas bubbles obtained from the experimental studies carried out under laboratory conditions (methane: [188, 189], air: [181 – 186]). It was found that only a small number of CO_2 bubbles studied within the QICS experiment match with the laboratory results for the Reynolds number range between 500 and 3500. However the majority of the QICS CO_2 bubbles had a large variation of the drag coefficient between 0.4 and 2.3 for a given Reynolds number, which on average is smaller than those of an individual bubble.

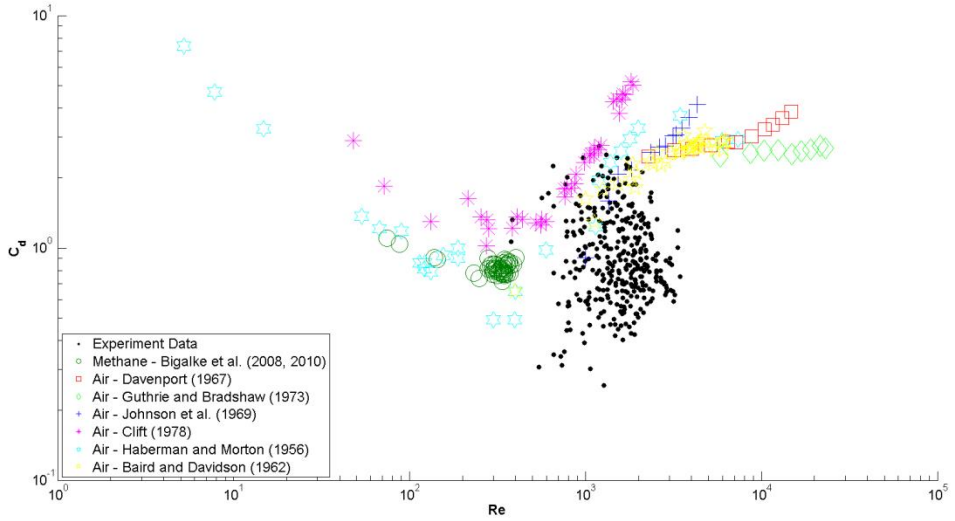

Figure 4-23 *– The raw drag coefficient data from the QICS experiment, calculated through Equation (4-17), compared with a number of experimental data sets for gas bubbles (methane: [188, 189], air: [181 – 186]).*

The variation can be explained due to a number of factors. The first consideration in the QICS experimental results for the drag coefficient is that the CO_2 bubbles are rising in a plume of bubbles, rather than an individual bubble rising, studied under laboratory conditions. In the QICS experiment, the velocity of the bubbles recorded are also the absolute velocities of the bubbles in a plume, rather than the relative velocity of an individual the bubble. For which, the dynamics of the plume vary and depend on the location of each bubble within the plume, where it has been found that, in general, larger velocities are experienced approaching the centre of the plume [215]. The factors due to induced currents from the force of the leak and tidal currents should be taken into account, giving a generally larger absolute vertical velocity of the bubbles in the plume, compared to the relative velocity of each bubble to the seawater therefore under-estimating the drag coefficient.

Another factor is the effects from interactions among the CO_2 bubbles studied within the plume in the QICS experiment. It is observed that larger bubbles breakup as they travel through the waters, meanwhile, coalescence of two or more CO_2 bubbles also occurs. The interactions change the velocity of the CO_2 bubbles, due to the difference in sizes from the collision of the CO_2 bubbles, or an exchange of momentum to smaller bubbles as the bubbles break [327], both providing velocity increases.

4.3.5.4 Discussion on Experimental Errors

Some observation errors are generated from the monitoring setup in the QICS experiment, such as the location of the rulers, and both focal and motion blur along with the lack of observation in three dimensions due to the use of a single camera, also the plume effect and the tidal effects should be measured and quantified. This may be improved by redesigning the system and simultaneously measuring the seawater velocity, providing the relative velocity for more reasonable bubble dynamics data.

The optical measurements have multiple uncertainties and sources of error along with collecting only a fraction of the data in comparison to that of the acoustic method. Due to the optical analysis being carried out on two dimensional image frames, measurements in the lateral direction are excluded in determining the size. The changing shape with time in each dimension, especially for larger bubbles, creates more uncertainties. Visual clutter and noise from the sediments and water deposits restricts the usefulness of the optical measurement technique, where motion and focal blur at the bubbles edge provides a dimensional error that must also be considered along with the pixilation and low resolution.

Manasseh et al. [328] found that measurements using the acoustic spectrum peak of the entire acoustic pulse from the bubble can overestimate the bubble size due to the frequency of the bubble oscillation reducing slightly with time. Interactions such as bubble breakup and dissolution would also have an effect on the bubble size. Leifer and Tang [296] also found that measurements from a natural hydrocarbon seep using Equation (4-12) over predict the bubble size by 20%. However Greene and Wilson [292] concluded from their laboratory work that the passive acoustic method provides the lowest measurement uncertainty compared to imaging and gas collection for small bubbles.

Bubble breakup and coalescence was seen to have an effect in the video imaging which cannot be accounted for through the acoustic methods which will affect the distribution and also alter the acoustics thus manipulating the results [328]. As the experiment was in-situ in open waters, a lot of high amplitude background noise and interference from moving particles in the waters was collected that could influence the FFT and individual

wavelength measurements. Surfactants and contamination in non-laboratory open water conditions can also alter the surface tensions and natural frequency, especially of smaller bubbles [292], however CO_2 bubbles of this size will dissolve very quickly and Manasseh et al. [328] consider tension effects to be of a second order.

The interactions between the CO_2 bubbles are a very important phenomenon to characterise analytically. Experiments with a larger leakage flux would generate a plume with strong bubble interactions due to the larger void fraction of the gas. Further experimental data on bubble interactions under different conditions (varied bubble size, bubble shape, directional velocities of seawater and the temperature, salinity, along with various water pressure/depths) would be useful in validating data for development of a suitable interaction sub-model.

The findings increase understanding of the errors and difficulties in bubble measurement when using either digital imaging or passive acoustic measurements The method comparisons and the suggested modifications defined will help refine each method in determining bubble sizes. However, it is concluded from the findings that the acoustic method is far better suited due to its automation, speed and quantity of useful data that may be collected, along with the accuracy provided in determining the full bubble distribution, however this needs to be improved further by the use of hydrophones and larger data sets.

4.4 Summary

As part of the work for this thesis, the in-situ dynamics of the rising CO_2 bubbles in seawater are investigated experimentally, observed from the QICS project. This data is compared to multiple sets of laboratory experimental data; including both published work and a further in-house experiment testing leakage rate measurement techniques. From the video footage of the bubble plume supplied by divers overseeing the QICS experiment, data is collected, analysed and dimensionless numbers such Re and Eo are predicted identifying the characteristics of leaked CO_2 bubbles. The results obtained show a variation in the drag coefficient when compared to published work due to differences between the open field environment and laboratory conditions. This is along with the differences in dynamics between individual bubbles in the laboratory and

plume dynamics in-situ, where it has been found that individual bubbles in general have a lower measured rise velocity, predicting a greater drag coefficient.

The observations and data measured from the QICS experiment show that using two dimensional imaging is inadequate in determining the bubble distributions due to a number of limitations and uncertainties from the camera resolution, focal and motion blur, along with bubble fluctuations in the three dimensions. Imaging and background noise from both the sediments and small water particles can also be misinterpreted as bubbles. These issues prevent automation of the data collection process and can also affect the validity of the data collection as it can give a large error in the measurements. A number of bubble measurements are therefore neglected when the error becomes too large for both small bubbles (affected by the resolution and noise), and the large bubbles (affected by three dimensional wobbling) giving a high degree of uncertainty. From this, there is a lack of accuracy in correctly predicting initial bubble size distributions forming on the sediments using the two dimensional imaging techniques. However, the imaging techniques allow the collection and measurement of other useful data including recordings of bubble velocities, shapes and interactions including breakup and coalescence affecting the plume dynamics and bubble size distribution.

Passive acoustic methods, as an alternative to imaging for initial bubble size measurements, provide a large amount of data that can be quickly and easily processed. This data is however limited in that it cannot measure bubble shapes, interactions or velocities, preventing analysis of mechanical characteristics and dynamics. Acoustic methods can also have inaccuracies in terms of background interference and acoustic noise that must be filtered out to gain a good data set.

Chapter 5 – Two Phase Small Scale Turbulent Ocean Model

5.1 Introduction

Using the bubble data established in Chapter 4, along with existing laboratory data for CO_2 droplets and utilising the turbulent ocean from Section 3.5, a two phase numerical model may be developed to simulate leakage case studies and scenarios in the North Sea and surrounding waters. The model designed in this thesis is based on the two phase flow governing equations in Chapter 3, predicting the physiochemical impacts in the near-field of CO_2 leakage into ocean.

This chapter consists of a description of the governing equations of a two-phase small scale turbulent ocean in Section 5.2. The sub-models for two phase interactions are developed in Section 5.3 and sub-models for fluid properties are shown in Section 5.4. Model calibration tests of liquid CO_2 and gaseous CH_4 from experimental leakage scenarios are carried out in Section 5.5, before finally a summary in Section 5.6.

5.2 The Governing Equations

The governing equations of small scale two-phase plume model consists of mass, momentum and energy developed in Chapter 3. Both phases, the dispersed phase of CO_2 and continuous phase of seawater, are treated by the Eulerian methodology [329]. Therefore the two phase equations are coupled in an Eulerian-Eulerian scheme through interactions in mass, momentum, and energy.

In addition to the velocities and temperature in both phases, the scalars for the continuous phase of seawater also include the salinity and the concentration of the CO_2 solution in order to simulate the stratification. For the dispersed phase of CO_2, the continuity equation is divided into two separate equations of void fraction and number density, which are treated as scalars, in order to estimate the bubble/droplet size.

The governing equations can be expressed as,

$$\frac{\partial \overline{\rho}_k \varphi_k}{\partial t} + \frac{\partial \overline{\rho}_k \varphi_k \overline{u}_{k,j}}{\partial x_j} = \dot{q}_{k,\phi} \tag{5-1}$$

where the dependant variables, φ, and source terms, $\dot{q}_{k,\phi}$, are listed in Table 5-1.

Table 5-1 – *A list of source terms for each dependent variable within the governing equations.*

Dependant variable φ_k	Source terms $\dot{q}_{k,\varphi}$
$\overline{\alpha}_1\overline{u}_{1,i}$	$\overline{\alpha}_1(\overline{\rho}_2-\overline{\rho}_1)g-\dot{q}_f$
$\overline{\alpha}_1$	$-\dot{q}_m$
$\frac{\overline{n}_d}{\overline{\rho}_1}$	$\dot{q}_n$
$\overline{\alpha}_2\overline{u}_{2,i}$	$-\frac{\partial\overline{p}}{\partial x_i}+\frac{\partial}{\partial x_j}\left(\overline{\alpha}_2\overline{\mu}^*\frac{\partial\overline{u}_{2,i}}{\partial x_j}\right)-\overline{\alpha}_2(\overline{\rho}_2-\overline{\rho}_{sw})g+\overline{F}s_{ij}+\dot{q}_f$
$\overline{\alpha}_2$	$\dot{q}_m$
$\frac{\overline{Y}_{CO_2}}{\overline{\rho}_2}$	$\frac{\partial}{\partial x_j}\left(\overline{\alpha}_2\overline{\rho}_2\overline{D}_{f,Y_{CO_2}}\frac{\partial\overline{Y}_{CO_2}}{\partial x_j}\right)+\dot{q}_m$
$\overline{\alpha}_2\overline{T}$	$\frac{\partial}{\partial x_j}\left(\overline{\alpha}_2\overline{\rho}_2\overline{K}_t\frac{\partial\overline{T}_2}{\partial x_j}\right)$
$\overline{\alpha}_2\overline{S}$	$\frac{\partial}{\partial x_j}\left(\overline{\alpha}_2\overline{\rho}_2\overline{D}_{f,S}\frac{\partial\overline{S}}{\partial x_j}\right)$

* $\overline{\mu}=\overline{\mu}_2-\overline{\mu}_t$, accounting for the turbulent eddy viscosity, where $\overline{\mu}_t=\overline{\rho}_2\nu_t$

5.3 Development of Sub-Models

Within the interaction terms described in Section 3.3, sub-models are required to calculate or predict certain fluid properties or parameters. This includes the Sherwood number and drag coefficient for both bubbles and droplets, along with a sub-model to determine the initial bubble or droplet size leaked from the seafloor and interactions whilst rising in the water column.

5.3.1 Drag Coefficient

As discussed in the previous chapters, the drag is a complex phenomenon, in part due to bubble and droplet deformation, along with the fluctuating boundary layer dynamics at the interface and therefore is also commonly predicted through empirical data. In general, the drag coefficient of a small bubble or droplet can be expressed through the Reynolds number alone, as smaller bubbles or droplets have low buoyancy and remain

spherical such as Figure 4-14 (a); for which correlations were compiled by Clift et al. [184].

Larger bubbles and droplets have greater buoyancy and therefore start to deform from spherical to elongated, with cap like shapes as shown in Figure 4-14 (e) where the effect on the flow, generated by the changes in the shape of the bubble or droplet, on the drag coefficient must be taken into account. In practice, additional dimensionless parameters may be used to define the shape such as Morton and Eötvös numbers as discussed in Section 4.3.4. These are employed in the construction of a correlation from Bozzano and Dente [266],

$$C_d = f_f \left(\frac{d_{mj}}{d_e} \right)^2 \tag{5-2}$$

$$f_f = \frac{48}{\mathrm{Re}} \left(\frac{1 + 12Mo^{1/3}}{1 + 36Mo^{1/3}} \right) + 0.9 \frac{Eo^{3/2}}{1.4\left(1 + 30Mo^{1/6}\right) + Eo^{3/2}} \tag{5-2b}$$

$$\left(\frac{d_{mj}}{d_e} \right)^2 = \frac{10\left(1 + 1.3Mo^{1/6}\right) + 3.1Eo}{10\left(1 + 1.3Mo^{1/6}\right) + Eo} \tag{5-2c}$$

where the drag coefficient is a combination of a friction factor, f_f, and a deformation factor $\left(d_{mj}/d_e\right)^2$ based on the bubble or droplet area, along with the effect of solid hydrate formations. Comparing with all the collected experimental data, [181 – 186, 188, 189, 262], it was found that there was not one individual model that has a perfect fit for the experimental data covering each phase.

The model by Bozzano and Dent [266] provided the closest match for the larger Reynolds numbers, however diverged away from the experimental data at the mid-range, Re = 10^1 - 10^3. For bubbles with Reynolds numbers larger than 400, the drag coefficient from Bozzano and Dent [266] is seen to match experimental data with or without hydrate formations as shown in Figure 5-1 and Figure 5-2. This is with the exception of the majority of the QICS experiment data as shown in Figure 5-1, discussed in the previous chapter. For droplets, the drag coefficient from Bozzano and

Dent [266] agrees well with experimental data with hydrate formations at Reynolds numbers larger than 1200, and without hydrate formations at Reynolds numbers larger than 800 as shown in Figure 5-3 and Figure 5-4.

For Reynolds numbers below these thresholds, four separate trends can be seen in the experimental data linked to each phase. Therefore, a best fit correlation is proposed for the drag coefficient between these Reynolds numbers, where the friction factor and deformation factor may be predicted,

$$f_f = \frac{24}{\mathrm{Re}} \tag{5-2b}$$

$$\left(\frac{d_{mj}}{d_e}\right)^2 = 1 + 0.045\,\mathrm{Re} - A\,\mathrm{Re}^2 + B\,\mathrm{Re}^3 \tag{5-2b}$$

formulated using parameters A and B, given in Table 5-2.

In the QICS experiment, the vertical seawater current data can be predicted based on the effect of the plume and induced currents on the rising velocity giving an estimated measurement error of 10-20% of the overall bubble velocity (~5 cm/s). This gives a predicted relative velocity of the bubbles in respect of the seawater, and in turn, drag coefficient approaching that of the other experimental data as shown in Figure 5-1.

***Table 5-2** – A and B constants for drag friction factor.*

	A	B
Droplet without hydrate	1.5×10^{-4}	1.6×10^{-7}
Droplet with hydrate	7.5×10^{-5}	8.0×10^{-8}
Bubble without hydrate	1.5×10^{-4}	3.2×10^{-7}
Bubble with hydrate	1.2×10^{-4}	3.2×10^{-7}

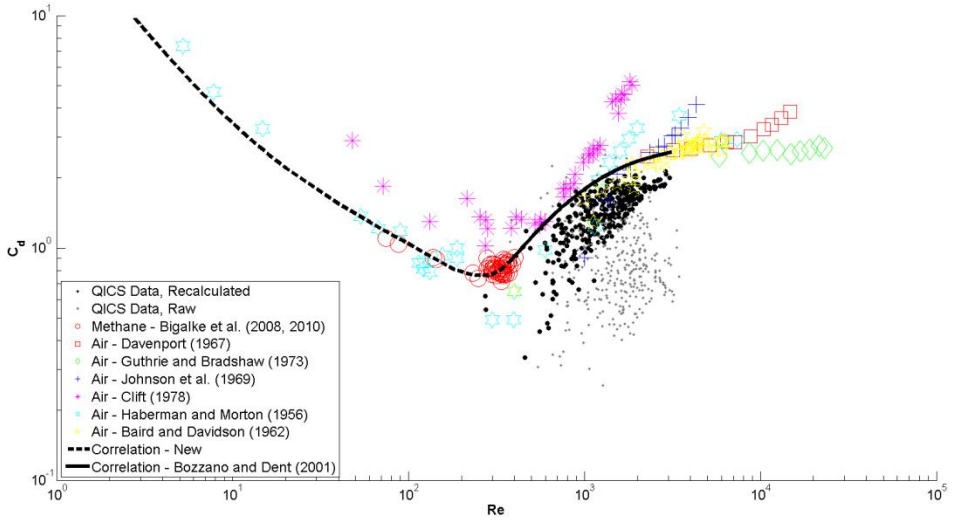

Figure 5-1 *– Comparison of the drag coefficient correlations with non-hydrate bubble laboratory experiment data (methane: [188, 189], air: [181 – 186]), and in-situ data from the QICS experiment.*

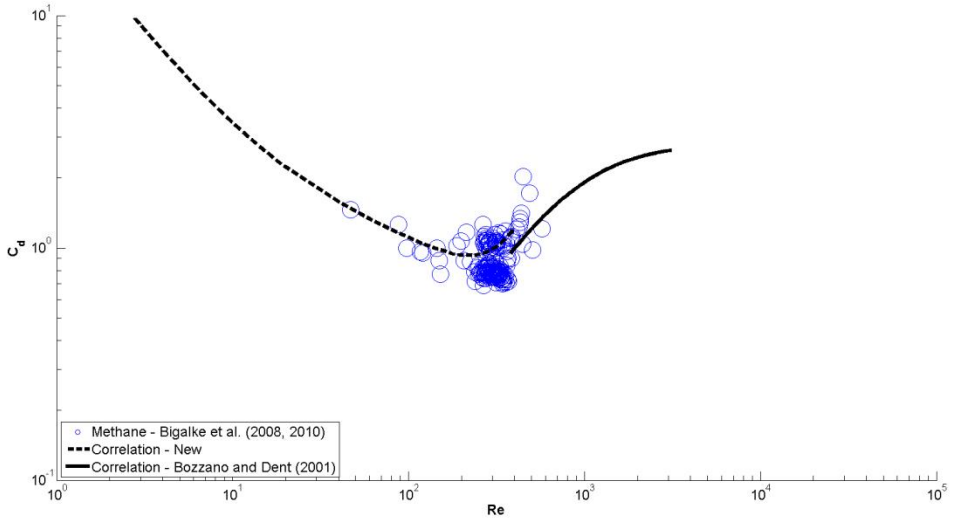

Figure 5-2 *– Comparison of the drag coefficient correlations with hydrate coated bubble laboratory experiment data (methane: [188, 189]).*

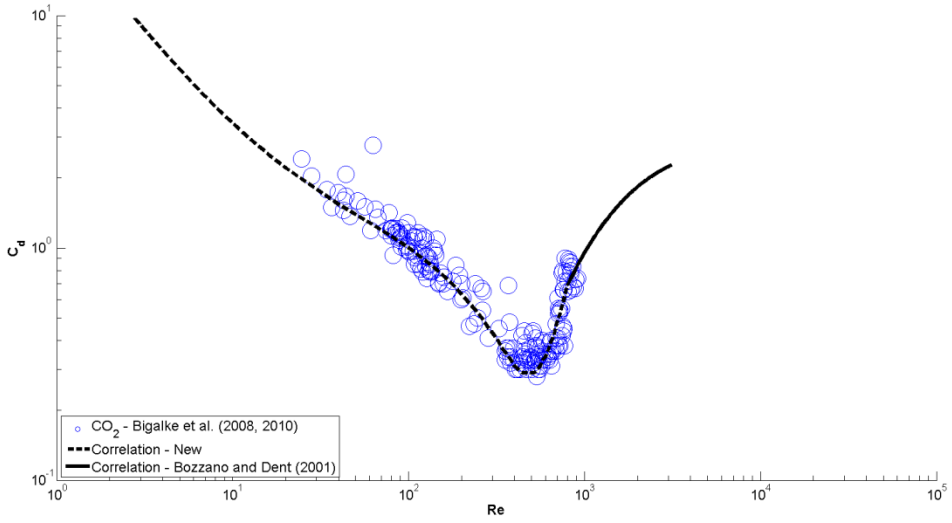

Figure 5-3 *– Comparison of the drag coefficient correlations with non-hydrate droplet laboratory experiment data (CO_2: [188, 189]).*

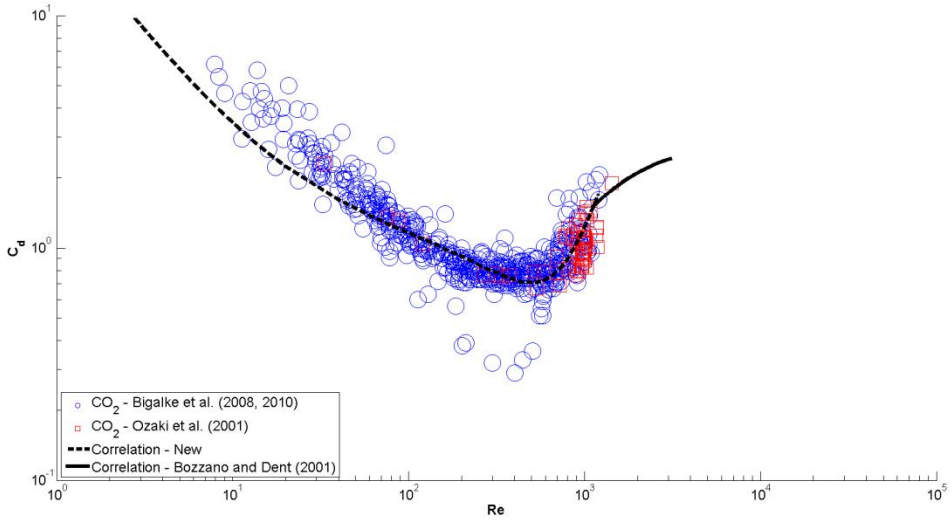

Figure 5-4 *– Comparison of the drag coefficient correlations with hydrate coated droplet laboratory experiment data (CO_2: [188, 189, 262]).*

5.3.2 Mass Transfer

There are two key parameters that govern the mass transfer (dissolution) of CO_2 in seawater; these are the solubility and effective mass transfer coefficient, which can be estimated in term of a Sherwood number.

Correlations of the Sherwood number for bubbles were proposed by Zheng and Yapa [233] based on equations developed by Clift et al. [184] and Johnston et al. [183], where the effective mass transfer coefficient, k_m, can be estimated by:

$$k_m = f_k(d_{\text{eq}}, u_{\text{rd}}) D_f^{\,n} \tag{5-3}$$

with an index of n = 1/2 for the diffusivity for all cases except those with CH_4 hydrates that increases to n = 2/3 due to the hydrate particles surrounding the bubble surface [187] acting like dirty bubbles [330, 331] and restricting dissolution. The function f_k varies dependant on the bubble diameter and corresponding shape [233],

$$f_k(d_{eq}, u_d) = \begin{cases} 1.13\left(\dfrac{u_{rd}}{0.45 + 20 d_{eq}}\right)^{0.5} & d_{eq} < 5mm \\ 6.5 & 5mm < d_{eq} < 13mm \\ \dfrac{0.219462}{d_{eq}^{\,0.25}} & d_{eq} > 13mm \end{cases} \tag{5-4}$$

where laboratory data sets of CO_2 and O_2 bubble dissolution in both tap water, or aqueous glycerol solution, provide a good correlation between the Sherwood number, Sh, and the bubble size, as shown in Figure 5-5.

For droplets, the Sherwood number is proposed by Chen et al. [169, 225] based on the Ranz and Marshal correlation [275, 276] with a deformation factor developed from experimental data [191 – 193],

$$Sh = \left(2 + 0.69\,\mathrm{Re}^{1/2}\, Sc^{1/2}\right)\left(\frac{A_{eff}}{A_{eq}}\right) \tag{5-5}$$

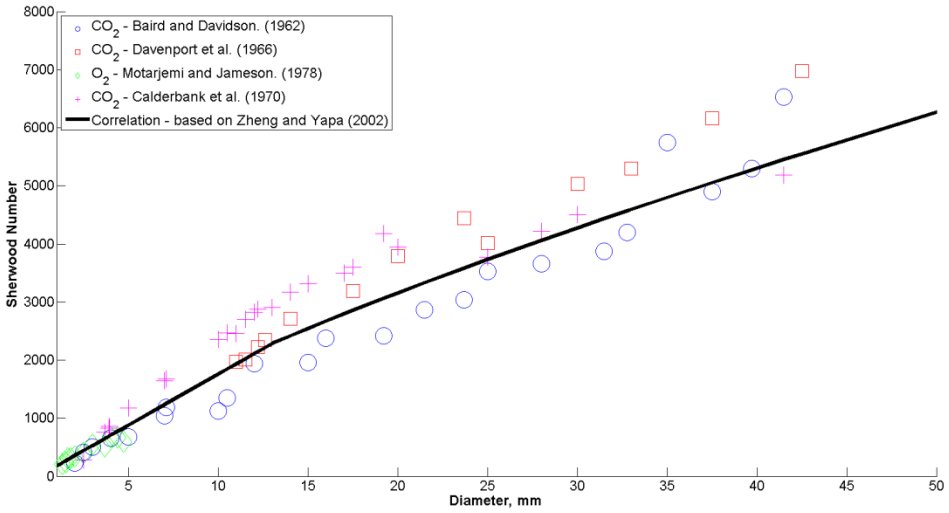

Figure 5-5 *– Comparison of the Sherwood number correlation based on that by Zheng and Yapa [233], with non-hydrate bubble laboratory experiment data (CO_2: [181, 186, 190], O_2: [180]).*

where the deformation factor is described as the ratio of total droplet area to that of an equivalent sphere:

$$\left(\frac{A_{eff}}{A_{eq}}\right) = \left(1 + 4.67075\times10^{-4}\,\mathrm{Re} - 1.1871\times10^{-6}\,\mathrm{Re}^2 + 1.4766\times10^{-9}\,\mathrm{Re}^3\right) \quad (5\text{-}6)$$

5.3.3 Bubble and Droplet Formation from the Seabed

The initial bubble and droplet size (and equivalent diameter) is vital as it determines the rate at which the CO_2 rises and the rate of dissolution. Leakages of larger bubbles or droplets at a given leakage rate have more buoyancy and therefore on average will rise faster. Smaller bubbles and droplets have more interfacial area at the given leakage rate due to a larger number of bubbles or droplets, so will dissolve quicker.

Considering the sediment as a porous medium, with a large number of mini-channels, CO_2 flows through the channels to form a single bubble/droplet. The process of bubble/droplet formation on the sediment surface can be described through the theories of Rayleigh instability. The diameter of the forming bubbles/droplets can be predicted through a force balance of buoyancy, tension and drag force due to the current as seen in Figure 5-6. The leaked CO_2 flowing through the channels will remain attached to the

channel walls until the drag and buoyancy forces exceed the tension between the bubble/droplet and the sediment surface [280].

If the bubble/droplet shape is considered a sphere and the tension is applied around the circumference of the sediment channel, the force balance is defined by the sum of the force vectors.

$$\left[\left(\rho_{sw}-\rho_{CO_2}\right)g\frac{{d_{eq}}^3}{6}\right]^2+\left[\frac{C_d}{8}\rho_{sw}u^2{d_{eq}}^2\right]^2=\left[d_{ch}\left(\sigma_{CO_2,sed}+\sigma_{sw,CO_2}\right)\right]^2 \quad (5\text{-}7)$$

As this relation assumes that there is a low flow rate, the pressure effects are neglected. At larger flow rates, the bubbles or droplets would be forced out of the channel by pressure, increasing the possibility of merging of bubbles or droplets. Collisions of bubbles or droplets from multiple channels are also neglected within this sub-model.

A range of diameters can therefore be produced, depending on the ocean currents, leakage depths and channel diameters. To find the maximum allowable bubble or droplet size formed at a certain depth, the current can be estimated at zero, removing the drag force and reducing the equation to a balance between the interfacial tension and buoyancy

$$d_e=\sqrt[3]{\frac{6\cdot d_{ch}\left(\sigma_{CO_2,sed}+\sigma_{sw,CO_2}\right)}{\left(\rho_w-\rho_{CO_2}\right)g}} \quad (5\text{-}8)$$

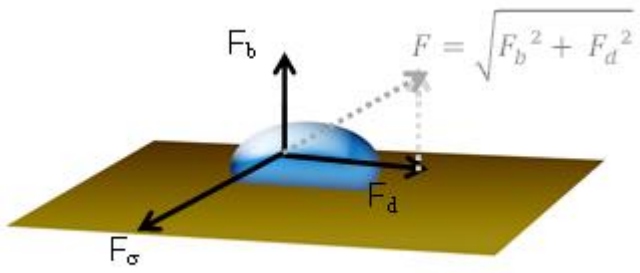

Figure 5-6 *– The initial bubble size force balance, buoyancy, drag and surface tension.*

To estimate the channel diameter from the available sediment data, such as porosity, $\phi = V_{ch} / V_{sed}$, an approximation is made, where considering a unit volume of cylindrical sediments containing a channel we have.

$$(1-\phi)V_{ch} = \phi V_{sed} \tag{5-9}$$

If the height of the channel is equal to the height of sediments, and the area of both the sediments and channel are both estimated as circular, the following is true.

$$(1-\phi)d_{ch}^2 = \phi d_{sed}^2 \tag{5-10}$$

Therefore using the assumption that the channels is uniformly distributed within the sediments, the channel diameter is found as.

$$d_{ch} = \sqrt{\frac{\phi d_{sed}^{\ 2}}{(1-\phi)}} \tag{5-11}$$

Data for the porosity and the diameter of the larger sediments particles are provided by data from samples taken from the QICS Project site on the west coast of Scotland [105]. This is not to be taken as an established calculation for channel diameter due to the high percentage of finer sand particles within the surface sediments [218]. Further assumptions include estimating a constant channel size over time, therefore sediment particles taken up through the eruption at high leakage rates, and falling debris at low leakage rates [216] have been neglected. The variations in sediments across the North Sea and the west coast of Scotland will have an impact on how the bubbles and droplets form. For these reasons, Equation (5-11) will be taken only as a predictive indication of what range of size of bubble/droplet may be formed.

Droplet formation data provided by Nishio et al. [332] and bubble formation data from both the laboratory experiment in Section 4.3.3, and the QICS experiment in Section 4.3.4 is compared to predictions using Equations (5-8) and (5-11) in Figure 5-7 (a). A reasonable agreement is found between the calculated maximum size (data points) and the experimental data range (bars) where the predictions of maximum size for each of the experiments gives a value between the mean and maximum measured diameter.

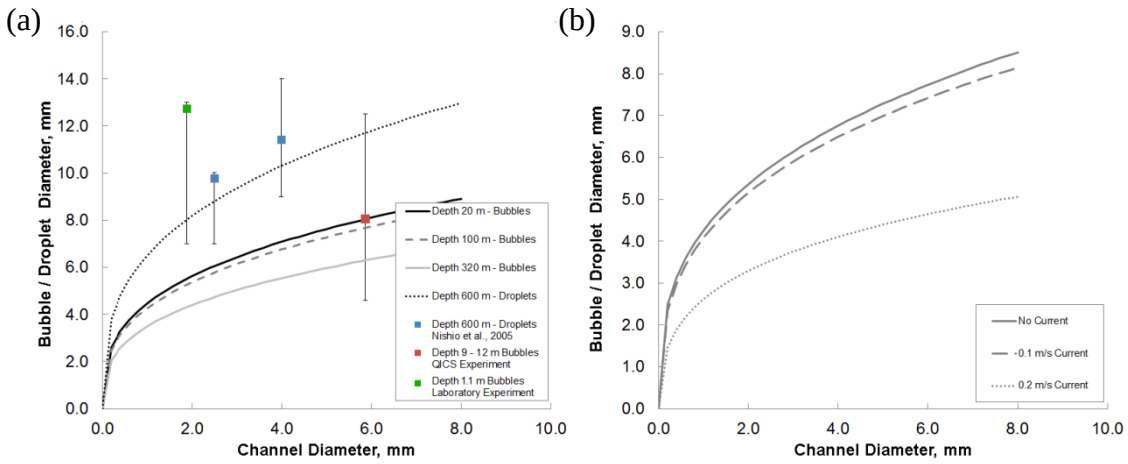

Figure 5-7 *– Sub-model for the initial bubble and droplet size formations (mm) [119]. (a) At varied depths with no seawater currents, including experimental data for droplets pressurised to 600 m from Nishio et al. [332], and the QICs experiment at 9 – 12 m depth, left; (b) At 100 meters depth with varied water currents, right.*

A range of bubble and droplet diameters are calculated dependant on the leakage depth and how water currents and leakage channels vary across the simulation. The effect of varying the depth, sediment particle size and sea water currents on the initial droplet or bubble diameter are predicted as shown in Figure 5-7. As can be seen for constant water currents and temperatures in Figure 5-7 (a), as the depth increases, the bubble diameters decrease. This shows that the reduction in tension has a more pronounced effect than the decrease in buoyancy force with depth. For droplets, the surface tension evens out as the phase change from a gas to liquid. However, a large decrease in the buoyancy force allows the droplets to greatly increase in diameter before breaking off the sediments. For increased currents, an increase in the hydrodynamic force acting against the surface tension produces smaller bubbles or droplets, as shown for bubble data sets at a depth of 100 metres in Figure 5-7 (b).

5.3.4 Bubble and Droplet Interactions

In bubbly flow, it has been shown in Chapter 4 that collisions can cause bubbles to breakup and/or coalesce, which further affects the bubble size distributions and can also alter the bubble and plume dynamics. The main driving dynamics in bubble coalescence can be described through random coalescence in turbulent flows, coalescence through laminar shear forces, and coalescence through wake entrainment. For bubble breakup the main driving mechanisms are bubble collisions with turbulent eddies, velocity gradients, large (cap) bubbles shearing smaller bubbles, and the complete breakup of

large (cap) bubbles [201]. Therefore, in developing the bubble interaction models, consideration of the distribution of bubble sizes and the ocean turbulence interactions with the bubbles is vital [205].

Mechanisms such as laminar shearing and interactions through velocity gradient are neglected from the models as they are not directly based upon the distribution of bubble parameters or void fraction [201]. The coalescence through wake entrainment also occurs with large bubbles in cap or slug like structures within pipelines [204], where Yao and Morel [209] state that smaller spherical or ellipsoidal bubbles will repel each other. Considering the frequency of bubble interactions, $\dot{q}_n$, this leads to the relationships of the breakup frequency ϑ_b and coalescence frequency ϑ_c, mainly due to the effects of turbulent eddies.

$$\dot{q}_n = \vartheta_c - \vartheta_b \tag{5-12}$$

Both the bubble coalescence and break up is defined through a term of efficiency, η_k, as the proportion of collisions that cause coalescence and break up, and a term for the collision frequency, f_k of the bubbles,

$$\vartheta_k = \eta_k f_k \tag{5-13}$$

for coalescence, subscript *k*=c, and for break up, *k*=b.

A number of models have been developed and reported in literature for the breakup and coalescence process within a pipeline setting [201 – 209], and a recent study on droplet formations from oil blowouts [238]. Care must be taken in the use of these models in bubbly plumes, as most of the existing models were designed to simulate interactions in pipeline flow with turbulence at larger Reynolds numbers that affect the overall prediction. However Hibiki and Ishii, [202] state that as the models are derived under the assumption of bubbles in an infinite space without taking into account the bubble interactions with the pipeline walls, the models could be appropriate for simulating cases in open waters. Therefore, the existing models are examined against data from the QICS experiment, with the selected models applied to the simulations.

Implementing each sub-model [201 – 209] into the two-phase plume model, the coalescence frequency is found to vary with depth. From the simulation of the QICS experiment, the best results for coalescence come from the sub-model proposed by Yao and Morel [209], using developments in the efficiency term from Nguyen et al. [205] as shown in Figure 5-8.

It is found that some models over predict the coalescence near the sediments, such as that by Wu et al. [201] and Yao and Morel [209]; where under prediction is found from the models by Hibiki and Ishii [202 – 204], Ishii and Kim [206] and Fu and Ishii [207].

Over and under prediction from the sub-models by Wu et al. [201] and Hibiki and Ishii [202 – 204] can be explained by the constant efficiencies and coefficients of the models were gained from fluids other than CO_2-seawater, that also vary between the authors. It has also been suggested that a constant void fraction may be employed to predict the bubble coalescence frequency within a pipe flow. However, in the open waters, the local void fraction varies and must be determined visually from the bubble plume, which is not a constant parameter.

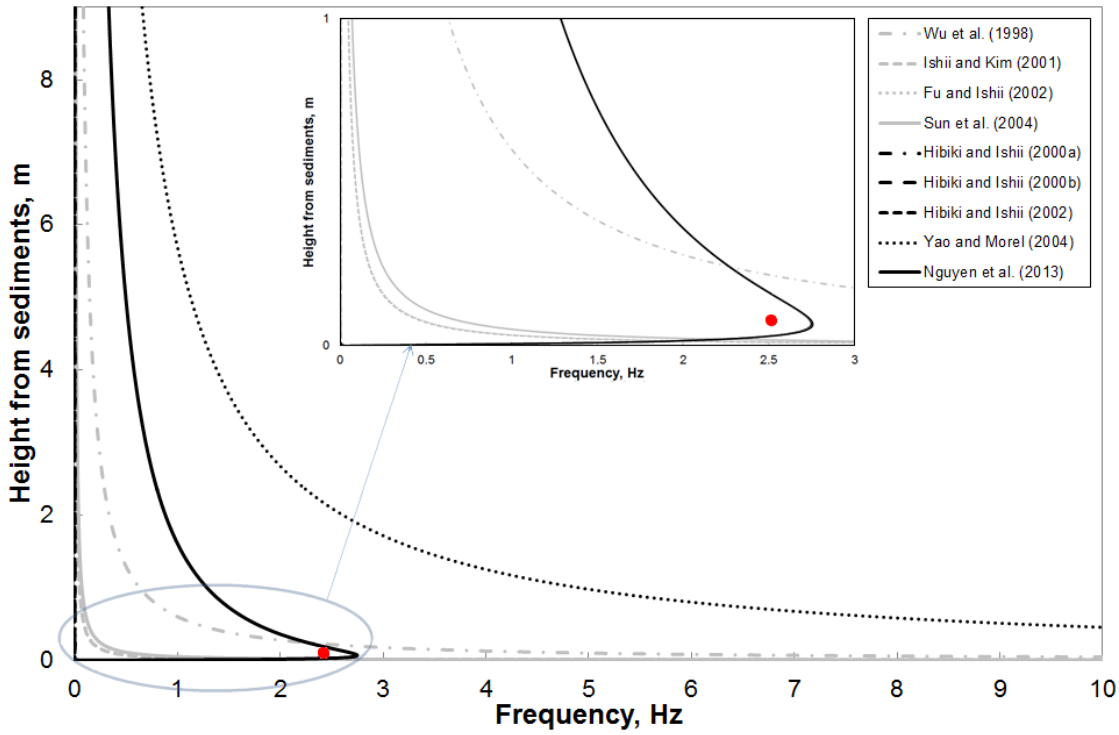

Figure 5-8 *– Coalescence frequency models [201 – 209], with the red point showing the experimental findings [118].*

Nguyen et al. [205] state that their model is an improvement on the model by Yao and Morel [209] due to the bubble distribution and turbulence suppression taken into account after collisions. This helps to explain why the frequency is closer to the experimental data, with a minimum coalescence frequency given in the first few centimetres. The frequency then rises to the same order as the experimental data, reaching a peak of 2.75Hz at 7.0 cm height from the sediments, before starting to decrease with greater distances from the seafloor shown in Figure 5-8.

5.3.4.1 Interaction efficiency

A number of models [201, 206 – 208] consider the coalescence efficiency to be a constant, at range from 0.004 to 0.056. Others [202 – 205, 209] base the coalescence efficiency on a model by Coulaloglou and Travlaraidès [333], modified to gas flow through a thin film model. The time for coalescence of bubbles is defined by Oolman and Blanch [334, 335] and Prince and Blanch [336], and the contact time for turbulent flows defined by Levich [337], giving the overall coalescence efficiency as

$$\eta_c = \Gamma_{RC} \exp\left(- Kc \frac{\rho^{1/2} d_{eq}{}^{5/6} \varepsilon^{1/3}}{\sigma^{1/2}} \right) \tag{5-14}$$

with Γ_{RC} and K_C as coefficients decided from experimental data. As shown by Nguyen et al. [205], the predicted efficiency can vary greatly depending on the use of the coefficients for a set energy dissipation rate. Both Γ_{RC} and K_C are suggested [202 – 205, 209] being in a wide range, from 0.188 to 2.86 and 0.26 to 1.29 respectively. Nguyen et al. [205] proposed to take the effects of bubble and eddy size into account by making $K_C = 0.913/\mathrm{C}^{2/3}$, giving

$$\eta_c = 2.86 \exp\left(- \frac{0.913 \rho^{1/2} d_{eq}{}^{5/6} \varepsilon^{1/3}}{\mathrm{C}^{2/3} \sigma^{1/2}} \right) \tag{5-15}$$

with C as a further coefficient, based on bubble size distribution, used to determine the turbulent eddy size in relation to the mean bubble [205].

$$C = \sqrt[11/3]{\frac{2.24(1-0.1u')\left(\left(\frac{d_{\max}}{d_e}\right)^{2/3}-\left(\frac{d_{\min}}{d_e}\right)^{2/3}\right)}{\left(\left(\frac{d_{\min}}{d_e}\right)^{-3}-\left(\frac{d_{\max}}{d_e}\right)^{-3}\right)}} \tag{5-16}$$

For breakup, all the efficiency models investigated simulate the efficiency based on Coulaloglou and Travlaraidès [333], where the ability of a bubble to resist the breakup is based on the surface tension [336]. Wu et al. [201] considers the energy to be proportional to the squared velocity, and in turn the weber number. It is also stated by Wu et al. [201] that only eddies of a similar size to that of the bubble will be effective in breakup. Hibiki and Ishii [204] and Nguyen et al. [205] go on to describe that larger eddies move groups of bubbles with minimum interaction and smaller eddies unable to provide enough interacting energy to the bubble. Therefore the breakup efficiency is based on a bubble breaking up with an eddy of equivalent size giving the following relation,

$$\eta_b = \Gamma_b \exp\left(-\frac{K_b}{We}\right) \tag{5-17}$$

with the breakup constant coefficients again found a wide range, where Γ_b is suggested to be between 0.021 to 1.6, and K_b is from 1.24 to 6.85 [201 – 204, 206 – 209]. However, Nguyen et al. [205] proposed to take the effects of turbulence suppression into account through $K_b = 1.581/(1.0-0.1u')$, giving Equation (5-18).

$$\eta_b = 1.6\exp\left(-\frac{1.581}{(1.0-0.1u')We}\right) \tag{5-18}$$

5.3.4.2 Interaction frequency

The collision frequency from Yao and Morel [209] is modelled on the basis of a prediction of the random collision rate, for either two or more bubbles for coalescence, or a bubble with a turbulent eddy of similar size for breakup. This is based on the kinetic theory of ideal gas molecule interactions, but also a development on the previous

models that both the time for collision, along with the time between each collision is required to predict the frequency for both bubble coalescence and breakup.

$$f_c = \frac{\varepsilon^{1/3}\alpha^2}{d_{eq}^{\ 11/3}} \frac{1}{g(\alpha) + 1.922\alpha\sqrt{We/1.24}} \tag{5-19a}$$

$$f_b = \frac{\varepsilon^{1/3}\alpha(1-\alpha)}{d_{eq}^{\ 11/3}} \frac{1}{1 + 0.42(1-\alpha)\sqrt{We/1.24}} \tag{5-19b}$$

The critical Weber number, We_{cr}, is given as 1.24 [205, 209] and $g(\alpha)$ is a limiting factor for when the bubbles are touching and the void fraction approaches its maximum value, $\alpha_{\max}$, where the time between collisions is negligible,

$$g(\alpha) = \frac{\left(\alpha_{\max}^{1/3} - \alpha^{1/3}\right)}{\alpha_{\max}^{1/3}} \tag{5-20}$$

where the maximum bubble void fraction $\alpha_{\max}$ is suggested to be 0.52 [205, 209].

Although the breakup is witnessed to be of orders lower than the coalescence within the QICS experiment, it was observed. However all the existing breakup models failed to predict breakup frequencies giving either a breakup rate of 0 Hz, such as the breakup model above, or became unstable due to an attempt to divide by 0. In the pipeline, critical weber numbers are given between 1.24 and 6.85 due to the unidirectional flow at high velocity [201 – 209], whereas low velocity buoyant bubbles would break at a lower weber number of 1.0 in still open waters. This would be reduced further in turbulent waters due to the Rayleigh-Taylor instabilities [258].

Although the coalescence model is also based on the large critical weber numbers, Nguyen et al. [205] states that the coalescence model is not significantly affected by the choice of critical weber number. Therefore utilising a lower critical weber number in the model may have given a better breakup prediction for breakup, but without further experimental data for validation of the choice of a new critical weber number, a statistical breakup model is taken based the measured QICS data in Section 4.3.4.

5.3.5 Dissolved Solution Chemistry and Measurements

From the dissolution of the CO_2, the concentration of the dissolved solution increases. This dissolved concentration may be measured by a number of terms including DIC, pCO_2 and pH changes.

5.3.5.1 Dissolved Inorganic-Carbon, DIC

The Dissolved Inorganic Carbon, DIC ($\mu mol/kg_{sw}$), also known as Total Inorganic Carbon, TIC, Total Carbon Dioxide, TCO_2 and Total Carbon, C_t are the total of the inorganic carbon species in a solution. CO_2 dissolution in water is driven by the chemical reactions

$$\begin{aligned} CO_2 + H_2O &\Leftrightarrow H_2CO_3 \\ H_2CO_3 &\Leftrightarrow H^+ + HCO_3^- \Leftrightarrow CO_3^{2-} + 2H^+ \end{aligned} \tag{5-21}$$

where the CO_2 and water react and dissociate into bicarbonate ions, HCO_3^-, carbonate ions, CO_3^{2-}, hydrogen ions, H^+, and small quantities of carbonic acid, H_2CO_3 that may be neglected due to low concentrations of less than ~0.3% [3]. The concentrations of each constituent vary with the pH of the solution [338]. However, if the background DIC is known, then the increase in DIC may be predicted by addition of the total dissolved solution concentration to the background concentration. As a conservative quantity, it is unaffected by pressure, temperature or salinity [3].

$$DIC = \sum \left[CO_2\right] + \left[HCO_3^-\right] + \left[CO_3^{2-}\right] \tag{5-22}$$

$$DIC = \sum DIC_{Background} + \frac{Y_{CO_2}}{44.01} \times 10^9 \tag{5-23}$$

5.3.5.2 Alkalinity and pH changes

The total alkalinity, A_t. is also a conservative parameter [3]. It is a measure of the number of moles per kilogram of hydrogen ions, H^+, equivalent to the sum of the that of each constituent with a dissociation constant, K_i, less than or equal to $10^{-4.5}$ acting as a base, minus those with a dissociation constant, K_i more than $10^{-4.5}$ acting as an acid.

Bases of interest in the seawater include bicarbonate, HCO_3^-, carbonate, CO_3^{2-}, tetrahydroxyborate, $B(OH)_4^-$, hydroxide, OH^-, hydrogen phosphates, HPO_4^{2-}, phosphate,

PO_4^{3-}, silicate, $H_3SiO_4^-$, ammonium, NH_3, bisulfide, HS^-… Whereas acids in the seawater can include hydrogen, H^+, hydrogen sulphate, HSO_4^-, hydrogen fluoride, HF, phosphoric acid, H_3PO_4… [339].

$$\begin{aligned} A_t &= \left[HCO_3^-\right] + 2\left[CO_3^{2-}\right] + \left[B(OH)_4^-\right] + \left[OH^-\right] \\ &+ \left[HPO_4^{2-}\right] + 2\left[PO_4^{3-}\right] + \left[H_3SiO_4^-\right] + \left[NH_3\right] + \left[HS^-\right]... \\ &- \left[H^+\right] - \left[HSO_4^-\right] - \left[HF\right] - \left[H_3PO_4\right]... \end{aligned} \tag{5-24}$$

The alkalinity measures how rapidly pH changes will occur in a solution. Equation (5-24) shows that with a high alkalinity, there are large quantities of base constituents able to neutralise the addition of acids. However, with a low alkalinity the pH changes will occur more rapidly as there is a reduced quantity of bases to buffer the addition of acids.

If the alkalinity of a solution is known, along with the concentration of each constituent, the number of hydrogen ions and therefore pH change may be predicted utilising iterative methods, where

$$pH = -\log\left(H^+\right). \tag{5-25}$$

To solve Equation (5-24), the concentration of each constituent requires knowledge of how the solution breaks up through dissociation, shown on Tables 1 and 2 in Dickson and Goyet [340, Ch. SOP3]. Dissociation coefficients are predicted for each constituent from Millero [341] for borates, phosphates, silicates and water, Roy et al. [342] for carbonates, Dickson and Riley [343] for fluorides, and Dickson [344] for sulphates, based on temperature and salinity. These are modified for dissociation coefficients under pressure by Millero [341, 345].

The seawater concentrations of boron is predicted by Uppström [346], sulphate is predicted by Morris and Riley [347], fluoride is predicted by Riley [348] and with phosphate and silicate estimated as negligible [340], where the concentration of carbon dioxide is provided by the model as dissolved solution.

The change in pH can be estimated through measuring the background pH, and the final pH level calculated with the CO_2 concentration added

$$\Delta pH = pH - pH_{background} \tag{5-26}$$

5.3.5.3 pCO_2

The pCO_2 measurement refers to the partial pressure of CO_2 in its ideal gas state in equilibrium with that of the seawater sample [3], the pCO_2 is calculated based on the fugacity of the CO_2 as a real gas, then corrected from to that of an ideal gas. The fugacity is often assumed to be the same as pCO_2, however minor variations occur that should be accounted for, as pCO_2 assumes ideal gas conditions [3].

Taking the dissociation constants for the carbonate, K_1, and bicarbonate ions, K_2, Equations A.11 and A.12 from Table 1 in Dickson and Goyet [340, Ch. 2] respectively, rearranged and substituted into Equation (5-22) gives

$$DIC = [CO_2]\left(1 + \frac{K_1}{|H^+|} + \frac{K_1 K_2}{|H^+|^2}\right) \tag{5-27}$$

therefore in terms of the remaining carbon dioxide content this is expressed as

$$[CO_2] = \frac{DIC \times |H^+|^2}{|H^+|^2 + K_1 \times |H^+| + K_1 K_2} \tag{5-28}$$

The fugacity can be related to the carbon dioxide content through another equilibrium constant, K_0 [340]

$$K_0 = \frac{[CO_2]}{f(CO_2)} \tag{5-29}$$

giving

$$f(CO_2) = \frac{DIC \times \left|H^+\right|^2}{\left(\left|H^+\right|^2 + K_1 \times \left|H^+\right| + K_1 K_2\right) K_0} \tag{5-30}$$

where the magnitude of the hydrogen ions, H^+, is predicted by Equation (5-24), K_0 may be expressed by Weiss [234], with K_1 and K_2 predicted by Millero [341].

The fugacity may be converted to the pCO_2 equivalent of ideal gas through a coefficient as a function of temperature and gas phase composition [340],

$$pCO2 = \frac{f(CO_2)}{f_{fact}} \tag{5-31}$$

where, f_{fact} is expressed by Weiss [234], combining the equation from Guggenheim [349],

$$f_{fact} = \exp(B + 2\partial) \times \frac{P_{atm}}{RT} \tag{5-32}$$

with mixture coefficient parameters, δ and B, from Hirscheflder et al. [350] and Sengers et al. [351] respectively as

$$\begin{aligned} B &= -1636.75 + 12.0408 \times T - 3.27957 \times 10^{-2} \times T^2 \\ &\quad + 3.16528 \times 10^{-5} \times T^3 \\ \partial &= 57.7 - 0.118T \end{aligned} \tag{5-33}$$

5.4 Fluid Properties

As the leakage of the fluids from the seafloor can be a mixture of gasses or liquids, the properties of both CO_2 and CH_4 are discussed in this section, where the properties of either fluid may be applied depending on the application. The model is developed utilising properties from both gasses including density, solubility, diffusivity and interfacial tensions based on experimental data and correlations.

5.4.1 Densities

The densities of CO_2 and CH_4 are calculated at the given temperature and pressure through interpolation of data from Ito [352], and Friend et al. [353] respectively. The densities are presented in Figure 5-9, compared with the density of seawater at a constant temperature of 7 °C and salinity of 34, calculated through the equation of state from UNESCO [354].

Both CO_2 and CH_4 are of a similar order at low depths, with the seawater being 2-3 orders higher. The density of the CO_2 increases as the pressure and depth increase at a greater rate than that of CH_4. At between 400 and 550 meters depth the phase transition from gaseous CO_2 to liquid CO_2 is highly pronounced, with the density jumping up almost 2 orders. This is in comparison to the density of CH_4 that, although transitions between gaseous and a supercritical fluid at a similar depth, it continues on the same order of magnitude as if it was a gas. The seawater has very little change in density in comparison to the other fluids, which is a far less compressible liquid.

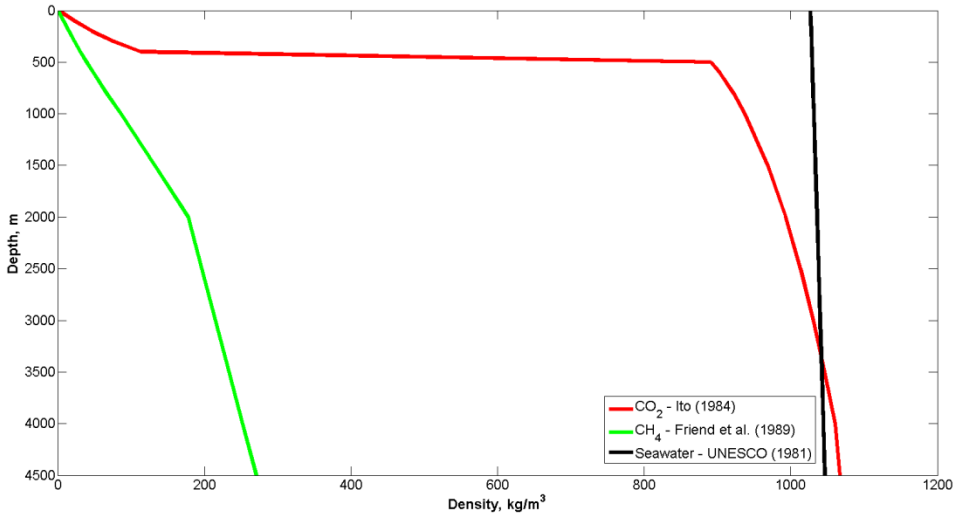

Figure 5-9 *– Comparison of carbon dioxide, CO_2, methane, CH_4, and seawater fluid densities, kg/m^3 at depth, with a temperature of 7 °C and salinity of 34.*

For CO_2, it has to be noted that the density approaches and then exceeds that of seawater at a depth of ~3 km. Therefore CO_2 bubbles or droplets above this point are positively buoyant, moving upwards approaching the sea surface, whereas CO_2 droplets at greater depths become negatively buoyant with the droplets moving downwards approaching the seabed.

As part of the stratification process, the changes in density of the seawater must be considered, as a function of pressure, temperature, salinity and the concentration of CO_2 solution. The CO_2 dissolution provides an increase in density of the seawater [355, 356] providing plume fall down. The correlation proposed by Song et al. [198] investigating the effect of the CO_2 mass fraction, Y_{CO_2}, is employed in this study,

$$\rho_{sol} = (1 + 0.273 Y_{CO_2})\rho_w \tag{5-34}$$

where the changes in density will affect the turbulent mixing and transportation of the dissolved solution in the local vicinity of the leakage [169, 225]

5.4.1.1 Solubility

CO_2, and CH_4, dissolution characteristics vary differently in waters, with the CO_2 being ~25 - 30 times more soluble than that of CH_4 [218]. The data for solubility of CO_2 and CH_4 are collected from a range of sources depending on the state of the fluid and presence of hydrates. For CO_2, experimental data is collected from Kimuro et al. [193] for droplets with hydrates, along with data from Stewart and Munjal [191] for both droplets and bubbles without hydrates, from which a model is developed by Chen et al. [225] shown in Figure 5-10.

For CH_4, experimental data is collected from Duan and Mao [357] for gas bubbles, and modelled through interpolation of the data at a given temperature, pressure and salinity. Hydrate formation occurs when the pressure exceeds a critical pressure, below a critical temperature; where Tishchenko et al. [358] developed a correlation for critical pressure calculated from the given temperature and salinity [358] also shown in Figure 5-10.

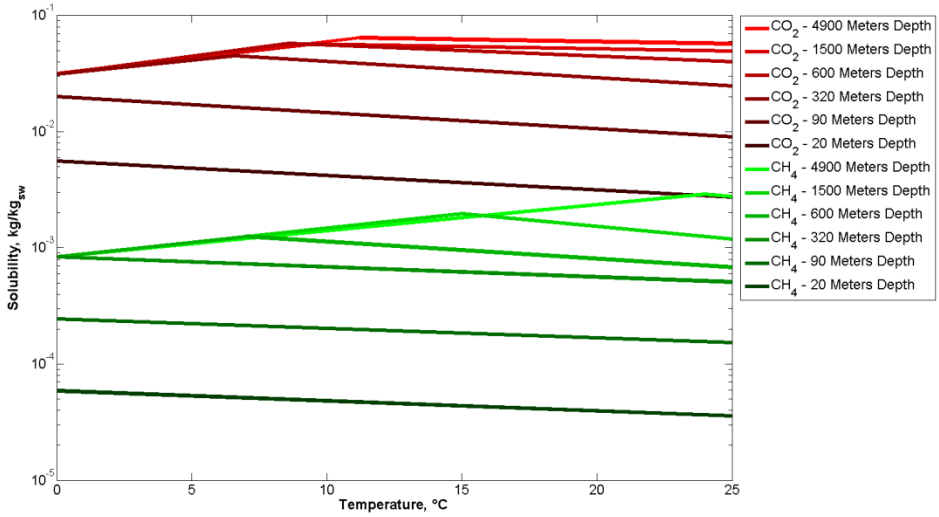

Figure 5-10 *– Comparison of Carbon dioxide, CO_2, and Methane, CH_4, solubility, kg/kg$_{sw}$, at depth.*

5.4.1.2 Diffusion

Diffusivity is an effect from random movement of molecules and ions [359]. The mass diffusivity correlations of CO_2 and CH_4 in seawater are given as a function of temperature from Ozaki [192] for CO_2

$$D_{f,CO_2/sw} = -2.8411\times10^{-8} + 1.7928\times10^{-10}T - 2.667\times10^{-13}T^2 \tag{5-35}$$

and from Jähne et al. [360] for CH_4.

$$D_{f,CH_4/sw} = 3047\times10^{-5}\times\exp\left(-\frac{18.36}{\mathrm{T}\times R}\right)\times1\times10^{4} \tag{5-36}$$

Both correlations are almost linear with a gentle curve, where the diffusion coefficient for CO_2 is increasing from 6.96×10^{-10} - 1.34×10^{-9} m^2/s as the temperature increases from 1 to 25 °C respectively. The diffusion coefficient for CH_4 is a little higher and also increases on a similar gradient from 9.68×10^{-10} - 1.85×10^{-9} m^2/s as the temperature increases from 1 to 25 °C respectively as presented in Figure 5-11 This matches diffusion coefficient findings from Kossel et al. [359].

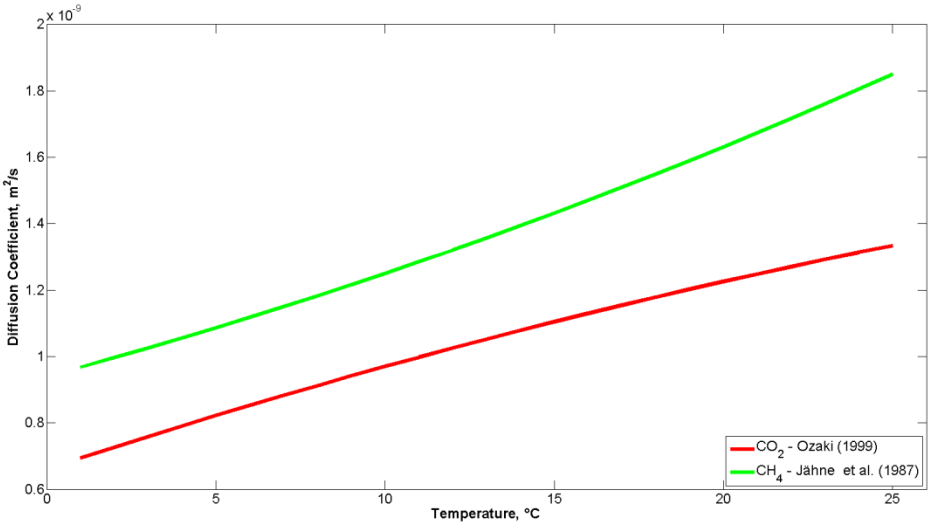

Figure 5-11 *– Comparison of carbon dioxide, CO_2, and methane, CH_4, diffusion coefficients against temperature.*

5.4.1.3 Interface tension

Surface and interfacial tension is the molecular attraction and van de Waals forces acting to hold the bubble/droplet and seawater or sediments together [361]. Correlations of the interfacial tension between CO_2, seawater and solid substrates have been applied from Espinoza and Santamarina [361], based on pressures at depth. The interfacial tension between the CO_2 and seawater provides a linear correlation from 72 - 25 mN/m, as the pressure increases with depth between 0 and 500 m, converting bubbles to droplets where it approaches a constant value of ~25 mN/m as seen in Figure 5-12.

$$\sigma_{CO_2/sw} = Max\begin{Bmatrix} 0.072 - \left(9\times10^{-5}\times depth\right) \\ 0.025 \end{Bmatrix} \tag{5-37}$$

Surface and interfacial tension between CH_4 and seawater have also been applied from that proposed by Sachs and Meyn. [362], modelled through interpolation of the data at a given pressure at depth. The interfacial tension provides a polynomial correlation from 72 - 52 mN/m, as the pressure increases with depth between 0 and 4.5 km where it approaches a constant value of ~52 mN/m as seen in Figure 5-12.

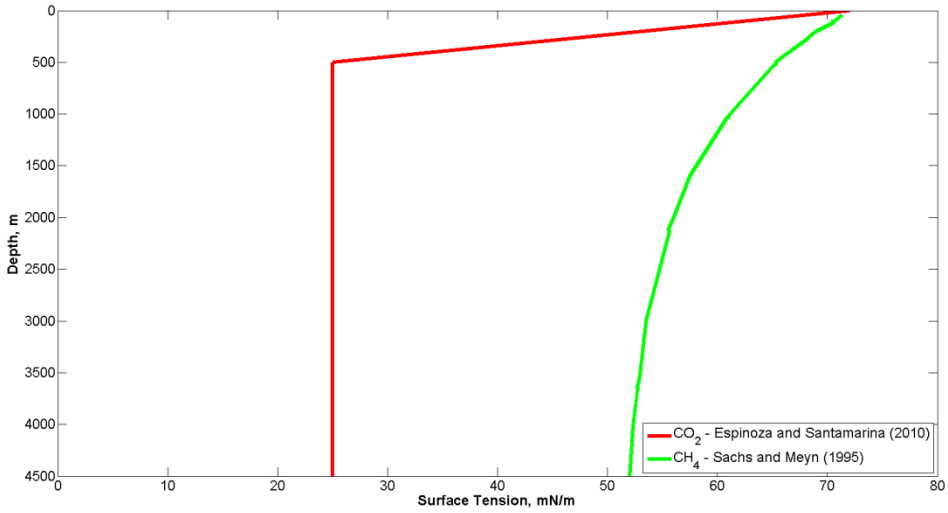

Figure 5-12 *– Comparison of carbon dioxide, CO_2, and methane, CH_4, interfacial tension against seawater at depth.*

However for the surface tensions between the gasses and sediments, the range varies and can be a complex and indirect measurement where the exact tension figures would depend on the sediment type, composition and impurities. Values have been used from Espinoza and Santamarina. [361], based on pressures at depth, where it is found that glass beads provide additional tension of 30 mN/m at the seawater surface, decreasing to 0 mN/m at a depth of ~700 m.

5.5 Calibration and Sub-Model Verification

As mentioned in Section 5.4, both CO_2 and CH_4 simulations are required to fully verify and validate the outputs from the numerical models. Therefore to validate the model developed in this section, CH_4 bubble data has been taken from an in-situ experimental release within Monterey Bay by Rehder et al. [197] along with in-situ experimental measurements of liquid CO_2 by Brewer et al. [212].

The seawater conditions for Monterey Bay are provided with the experimental data, where the temperature varies between 4 and 7.5 °C during the CH_4 bubble rising experiment [197]; and is recorded as 4.4 °C during the CO_2 droplet rising experiment [212], with the salinity also predicted as 34 [212]. For the hydrate free CH_4 bubble case, the initial bubble size released is 7.5 mm at a depth of 479 m, and 8.1 mm for the CH_4

bubble with hydrate case at a depth of 704 m [187, 197]. For the CO_2 droplets with hydrate, two droplets are tracked with an initial droplet size of 9.0 mm, released at depths of both 804.5 and 649.1 m [212].

5.5.1 Individual Bubble / Droplet Model

Comparisons with the experiment data by Brewer et al. [212] and Rehder et al. [197], are made through a free rising individual bubble / droplet model (See Appendix A for governing equations). This validates the sub-models and correlations from this chapter, determining the dissolution rate through the Sherwood number as shown in Figure 5-13, and the rising velocity through the drag coefficient as shown in Figure 5-14.

The results show that the simulations using the correlations discussed in this chapter provide good agreement with the in-situ experimental data for bubbles and droplets. However discrepancies are present, where the largest variations come from the rise height for the CH_4 bubbles, shown in Figure 5-14 (a). The measured velocity (average of 29.2 cm/s) is exaggerated by the drag force of the imaging box by ~12%, estimated by Rehder et al. [197]. However, modelling by McGinnis et al. [187] suggests the exaggeration is larger, with a lower predicted relative velocity.

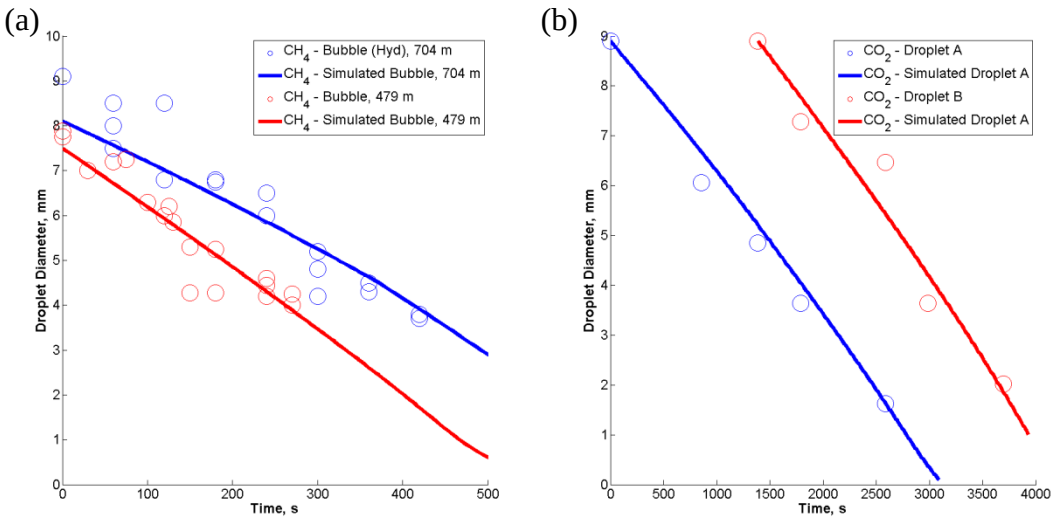

Figure 5-13 *– Individual bubble / droplet model and experimental data for in-situ dissolution rates, testing the Sherwood number. (a) Methane, CH_4 bubbles (hydrate and non-hydrate region) by Rehder et al. [197], left; (b) CO_2 droplets (in the hydrate region) by Brewer et al. [212], right.*

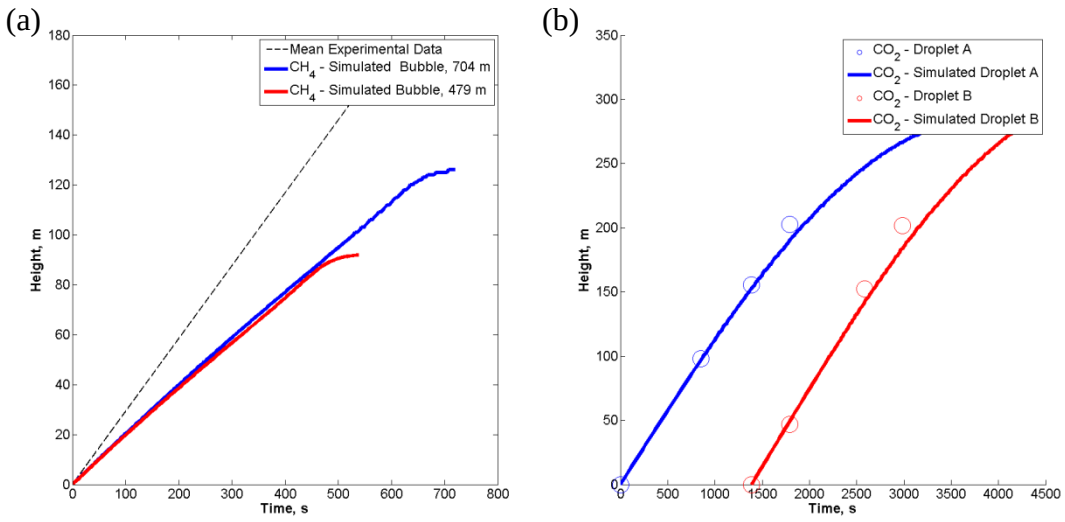

Figure 5-14 *– Individual bubble / droplet model and experimental data for in-situ rise rates, testing the Drag coefficient. (a) Methane, CH_4 bubbles by Rehder et al. [197], left; (b) CO_2 droplets (in the hydrate region) by Brewer et al. [212], right.*

For the CO_2, as the droplets reduce in size due to dissolution, Brewer et al. [212] has recorded an increase in velocity of the droplets, rather than an expected decrease due to reduced buoyancy, causing the data to split from the model in Figure 5-14 (b).

5.6 Summary

The small scale two-phase turbulent plume dynamics model was developed based on LES theories in the Eulerian-Eulerian scheme. Sub-models have been proposed or discussed to predict the phase interaction and exchange rates, including the physicochemical properties. The sub-models are calibrated with data from tracking of an individual bubble/droplet freely rising and dissolving in the ocean; and through use of these sub-models, the two phase modelling equations have been closed.

Interactions of breakup and coalescence are compared to that of the QICS experiment, where although only one data point is given from the experiment as a mean value from three video clips, one of the numerical models is selected which gave a very good prediction of the coalescence rate. However, the breakup rate is under predicted, where it is thought that the bubbles are breaking up due to their size and shape becoming unstable in the QICS experiment, rather than through turbulent eddy interactions.

Chapter 6 – Computational Fluid Dynamics: Numerical Modelling Methodology

6.1 Introduction

Given the governing partial differential equations (PDEs) in Section 5.2, algebraic formulations are required that may be numerically solved to describe the flow though computational fluid dynamics (CFD) [363]. There are multiple numerical methods and techniques for solving the governing PDEs, each with advantages and drawbacks depending on the application. Selected techniques are used in this thesis to develop the numerical solver based on ideas described by Patankar [364]. The model is then implemented on a high end computer to simulate the two phase flow.

Section 6.2 presents a brief background summary into CFD, with discretisation methods for solving the governing equations. The chosen finite volume numerical scheme is discretised and resolved in Section 6.3, with Section 6.4 summarising the model.

6.2 Background to Computational Fluid Dynamics

As described in Chapter 2, there are a number of methods for predicting fluid flow including that of laboratory, in-situ and experimental techniques. The most reliable data is that which can be measured. However, smaller scale in-situ and laboratory experiments do not provide all the data needed to analyse the impacts on the marine environment from a full scale leakage scenario. In situations where experiments are possible, difficulties in measurements can also be present as shown in the QICS experiment measurements in Chapter 4.

Therefore theoretical calculations are applied to predict the fluid flow mechanisms through the governing equations given in Chapter 3 and Section 5.2. However, solving these complex PDE equations through classical mathematics is not possible [364]. Thus solutions require to be found through discretisation of the governing equations, predicting values for dependant variables such as mass, velocity etc. at discrete locations within a domain volume [364].

The methods described in this section are not an exhaustive list, with many more grid and non-grid based models available. However, it does cover the most popular mechanisms and describes the advantages and disadvantages of each.

6.2.1 Traditional CFD Discretisation Methods

Traditional CFD methods are one of the mechanisms of predicting the dependant variables at discrete locations. A domain is filled with a grid and algebraic equations based on the governing PDEs are solved for the dependant variables at each location. The discretised algebraic equations contain the same physical properties as the governing PDEs and at each grid location are influenced by only the immediate neighbouring grids. Increasing to an infinitesimal grid size would mean that the changes in dependant variables across each grid would be small, bringing the solution of the discretised equations to that of the exact solution of the governing PDEs [364].

A number of traditional discretisation methods for solving the governing equations are available, where differences arise from the profile assumptions and derivation [364]; each with its own merits and applications.

6.2.1.1 Finite difference

Finite difference applications are usually calculated through a truncated Taylor series approximations as shown in Equations (6-1a) and (6-1b), neglecting the third and higher order terms.

$$\varphi_1 = \varphi_2 - \Delta x\left(\frac{d\varphi}{dx}\right)_2 + \frac{1}{2}(\Delta x)^2\left(\frac{d^2\varphi}{dx^2}\right)_2 ... \qquad (6\text{-}1a)$$

$$\varphi_3 = \varphi_2 + \Delta x\left(\frac{d\varphi}{dx}\right)_2 + \frac{1}{2}(\Delta x)^2\left(\frac{d^2\varphi}{dx^2}\right)_2 ... \qquad (6\text{-}1b)$$

Through simultaneous equations, the first order linear and second order approximations around an arbitrary grid point 2 can be found based on the neighbouring grid points 1 and 3.

$$\left(\frac{d\varphi}{dx}\right)_2 = \frac{\varphi_3 - \varphi_1}{2\Delta x} \qquad \left(\frac{d^2\varphi}{dx^2}\right)_2 = \frac{\varphi_1 + \varphi_3 - 2\varphi_2}{(\Delta x)^2} \tag{6-2}$$

Although this is relatively straightforward, it doesn't provide flexibility in the profile assumptions. This can be problematic for solutions of complex mathematical functions, such as exponential terms [364].

6.2.1.2 Finite element

Finite element is a powerful method of solving PDEs, where each grid element is represented by a set of equations. These grid equations are then combined into a global system of equations to be solved [365].

The element equations are simple algorithms that approximate the profile of the governing PDEs through trail functions fitted to the PDEs within the grid. The trial function would giving a residual from the approximation, where weight functions are fitted utilising polynomials to reduce this residual [364]. The inner product of the integral of the residual and weight functions is required to approach zero for an accurate solution to be found [366].

$$\int WR\,dx = 0 \tag{6-3}$$

This process removes the derivatives, approximating a local solution through algebraic equations. A global system of equations is then generated by extending the coordinates of the element equations from the local sub-domain of the element, to that of the entire domain [365].

The benefits are that the grid does not need to be structured, and can contain complex geometry through curved, triangular or quadrilateral elements that can be handled with ease [363]. However, the biggest issue in terms of fluid flow is that approximations are used to solve the PDEs though use of weighting functions, therefore the algebraic equations for mass momentum and energy in the finite element methods are not necessarily conservative [367].

6.2.1.3 Finite volume

A solution to the approximations in the finite element method is to use a finite volume approach. Utilising a weighting function of one in each sub-domain at a time and zero elsewhere in the domain, Equation (6-3) implies that the integral of the PDE in each control volume must equal zero. This provides conservation of quantities such as mass momentum and energy in each grid volume, and in turn, the full domain [364].

To find the integral of the PDEs in each grid location, algebraic conversions are developed using piecewise profiles between each face [364]. This is shown from the conservation of mass governing PDE in Equation (3-6); integrated through time between t and t-1, and spatially between the westerly, w, and easterly, e, grid face.

$$\int_{w}^{e}\int_{t-1}^{t}\frac{\partial \alpha\rho}{\partial t}\,dt\,dx+\int_{w}^{e}\int_{t-1}^{t}\frac{\partial \alpha\rho u_j}{\partial x_j}\,dt\,dx-\int_{w}^{e}\int_{t-1}^{t}\dot{q}_m\,dt\,dx=0 \tag{6-4}$$

Assuming an implicit formulation [364], where the second term and source terms are calculated at time t, the algebraic solution through piecewise profiles is calculated.

$$\left(\alpha_t\rho_t-\alpha_{t-1}\rho_{t-1}\right)\Delta x+\left(\alpha_{e,t}\rho_{e,t}u_{e,t}-\alpha_{w,t}\rho_{w,t}u_{w,t}\right)-\dot{q}_{m,t}\Delta x=0 \tag{6-5}$$

In finite element, an approximate solution is given by both grid values and functions, whereas in finite volume the grid point values alone give the solution to the PDEs at that specific location and time, without the need to assess how the value varies across the domain [364].

6.2.2 Non-Traditional Methods

Non-traditional numerical methods are also possible. By non-traditional it is meant that they do not necessarily discretise the governing equations for mass momentum and energy over a set domain. Methods such as the Lattice Boltzmann Method (LBM) solve governing equations other than those provided in Chapter 3. Whereas other methods, such as smoothed particle hydrodynamics (SPH) solve discretised equations without the use of a fixed grid or volume.

6.2.2.1 Lattice Boltzmann method

The lattice Boltzmann method, rather than solving the momentum through the Navier-Stokes equations, solves the discrete Boltzmann equation to simulate the flow of particles. The addition of collision models gives a stream and collision mechanism [368] resolving the flow of particles over a discrete lattice mesh.

There are some advantages over traditional CFD methods. As the collision and moving processes at each node calculated independently, it can be designed to run efficiently across parallel computer architecture [369]. However, when transport and mixing occur at multiple scales, such as in the ocean, resolving the flow at the microscale for the macroscale solution would make it computationally expensive [370].

6.2.2.2 Smoothed particle hydrodynamics

Smoothed particle hydrodynamics, like the lattice Boltzmann method, divides the fluid up into discrete particles [371]. However, these particles are not aligned on a grid or mesh, but the coordinates move with the fluid as a Lagrangian scheme [372]. Each of the particles mentioned has a spatial distance over which their properties are smoothed through a kernel function. Therefore to determine a physical quantity of a particle, the summation of relevant properties of each of the particles within this kernel function distance must be calculated [371].

The advantages of smoothed particle hydrodynamics over traditional CFD methods are that mass is conserved without additional computation as the mass can be represented by the particles themselves [371]. The pressure is also determined though a weighted contribution of the surrounding particles removing the need for predictions through linear systems of equations [371]. One of the largest advantages however is that if there are significant locations that are empty, they are neglected by smoothed particle hydrodynamics, increasing efficiency [373]. However, large spatial discontinuities are poorly handled [374]. Also, to simulate at the same resolution as traditional methods can be computationally expensive. This is because a far greater number of particles is required to show the same data as in one traditional grid of data [374].

6.2.3 Discretisation Method Selection

Analysing the discretisation methods discussed above, it can be seen that many methods may be used to model the two phase flow small scale ocean. However, some will provide more efficient or better solutions. Firstly both non-traditional CFD methods are unsuitable as described in Section 6.2.2. The lattice Boltzmann method cannot simulate macroscopic small scale ocean flow as it also contains microscopic flow features that would make the resolution prohibitively large. The smoothed particle hydrodynamics has also been neglected for the need for a large number of particles to simulate the same resolution as traditional methods, also making it computationally expensive.

For the traditional methods in Section 6.2.1, the challenges listed in the finite difference method make it infeasible, except for very basic first order linear and second order polynomial flows. The finite element mechanism is a step up, able to model highly complex simulations; however the lack of conservation of properties such as mass, momentum and energy is likely to provide numerical errors. This leaves the finite volume method which solves the governing PDEs across grid volumes, with conservation of the fluid properties making it the ideal solution.

An in-house computer code of the model is therefore written in FORTRAN, built utilising the finite-volume method to solve the governing equations from Section 5.2.

6.3 Finite Volume Discretisation

An example of finite volume discretisation is given in Equations (6-4) and (6-5), containing an unsteady term, along with a convection and source term. The governing equations in Section 5.2 often also contain a diffusion term making them somewhat more complex.

One of the equations that contains all of the physical terms is the Navier Stokes equation from Equation (3-13), therefore this equation will be discretised to solve for the horizontal seawater velocity ‘u’. However, the principles used are applicable to all the governing equations. The equation will be derived in a single dimension, before extended to the final 3D solution. First the equation is broken into each term, with the left hand side of the equation containing an unsteady and convection terms as U_n and C_n

respectively, and the right hand side of the equation containing source and diffusion terms as S and D_f respectively, where $U_n+C_n=D_f+S$.

$$U_n = \frac{\partial \alpha \rho u}{\partial t} \qquad C_n = \frac{\partial \alpha \rho u u}{\partial x} \tag{6-6a}$$

$$S = -\frac{\partial P}{\partial x} - \alpha(\rho - \rho_{sw})g + Fs_{ij} + \dot{q}_f \qquad D_f = \frac{\partial}{\partial x_j}\left(\alpha \mu \frac{\partial u}{\partial x}\right) \tag{6-6b}$$

As shown in Section 6.2.1.3 for single dimension flow, these terms should be integrated over each grid in terms of time from t-1 to t and in space between the westerly, W, and easterly, E, points at the respective grid faces w and e, as shown in Figure 6-1. Assuming piecewise (central difference, linear) profiles of the solution between the grid faces and time steps, algebraic equations are derived. The effect of time is dealt with later; for now it should be assumed that these only affect the unsteady term.

$$\int_w^e \int_{t-1}^t U_n \, dt \, dx = \left[\left(\alpha_{p,t}\rho_{p,t}u_{p,t}\right) - \left(\alpha_{p,t-1}\rho_{p,t-1}u_{p,t-1}\right)\right]\frac{\Delta x}{\Delta t} \tag{6-7a}$$

$$\int_w^e \int_{t-1}^t C_n \, dt \, dx = \left(\alpha_e \rho_e u_e u_e\right) - \left(\alpha_w \rho_w u_w u_w\right) \tag{6-7b}$$

$$\int_w^e \int_{t-1}^t D_f \, dt \, dx = \left(\alpha_e \mu_e \frac{\partial u_e}{\partial x_e}\right) - \left(\alpha_w \mu_w \frac{\partial u_w}{\partial x_w}\right) \tag{6-7c}$$

$$\int_w^e \int_{t-1}^t S \, dt \, dx = -\left(p_e - p_w\right) + \left(-\alpha(\rho - \bar{\rho}_{sw})g + Fs + \dot{q}_f\right)\Delta x \tag{6-7d}$$

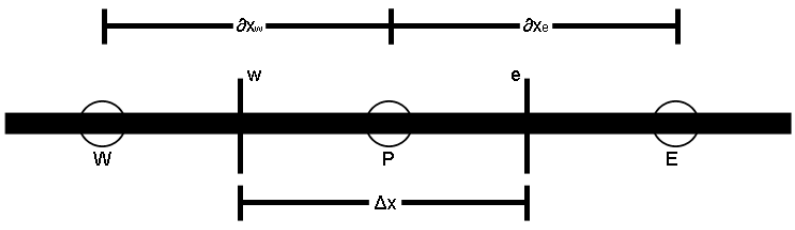

Figure 6-1 *- One dimensional grid point cluster*

The integral of each term alone shown in Equations (6-7a) - (6-7d) does not prove useful in determining the value of a dependant variable at a point, P. Therefore it is helpful to rearrange the full equation into a form where the value of the dependant variable at point P (in this case the horizontal seawater velocity 'u') can be found based on the neighbouring points.

$$a_p u_p = a_E u_E + a_W u_W + b \tag{6-8}$$

As can be seen in Equations (6-7a) - (6-7d), the values the points such as u_E, u_W and u_P are not given. However, the values at the grid faces are provided, such u_e, u_w.

6.3.1 Numerical Scheme and Profile Assumption

As shown in the previous section, the governing PDEs can be divided into four terms, with the convection and diffusion terms referring to the values or gradients at the grid faces. However, for Equation (6-8) the values at the neighbouring grid points are required rather than those at the grid face. Therefore an assumption of the profile between the grid points is required, with some examples shown in Figure 6-2.

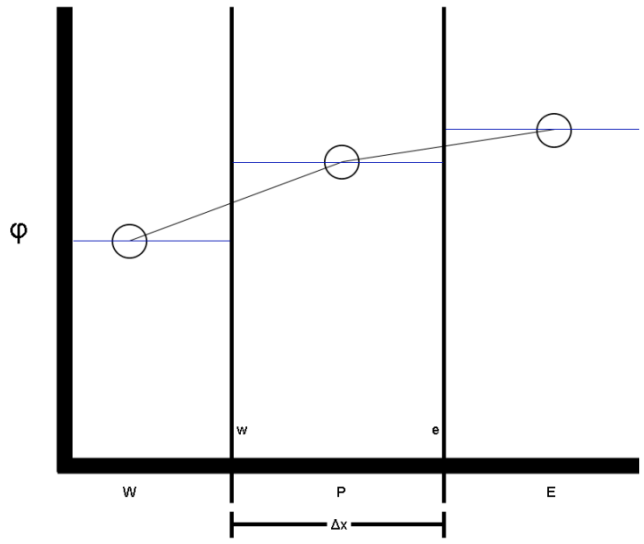

***Figure 6-2** - Profile assumptions to determine the value of the dependant variable at the faces w and e, based on westerly and easterly point data; with piecewise profiles as thin black lines and stepwise profiles as the thin blue lines.*

6.3.1.1 Central difference

The central difference, also known as the piecewise or linear scheme, is the simplest scheme where linear interpolation is used to relate the values at the grid faces to that of the grid points as shown in Figure 6-2. If the grid face is in the middle of the two points then the value can be simply calculated.

$$u_w = \frac{u_W + u_P}{2} \tag{6-9}$$

This profile assumption can however cause numerical instability when the convection term is twice that of the diffusion term as shown in Patankar [364], therefore further schemes are investigated.

6.3.1.2 Upwind

The upwind scheme, first suggested by Courant et al. [375] is a method that uses stepwise profiles as shown in Figure 6-2, based on the upwind direction. Therefore if the flow is travelling from west to east, the value at the westerly grid face would be taken from the westerly grid point and if it was travelling the opposite direction, the value at the westerly grid face would be taken from the grid point P.

$$\begin{aligned} u_w &= u_W \quad if \quad \left(\rho_W u_W - \rho_P u_P\right) > 0 \\ u_w &= u_P \quad if \quad \left(\rho_W u_W - \rho_P u_P\right) < 0 \end{aligned} \tag{6-10}$$

This differs from the central difference scheme, where the value at the grid face is the weighted average of that between the westerly grid point and the grid point P.

The mechanism of this flow can be understood through looking at fluid flow in a river, where the flow comes from upwind direction bringing its properties without being affected by the properties further downstream. This profile assumption can however cause false diffusion when the ratio of convection to diffusion is below two as shown in Patankar [364]. This can be refined with a finer mesh; however there are better matched schemes available that do not present these difficulties and constraints.

6.3.1.3 The exact solution

The exact solution is possible to be calculated, neglecting the unsteady and source terms, giving the convection term equal to that of the diffusion and assuming both terms are constant [364]. This solution approaches an exponential at high ratios of convection to diffusion, explaining why the central difference scheme is unstable except in low diffusion situations, with the upwind scheme usually more close to the solution. A scheme that matches the solution presented by Patankar [364] is developed by Spalding [376] known as the exponential scheme.

6.3.1.3.1 Exponential scheme

Substituting the exact solution into Equation (3-13), neglecting the unsteady and source terms gives the following.

$$u_w = u_W + \frac{u_W - u_P}{\exp\left(\frac{\rho_w u_w \partial x_w}{\upsilon_w}\right) - 1} \tag{6-11}$$

Although this contains terms for both the face values and the grid point values, this is due to the manner in which the equation is being shown in one dimensional flow where $\rho_w u_w$ is the convection term for the flow of the dependant variable u_w. However, the solution is also not exact for multi-dimensional flows or for calculations with source terms. Also, as exponentials are computationally heavy, further schemes have been suggested to approximate this solution [364].

6.3.1.4 Best approximation of the solution

There are two schemes developed to best approximate the solution based on the exact solution and the exponential schemes. The first is known as the hybrid scheme, originally named the high-lateral-flux modification [377], and the second is known as the power law scheme [378].

6.3.1.4.1 Hybrid scheme

The hybrid scheme returns back to the up-wind and central difference schemes, utilising cut off values to switch between upwind and central difference schemes.

$$
\begin{aligned}
u_w &= \frac{u_W + u_P}{2} \quad \text{if} \quad -2 < \rho_w u_w \delta x_w / \upsilon_w < 2 \\
&\qquad \text{else} \\
u_w &= u_W \quad \text{if} \quad \left(\rho_W u_W - \rho_P u_P\right) > 0 \\
u_w &= u_P \quad \text{if} \quad \left(\rho_W u_W - \rho_P u_P\right) < 0
\end{aligned}
\tag{6-12}
$$

This provides a reasonable match to the exact curve as shown in Patankar [364], however at values when the convection term is around twice that of the diffusion there is a rather large departure from the solution.

6.3.1.4.2 Power-law scheme

The power law scheme is a curve, fitted to that of the exact exponential solution removing the large departures witnessed in the hybrid scheme.

Each scheme can be shown in the form derived in Equation (6-8) finding the coefficients aE and aW, with Table 6-1 defining the function $A(|P|)$ [364], where the double square brackets give the largest value of the enclosed terms.

Table 6-1 – *The A(|P|) function for the different numerical schemes and profile assumptions [364].*

Scheme	Formula for the A(|P|) function
Central Difference	$1.0 - 0.5\left\|\frac{u\delta x}{\mu}\right\|$
Upwind	1.0
Hybrid	$\left[\left[0, 1.0 - 0.5\left\|\frac{u\delta x}{\mu}\right\|\right]\right]$
Power law	$\left[\left[0, \left(1.0 - 0.1\left\|\frac{u\delta x}{\mu}\right\|\right)^5\right]\right]$
Exponential (exact)	$\frac{\left\|\frac{u\delta x}{\mu}\right\|}{\exp\left(\left\|\frac{u\delta x}{\mu}\right\|\right) - 1.0}$

$$a_p u_p = a_E u_E + a_W u_W$$

$$\begin{aligned} a_E &= \frac{\alpha_e \mu_e}{\delta x_e \rho_e} A(|P|) + [[-\rho_e u_e, 0]] \\ a_W &= \frac{\alpha_w \mu_w}{\delta x_w \rho_w} A(|P|) + [[-\rho_w u_w, 0]] \\ a_P &= a_E + a_W \end{aligned} \tag{6-13}$$

6.3.1.5 The unsteady term

The formulation in the example of finite volume in Section 6.2.1.3 states that an implicit formulation is assumed with no further details into why the assumption is made. This was to provide a brief workable example, however will be discussed further here.

When integrating a governing equation by time, the unsteady term solves through a piecewise central difference profile assumption giving the changes over the time step. The convection and diffusion terms can however be calculated at any point in the time step. Therefore it is possible to solve the convection and diffusion terms at the start of the time step as an explicit formulation, where the old values prevail all the way until the new time step. Another option is to solve the convection and diffusion terms at the end of a time step as a fully implicit formulation, when the new values prevail immediately after the previous time step. The final possibility is to have a linear variation across the time step, known as the Crank-Nicolson scheme.

As stated in Patankar [364], the first sensible choice would be to use the Crank-Nicolson scheme, which is most accurate at small time steps. However this and the explicit scheme both have a serious limitation that requires a very small time step, especially at fine grid sizes, to maintain numerical stability.

To ensure that the model remains numerically stable under all conditions, the fully implicit scheme is the best choice, even if it is slightly less accurate at small time steps. Therefore, as shown in Equations (6-7b) to (6-7d) the values are calculated at the new time step implicitly.

6.3.2 The Discretised Equation

The unsteady one dimensional discretised equation is derived from Equations (6-7a) to (6-7d), rearranged into the form of Equation (6-8). Adding the components of Equation (6-7) together, the full discretised equation for the horizontal velocity 'u' can be found.

$$\begin{aligned}&\left[\left(\alpha_{p,t}\rho_{p,t}u_{p,t}\right)-\left(\alpha_{p,t-1}\rho_{p,t-1}u_{p,t-1}\right)\right]\frac{\Delta x}{\Delta t}+\left(\alpha_e\rho_e u_e u_e\right)-\left(\alpha_w\rho_w u_w u_w\right)\\&=\left(\alpha_e\mu_e\frac{\partial u_e}{\partial x_e}\right)-\left(\alpha_w\mu_w\frac{\partial u_w}{\partial x_w}\right)-\left(p_e-p_w\right)+\left(-\alpha(\rho-\bar{\rho}_{sw})g+Fs+\dot{q}_f\right)\Delta x\end{aligned} \tag{6-14}$$

Different profiles between the grid points have been discussed at length in the previous section, along with the unsteady term. Therefore using Equation (6-13) and the power law profile, the discretised equation is derived where the source terms, with the exception of the pressure field, are included through 'b' in Equation (6-8).

$$a_p u_p = a_E u_E + a_W u_W + b - \left(p_e - p_w\right) \tag{6-15}$$

$$a_E = \frac{\alpha_e\mu_e}{\delta x_e\rho_e}\left[\left[0,\left(1.0-0.1\left|\frac{u_e\delta x_e}{\mu_e}\right|\right)^5\right]\right]+\left[\left[-\rho_e u_e,0\right]\right]$$

$$a_W = \frac{\alpha_w\mu_w}{\delta x_w\rho_w}\left[\left[0,\left(1.0-0.1\left|\frac{u_w\delta x_w}{\mu_w}\right|\right)^5\right]\right]+\left[\left[-\rho_w u_w,0\right]\right]$$

$$a_P^{t-1} = \frac{\alpha_p\rho_p\Delta x}{\Delta t}$$

$$b = \left(-\alpha(\rho-\bar{\rho}_{sw})g+Fs-\dot{q}_f\right)\Delta x + a_P^{t-1}u_P^{t-1}$$

$$a_P = a_E + a_W + a_P^{t-1}$$

As the time step, Δt, approaches zero, the unsteady term disappears reducing Equation (6-15) to a steady state equation similar to that of Equation (6-13).

6.3.2.1 The unsteady, three dimensional discretised equation

The unsteady dimensional discretised equation for velocity 'u', is extend to three dimensions giving further coefficients for the north, south, top and bottom directions as subscripts N, S, T and B respectively. Equations in the form of Equation (6-8) can also be derived for the other velocities, along with mass, temperature, salinity and number density in the same manner using Equation (5-1) and the data described in Table 5-1. When a governing equation does not include diffusion, the scheme automatically reverts to an upwind scheme for the convective flow.

$$a_p u_p = a_E u_E + a_W u_W + a_N u_N + a_S u_S + a_T u_T + a_B u_B + b - \left(p_e - p_w\right)\Delta y \Delta z \qquad (6\text{-}16)$$

$$a_E = \left(\frac{\alpha_e \mu_e}{\delta x_e \rho_e}\left[\left[0, \left(1.0 - 0.1\left|\frac{u_e \delta x_e}{\mu_e}\right|\right)^5\right]\right] + \left[\left[-\rho_e u_e, 0\right]\right]\right)\Delta y \Delta z$$

$$a_W = \left(\frac{\alpha_w \mu_w}{\delta x_w \rho_w}\left[\left[0, \left(1.0 - 0.1\left|\frac{u_w \delta x_w}{\mu_w}\right|\right)^5\right]\right] + \left[\left[\rho_w u_w, 0\right]\right]\right)\Delta y \Delta z$$

$$a_N = \left(\frac{\alpha_n \mu_n}{\delta x_n \rho_n}\left[\left[0, \left(1.0 - 0.1\left|\frac{v_n \delta x_n}{\mu_n}\right|\right)^5\right]\right] + \left[\left[-\rho_n v_n, 0\right]\right]\right)\Delta z \Delta x$$

$$a_S = \left(\frac{\alpha_s \mu_s}{\delta x_s \rho_s}\left[\left[0, \left(1.0 - 0.1\left|\frac{v_s \delta x_s}{\mu_s}\right|\right)^5\right]\right] + \left[\left[\rho_s v_s, 0\right]\right]\right)\Delta z \Delta x$$

$$a_T = \left(\frac{\alpha_t \mu_t}{\delta x_t \rho_t}\left[\left[0, \left(1.0 - 0.1\left|\frac{w_t \delta x_t}{\mu_t}\right|\right)^5\right]\right] + \left[\left[-\rho_t w_t, 0\right]\right]\right)\Delta x \Delta y$$

$$a_B = \left(\frac{\alpha_b \mu_b}{\delta x_b \rho_b}\left[\left[0, \left(1.0 - 0.1\left|\frac{w_b \delta x_b}{\mu_b}\right|\right)^5\right]\right] + \left[\left[\rho_b w_b, 0\right]\right]\right)\Delta x \Delta y$$

$$a_P^{t-1} = \frac{\alpha_p \rho_p \Delta x \Delta y \Delta z}{\Delta t}$$

$$b = \left(-\alpha(\rho - \bar{\rho}_{sw})g + Fs - \dot{q}_f\right)\Delta x \Delta y \Delta z + a_P^{t-1} u_P^{t-1}$$

$$a_P = a_E + a_W + a_N + a_S + a_T + a_B + a_P^{t-1}$$

This may be re-written in short hand as,

$$a_p u_p = \sum a_{nb} u_{nb} + b - (p_e - p_w)\Delta A_{nb} \tag{6-17}$$

$$a_{nb} = \left(\frac{\alpha_{nb}\mu_{nb}}{\delta x_{nb}\rho_{nb}} \left[\left[0, \left(1.0 - 0.1 \left| \frac{u_{nb}\delta x_{nb}}{\mu_{nb}} \right| \right)^5 \right] \right] + [[(+_{nb,i-1} \ or \ -_{nb,i+1})\rho_{nb}u_{nb}, 0]] \right) \Delta A_{nb}$$

$$a_P^{t-1} = \frac{\alpha_p \rho_p \Delta x \Delta y \Delta z}{\Delta t}$$

$$b = \left(-\alpha(\rho - \bar{\rho}_{sw})g + Fs - \dot{q}_f \right) \Delta x \Delta y \Delta z + a_P^{t-1} u_P^{t-1}$$

$$a_P = \sum a_{nb} + a_P^{t-1}$$

with the subscript nb referring to the neighbouring terms, i-1 and i+1 are the upstream and downstream conditions respectively and ΔA_{nb} is the surface area acted on.

6.3.3 Solver

Now that a governing equation has been derived in discretised form, a solution is required for the algebraic equation. Direct solutions to Equation (6-16) are computationally expensive, requiring a large amount of computational storage and time [364]. However a solution for the single dimension flow in Equation (6-15) can be easily obtained through a straightforward Gaussian elimination algorithm known as the Thomas algorithm or Tri-Diagonal Matrix Algorithm (TDMA).

6.3.3.1 Tri-diagonal matrix algorithm

The tri-diagonal matrix algorithm takes Equation (6-8) and knowing the boundary values or conditions, all the other values in the system may be solved. The main idea behind the solver is that we want to find the value of the velocity 'u', based on neighbouring values. This is possible through,

$$u_P = P_P u_E + Q_P \tag{6-18a}$$

$$u_W = P_W u_P + Q_W \tag{6-18b}$$

where the component, P, is a function of a neighbouring value, and a component, Q, is a constant built from the source terms time dependency and neighbouring coefficients. Substituting Equation (6-18b) into Equation (6-8) gives,

$$a_p u_p = a_E u_E + a_W \left(P_W u_P + Q_W\right) + b \tag{6-19}$$

where rearranging this into the form of Equation (6-18a), P_P and Q_P can be found.

$$P_P = \frac{a_E}{a_P - a_W P_W} \tag{6-20a}$$

$$Q_P = \frac{b + a_W Q_W}{a_P - a_W P_W} \tag{6-20b}$$

Therefore the value for the velocity 'u' at point P can be calculated through the terms P_P and Q_P using equation (6-18a), which is based on the coefficients of the neighbouring and source terms as shown in Equations (6-20a) and (6-20b).

6.3.3.2 Iterative methods

The above solution to the governing equations does not have to solved be in one direction. Although the above shows a solution in the westerly direction based on easterly values, it can also be solved in reverse in the easterly direction based on the westerly values. For non-linear problems a combination of both directions solved iteratively is required, using updated coefficients to approach the solution.

Relaxation factors are used to accelerate or slow down changes in values from the previous iteration to get a converged result. This is done through taking the difference between the iteration values, and multiplying it by a relaxation factor before adding to the old value. If the relaxation factor is greater than one it is overrelaxation, forcing the iterations to change at a greater rate, and if it is less than one it is underrelaxation, slowing down the changes between iterations.

Again referring to Equation (6-8), the value of the velocity at the present iteration, i, may be found.

$$u_{p,i} = \frac{a_E u_E + a_W u_W + b}{a_p} \tag{6-21}$$

If the previous iteration, i-1, is taken into account, it must be added and subtracted to this giving the same solution.

$$u_{p,i} = u_{p,i-1} + \frac{a_E u_E + a_W u_W + b}{a_p} - u_{p,i-1} \tag{6-22}$$

The last two terms are the terms multiplied by the relaxation factor, α, to over or under relax the changes between iterations.

$$u_{p,i} = u_{p,i-1} + \alpha\left(\frac{a_E u_E + a_W u_W + b}{a_p} - u_{p,i-1}\right) \tag{6-23}$$

6.3.3.2.1 The multi-dimensional problem

Linear multi-dimensional problems that only need to be solved once only may be suitable for a direct solution due to the amount of computational resources required to solve direct solutions [364]. However, with Equation (6-16) and the majority of the three dimensional governing equations, the non-linearity requires another solution as direct solutions are uneconomical.

Many iterative methods are possible [364], the Gauss-Seidel method solves each point in a certain order, based on estimations from initial guesses or the previous iteration value, approaching the solution after a number of iterations. However the solution can be slow to converge and can in some cases diverge, giving numerical errors. Therefore a more convenient method of solving multi-dimensional problems is a line by line method.

The line by line method works by starting on a grid line of the X, Y or Z dimension and solving utilising the TDMA in section 6.3.3.1. This is solved for each line in that

direction, before using the same process in the other dimensions. Once each dimension has been solved, they should be updated through an iterative process until convergence. Altering the direction of the solver can speed up convergence as it allows the data in each of the boundaries of the simulation to transfer through the grid [364].

6.3.4 Pressure and Flow Field Challenges

The main numerical solver has been described in the previous sections. However there are a couple of terms that can cause challenges to the model that need exploring. Both issues relate to the pressure and flow field, with the first being due to a numerical anomaly where a fluctuating pressure or mass across a grid can be calculated as uniform under certain circumstances. The second challenge is the prediction of the pressure field source term in the momentum equations.

6.3.4.1 Numerical anomaly in the pressure terms and continuity equation

Looking at the first expression in Equation (6-7d) for the source term, this gives the pressure flow field. If a piecewise linear profile is assumed then this gives,

$$p_w - p_e = \frac{p_W + p_P}{2} - \frac{p_P + p_E}{2} = \frac{p_W - p_E}{2} \tag{6-24}$$

and in the same manner, if a steady state, incompressible version of the continuity equation with no source terms is found then the following would also be true.

$$\frac{\partial u}{\partial x} = u_e - u_w = \frac{u_E - u_W}{2} \tag{6-25}$$

This gives the anomaly where the calculation of either the pressure changes or the flow over point P, in fact neglects any information in point P itself. In other words, the alternate rather than adjacent grid points are involved in the calculations. This creates a challenge in a situation as shown in Figure 6-3, where zigzag pressure or velocity fields occur at the grid locations[1]. Here the solver would accept these fields as uniform rather than fluctuating.

Figure 6-3 *– Zigzag pressure or velocity field*[1]

The solution to this challenge is to operate the velocities on a staggered grid, first proposed by Harlow and Welch [379] where the grid points in the direction of flow for the velocities are on the grid faces for the other equations. A beneficial consequence is that the continuity equation does not have to determine the velocities at the grid faces. However, the main benefits of the staggered grid are that adjacent velocity components are analysed in the governing equations, removing the inconsistencies if a locally fluctuating flow was to occur. In the same manner, the pressure field would also occur over adjacent velocity components [364].

The momentum equations can therefore be re-derived with a staggered grid, where the grid points are on the grid faces of the other governing equations. This gives the benefit that Equation (6-24) no longer needs to be interpolated, with the pressure difference being the across the grid points $p_P - p_E$. The first term in Equation (6-15), (6-16) or (6-17) may therefore be rewritten as

$$a_p u_p = \sum a_{nb} u_{nb} + b + (p_W - p_P)\Delta A \tag{6-26}$$

6.3.4.2 The pressure field

The previous section showed how to remove anomalies in the pressure field in the momentum equations using a staggered velocity grid. However, to solve the momentum equations, one must also determine the pressure field itself. If the pressure is not given, it must be estimated. However, if an incorrect pressure is estimated then the continuity equation will no longer be satisfied [364] giving poor simulation accuracy and unreliable results.

[1] These are arbitrary numbers and could be of any quantity, the point is that either the adjacent velocity values or the adjacent pressure values differ, yet the alternate values are the same.

The aim is therefore to guess the pressure, and then improve this guess through corrective pressures until it satisfies the continuity equation. If p^* is the guessed pressure, u^* is the subsequent calculated velocity, p' is a pressure correction and u' is a velocity correction, then the following is true.

$$a_p u_P^* = \sum a_{nb} u_{nb}^* + b + \left(P_W^* - P_P^*\right)\Delta A \tag{6-27}$$

$$p = p^* + p' \qquad\qquad u = u^* + u' \tag{6-28}$$

Subtracting Equation (6-27) from Equation (6-26) and removing the convection/diffusion terms for convenience gives the corrected velocity in terms of the corrected pressure [364].

$$a_p u'_p = \left(p'_W - p'_P\right)\Delta A_P \tag{6-29}$$

Dividing by the coefficient a_p gives the velocity-correction formula,

$$u'_p = \frac{\Delta A_P}{a_p}\left(p'_W - p'_P\right) \tag{6-30}$$

where substituting Equation (6-30) into Equation (6-28) gives the updated velocity in terms of the guessed velocity and corrected pressures.

$$u_p = u_P^* + \frac{\Delta A_P}{a_p}\left(p'_W - p'_P\right) \tag{6-31}$$

The updated velocities in the y direction and z direction for ‘v’ and ‘w’ may be calculated in the same manner. To check the velocity and pressure guesses, the continuity equation must be derived in the same manner as the momentum equation in this section. Then, substituting Equation (6-31) for each velocity and rearranging solves the pressure correction; where the mass source term, b, will equal zero when the velocities satisfy the continuity equation [364].

$$a_p p'_p = \sum a_{nb} p'_{nb} + b \tag{6-32}$$

$$a_{nb} = \rho_{nb} \frac{\Delta A_{nb}}{a_{nb}}$$

$$a_P = \sum a_{nb}$$

$$b = \frac{(\rho_P^{t-1} - \rho_P)}{\Delta t} \Delta x \Delta y \Delta z + \left(\left(\rho u^* \right)_w - \left(\rho u^* \right)_e \right) \Delta y \Delta z + \left(\left(\rho v^* \right)_t - \left(\rho v^* \right)_b \right) \Delta x \Delta z + \left(\left(\rho z^* \right)_s - \left(\rho z^* \right)_n \right) \Delta x \Delta y$$

An algorithm is therefore required to go through the pressure and velocity guess values and corrections until mass continuity is reached. The procedure used is known as the SIMPLE algorithm, which stands for semi-implicit method for pressure linked equations [376]. The steps are as follows as described by Patankar [364].

1. Guess the pressure field p^* and solve the momentum equations in Section 6.3.2.
2. Solve the p' in Equation (6-32).
3. Calculate new corrected pressure and velocity terms using Equation (6-28).
4. Treat the new pressure as the guessed value and repeat cycle until convergence.

6.4 Summary

An in-house computer code of the model, written by FORTRAN, is built utilising the finite-volume method to solve the governing equations from Section 5.2. An example for discretisation is given for the Navier Stokes momentum governing equation in seawater; derived in both single-dimension and multi-dimensions; where the remaining governing equations are derived in the same manner.

The Navier Stokes momentum equation was shown as it is the most complex of the discretised governing equations, covering not only unsteady, convection, diffusion and source terms, but also challenges with the flow and pressure field. These challenges are overcome through use of both staggered grids preventing numerical instabilities and the SIMPLE algorithm to predict the pressure field in the momentum equations.

The developed numerical model will be further tested and validated against bubbly plume observation data from the QICS experiment in Chapter 7. It will then be applied to locations in the North Sea and surrounding waters, utilising localised parameters to further develop the turbulent ocean in Chapter 8.

Chapter 7 – Model Applications: The QICS Experiment

7.1 Introduction

Consider CO_2 leakage from the QICS experiment; the CO_2 acts as a plume rising into the open waters and will begin to dissolve with the natural waters being under-saturated in terms of CO_2 [40], shown in Figure 3-1. The questions raised are firstly whether the modelled CO_2 reaches the atmosphere as found in the experiment in Section 4.3.4, and secondly, how does the dispersion and dissolution of the CO_2 bubbles in the seawater affect the seawater chemistry, vital to determine the effect on the local biology and ecosystem.

The physicochemical impact of a CO_2 leak from the seabed investigated in the QICS experiment is therefore numerically modelled as part of this thesis, with results recorded for the rise height of the bubbles and concentration of the dissolved solution in terms of pCO_2. These are analysed and compared with the experimentally measured impacts from the leakage on the seawater to validate and verify the model findings at CO_2 sediment injection rates of 80, 170 and 208 kg/day.

Section 7.2 presents calibration of the numerical model to the QICS site, with simulations applied to the QICS experiment designed to predict the impact through the two-phase, small-scale, turbulent numerical ocean model detailed in Section 7.3. Finally, Section 7.4 summarising the findings from the QICs model, compared to that of the experiment data.

7.2 Calibration and Model Setup

7.2.1 Computational Domain

As the QICS experiment was a single point injection of CO_2, the pockmarks occur in a small area of 15 × 15 m in a water depth of 9 – 12 m. Therefore the small scale ocean is set as 50 × 50 × 9.5 m to simulate the localised physicochemical changes. To enable to forcing of the kinetic energy through a simple FFT algorithm, the number of grid cells is required to be a power of 2. Utilising an equidistant grid of 256 × 256 × 32 elements gives a grid size in the horizontal plane of 19.53 cm, and 29.69 cm in the vertical direction. This size is considered to be approximately the size of each pockmark

location, designed to predict the effects of small scale leakage from multiple separate pockmarks and the local impacts on the marine environment.

With a rise rate from Section 4.3.4.2.3 measured in the QICS experiment giving 20 - 45 cm/s and with a vertical grid size of 41.3 cm, the time to travel between each grid element can be approximated by the grid size over the velocity.

$$t \approx \frac{Grid\ size}{Bubble\ velocity} \approx \frac{29.69}{(20\ to\ 45)} \tag{7-1}$$

Therefore a modelling time step of between 1 and 2 seconds is required so that the dynamics can be recorded between grids to provide numerical stability. A time step of 1.5 seconds is used within the QICS experiment and the data output is recorded every 15 minutes until a semi-steady state has been reached, from which the data can be analysed and investigated.

The boundary conditions are set with the seabed as a non-slip closed-wall boundary, except for the CO_2 bubbles at the leakage pockmarks where an inlet boundary provides the means to release CO_2 bubbles. The top boundary, towards the water surface is considered a free surface with no mass transfer for the seawater/atmosphere. Therefore any uptake of CO_2 from atmosphere to the seawater and vice versa is considered to be negligibly small within the time scale of the simulations. However, bubbles reaching to the top boundary will flow out of the computational domain and are assumed to reach the atmosphere.

The horizontal currents at the boundaries are periodically updated to give a continuous flow in the direction of the seawater. Having released the CO_2, the outlet boundaries are set as open for the dissolved solution. To prevent any fouling of data, the computation domain is made sufficiently large to mitigate any effects from the boundary on the dissolved CO_2 and bubble plumes within the timeframe of the simulation.

7.2.2 Turbulence

Given the small grid height, LES is unsuitable to simulate turbulence due to the need to include a non-slip boundary at the seabed as shown in Section 3.5. This requires

excessively high resolution at the sediment wall for the extensive energy dissipation in this region [319]. Therefore it is suggested that a RANS turbulence model would show a better match to that of experimental data in the low depth QICS simulations [319].

To generate the turbulent ocean kinetic energy, the model is numerically forced at its uppermost wavelength using observation data collected from the QICS experiment site by Taylor et al. [115]. The energy dissipation is then modelled by a simple mixing length model, where Kolmogorov [303] determined that the kinematic viscosity, with the rate of energy dissipation, can be used to define a characteristic length of the energy dissipation.

$$\Delta x \propto \frac{\nu^{3/4}}{\varepsilon^{1/4}} \tag{7-2}$$

Rearranging this, the turbulent eddy viscosity may be found, required to calculate the small scale turbulent stress in the Navier-Stokes Equation shown in Equations (3-38a) and (3-38b). In the small scale, the characteristic length is predicted based on the grid over which the energy dissipation is occurring.

$$\nu_t = \varepsilon^{1/3} \Delta x^{4/3} \tag{7-3}$$

The rate of energy dissipation, ε, is predicted from the observation data of the kinetic energy spectra [115], as the energy dissipation in the smaller scales is equal to that transferred to small scale from the larger scales [380].

7.2.3 QICS Experiment Fluid Properties

In-situ measurements from Section 4.3.4 are taken from the leakage locations and used to set and calibrate the model. Simulations are performed to predict the plumes generated on the morning of the 12th of June 2012 when the bubbles were filmed. The recorded seawater data included a temperature of 10.7 °C and salinity of 34.7, with background levels of pH and pCO_2 of 8.05 - 8.1 and 360 µatm respectively and currents varying between -5 and +5 cm/s in the horizontal plane.

According to the experiment observations, the water depth in the model simulations is set with low and high tides at 9 m and 12 m respectively. The initial conditions are set for each simulation with the seawater temperature, salinity and background pCO_2 as recorded above. The leaked CO_2 bubbles are released into the computation domain through the grid location of each pockmark, with the initial bubble diameter based on statistical distributions shown in Figure 4-21 which varies periodically and spatially as shown in Figure 7-1.

7.3 QICS Project Experimental Simulations

The first modelling scenario is designed to simulate the QICS experiment leakage at low tide, with a high injection rate of 208 kg/day providing a sediment leakage rate of 31.2 kg/day (~15 % of injection rate), from which the effect of bubble interactions on the plume development are examined.

The impacts of the leaked CO_2 on the experiment waters for the period from the start to end of the injection are also simulated to check the affected areas at each leakage rate in terms of the changes in pCO_2 of seawater. The final study is designed at low tide, as the presumed worst case for diagnostics of the leakage mechanisms, where the leakage rate is set to 100% of the injection rate of 208 kg/day. The effects of the simulations may be compared with that in the experiment to verify the model and validate its findings.

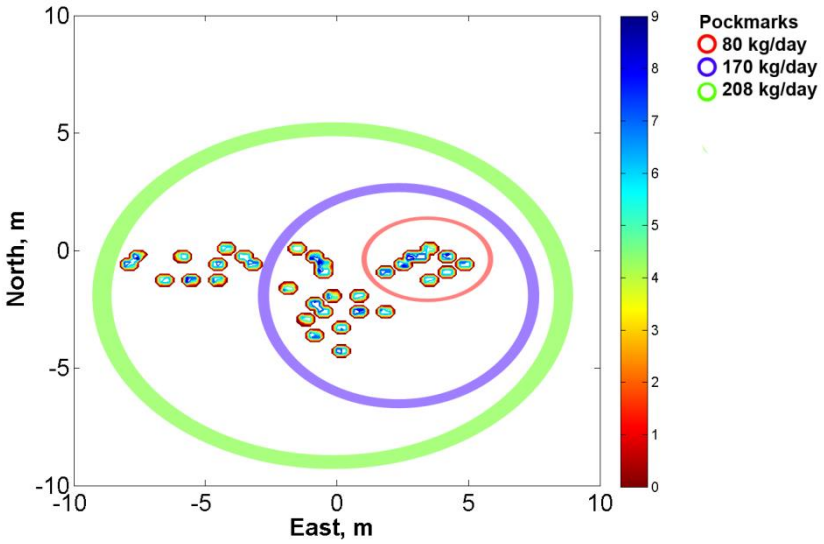

Figure 7-1 *– The pockmark locations, circled to show activity at each injection rate, with the initial bubble diameter shown in mm by the colour map, where 10, 25 and 35 pockmarks are suggested to be active during the injection rates of 80, 170 and 208 kg/day [118].*

The data are presented from the simulation 4 hours after the leakage commences when the simulation plumes have reached a semi-steady state. This is where the variation of the maximum pCO_2 in the plumes settles at a small value and the rate of change of the mean pCO_2 within the location of the pockmarks reduces to less than one percent of the initial rate of change, with minor fluctuations due to the changes in current.

7.3.1 Bubble Plume

When the bubble interactions are neglected from Section 5.3.4, the modelling simulations predict that the leaked CO_2 bubbles visually ascend up to 8.8 m from the seabed before being considered completely dissolved as shown in Figure 7-2 (a). The maximum bubble diameter is recorded as 8.3 mm, with a mean bubble diameter of 1.37 mm. However, when including the bubble interaction models from Section 5.3.4, the bubble size increases up to 9.8 mm in the first few centimetres through coalescence with the larger bubbles ascending further in the water column. These bubbles can be seen to be approaching the surface as shown in Figure 7-2 (b), where undissolved bubbles were observed from the QICS experiment at low tide [105].

There are a number of considerations that will affect the bubble plume simulation. As the minimum bubble size that can be numerically modelled in the simulations is 0.01 mm, smaller bubbles may rise further out of the water column. There is also the effect from vertical currents generated by tidal waves on the sea surface in shallow water regions meaning that measured velocities can be higher than those modelled.

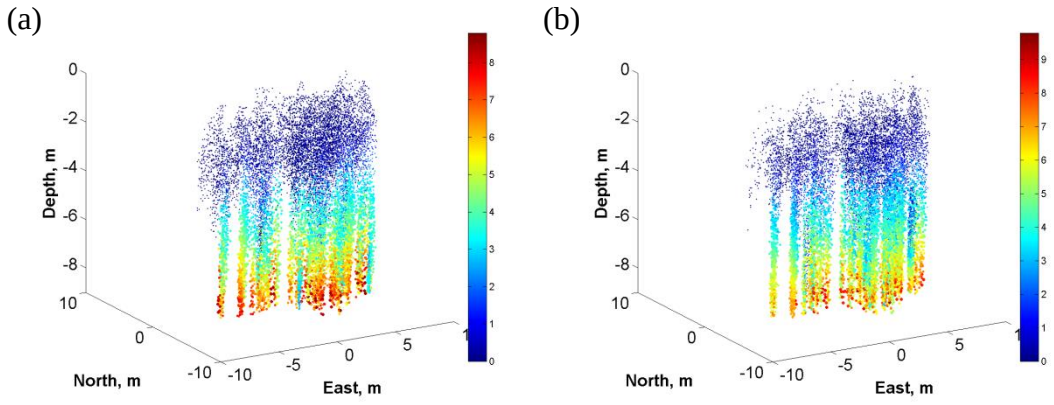

Figure 7-2 *– The low tide bubble plume at the measured leakage rate, with the bubble diameter shown in mm by both the colour map and the size of the marker [118]. (a) Bubble plume prediction with no bubble interactions, left; (b) Bubble plume prediction with bubble breakup and coalescence interactions, right.*

Finally, the initial bubble size distribution, employed from the experimental observations shown in Figure 4-21, is taken from data observed in three out of around thirty five pockmarks, where there could be some larger bubbles that may form from other pockmarks during the leakage.

To investigate and compare the fate of an individual bubble with those in a plume, the free rising model of an individual bubble (Appendix A) is applied to the QICS experiment in a quiescent ocean. This found that individual bubbles with a diameter smaller than 14.0 mm will completely dissolve before reaching the water surface as shown in Figure 7-3. This is in comparison with the results from the plume modelling in Figure 7-2 (b), where the bubbles with initial diameter of about 10 mm almost migrate to the water surface.

It can be seen that the bubble interactions in the plume, the vertical current generated by the plume, and the reduction of the dissolution rate due to the surrounding CO_2 concentrations in the plume affect the fate of bubbles, providing the differences with that of an individual bubble.

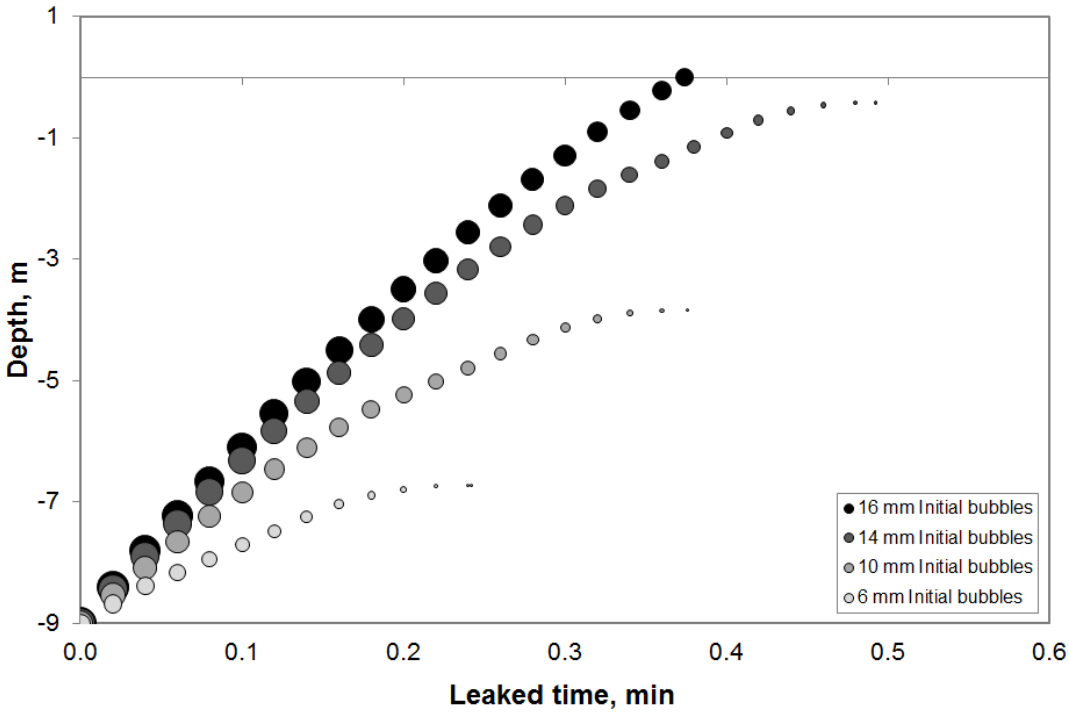

Figure 7-3 *– Bubble dissolution at 9 meters depth, showing individual bubbles with initial size > 14 mm reaching the water surface and leaking into the atmosphere [118].*

From this result, it can be assumed that the largest bubbles leaked from the various pockmarks from the QICS experiment sediments are in a range of 10 - 14 mm in diameter. This also highlights the effect of plume dynamics on bubble motion and dissolution, providing a greater rise height of the gas bubbles both in the experiment and from the plume model.

7.3.2 pCO_2

Reconstructing the bubble size distribution through interactions also provides an improvement on the spatial distribution of the CO_2 solution plume, indicated by the pCO_2 levels shown in Figure 7-4 (a) without bubble interactions and Figure 7-4 (b) accounting for the interactions. The simulations show that the interactions cause the maximum pCO_2 of the seawater slightly decreases from 445 µatm in Figure 7-4 (a), to 443 µatm in Figure 7-4 (b). As the dissolution is more distributed with larger bubbles forming through the interactions, the bubble surface area and in turn the dissolution rate is reduced, providing a slightly lower concentration of pCO_2 in the seawater.

It has to be noted that the bubble interactions in such dilute plumes seem to play a rather insignificant role on the creation pCO_2 plumes. However, the differences established from the model with and without bubble interactions indicate that the model with bubble interactions can provide better results and has the potential to be applied to simulate more dense bubble plumes that may have stronger effects in terms of a greater number of bubble collisions and interactions, changing the plume dynamics.

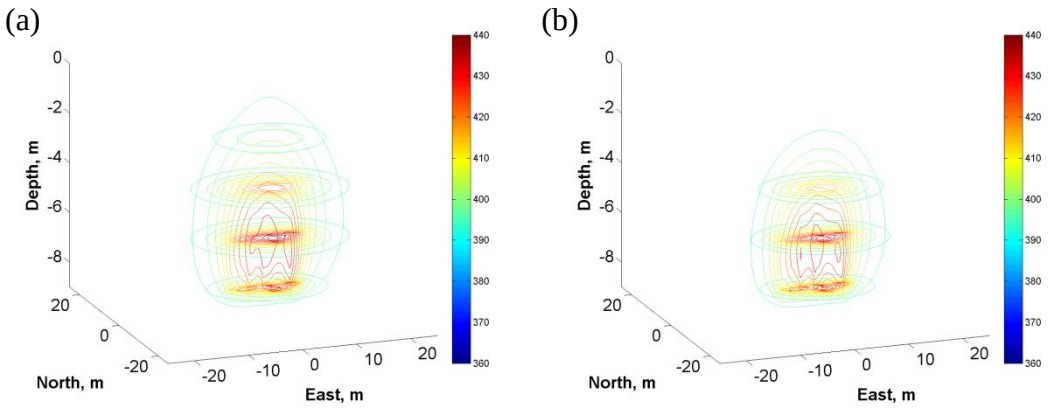

Figure 7-4 *– Contours of low tide pCO_2, µatm, in the seawater at the measured leakage rate and bubble sizes, shown at depths of 2, 4, 6 and 8 meters [118]. (a) pCO_2 plume with no bubble interactions, left; (b) pCO_2 plume with bubble breakup and coalescence interactions, right.*

In comparison with the observation data, which gave a mean pCO_2 of 390 - 400 µatm, increasing up to 1500 µatm, before reducing back to between 400 and 500 µatm [105], a large difference in pCO_2 can be seen. Although the model pCO_2 of 443 – 445 µatm matches the latter values, the prior large increases in pCO_2 are not accounted for. However, it is confirmed that at the levels of pCO_2 from the QICS experiment, there should be a negligible impact on the marine environment. Accumulated experimental data [381] shows that a pCO_2 of 1000 µatm is required to have a major effect on marine larvae, embryos and juveniles, with effects dependant on the species. Although in the experiment, this pCO_2 exceeded this value, rising to 1500 µatm, this was very local, directly above the leakage pockmarks.

7.3.3 The Impacts of Leaked CO_2 on Seawater From the QICS Experiment

A full simulation of the QICS experiment at low tide has been implemented in the model by taking the three injection rates as shown in Figure 7-5 (a) at the early, middle and late stages of the experiment. The injection rates were measured as 80, 170 and 208 kg/day, where the leakage rates are estimated as 2.3 kg/day, 17.0 kg/day and 31.2 kg/day respectively as shown in Figure 7-5 (b).

The simulations are performed step by step for each of the three leakage rates by injecting CO_2 into the water column at the given leakage rate until the plumes develop to a semi-steady state, at which point the next leakage is released. In the first stage, it is estimated that leakage occurs from 10 pockmarks closest to the injection site, increasing to 25 pockmarks in the second stage moving in a south westerly direction, and up to 35 pockmarks at the final stage of the simulations as shown in Figure 7-1. The results from the simulations are represented by the seawater volumes affected by pCO_2 increases as seen in Figure 7-5 (c), along with the maximum pCO_2 levels as seen in Figure 7-5 (d).

As the injection rate increases during the QICS experiment, the leakage rate increases. The number of bubbles also increases accordingly in order to maintain the bubble size distribution as seen in Eq. 2. This provides a greater interfacial area of the plume bubbles and seawater, enhancing the dissolution rate and generating larger volumes of pCO_2 changes, shown in Figure 7-5 (c). In turn this also provides a greater maximum pCO_2 as shown in Figure 7-5 (d).

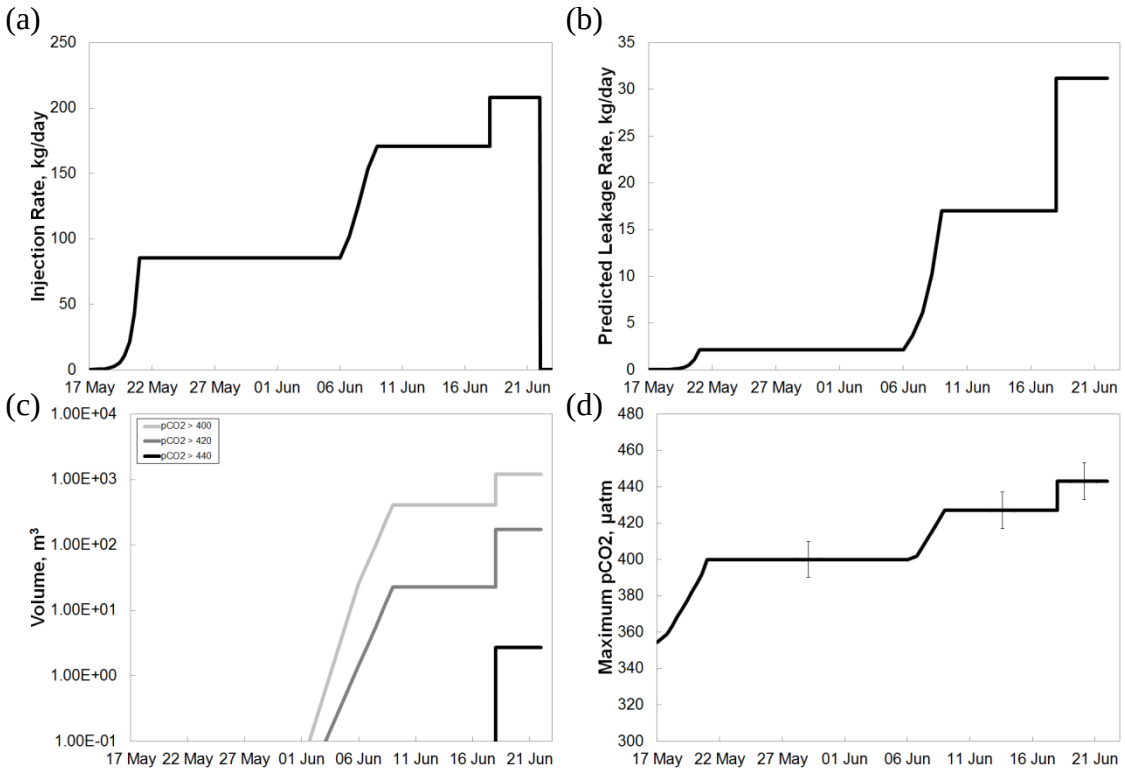

Figure 7-5 – (a) QICS experiment CO_2 injection rate, kg/day [118], top left; (b) Estimated CO_2 leakage rate and injection rate into the model simulation, kg/day [118], top right; (c) Volume of pCO_2 from the simulation, m^3 [118], bottom left; (d) Maximum pCO_2 from the simulation, µatm [118], bottom right.

The background pCO_2 fluctuates with the tide by +/- 10 µatm, with a maximum simulated pCO_2 in the first 20 days of 400 µatm, increasing to 427 µatm when the injection rate is increased to 170kg/day, and 443 µatm at the injection rate of 208 kg/day. In comparison with the observation data from Blackford et al. [105] where the pCO_2 varies between 390 µatm and 1500 µatm in the high injection stages, it has to be concluded that either the leakage rate is greater than measured in the experiment (~15% of total injection rate) through either small, fast dissolving bubbles, or dissolved solution in the sediments which is forced into the water column by the high injection rate. This may also be due to changes in activity across the pockmarks during the release period; although 35 pockmarks are active across the large leakage rate timeframe, they are not all active at the same time, with some more active than others causing greater pCO_2 concentrations. The final possibility is that the pCO_2 measurements are of a higher resolution than the simulations (0.0113 m^3) providing a greater peak direct over the bubble plume, rather than the mean over a 19.53 cm × 19.53 cm area.

7.3.4 The Impacts, Considering a Larger Leakage Rate to the Seawater

With an increased leakage rate (up to 100% of the injection rate at 208 kg/day), a denser bubble plume is produced with a far greater number of bubbles. A maximum initial size of 9.8mm is again dominating at the leakage site as shown in Figure 7-6 (a). Bubbles in such a dense plume rise faster at a larger absolute velocity due to the bubble plume generating a vertical movement of seawater, but also dissolve at a relatively low rate once a semi-steady state is reached due to the large surrounding concentration of CO_2 in the plume with the lack of under-saturated water. This coupling mechanism leads to the bubble plume reaching the water surface, unlike in the more diluted bubble plume simulated using the leakage rate measured in the experiment, where bubbles of the same maximum size only partially rise to the surface at low tide (Figure 7-2). Therefore it can be identified that the fate of dense bubble plumes is significantly different compared to the fate of an individual bubble alone.

The impacts of a leakage with 100% of the experiment injection rate are also more significant, with a maximum pCO_2 of 713 µatm shown in Figure 7-6 (b). To further investigate the effect, both the volume of pCO_2 in the surrounding waters and the vertical distribution of pCO_2 directly above the leakage source are measured and compared to those experienced in the previous QICS experiment simulations.

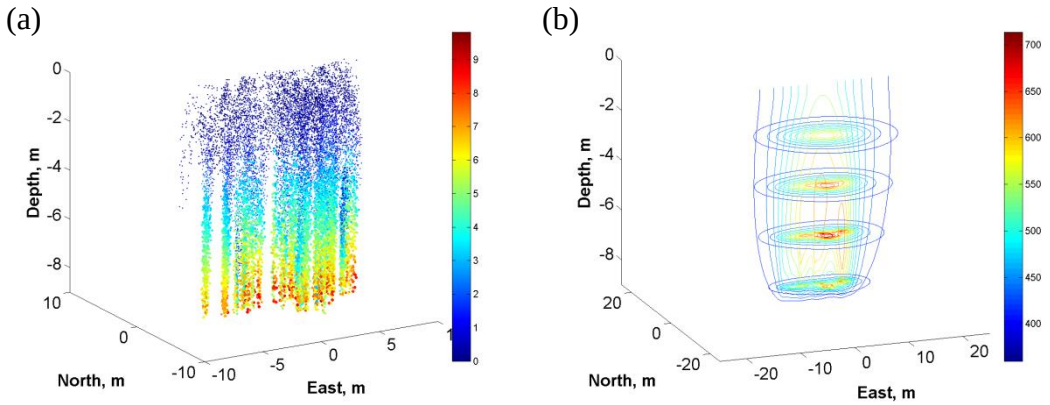

Figure 7-6 *– (a) A low tide bubble plume at 208 kg/day leakage rate, with the bubble diameter, mm, shown by both the colour map and the size of the marker [118], left; B) A low tide seawater pCO_2, µatm, plume at 208 kg/day leakage rate, with contours of pCO_2 shown at depths of 2, 4, 6 and 8 meters prediction [118], right.*

The volume of pCO_2 changes within the seawater, in addition to the maximum change in pCO_2, enables an assessment of the impacts that leaked CO_2 has on the marine environment, generated by the coupling dynamics of the CO_2 bubble plume and the ocean turbulence. As can be seen in Figure 7-6 (b) for the 100% injection rate leakage scenario, the maximum pCO_2 changes only occur directly above the leakage area. However, volumes in which the pCO_2 reaches 500, 600 and 700 µatm are found to be 685, 112 and 0.65 m^3 respectively.

From these results, it can be identified that the impacts on the marine environment are likely to remain close to the leakage source if the leak continued for an extended period of time. For monitoring and detecting the leakage, the results show that the changes in pCO_2 are difficult to detect because of the relatively small changes and associated volumes, which would require monitoring equipment with a high resolution and strategic positioning.

Another parameter to measure the leakage impact is the vertical profile of the horizontal mean pCO_2 directly above the leakage pockmarks, where the horizontal mean pCO_2 in a 25 × 25 m area above the pockmarks is predicted and demonstrated in Figure 7-7. The simulation of the low tide provides a peak mean pCO_2 of 400 µatm a few meters above the leakage area.

The high tide provides a lower leakage rate and therefore far less effect on the environment, with the greatest mean pCO_2 directly above the leakage location of 393 µatm. In contrast, the results from the leakage of the full injection rate where all the injected gas would leak to the water column show that the greatest mean pCO_2 increases to 434 µatm ~2 meters above the leakage pockmark area.

The development and the structure of CO_2 solution plumes determine the highest change in pCO_2 and its location. The highest changes in pCO_2 were expected to be on the seafloor due to the increase in density of the waters from the dissolved solution. However, the greatest change is found from the simulations a meter or two above the leakage pockmarks of the experiment in the shallow water.

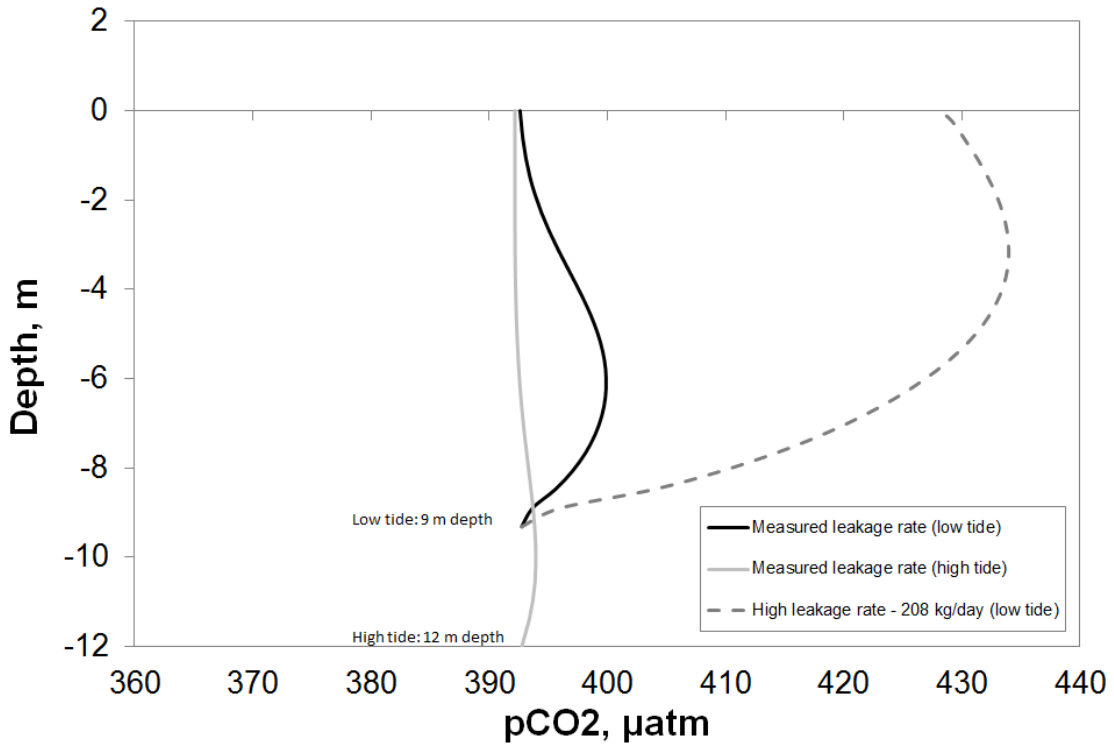

Figure 7-7 *– The vertical profile of the mean pCO_2, µatm, directly above the leakage pockmarks in a 25 × 25 m area for each of the scenarios [118].*

What is also noticed is that the CO_2 solution rises higher than the bubble plume, shown in Figure 7-6. This is investigated by the numerical model, where it is found that momentum from the rising bubble plume is transferred to the seawater, shown by the vertical velocity of bubble plume relative to the seabed in Figure 7-8 (a). This provided a greater upwards force than the negative buoyancy force from the increased density of the CO_2 solution demonstrated by the vertical velocity of dissolved CO_2 solution plume in Figure 7-8 (b).

The plume development and structure are different with those from the deep ocean, where at larger leakage rates from the deep ocean floor, the CO_2 solution plume would peel away from the bubble/droplet plume, as identified by laboratory experiments [382]. The larger CO_2 concentrations from the greater solubility of CO_2, lead to dominating gravitational effects giving this effect.

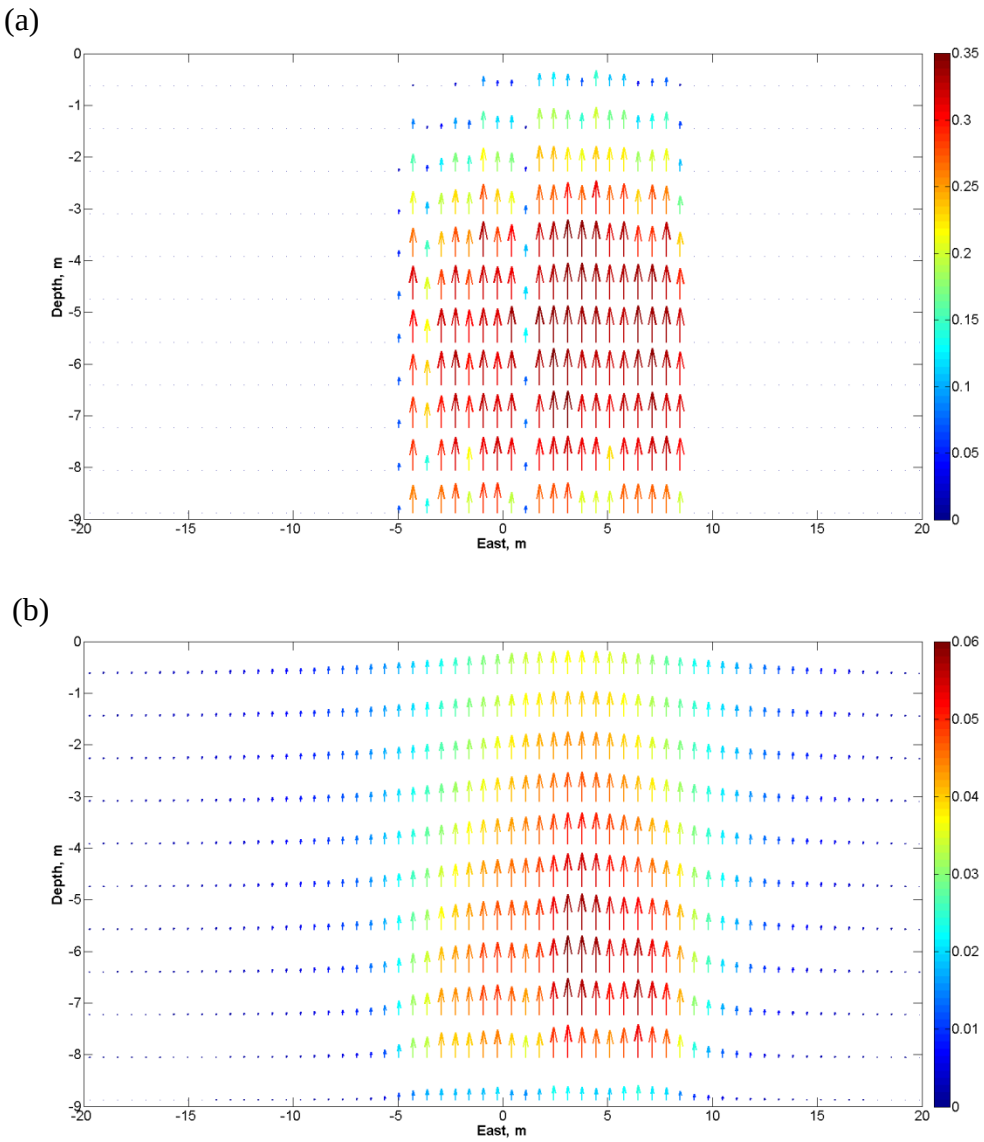

Figure 7-8 *– The vertical velocity, m/s, of both plumes at a cross section in the 208 kg/day scenario, with the arrows showing the mean upwards motion. (a) Bubble plume, top; (b) Dissolved CO_2 solution plume, bottom.*

7.4 Summary

The dynamics of rising CO_2 bubbles in seawater are investigated experimentally and through numerical modelling within the QICS project, Chen et al. [383] suggests that it may be possible to neglect interactions for bubbly flow due to weak interactions and a low range of distribution in bubble sizes. However, the experimental results from the QICS experiment showed multiple bubble interactions and a larger range of bubble size distribution, even in a low void fraction and low current bubbly flow, giving the need to investigate further. This need has been confirmed by the inclusion of interaction sub-

models in the simulations, which although have a minor effect on the maximum and mean bubble sizes, do have an effect on the distribution of bubble sizes and shapes. In turn this affects the dissolution rate of bubbles and the structure of the dissolved CO_2 plume.

The simulations with bubble interactions bring the bubble rise heights closer to that observed from the experiment, where some bubbles were found to reach the surface. A greater range of bubble sizes from other pockmarks than those from three recorded is suggested as a source of possible differences from the simulations.

To predict the observation data and mean pCO_2 over the leakage zone, it is suggested that the full injection rate of 208 kg/day is required due to the leakage mechanism experienced at the end of the injection. Even though only 15% of the CO_2 is leaked as bubbles observed from selected pockmarks, the surrounding sediments around the leakage chimney could be approaching a saturated state. The effect of this is an increased pressure from the increased leakage rate, providing a fast migration of the CO_2 through the chimney. This could allow 100% of the CO_2 to leak to the water column, providing the pCO_2 in the simulations of 713 µatm. Although this is lower than the peak recorded within the experiment of 1500 µatm, it is approaching the mean pCO_2 across the time frame of 740 µatm.

This could be explained through a number of situations, the first is that although there are ~35 pockmarks, not all the pockmarks are leaking at the same time and they do not have an even distribution of leakage rate meaning some pockmarks are more active than others, providing a greater concentration of pCO_2. The other possibility is that, as the leakage rate is increased, the strong bubble steams force the saturated brine from the sediments erupting to the seawater, increasing the pCO_2 to the peak levels of 1500 µatm close to the seafloor, before settling back down at between 400 and 700 µatm. The simulation results for the high tide case show the pCO_2 level of 390 µatm matches the observation data from the experiment, until the point where the leakage rate is increased, which partially supports these two possible outcomes.

The simulations, and the related data from the QICS experiment, are both small scale in time frame and spatial dimensions for the leakage from shallow seawater relative to the majority of the ocean. However, the results can be of reference with investigations of the assessment and monitoring of CO_2 leakage from greater depths down to about 400m at which depth the CO_2 is still in the gas phase; where differences may be shown through comparing North Sea and surrounding water case studies in the following chapter. An issue that does however also need further investigation is with such a shallow leak, how large localised concentrations affect the water-air surface mass transfer directing dissolved CO_2 to the atmosphere (secondary leakage), along with the effect of the topography on the development of the plumes.

Chapter 8 – Model Setup: The North Sea and Surrounding Waters

8.1 Introduction

Consider CO_2 leakage from an underground storage reservoir or pipeline in the North Sea and surrounding waters; the CO_2 also acts as a plume rising into the open waters and will begin to dissolve with the natural waters being under-saturated in terms of CO_2 [40]. This is similar to that of the QICS simulations; however at a greater depth, greater leakage area and greater leakage rate as a more likely case. The questions raised by these changes are however similar to before, whether the CO_2 reaches the atmosphere, and where significant increases in CO_2 concentration and pH changes of the waters occur that would cause harm to marine life and the ecosystem.

The dispersion and dissolution of CO_2 bubbles or droplets in seawater are of great interest from a biological point of view due to the effects on the water chemistry. Changes in pH are vital data for biogeochemical and ecological scientists in order to predict the impact from CO_2 leakages on the marine ecosystem in a variety of situations. Dissolution characteristics and plume dynamics are dependent on the temperature, pressure and salinity of water at depth, along with the local turbulent ocean flows. However, the biggest influence on the plumes comes from properties such as the leakage rate and bubble or droplet size [384]. The target water in this study is the North Sea, which has been considered as a potential area for European CO_2 under seabed storage [40].

Therefore in this chapter Section 8.2 presents a setup of the computational domain to fit the North Sea, with the turbulence model designed in Section 8.3 based on the experimental data from Section 3.5.1. Section 8.4 describes how the thermal energy and stratification is also included into the turbulence mode and Section 8.5 evaluates the turbulent ocean in a single phase, LES model based upon these theories and findings. Section 8.6 defines the fluid properties in the North Sea and surrounding waters and finally, Section 8.7 summarises the findings.

8.2 Computational Domain

The computational domain for CO_2 leakage is larger than that in the QICS experiment, with leakage occurring at larger rates over an area of up to 500 meters diameter. The

small scale turbulent ocean is therefore reconstructed in a computational domain of 1.0 km by 1.0 km and 100 m depth. As the simulation is within 10 km, it is in the small scale region [223], shown in Section 3.5.2 to be more suitable for LES turbulent water simulation as long as the grid size is large enough to neglect the frictional effects of the sediment wall on the seafloor [319].

To enable to forcing of the kinetic and thermal energies in LES, and to extract both energy spectra through a simple FFT algorithm, the number of grid cells is again required to be a power of 2. Due to the limited computational memory available from the operating system, the maximum number of possible points the model could use for each calculation was 128^3. To keep the dimensions of the vertical grid in the same order as both horizontal grids, but not too large that the dispersed bubble/droplet plume does not rise beyond the first element, a grid was developed of size 128 × 128 × 32. This gives a grid size of 8 m in the horizontal and 3 m in the vertical.

However, in the Skagerrak case, with a greater rise height, a larger vertical grid size of 8 m is required and a reduced vertical grid size is used in the low depth leakages of 1.5 m over 8 grid elements. For the leakage scenarios, the elongated conduit extends over 2.0 km requiring a horizontal grid size of 40 m, and the leaky well which extends to only 10 m requiring a horizontal grid size of 1.5 m, maintaining the same number of grid elements.

The grid is chosen to show as close as possible the full leakage around the bubble plume, along with showing the full changes in pH greater than 0.1 over the time period it takes to reach steady state. As the leakage occurs over a number of grids, the data for the horizontal grid is converged; therefore a higher resolution would not show much change in the results and reduce efficiency in terms of computational time. The resolution is developed to fit within the boundaries of LES, with the use of a non-slip wall for the sediment basin made possible by the large vertical grid size, removing the need for high resolution at the wall boundary to cover the flow structures and vortices that dominate the near-wall flow [319].

As with the QICS experiment in the previous chapter, predicting the modelling time step required for numerical stability can be done through estimating the bubble terminal velocity of 20 - 45 cm/s and the rise height of 3 meters using Equation (7-1) giving a time step of 10 seconds for the majority of the cases. With the Skagerrak case this increases to 30 seconds, and in the low depth case studies decreases to 5.0 seconds.

8.3 Turbulence

As described above, the North Sea numerical model is designed so that it is capable of simulating turbulence through LES. There are two fields of interest, one which may be simulated, and the other that must be modelled. The simulated eddy field $\bar{u}_{ij}$, is where the turbulent flow features are directly calculated within the Navier-Stokes, N-S, equations. However, this also require terms from the sub-grid field that must be modelled to include the effects from the smaller scale turbulent features [314].

8.3.1 Sub-Grid Scale Model

There are a number of models for the eddy viscosity in the sub-grid field, which come under two different categories, functional and structural models. Functional models [385 – 387] are designed to replicate the dissipation effects from the unresolved scales in the sub-grid on the resolved scale flow through enforcing set physical dissipation rates [388]. Structural models [389 – 391], on the other hand, aim to directly predict the kinetic energy spectrum locally in the sub-grid, producing an approximation of the sub-grid energy/dissipation within each resolved grid [388]. This allows the sub-grid model to take into account the local variations of the flow [314].

Evidence from a large number of LES models show that the sub-grid scale modelled turbulence is only a small contribution to the overall turbulence within the simulation. The quality of the results from the overall LES are not that sensitive to the quality of the sub-grid scale model, and therefore the choice of model is only of some importance to the results of the simulation [314] with other factors such as the grid size and filtering taking greater importance. However, a structure function model is chosen for its ability to take into account the intermittency and inhomogeneity of the larger scale flow through local kinetic energy spectrum analysis.

The model is based on a model by Chollet and Lesieur [392] with the non-dimensional eddy viscosity, ν_t^+, normalised by the square root of the kinetic energy over the wavenumber in the Fourier space.

$$\nu_t = \nu_t^+ \sqrt{\frac{E(k)}{k}} \tag{8-1}$$

with ν_t^+ = 0.267. Métais and Lesieur [390] found that using this constant for the viscosity, the energy cascade from the larger scales was too low. Therefore, through use of the Kolmogorov spectrum [303], predicted the average non dimensional viscosity at ~0.4.

$$\nu_t \approx 0.4 \sqrt{\frac{E(k)}{k}} \tag{8-2}$$

In the physical space, consideration of the second order velocity structure function of the local grid, F_2, is required to determine the kinetic energy in the local sub-grid.

$$F_2 = \left\langle \left\| u_i - u_{i+1} \right\|^2 \right\rangle \tag{8-3}$$

To link the kinetic energy spectrum in the Fourier space to the local velocities in the physical space Batchelor [393] and Orszag [394] utilise Kolmogorov's cascade in Equation (3-37) to determine the equivalent of the cascade in the physical space giving

$$F_2 = 4.82 C_k \left(\varepsilon \Delta x\right)^{\frac{2}{3}} \tag{8-4}$$

which is in the same format as Kolmogorov's original formula. Rearranging Equation (8-4) and (8-3) into (3-37) through equating in terms of the energy dissipation, ε, gives

$$E(k) = \frac{1.0}{4.82 \pi^{\frac{5}{3}}} \Delta x \, F_2 \tag{8-5}$$

Substituting Equation (8-5) into (8-2) gives

$$v_t = 0.0396 \Delta x \sqrt{F_2} \tag{8-6}$$

A final modification was made to the constant by Métais and Lesieur [390] to correct for the smaller scales in the sub-grid, but still maintaining Kolmogorov's law yields the structure function model.

$$v_t = 0.063 \Delta x \sqrt{F_2} \tag{8-7}$$

This turbulent eddy viscosity may be used to calculate the sub-grid scale turbulent stress in the Navier-Stokes Equation as shown in Equations (3-38a) and (3-38b). The model has been compared with that of DNS [390], along with other LES models [314], where it is found that the structure function model provided the best agreement with the Kolmogorov dissipation rate [303].

8.3.2 Sub-Grid Filtering

The transition point from the small scale field to the sub-grid field (what is computed and what is numerically modelled), is known as filtering [315]. The filter to eliminate the small scales is selected both in terms of the available computational resources, along with the ability of the flow to maintain turbulent and dissipation theories [395].

The choice of filter size is not an exact science as it often requires some trial and error, where the refining of the filter scale can be extremely expensive in terms of time and computational resources [396]. However, there are some general conditions that help define what filter size should be used. The first rule is that the filter should not be smaller than the grid size [397], this would miss the fluctuations and eddies between the grid size and the sub-grid model and therefore be numerically unstable. Further to this, due to the discretization of the Navier-Stokes equation in the model, the numerical error can be as great as the contribution from the sub-grid model if the filter size is not somewhat larger than the grid size [398]. Another rule is that energy should not be generated at the smaller scales, as it should be dissipated into molecular viscous heat [240]. Therefore if the energy spectrum is seen to be increasing, then the filter is not dissipating the correct amount of energy, and is of the incorrect size.

Through trial and error, the best sub-grid filter to maintain the kinetic energy spectra was found to be around twice the grid size in both the horizontal and vertical directions. With the cut off filter width having an associated wave number [399], this may be applied directly to the kinetic energy spectra.

The method of filtering used within the simulations is based on the Fourier space through use of a cut off when kinetic energy falls below the filter wave number. Various similar filter functions may be used rather than through a Fourier cut off [315]. However, the original kinetic energy spectrum, analysis of the changes in the kinetic energy spectrum throughout the simulation, and the numerical forcing of the highest wavelengths are conducted using FFT and inverse FFT approaches. Therefore to reduce the computational time and number of calculations, these processes can all be completed within a single FFT/IFFT operation, maximising computational efficiency.

8.3.3 Large-Scale Forcing

From the kinetic energy spectra in Figure 3-10, a correlation is developed from curve fitting,

$$\log_{10}\left(\frac{E(k)}{k}\right) = -\frac{4}{3}\log_{10}(k) - \frac{5}{3} \tag{8-8}$$

for forcing the kinetic energy at a narrow band of wavenumbers (4 points in the Fourier space, 6.38×10^{-5} m^{-1} to 2.55×10^{-4} m^{-1}) in the X and Z directions to develop the larger fluctuation waves as shown in Figure 8-1. These waves will then transfer into the lower wavelengths (higher wavenumbers) and dissipate in the resolved and sub-grid space through the viscosities discussed in the previous section.

For the Y direction (vertical) no kinetic energy forcing is introduced, where, as can be seen in Figure 3-10 (b) the kinetic energy in the Y direction is around an order lower than for the X and Z directions. Therefore the majority of the vertical energy generated and dominated by the horizontal and thermal energy, with both stratification and rotation dampening these effects [400].

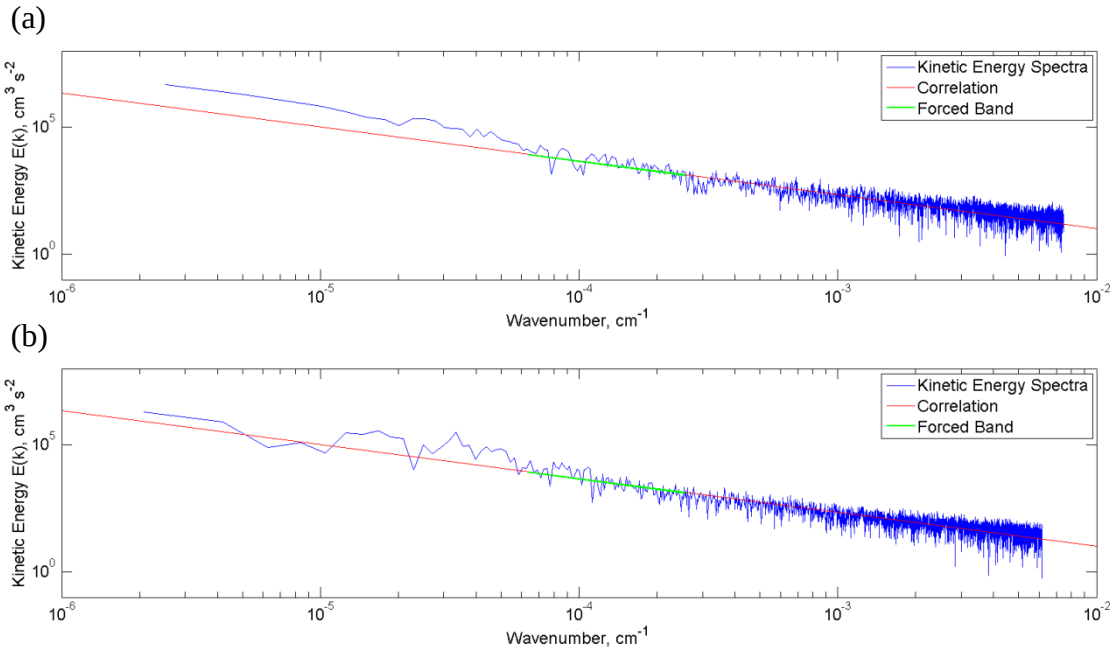

Figure 8-1 *– Fluctuating kinetic energy spectra (blue line) taken from data analysed of the central North Sea (58°24'23.11"N 2°1'25.33"E) with the correlation from Equation (8-8) (red line), and the narrow band of forced kinetic energy (green line). (a) X direction, top; (b) Z direction, bottom.*

8.4 Thermal Energy

As shown in Section 3.2.4, changes in energy are proportional to the change in temperature. Therefore data for the temperature is also taken from 2 separate locations as a time series from March to September 2014 in the southern North Sea, and July to September 2014 in the central North Sea [401].

Thermal spectra are then taken from this data as shown in Figure 8-2, which provides the correlation,

$$\frac{T(k)}{\mathrm{k}} = \left(2k \times 10^{\left(-\frac{5}{2}\log_{10}(k) - 10.0 \right)} \right)^{0.5} \tag{8-9}$$

for forcing the thermal energy at a narrow band of wavenumbers to develop the larger thermal waves.

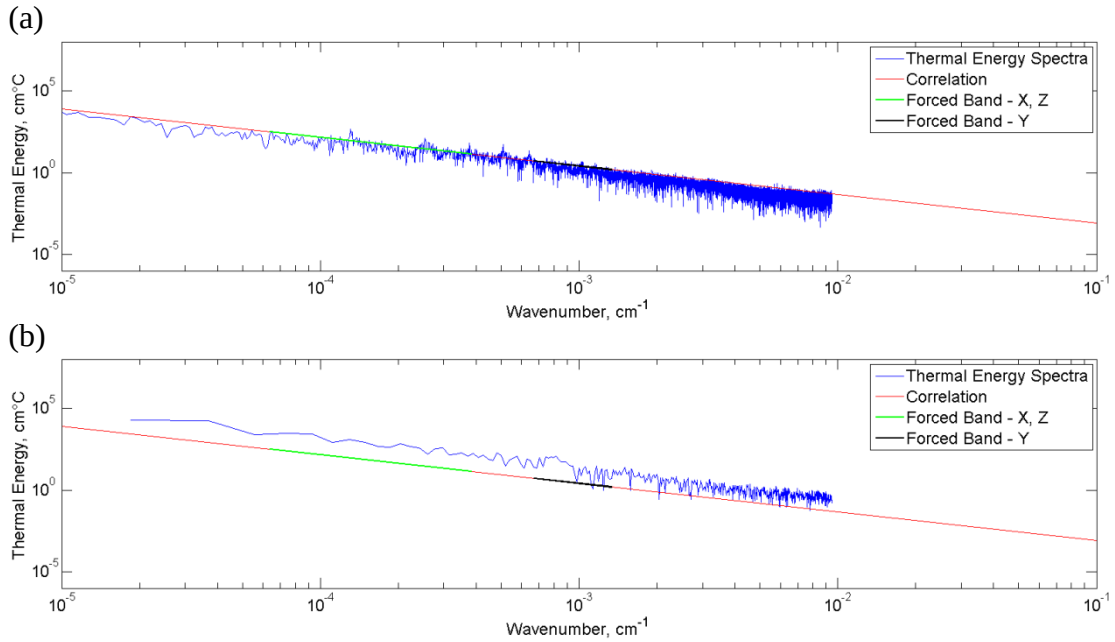

Figure 8-2 *– Thermal spectra taken from the two locations in the North Sea (blue line) [401] with the correlation from Equation (8-9) (red line), and the narrow band of forced thermal energy (green line for horizontal directions, black line for vertical direction). (a) March to September 2014 in the southern North Sea (51°59'55.0"N 3°16'35.0"E), top; (b) July to September 2014 in the central North Sea (57°12'03.6"N 0°30'00.0"E), bottom.*

As with the kinetic energy, these thermal waves will then dissipate into the lower wavelengths (higher wavenumbers) through the turbulence and viscosities. This provides a simulated spectrum at steady state, with the wavenumber forced in 6 points in the Fourier space (the range between 6.38×10^{-5} and 3.83×10^{-4}) in the X and Z directions, and 1 point (between 6.70×10^{-4} m^{-1} and 1.34×10^{-3} m^{-1}) in the Y direction due to its smaller scale, shown as the green and black lines in Figure 8-2.

8.5 Reconstructed Small Scale Turbulent Ocean

8.5.1 Kinetic Energy

The ocean momentum is solved through use of the Navier-Stokes equation in Equations (3-38a) and (3-38b), forcing the kinetic and thermal energy in each direction (as shown in Figure 8-1 and Figure 8-2) to allow the turbulent ocean to develop. As the energy has a dissipation rate, it takes time for energy to transfer from the larger to smaller scales to develop into steady state turbulence. The first few time step readings show the energy being forced, but with enhanced dissipation at the higher wavelengths (lower wavenumbers) in the kinetic energy spectra as shown in Figure 8-3 after 10 seconds.

After a short period of time the turbulent waves travel down into smaller wavelengths, with the upper wavelengths continuing to be forced. This creates a fluctuating turbulent ocean, which slowly begins to stabilise constructing a steady state turbulent ocean. This gives the near constant kinetic energy spectra as shown in Figure 8-4, generated 6.5 hours after the initial wavelength forcing.

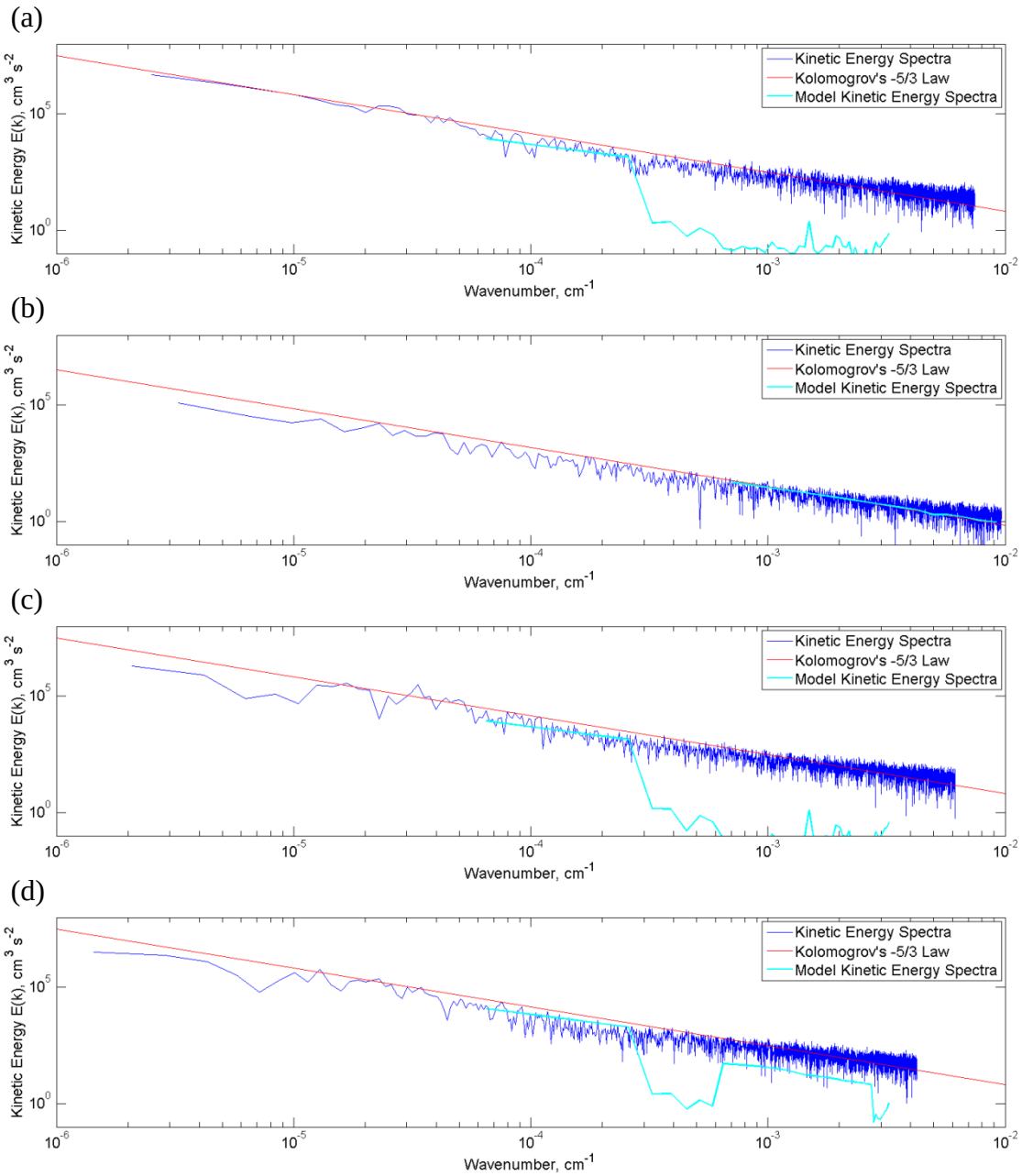

Figure 8-3 *– Fluctuating kinetic energy spectra taken from the small scale turbulent ocean model after 10 seconds (cyan line), compared with data analysed of the central North Sea (58°24'23.11"N 2°1'25.33"E) (blue line), Kolmogorov's -5/3 gradient law [303] (red line). (a) X direction, top; (b) Y direction (vertical), middle top; (c) Z direction, middle bottom; (d) total magnitude, bottom.*

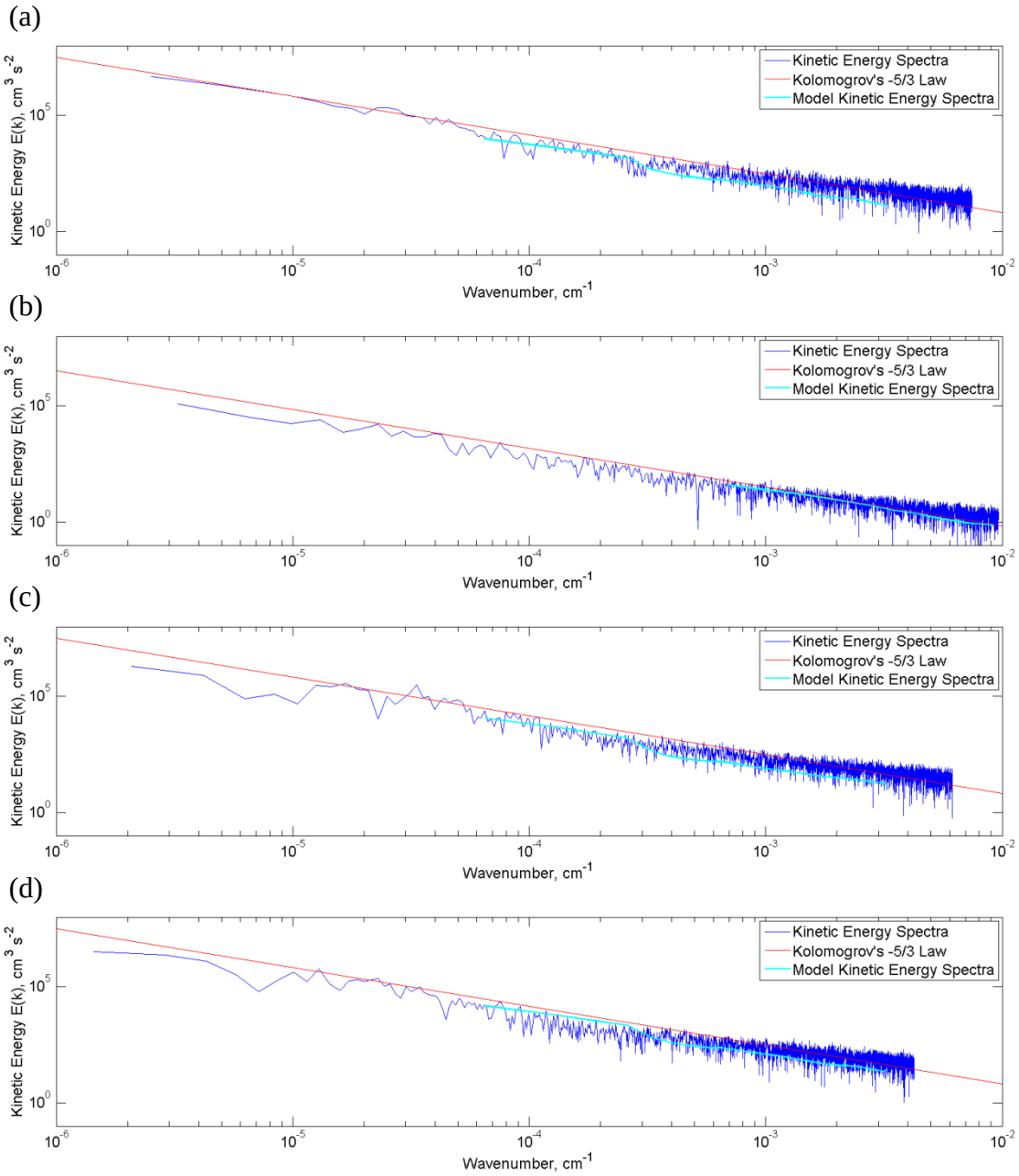

Figure 8-4 – Fluctuating kinetic energy spectra taken from the small scale turbulent ocean model at steady state after 6.5 hours (cyan line), compared with data analysed of the central North Sea (58°24'23.11"N 2°1'25.33"E) (blue line), Kolmogorov's -5/3 gradient law [303] (red line). (a) X direction, top; (b) Y direction (vertical), middle top; (c) Z direction, middle bottom; (d) total magnitude, bottom.

The kinetic energy spectra in each direction from the numerical model in Figure 8-4 shows a good agreement with both Kolmogorov's -5/3 law [303] for the reconstructed small scale turbulent ocean, as well as with the observation data extracted from the North Sea. This is validation of the LES small-scale simulation and sub-grid model

developed for the turbulent ocean, where the LES for the isotropic turbulent features at the scales analysed in the model are in line with those present in the North Sea. As can be seen in Figure 8-4 (b), the vertical kinetic energy spectrum develops (with no forcing) from the effects of the transfer of energy from the horizontal directions, and the flow of thermal energy affecting the stratification.

Cross sectional images in Figure 8-5 show the energy spectra in the physical space at a single point in time, showing the horizontal currents, u, in the X-Y direction and w, in the Z-Y direction, along with the vertical current, v, in the X-Y direction.

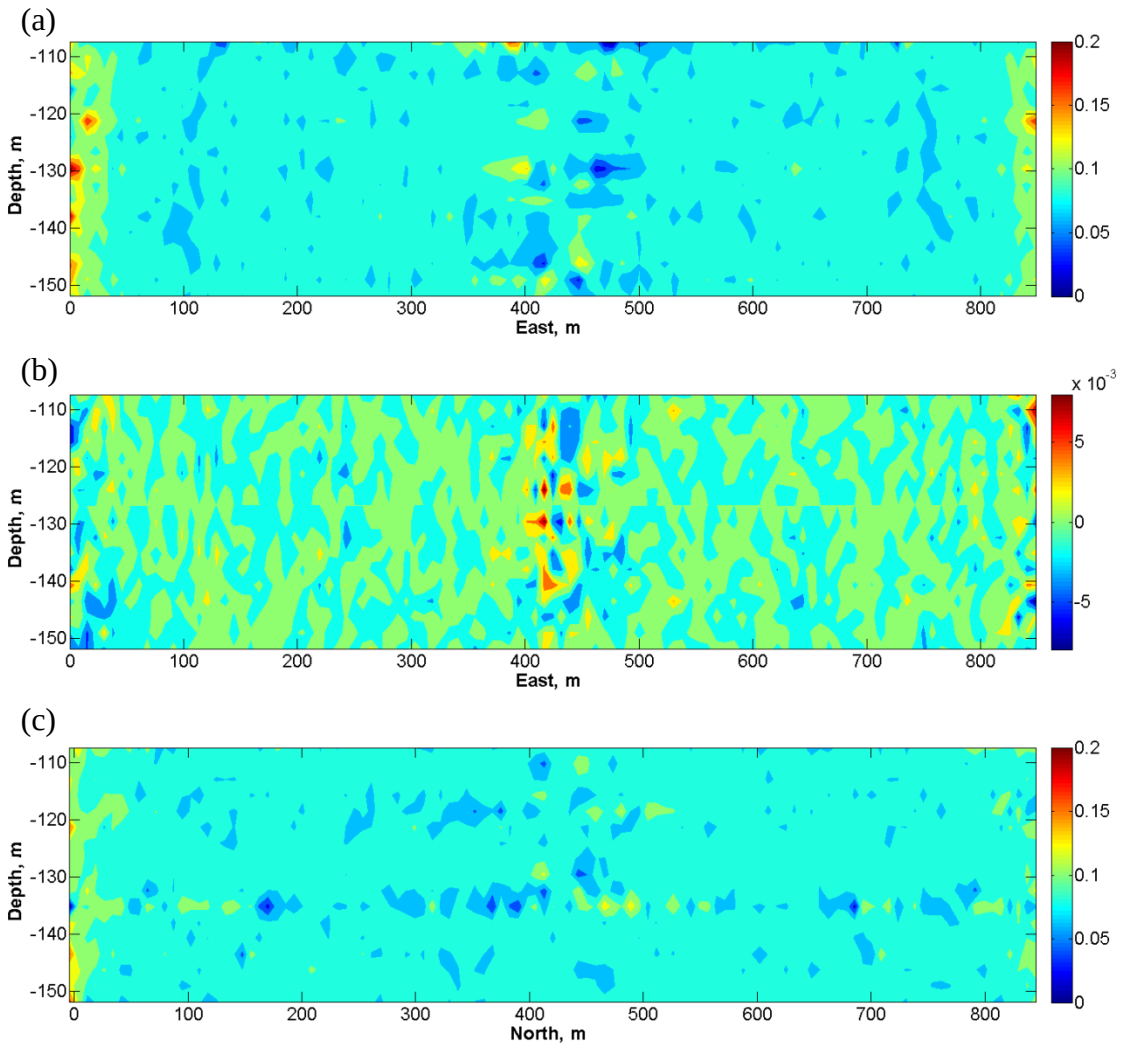

Figure 8-5 *– Cross sectional current images (m/s), once the spectra has reached a steady state after 6.5 hours. (a) X direction current, u, in X-Y plane, top; (b) Y direction current (vertical), v, in X-Y plane, middle; (c) Z direction current, w, in Z-Y plane, bottom.*

8.5.2 Thermal Energy

In the same manner as with the kinetic energy, the thermal energy spectra are predicted after 10 seconds and 6.5 hours. However, as the fluctuations in the thermal energy are much lower than the kinetic energy, it stabilises and becomes steady state within in the first time few steps, showing very little difference in the time zones as shown in Figure 8-6. The simulated spectrum is noted to also provide a good match with the experimental data.

8.6 North Sea and Surrounding Water Fluid Properties

As the largest potential CCS storage resource in Europe [402], in the North Sea and surrounding waters, the majority of the seawater depth is less than 550 m, with the average depth of 94 m [403]. The North Sea shelf drops to a maximum of approximately 150 m, and the Norwegian Channel to 400 m. However, a small section in the Skagerrak goes as far as 700 m [404]. This provides rising bubbles in each case except the latter, with the Norwegian Channel providing the ability for hydrate coated bubbles to form, and the Skagerrak allowing hydrate coated CO_2 droplet formations.

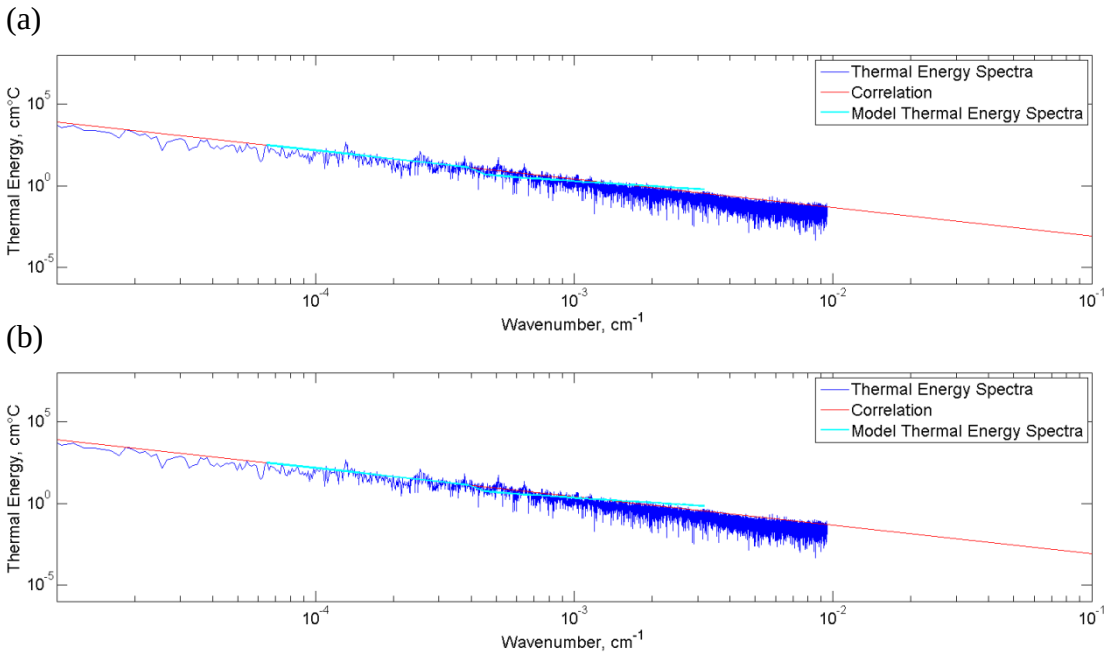

Figure 8-6 *– Comparison between the experimental (blue line) and simulated thermal energy spectra (purple line) taken from March to September 2014 in the southern North Sea [401] (51°59'55.0"N 3°16'35.0"E). (a) After 10 seconds, top; (c) after 6.5 hours, bottom.*

To produce reasonable predictive simulations investigating various leakage case studies within the North Sea and surroundings, a full set of locational data and parameters are required to predict the leaked CO_2 plume dynamics and dissolution [217]. This set of data includes water temperature, salinity and ocean current data at specified depths and locations, along with background levels for alkalinity and pH taken from Blackford and Gilbert [405]. The mean ocean current, and mean summer temperature data and turbulent fluctuations have been taken as detailed in Section 3.5 for the North Sea, with salinity along with the temperature shown in Figure 8-7 taken from Coriolis [401]. Ocean currents are seen to increase in deeper waters from a mean of ~10 cm/s on the North Sea shelf, with more flow from the Norwegian Sea and Atlantic Ocean allowing currents up to 50 cm/s within the Norwegian Channel, increasing further up to 1.0 m/s in the Skagerrak [406].

The leakage rate for CO_2 from the seabed is difficult to predict and would depend on the type of leak as well as the location it occurs. It also depends in part on whether it is a leakage from a sub-geological reservoir or from a transportation pipeline. An extreme case would be a well blowout or burst pipeline which could create leakage through a jet of up to 578 kg/s (50 kt/day) [40]. Other leakages are estimated to be of a far lower order, with predictions of rates below 0.006 kg/s (200 t/yr) [40].

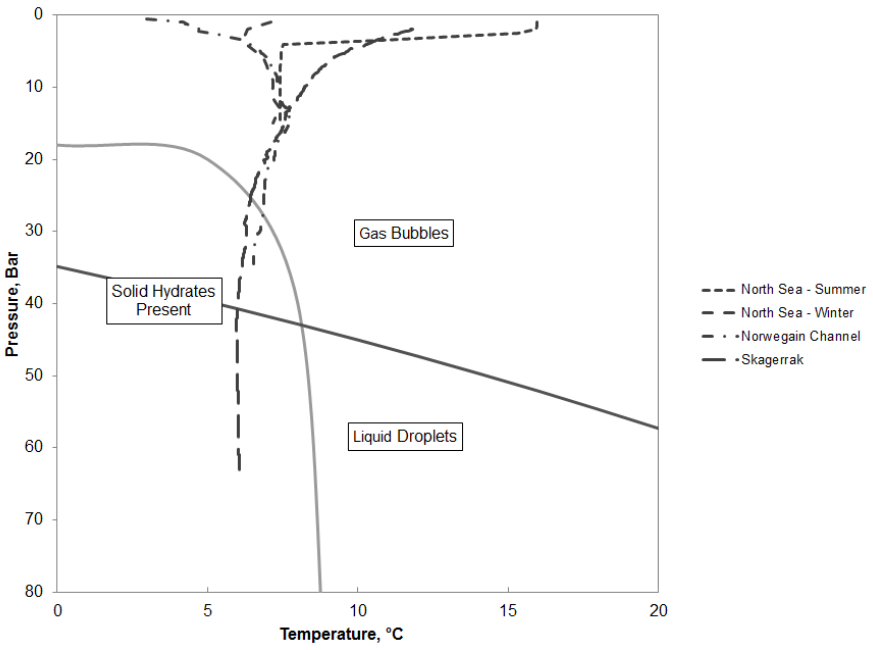

***Figure 8-7**- The North Sea and surrounding waters temperature data [119, 401]*

Simulations of leakage through the geology surrounding a wellbore, suggested to be the most likely leakage point, have been designed by Pan et al [407] finding leakage rates in both fresh water and brine; with leakage from an infinite sized reservoir into seawater at the wellhead predicted at a rate of 1.63 kg/s of CO_2 (~141 t/day). The recent investigations in the ECO_2 project also define leakage rates and areas for specific scenarios based on simulations of leakage through the cap rock and sediments [9].

The initial bubble sizes predicted through the model in Section 5.3.3 and the boundary conditions are set as the same as for the QICS experiment, however with a slip boundary for the seabed made possible by the larger vertical grid size.

8.7 Summary

A small scale LES turbulent model of the turbulent ocean has been developed based on analysis of observation data both thermal and kinetic energies. Through analysing and comparing models of turbulent fluid simulation, it is identified that Large Eddy Simulation applying the forced-dissipation mechanism is suitable to simulate the small-scale turbulent ocean in this instance; where the large scale turbulent features are numerically solved, and the smaller features are numerically modelled. Comparing sub-grid models for these features, a structure function model was chosen to simulate the variations in energy dissipation across the volume based on the local kinetic energy spectrum.

Model simulations show that a good agreement is found with the kinetic energy spectra produced, when compared to Kolmogorov's law [303], and the kinetic energy spectra calculated from observation data in the North Sea. The thermal energy spectra is also reproduced in the numerical model, which approaches a steady state very rapidly, also matching data the thermal energy spectra taken from North Sea observation data [401].

The single phase simulation for the small-scale turbulent ocean is developed and validated against experimental data. The reconstructed small-scale turbulent ocean is therefore ready, with the described North Sea and surrounding water fluid properties to couple for plumes of two-phase dynamics, with the dissolution of the bubbles or droplets in a two phase numerical model for CO_2 leakage.

Chapter 9 – Model Applications: North Sea and Surrounding Waters

9.1 Introduction

The physicochemical impact of larger scale CO_2 leakages from the seabed are investigated, focusing on in geological locations similar to that of Statoil's Sleipner Project, local to the North Sea and surrounding waters. Results for the rise height of the bubbles and concentration of the dissolved solution in terms of pH are analysed for the physiochemical impacts of the leakage on the seawater.

With the LES model applied to the simulation for ocean turbulence, the model is numerically driven to a steady state turbulent ocean. This is done by forcing the upper wavelengths over a mean current allowing the force-dissipation mechanism to develop before the CO_2 bubbles or droplets are released through the suggested leakage footprints. Initial simulations will investigate the effects of varying different parameters, such as the leakage rate or water currents, with further simulations focused on those developed in the ECO_2 project for a well blowout, chimney reactivation, elongated conduit (fault, fracture or chimney) and a leaky well [9].

Section 9.2 presents the case studies and scenarios defined for the North Sea including those as defined in the ECO_2 project [9]. Simulations are then applied to the case studies and scenarios, designed to predict the impact through the two-phase, small-scale, turbulent numerical ocean model, with findings detailed in Section 9.3. Section 9.4 presents the effect that a bubble leakage has on the local kinetic energy spectra in the turbulent waters, and finally Section 9.5 summarises the findings.

9.2 Case Studies and Scenarios

Case studies have been developed through the use of the oceanic data, allowing a prediction of leakage case studies for the selected locations in the North Sea, Norwegian Channel and the Skagerrak. These show how the dynamics and dissolution are affected from summer to winter through seasonal data, along with the effect of the leakage depth, tidal currents and initial bubble sizes based on the selected leakage location and the leakage rate, with leakage parameters listed in Table 9-1.

Table 9-1 – *Leakage case studies and scenarios.*

	North Sea case studies	Depth	Footprint	Leakage Rate	Current
1	Winter	100 m	45 × 45 m	1.63 kg/s	10 cm/s
2	Summer	100 m	45 × 45 m	1.63 kg/s	10 cm/s
3	Reduced leakage rate	100 m	45 × 45 m	1.0 kg/s	10 cm/s
4	Low ocean current	100 m	45 × 45 m	1.63 kg/s	1.0 cm/s
5	Low depth winter	30 m	45 × 45 m	1.63 kg/s	5.0 cm/s
6	Low depth summer	30 m	45 × 45 m	1.63 kg/s	5.0 cm/s
	Surrounding water case studies	**Depth**	**Footprint**	**Leakage Rate**	**Current**
7	Norwegian Channel	320 m	45 × 45 m	1.63 kg/s	20 cm/s
8	The Skagerrak	600 m	45 × 45 m	1.63 kg/s	20 cm/s
	ECO_2 – North Sea scenarios	**Depth**	**Max Footprint**	**Leakage rate**	**Current**
9	Well blowout	94.88 m	50 m Ø	150 t/day	13 cm/s
10	Chimney reactivation	94.88 m	500 m Ø	150 t/day	13 cm/s
11	Leaky well	94.88 m	10 m Ø	20 t/yr	13 cm/s
12	Elongated conduit	94.88 m	200 × 2000 m	15 t/day	13 cm/s

The last four scenarios are developed based on the findings from the ECO_2 project, giving suggested leakage rates and areas for the various leakage scenarios on the North Sea shelf near the Sleipner field, to provide information on realistic leaked CO_2 gas and solutions, including the detectability of bubbles and the CO_2 solution plumes affected by turbulent currents. As with the QICS scenarios, the data are recorded from the simulation when the simulated plumes have reached a semi-steady state, where the maximum pH change settles at a reduced value in the plume and the rate of change of the mean pH change within the grid of the leakage reduces to less than one percent of the initial rate of change, with minor fluctuations due to the fluctuations in current.

9.3 North Sea and Surrounding Waters Simulations

9.3.1 Bubble and droplet plume

For most of the leakage locations, the bubble plume, with initial sizes of ~7.0 mm, reached a terminal height within the first two and a half minutes of the leakage occurring. This is with the exception of the leakage in the Skagerrak, taking more than

one hour to reach its full droplet plume height, due to the larger mass of the individual droplets, the reduced dissolution rate from the hydrate formation and the reduced rise velocity from a lower buoyancy force.

Reductions in buoyancy force and changes in temperatures cause slightly larger initial bubbles at increased depths, with the Norwegian Channel case producing larger bubbles than the North Sea shelf. This is in contrast to the predictions in Figure 5-7 that are at a constant temperature for the CO_2 and seawater. The bubble plumes for selected case studies are shown in Figure 9-1, with further data presented in Table 9-2 including the leakage flux, the predicted initial bubble size and the bubble plume rise height. It is predicted that as the depth increases, the rise height for the bubble plumes increases from the reduced interfacial area of the larger density bubbles. Chen et al. [224] found that bubble plume rise heights are more affected by bubble size than depth. However in the case of bubbles with hydrates and droplets, the larger mass of each individual droplet or bubble increases the plume height.

Taking the plume height shown in Figure 9-1 and Table 9-2, it can be seen that for most of the leakage locations the leaked CO_2 forms as gas bubbles that fully dissolve within 10-15 m. This is with the exception of leakage in the Skagerrak where the CO_2 is in liquid droplet form giving a far greater rise height of beyond 150 m. Nonetheless, full dissolution occurs within 30 % of the depth of the waters under these conditions, well before reaching the surface and atmosphere. However it should be recognised that increases in buoyancy from larger bubble size formations, especially in shallower waters, could allow the bubbles to rise further towards the atmosphere.

The changes in season from winter to summer in the greater depth North Sea shelf beyond ~100 m have a negligible effect on the bubble plume height or the initial formation size of bubbles; the 1°C temperature difference providing only a small change in the density for both the seawater and the CO_2. In contrast, in shallower oceans with an increase in temperature (by up to 8 °C) reduces the bubble plume height by ~1.5 m. This is due to the increase in temperature having a greater effect on the density of the seawater than of the CO_2, -1.46 kg/m^3 and -0.16 kg/m^3 respectively, giving a reduced

buoyancy force and rising velocity. This shows that in this case, the buoyancy has a greater effect than the decreased solubility from the temperature increase.

Within the Norwegian Channel, the increase in the depth has the effect of increasing the bubble diameter forming from 7.03 to 7.19 mm. Due to the increase of mass of the individual bubbles with depth from the increased density and the hydrate formation, the bubbles would take slightly longer to dissolve providing an increase in rise height of 12.5 m when compared to the North Sea shelf of 10.0 m. Droplet plume formations such as in the Skagerrak also rise to higher levels than those in the bubble cases. This is in part due to the larger initial droplets of 11.37 mm forming due to a lower buoyancy force. However, the major effect is from droplets having a far greater mass than bubbles of equivalent volume. Therefore even with the higher solubility they'll take longer to dissolve, rising up to 150 meters before experiencing a phase change to bubbles which will dissolve within ~20 meters.

Table 9-2 – *Leakage case study and scenario results for bubble/droplet leakage flux and formation sizes.*

North Sea case studies		Leakage flux (kg/m^2s)	Initial diameter (mm)	Rising height (m)	Rising height (% of depth)
1	Winter	7.90×10^{-4}	7.03	10	10
2	Summer	7.90×10^{-4}	7.03	10	10
3	Reduced leakage rate	4.94×10^{-4}	7.03	10	10
4	Low ocean current	7.90×10^{-4}	7.03	10	10
5	Low depth winter	7.90×10^{-4}	7.00	7.5	25
6	Low depth summer	7.90×10^{-4}	7.00	6.0	20
Surrounding water case studies		**Leakage flux (kg/m^2s)**	**Initial diameter (mm)**	**Rising height (m)**	**Rising height (% of depth)**
7	Norwegian Channel	7.90×10^{-4}	7.19	12.5	3.91
8	The Skagerrak	7.90×10^{-4}	11.37	160	26.7
ECO_2 – North Sea scenarios		**Leakage flux (kg/m^2s)**	**Initial diameter (mm)**	**Rising height (m)**	**Rising height (% of depth)**
9	Well blowout	8.84×10^{-4}	7.03	10.00	10.54
10	Chimney reactivation	8.84×10^{-6}	7.03	11.11	11.71
11	Leaky well	8.07×10^{-6}	7.03	13.884	14.63
12	Elongated conduit	2.88×10^{-6}	7.03	10.00	10.54

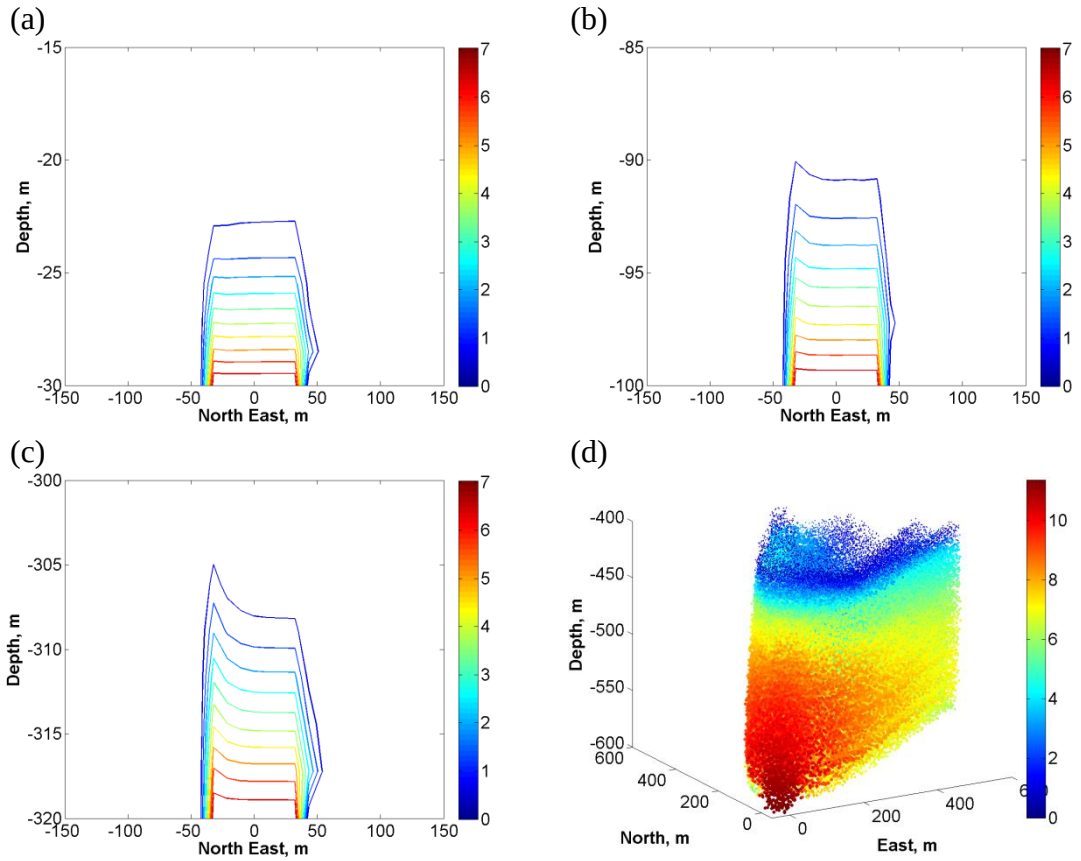

Figure 9-1 *– The bubble / droplet plume, with the bubble / droplet diameter shown in mm by the colour map and the current applied in the North Easterly direction. (a) The North Sea shelf at 30 m depth (bubbles), top left; (b) the North Sea shelf at 100 m depth (bubbles), top right; (c) the Norwegian Channel at 320 m depth (bubbles with hydrates), bottom left; (d) the Skagerrak at 600 m depth (droplets), bottom right.*

In Figure 9-2 the bubble plumes for further leakage scenarios are shown. The model has predicted the average initial bubble size to be 7.03 mm, rising from the sediments up to a height of 10 to 14 m. With the exception of the blowout scenario with a dense bubble plume at the wellbore, a bubble plume would be difficult to detect. Although the same number of bubbles are present in the chimney reactivation as the well blowout, the release is over a far greater area of 196,350 m^2, giving a flux of 8.84×10^{-6} kg/m^2s, one hundred times lower than the well blowout case at the same leakage rate. The leaky well leakage rate is ~2700 times less than that of the well blowout, therefore even with the smaller leakage area, the flux is of the same order to that of the chimney reactivation at 8.09×10^{-6} kg/m^2s. The elongated conduit also has a lower leakage rate, with a leakage area somewhere between the well blowout and the chimney reactivation, giving a flux ~500 times lower than the blowout scenario.

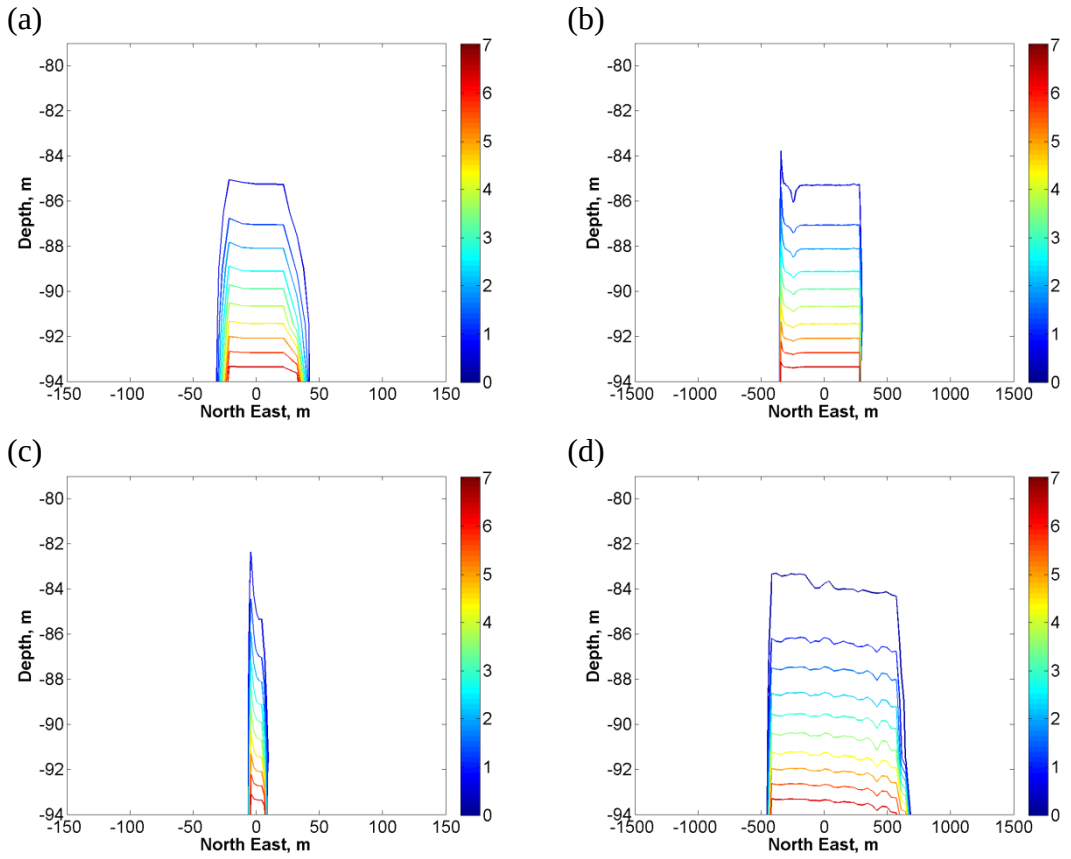

Figure 9-2 *– The bubble / droplet plume, with the bubble / droplet diameter shown in mm by the colour map and the current applied in the North Easterly direction. (a) The well blowout, top left; (b) the chimney reactivation, top right; (c) the leaky well, bottom left; (d) the elongated conduit, bottom right.*

9.3.2 pH changes

As the CO_2 dissolves, it creates a change in the acidity in the waters, recorded as a pH change. This CO_2 solution is larger in density than the surrounding seawater and therefore the plume will develop and eventually drop to the ocean floor forming the largest pH change and dissolved CO_2 levels on the seabed, near the leakage source. The structure of the CO_2 solution plume, indicated by the changes in pH, is demonstrated in Figure 9-3 for a selection of the leakages to the North Sea and surrounding waters.

From the vertical cross section, as shown on the left side of the Figure 9-3, it is found that the largest pH changes are close to the leakage source and overlap with the bubble/droplet plume. As the dissolved solution plume develops, driven by the turbulent currents, it disperses horizontally sinking to the seafloor eventually diluting.

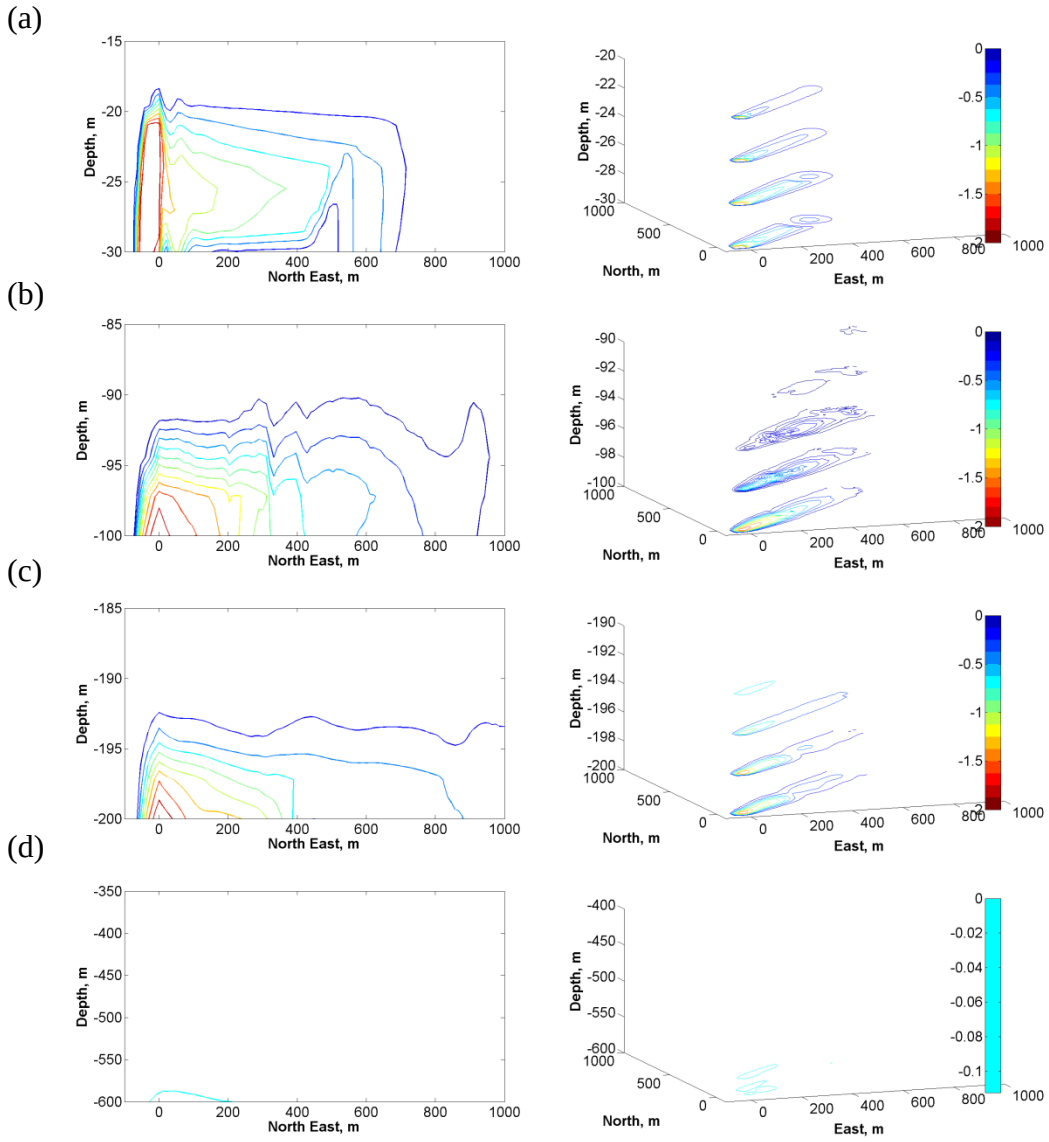

Figure 9-3 *– Contours of pH changes in the seawater plume, with each contour representing -0.2, with the current applied in the North Easterly direction; left: 2D cross section of the plume. Right: Horizontal plane cross sections of the plume shown at 2.5 - 3.0 meter intervals, except in the Skagerrak, shown at 50 meter height intervals. (a) The North Sea shelf at 30 m depth in winter, top; (b) the North Sea shelf at 100 m depth in winter, middle top; (c) the Norwegian Channel at 320 m depth, middle bottom; (d) the Skagerrak at 600 m depth, bottom.*

The development of the CO_2 solution plume and its distribution can be better illustrated by the horizontal cross sectional images of the plume, given on the right side of the Figure 9-3, where at greater distances from the leakage source, the plume becomes more diluted.

To further investigate the impact, volumes of seawater with pH changes greater than -0.5, -1.0 and -1.5 are recoded from the simulations in Figure 9-4. Changes in pH at these values give seriously significant impacts to marine organisms as discussed in Section 2.5.2. Further parameters, such as the maximum pH change, and both the seabed area and volume of seawater affected by pH changes greater than -0.1 are listed in Table 9-3 for each simulation.

As can be seen, the rate of change of pH reduces with time, approaching a semi-steady state for most of the leakage cases within 9.5 hours from leakage commencing (16 hours from initiating the ocean turbulence through LES). However, the pH plume in the shallow depth leakages (dashed lines in Figure 9-4) were unable to reach a steady state due to the low current providing a continuous build-up of the dissolved CO_2 concentration in the plume.

For both the shallow leakage at 30 m depth and the 100 m North Sea shelf, the change in temperature has an effect on the plumes. The lower temperature from winter creates a reduction in both the maximum ΔpH, and the volume of the dissolved solution plume. This is more prominent in the shallow leakage with a temperature difference up to 8°C, giving a difference in the maximum pH change of -0.8, compared to -0.1 on the North Sea shelf with a 1°C difference. The leakage during the summer season in both the shallow water and the North Sea shelf have a reduced rising velocity as discussed in the previous section, where the CO_2 dissolves within a smaller distance. This provides larger changes of pH in the affected seawater volumes, along the seabed area and in terms of the maximum pH change; as can be found in Table 9-3.

It is expected that the decrease in leakage rate by 61% is likely to produce a weaker impact in terms of the volume and affected seabed area; however, the maximum change in pH is less sensitive, giving -1.764 compared to -1.941 at full rate. A reduction in the water current reduces the ability for the plume to distribute horizontally. This therefore greatly increases the maximum change in pH to -2.694, but the volume of the pH change decreases due to the reduced distribution.

(a)

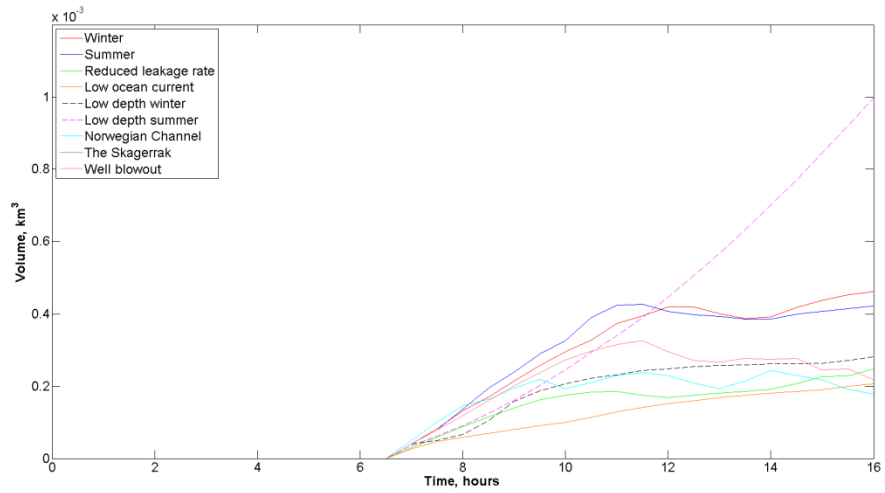

(b)

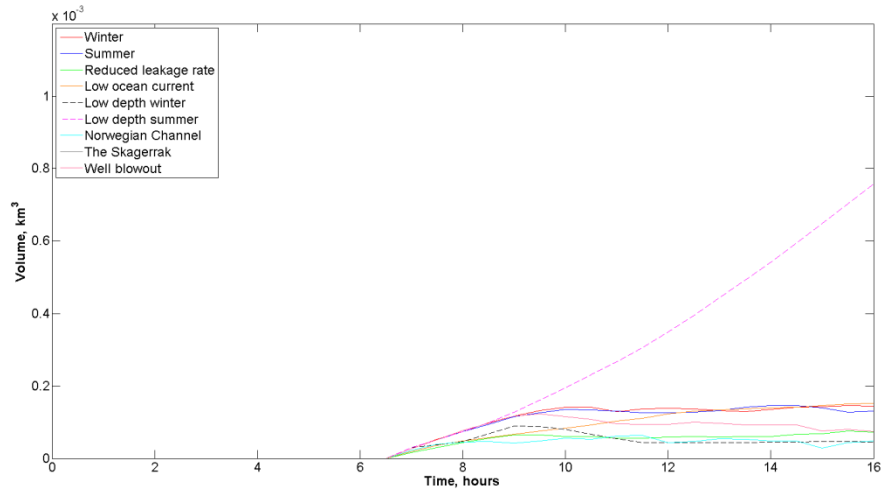

(c)

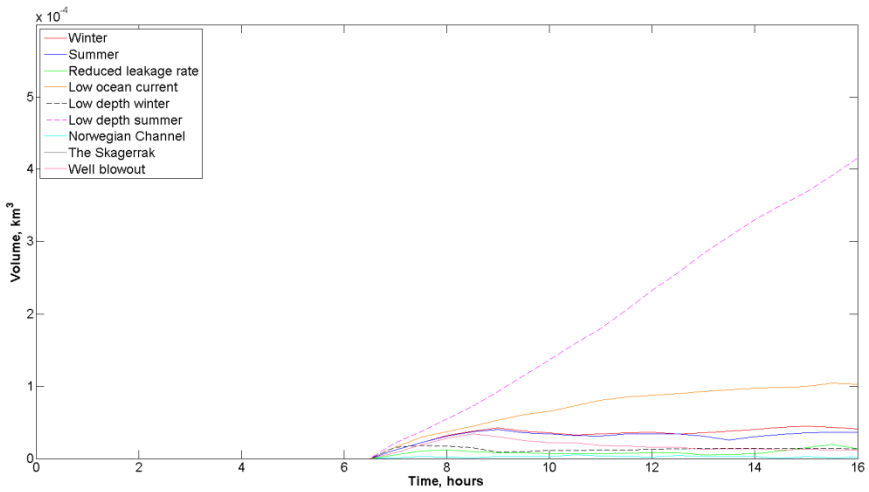

Figure 9-4 *– The volume of pH concentrations within the seawater plume from each case study and leakage scenario, observing a 1 km horizontal distance for changes in pH. (a) Greater than -0.5, top; (b) greater than -1.0, middle; (c) greater than -1.5, bottom.*

Table 9-3 – *Leakage case study and scenario results for maximum and volumes for pH changes.*

North Sea case studies		Leakage flux (kg/m2s)	Maximum ΔpH	Volume ΔpH > -0.1 (m^3)	Seabed Area ΔpH > -0.1 (m^2)
1	Winter	7.90×10^{-4}	-1.941	2.69×10^6	176,980
2	Summer	7.90×10^{-4}	-2.042	2.82×10^6	178,357
3	Reduced leakage rate	4.94×10^{-4}	-1.764	1.89×10^6	150,205
4	Low ocean current	7.90×10^{-4}	-2.694	0.36×10^6	24,106
5	Low depth winter	7.90×10^{-4}	-1.583	1.58×10^6	88,102
6	Low depth summer	7.90×10^{-4}	-2.407	1.81×10^6	228,722
Surrounding water case studies		Leakage flux (kg/m2s)	Maximum ΔpH	Volume ΔpH > -0.1 (m^3)	Seabed Area ΔpH > -0.1 (m^2)
7	Norwegian Channel	7.90×10^{-4}	-1.633	1.57×10^6	175,861
8	The Skagerrak	7.90×10^{-4}	-0.114	5,739	688.75
ECO_2 – North Sea scenarios		Leakage flux (kg/m2s)	Maximum ΔpH	Volume ΔpH > -0.1 (m^3)	Seabed Area ΔpH > -0.1 (m^2)
9	Well blowout	8.84×10^{-4}	-1.883	1.82×10^6	163,406
10	Chimney reactivation	8.84×10^{-6}	-0.2678	1.52×10^6	327,902
11	Leaky well	8.07×10^{-6}	-0.010	~0	~0
12	Elongated conduit	2.88×10^{-6}	-0.021	~0	~0

Factors of large currents and reduced dissolution rates due to the formation of hydrates in the Norwegian Channel distribute the dissolved CO_2 solution plume generating a reduced maximum change in pH of -1.633 and smaller volumes of pH changes greater than -0.1. However, it is assumed that there is a larger volume of small pH changes below -0.1 that extend beyond the simulation domain due to the high current. For leakage in the Skagerrak, the lower dissolution rate experienced is due to the reduction in interfacial area (0.2 % of that of equivalent sized bubbles in the North Sea shelf), along with the increase in the current. This counteracts the 2.77 times increase in solubility giving a significant distribution of the CO_2 solution plume. Therefore a far lower maximum change in pH is found than that in the North Sea, -0.114 compared to -1.941. The volume of pH changes greater than -0.1 is also only 0.006 km^3, but a far larger volume of very low pH changes would also be produced. It must be noted that the prediction of changes in pH are quite sensitive to the spatial resolution due to the

dissolved concentration, Y_{CO2} (kg/m^3), being related to the grid size. In this deep ocean leakage case utilising a higher resolution simulation, the maximum pH almost doubled to 0.224 with the volume of pH changes greater than -0.1 increasing to 0.023 km^3. Therefore, when discussing and comparing the impacts from the pH or mass concentration of dissolved CO_2 from simulations, care must be taken to identify under what resolution these plumes are predicted.

From the leakage to the shallow ocean, in addition to the effects from the currents and seasons as discussed, a particularly interesting phenomenon is experienced where the leaked CO_2 in winter generates vertical waves affecting the CO_2 solution plume. A large vertical temperature gradient of 0.138 ^{o}C/m is present in the top 50 meters of the North Sea in the winter season as can be seen in Figure 8-7. This creates strong stratification where vertical flow from the leaked CO_2 disturbs the stratification layers at the leakage source through momentum generating vertical waves. These waves transfer to the CO_2 solution plume, forcing it upwards over the bubble plumes. This effect can be witnessed when comparing Figure 9-1 (a) with Figure 9-3 (a). The waves also further dilute the plumes leading to the reduction in the maximum pH change.

The pH plumes generated by leakage from a well blowout and chimney reactivation are investigated and compared as shown in Figure 9-5. The well blowout is the worst case scenario, with the chimney reactivation as a natural leakage structure giving similar leakage rates as suggested by the risk assessment group in the ECO_2 project [107]. For the blowout scenario, the dissolved solution gives maximum pH changes along the seafloor of up to -1.871 very local to the leakage zone when the plume has developed to a relatively steady state. A pH change of -1.0 is detectable at ~300 m downstream, and the lowest detectable pH change of -0.2 is just beyond 1 km downstream dependent on the current. The seawater with lower pH changes flows beyond the computational domain of the simulation. It can be estimated that such large changes in pH would disturb the local marine life on the seabed, such as sea urchins [150, 151, 154, 158] and starfish [155 – 157], along with floating marine organisms that flow with the high concentration dissolved CO_2 waters [164].

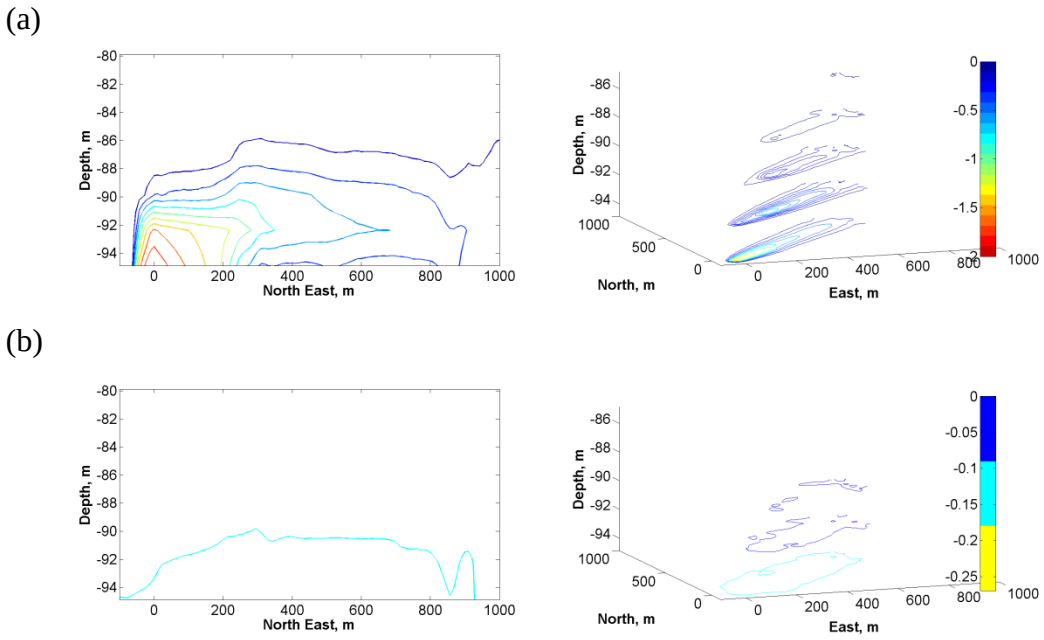

Figure 9-5 – *Contours of pH changes in the seawater plume, with each contour representing -0.2, with the current applied in the North Easterly direction; left: 2D cross section of the plume. Right: Horizontal plane cross sections of the plume shown at 2.7 meter intervals. (a) The well blowout, top; (b) the chimney reactivation, bottom.*

For leakages from chimney reactivation, elongated conduit or leaky wells, the very small leak flux create a more dilute bubble and CO_2 solution plumes, which is beneficial in the view of biological impacts. However, this brings a challenge to the monitoring and detecting of leakage. From the chimney reactivation simulation it is clear that the pH changes would be difficult to measure, if not undetectable, with a maximum pH change of only -0.2678, and a volume of 0.0015 km^3 containing the changes in pH greater than -0.1, compared to a volume of 0.0018 km^3 in the well blowout leakage containing far larger pH changes up to -1.9.

9.4 Effect of Leakage on the Small-Scale Ocean Turbulence

Energy may be transferred to the water column when bubbles and droplets leak. Momentum exchanges with the water column through the drag force as the bubbles or droplets rise. However, momentum is also generated from the falling dissolved solution plumes transferring energy to the water column. To investigate the local role of a bubbly plume on the small scale ocean turbulence, the kinetic energy spectra for each case study and leakage scenario is recorded after leakage and compared to the kinetic energy spectra prior to leakage, with the blowout case shown in Figure 9-6.

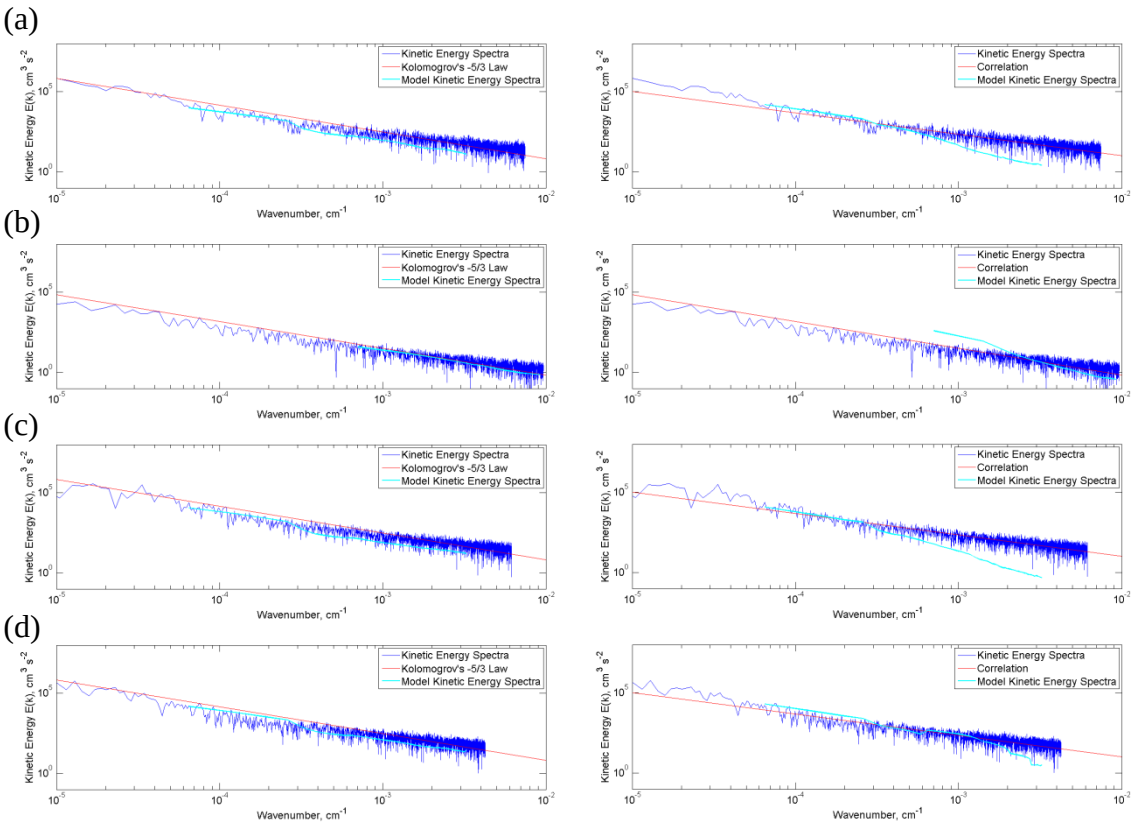

Figure 9-6 *– Fluctuating kinetic energy spectra taken from the small scale turbulent ocean model, compared with data analysed of the central North Sea (58°24'23.11"N 2°1'25.33"E) (blue line), Kolmogorov's -5/3 gradient law [303] (red line); Left: At steady state after 6.5 hours of no leakage(cyan line); Right: At steady state after 6.5 hours of leakage (cyan line). (a) X direction, top; (b) Y direction (vertical), middle top; (c) Z direction, middle bottom; (d) total magnitude, bottom.*

For each case the energy in the vertical direction for large waves increases, where the momentum and energy gained from the rising bubbles and falling solution is larger than the turbulent fluctuations as shown in Figure 9-6 (b). In the horizontal plane, some of this momentum and energy is transferred to the X and Z directional currents giving a slight increase in kinetic energy at larger wavelengths as shown in Figure 9-6 (a) and Figure 9-6 (c). These horizontal kinetic energy increases are within the natural background fluctuations and therefore would not be noticeable in the waters. However, an effect in each direction is that the larger currents and energy waves produced from the leak absorb the smaller fluctuations. Therefore there is a recorded increase in energy dissipation to the smaller wavelengths as shown in Figure 9-6 (a-d). This changes the gradient of the local energy dissipation from Kolmogorov's law of -5/3 [303] with no leakage, to an increasing gradient with the leakage rate and buoyancy force of the bubble plume. In this study, dissipation gradient measurements of up to -9/3 are found

in the vertical flow and -7/3 in the horizontal flow during the well blowout shown in Figure 9-6.

9.5 Summary

The model is able to provide data, not only on the changes in pH required for biological scientists, but also for developing optimized monitoring strategies for early leak detection when linked to larger scale models. Results show that for the cases designed in this study the biggest changes in pH will be along the seabed due to the fast dissolution and larger density of the dissolved solution. However, the CO_2 solution also dilutes quickly within the waters, especially at higher currents with strong turbulence, giving challenges for leak detection and limiting effects to the vicinity of the leakage zone. It is predicted from this study that most, if not all of the CO_2 may dissolve within the seawater prior to reaching the ocean surface where the dissolved CO_2 solution would eventually disperse as it mixes with seawater over a larger scale and timeframe [6].

Changing individual leakage parameters, such as the depth, season or current, while maintaining other properties investigated in this study can have a great effect on the development of the plumes due to differences in the dynamics of bubbles and droplets in seawater. Droplets have a density at least 100 times that of a bubble of the same volume, therefore larger droplets would take far more time and distance to dissolve. A larger number of equivalent sized bubbles are generated at the same leakage rate for lower depth leakages due to the reduced density. This increases the interfacial surface area, enhances the dissolution rates and therefore gives lower terminal heights along with greater pH changes and concentrations in the seawater.

These simulations are small scale both in time frame and spatial dimensions in comparison to that of regional or global models, where larger scale oceanic forcing effects are taken into account from oceanic observation data. To investigate seasonal water-air surface mass transfer directing CO_2 back to the atmosphere and transportation into deeper waters, potential coupling with a meso/regional scale model for longer term analysis of the leak is possible.

For each case study and leakage scenario, the CO_2 fully dissolves within the waters with the largest risk to marine life found locally in lower depth leakages. This is due to the lack of large currents dispersing the gas concentration in seawater and fast dissolution rates, giving large levels of CO_2 and a ΔpH of between -1.6 and -2.7 from gas bubble plumes. Due to the quick dissolution of bubbles, this type of leak can also be complex to detect [218]. In contrast, the Skagerrak case study shows a maximum ΔpH of -0.1 due to the large distribution of the dissolved solution from slow dissolution. In terms of bubble or droplet height as a percentage of leakage depth, the greatest risk was found to be from the highest depth leakage in the Skagerrak at 26.7 %, with the lowest depth leakage following a close second at 25 %. However in terms of distance, the lowest depth leakage had the smallest bubble plume rise height, where the highest depth leakage in the Skagerrak rises the furthest distance due to the droplet formation. As this is of a greater depth, there is a reduced risk of return back to the atmosphere and will provide a better distribution of dissolved solution within the ocean.

Comparing the bubble case study results with that of other numerical models at varied scales and leakage rates, along with data from the QICS experiment [408], it can be seen in Figure 9-7 that the area of pH changes greater than -0.1 on the seabed varies logarithmically with the leakage rate. This matches very well between different numerical models; with variations also from the leakage parameters: depth, bubble size, topography, currents, seasonal data, background chemistry, but most of all the leakage area and therefore mass flux. However, the droplet plume does not fit due to the clear differences in the plume dynamics and dissolution giving a better vertical distribution of the dissolved solution.

It is clear from the results that shallow, low current leakages are the most dangerous to localised marine life due to the high pH changes and CO_2 concentrations. Milder effects can be seen at larger currents at deeper leakages, but in terms of monitoring, these effects become less easy to detect when a leak occurs. At very shallow depths and large bubble formations, there would be a chance of the bubbles rising into the atmosphere.

The maximum pH changes recorded during leakage scenarios are clearly from well blowouts. With a flux 100 times larger than the other scenarios, far more dissolved

solution is leaked in the space giving a large concentration of the dissolved solution, with the maximum pH change of -1.87 recorded over a 160 m^3 grid. The remainder of the scenarios (leaky well, elongated conduit and chimney reactivation) present a detection and mitigation problem. Even at the high leakage rate, as the flux is so low, it would be very difficult to detect in the marine environment unless the geological structures are known with sensors strategically placed. On the other hand due to the low flux, there is relatively low risk to the ecosystem from a leak, and one needs to consider the difference between small leaks of less than 0.1% of that injected going into the water column, compared to 100% of the gas going into the atmosphere with ~30 % of this absorbed into the ocean [6, 26].

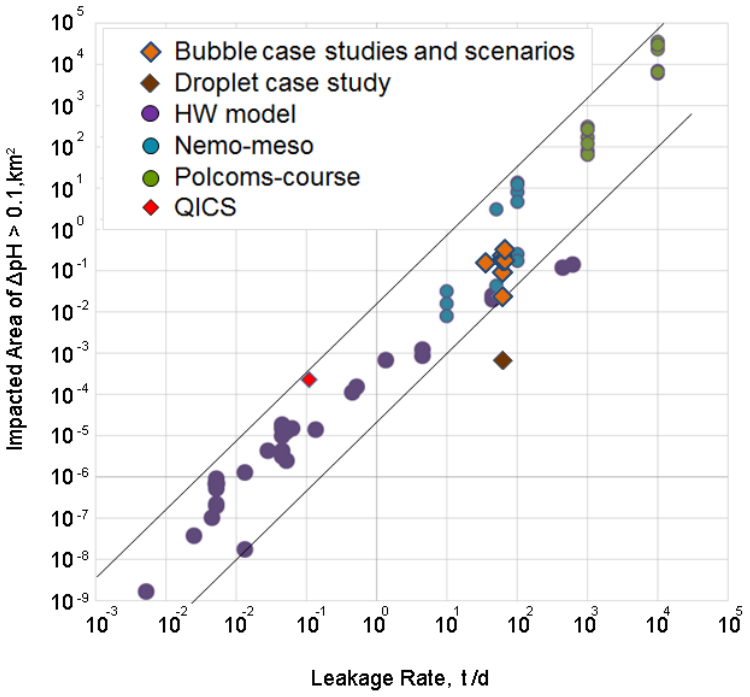

Figure 9-7 *– Comparing the case study and leakage scenario results for an area of pH changes greater than -0.1 from that of smaller scale bubble simulations: the HW nozzle spray model; and from larger scales: the QICS experiment, the Nemo-meso model and the Polcoms-course model, with data courtesy of Blackford et al. [408]*

Chapter 10 – Summary of the Conclusions and Proposals for Future Work

10.1 Research Assessment

The overall aim of this thesis was to develop a small scale, two phase large eddy simulation numerical model of the turbulent ocean to predict the physicochemical impacts and risk to the marine ecosystem from a leakage of CO_2 into the North Sea and surrounding shallow waters. Leakage site case studies and scenarios are purposefully chosen to cover varied depths allowing analysis of the phase and formation of hydrates through a model of both bubble and droplet leakages. Sub-models are developed and calibrated including the drag coefficient, Sherwood number, bubble and droplet size generation and distributions, along with plume interactions. Large Eddy Simulation for turbulence, based on laboratory and in-situ experimental data and observations, is also developed. Finally the effect on the marine ecosystem measured in terms of pCO_2 and pH changes of the seawater. These objectives have been successfully achieved, with key findings summarised below. Additionally, a laboratory experiment was designed and conducted, testing the data collection methods for use within the QICS project field experiment.

10.2 Conclusions Summary

The greatest concern on performing CCS storage in geological locations is the risk and impacts of potential CO_2 leakage from the storage reservoirs, past the multitude of trapping mechanisms through geological features and into the shallow water column, marine environment and atmosphere [98]. Small scale in-situ and laboratory experiments have been carried out with the aim of determining the effect of leakage. However, no full scale leakage has yet been investigated in the natural environment due to the costs and risks involved. Therefore gaps are still present in the available data, where other investigative means are required to analyse the impact and effect this would have. This includes the use of both the natural leakage data, along with numerical simulations to show the effects and impacts of releasing large quantities of CO_2 in the ocean.

The impacts of a CO_2 leak can be compared with surveys and modelling of natural CO_2 volcanic seeps showing effects within the local vicinity of the seep. A natural gas or oil

leak can cause far more catastrophic effects and loss of life [409]. In contrast, an offshore CO_2 leak would have implications that are far less dangerous with respect to humans, the environment, and the ecosystem. Even under the most extreme circumstances this would only strongly affect a small scale [9].

It is impossible to say where, or the scales from which leakage would occur. Due to this uncertainty, the impacts estimated by this study are a prediction alone. Full scale field experiments are difficult and expensive along with harmful risks to the environment [410]. Therefore experiments have been restricted meaning that suitable models are required to investigate and fill the gaps [227]. However, through analysis of two phase flow the correlations used to develop sub-models are designed based on experimental data to look at varied range of leakage possibilities. This allows predictions beyond the experimental data available. Field data from the QICS experiment and future small scale in-situ experiments should prove useful in both providing a prediction of the experiment results; but also receiving vital data for both calibration of the model and verification of the model's viability.

10.2.1 Experiments

With an abundance of liquid CO_2 droplet data available, the dynamics and distributions of rising gas CO_2 bubbles in seawater were investigated both experimentally and through numerical modelling within the QICS experiment. Using video footage of the bubble plume, data was compared with data published of the motion of individual gas bubbles in laboratory conditions, where agreement can be seen for a number of properties. However, a variation for the drag coefficient is found due to the difference between the experimental conditions in the laboratory and open field experiments.

Bubbles leaked from QICS experiment have initial diameters ranging up to 12.0 mm in diameter in a range of shapes from almost spherical to wobbling and cap shapes. The related velocity varies from 20 cm/sec to 45 cm/sec, giving a Reynolds number range from 500 to 3500, respectively. The measurements were carried out through a combination of imaging and passive acoustic techniques, which provided a reasonable match, but with some variations caused through errors in imaging and background noise in the acoustics.

Given the simulation results from this thesis, the most important parameter is identified as the leakage flux and leakage rate. This can vary with tidal conditions but measured at one stage during the QICS experiment at ~15% of that injected into the sediments in a gaseous form [106].

The interaction between the CO_2 bubbles and seawater is a very important phenomenon to characterise analytically as has been shown in this work. Experiments with larger leakage rates would generate a plume with strong bubble interactions, from which more suitable data can be obtained for development of correlations for a plume model. In order to validate the sub-models for coalescence or breakup of CO_2 bubbles, experimental work on observing the bubble interactions under different water conditions, bubble sizes, shapes, directional velocities, temperatures and salinities are suggested to be carried extensively in the laboratory as well as the field.

The leaked bubbles experience break-up and coalescence interactions, where a critical break-up Eötvös number is found to be E_{ob}> 20, when bubbles are characterized by the major dimension, d_{mj}, rather than their equivalent diameter d_e, and a coalescence frequency of 2.5 Hz is recorded.

The results showed a number of sources of error due to the nature of the experiment, which distorts the findings somewhat. However, this should be compared with findings under laboratory conditions that can give far more accurate measurements, but miss both plume and tidal effects that may further distort the findings giving low quality data for seawater conditions.

10.2.2 Modelling and Results

A small scale, two phase large eddy simulation numerical model of the turbulent ocean was developed in an Eulerian-Eulerian scheme considering the bubbles/droplets as a dispersed phase. An in-house computer code of the model written by FORTRAN was applied to this study designed, utilising a finite-volume method.

Based on the in-situ experimental data from QICS for CO_2 bubbles, along with further in-situ and laboratory data, correlations have been used in the development of sub-

models and correlations for drag coefficient, Sherwood number, bubble formations and bubble interactions.

Simulations are then designed based on fluid properties (density, viscosity, solubility, diffusivity, interfacial tension) and fluid chemistry (changes in DIC, pH and pCO_2) calculated from the dissolved mass concentrations of the CO_2. Calibration tests are then applied against in-situ bubble and droplet data to validate the model. These tests were further verified through simulations of the QICs experiment, where an extensive amount of data was collected including changes to the seawater chemistry.

The simulations are of a small scale both in time frame and space volume, where large effects would have an effect in longer term analysis of the leak in the larger meso/regional and global scales. There is also a need to investigate seasonal water-air surface mass transfer directing CO_2 back to the atmosphere and transportation into deeper waters such as the North Atlantic Ocean [218, 411 – 413] and globally [211].

10.2.2.1 QICS experiment

Utilising the interactions sub-model, the bubble rise height can be seen to rise to almost that of the in-situ experiment during low depth tide (~9 m). This validates the dissolution rate and rising velocity predicted in the two phase plume model. Including the bubble interactions in the model brings the simulation more in line with the experimental observations. The initial bubble size prediction sub-model is also in line with that of the measured distributions.

Some uncertainties remain over the variations of pCO_2 measurements compared with those modelled. There is the possibility of either small bubbles quickly dissolving, dissolved solution in the sediments taken up by the leakage, or higher resolution measuring equipment detecting a peak directly above the leakage. However, the model shows the pCO_2 effects in the very local vicinity of the leak, where further downstream the pCO_2 is dispersed very quickly matching that of the experiment.

10.2.2.2 North Sea case studies

Case studies were developed changing individual leakage parameters such as the depth or current while maintaining other properties, showing that these can have a great affect, with clear differences between bubbles and droplets. Droplets have a density at least 100 times that of a bubble of the same volume, and therefore take more time and distance to dissolve, even with a higher solubility at greater depths. Due to the lower density of gas at lower depths, there will be a larger number of bubbles than that of droplets at the same leakage flux. This increases the interfacial surface area enhancing dissolution rates further, producing lower terminal heights along with greater pH changes and concentrations.

Analysing the data shows the rising height of the bubble plume is mostly affected by both the depth and the initial bubble size. At greater depths larger bubbles are found to form that take longer to dissolve increasing the plume height. None of the simulated case studies provided leakage to the atmosphere. However, one needs to recognise that lower depth leakages such as the QICS experiment, with larger bubble formations, are most likely to be at risk of rising to the atmosphere directly above the bubble plume.

The maximum pH changes and volumes of pH changes experience a change as each parameter varies. An increase in temperature provides an increase in both maximum pH and the seabed surface area affected by pH changes through a reduction in the density of the seawater and therefore buoyancy of the gas bubbles. A reduced leakage rate and flux provides both a lower maximum pH change and smaller volumes of the pH changes. Lower water currents provide greater pH changes, but reduce both the volume and area affected on the seabed. Finally greater depths also produce a reduced volume of larger pH changes due to the greater distribution meaning the concentration is lower, even though the total area and volume affected is much larger.

The largest pH changes are recorded during low current scenarios with high leakage rates and low depth leakage. A maximum pH change of -2.7 is recorded over a 160 m^3 volume in the low ocean current case study. However, the greatest volume of pH changes > 0.1 is experienced in the North Sea shelf leakage during summer, with a volume of 2.82×10^{-3} km^3. The greatest seabed area coverage > 0.1 of 228,722 m^2 is

experienced due to the fast dissolution rates in the shallow North Sea; also in the summer.

10.2.2.3 Leakage scenarios

Further simulations focused on specific scenarios from the ECO_2 project, for a well blowout, chimney reactivation, elongated conduit (fault, fracture or chimney) and a leaky well. These scenarios are based on realistic data from geological modelling of leakage through sediment structures. Each simulation records approximately the same bubble rise height of 11-14m, with the greater rise height coming from the lower leakage fluxes. This is due to the negligible downforce of the dissolved solution and reduced peeling surrounding the bubble plume due to its small concentration. However, variations in the initial bubble diameter would affect the rise height further.

For the well blowout scenario, similar data is found to the case studies, where the leakage rate is 6 % higher, but the depth is 5 % shallower and the current is 30 % higher than in the initial case study for the North Sea. This gives a slightly lower volume and seabed surface area of pH changes over -0.1 from the increased current reducing the plume height and giving a larger distribution of the pH changes, decreasing in the maximum pH. The remaining scenarios have very low pH changes, with the chimney reactivation only reaching a pH change of -0.27 at the same leakage rate but over a far greater area. This is 14 % of that from the well blowout, covering a slightly lower volume of pH changes, but almost double the seabed surface area. The final scenarios for the leaky well and elongated conduit are so low in terms of pH changes that they are within background levels and would be very difficult to detect, even on this small scale. This means that in larger waters the only way these types of leakages could be detected is strategically placed monitoring sensors and knowing possible leakage locations to detect the bubble plumes from the baseline study.

10.3 Future Work Proposals

The developed two-phase, small-scale large-eddy simulation turbulent ocean model for liquid and gas leakages in the ocean is a great advance. It allows up-scaled data that due to severe costs (financial, environmental, health and political) cannot be achieved through experiments alone but are required for risk assessments. This is true for CO_2

storage, as explored in this study, or potentially developed to oil or natural gas extraction. In terms of the continuation in this line of work, the following suggestions are provided to develop the numerical models further:

- The design of the initial bubble and droplet sub-model forming from the sediments into the water column is a very useful, yet basic definition. This sub-model could be further developed utilising a greater level of detail on the physical and chemical properties of the gas and the sediment structure removing some of the assumptions. Some things to consider are the contact angles between the gas and the seawater to better define the point at which the bubble leaves the sediment in its fully formed size. The effects of flow rate and pressure of the gas as it leaves the sediments are also of great interest, where a pressurised flow has to consider the extra forcing and subsequent bubble or droplet interactions to determine the predicted bubble size with accuracy.
- The bubble interactions of breakup and coalescence require a small modification to be utilised in droplet formations. The likelihood of collisions will not change for the equivalent size and number of droplets, however due to the changes in surface tension under pressure, the number of collisions that cause coalescence or breakup will be affected.
- The transition and breakup from droplets to bubbles across the saturation curve (see Figure 4-1 and Figure 5-9) is a phenomenon that requires further study to be included within the numerical model. The mass of the fluid will remain constant, however as the density decreases the droplets will increase in size to a critical value. At this point multiple forming bubbles will break out from each individual droplet in a range of sizes depending on a number of conditions. This will provide a great increase in the number density as well as a larger volume distribution of the mass.
- Bubble break up due to instability rather than turbulent eddy collisions is also something that requires investigation in relation to the bubble plumes as found from the QICS experiment, where a larger than numerically predicted breakup rate was experienced.

- The model may be optimised by including the effect of the topography of the location that is being considered as a case study. As the shape of the seabed varies dramatically from location to location this has the potential to have a great impact on the fluid flow and in turn the flow and concentration of the dissolved solution.
- For low depth leakages the seawater to air mass transfer would be of interest to see in the small scale how much of the dissolved solution transfers back into a gas in the atmosphere.
- Nesting the small scale plume model to larger scale models, such as the Oceanic General Circulation Model (OGCM), may provide buffering through dilution and dispersion over a far longer period of time in the larger, meso/regional and global scales. This includes transportation into deeper waters and surface water to air CO_2 exchange may be simulated. This integrated model system would allow the overall prediction of the biological impact in large-scale under seabed carbon sequestration in the ocean in the small, regional and global scale over related timeframes.

Appendix A – The Individual Bubble and Droplet Model

An individual bubble/droplet numerical model is developed consisting of the same governing principles as the two phase model; CO_2 mass transfer through the shrinking rate, and CO_2 rising velocity through momentum. The fluid dynamics are numerically determined based on a Lagrangian scheme, where the history of an individual bubble in space and time is tracked and recorded [329].

Shrinking Rate

The CO_2 dissolution rate can be predicted by the shrinking rate of an individual bubble or droplet, where the equivalent diameter of the droplet or bubble reduces through the difference in concentration of CO_2 with that already dissolved in the seawater, along with the convective mass transfer, modelled in terms of the Sherwood number, Sh. However as a gas bubble rises in the waters, the pressure and temperature vary, affecting the density [352], therefore, as gases are compressible, the changes in density must also be taken into account giving

$$\dot{d}_e = -\frac{1}{\rho_{CO_2}}\left(\frac{d_e}{3}\dot{\rho}_{CO_2} + \frac{2Sh \cdot D_f\left(C_S - C_0\right)}{d_e}\right) \tag{A1-1}$$

Rising Velocity

The CO_2 rising rate can also be predicted by the terminal velocity of an individual bubble or droplet, where the buoyancy force provides an upwards momentum, but acting against this and dampening the bubble or droplet acceleration is the drag force, modelled in terms of the drag coefficient, C_d. As with the shrinking rate, the changes in mass from compression or expansion must also be taken into account giving

$$\dot{V}_r = \frac{\rho_{sw}}{\rho_{CO_2}}\left(\left(1-\frac{\rho_{CO_2}}{\rho_{sw}}\right)g - \frac{3}{4}\frac{V_r^{\,2}}{d_e}C_d\right) - V_r\frac{\dot{m}_{CO_2}}{m_{CO_2}} \tag{A1-2}$$

REFERENCES

[1] W. J. M. Tegart, G. Sheldon, D. C. Griffiths, Intergovernmental Panel on Climate Change, World Meteorological Organization, United Nations Environment Programme, and Intergovernmental Panel on Climate Change, Eds., *Climate change: the IPCC impacts assessment*. Canberra: Australian Govt. Pub. Service, 1990.

[2] M. Bowen, *Thin Ice: Unlocking the Secrets of Climate in the World's Highest Mountains*, Reprint edition. New York: Holt Paperbacks, 2006.

[3] R. E. Zeebe and D. A. Wolf-Gladrow, *CO2 in Seawater: Equilibrium, Kinetics, Isotopes*. Gulf Professional Publishing, 2001.

[4] C. Marchetti, 'On geoengineering and the CO2 problem', *Climatic Change*, vol. 1, no. 1, pp. 59–68, Mar. 1977.

[5] R. K. Pachauri, M. R. Allen, V. R. Barros, J. Broome, W. Cramer, R. Christ, J. A. Church, L. Clarke, Q. Dahe, P. Dasgupta, and others, *Climate Change 2014: Synthesis Report. Contribution of Working Groups I, II and III to the Fifth Assessment Report of the Intergovernmental Panel on Climate Change*. 2014.

[6] B. Metz and Intergovernmental Panel on Climate Change, Eds., *IPCC special report on carbon dioxide capture and storage*. Cambridge: Cambridge University Press, for the Intergovernmental Panel on Climate Change, 2005.

[7] O. Edenhofer and Intergovernmental Panel on Climate Change, Eds., *Climate change 2014: mitigation of climate change: Working Group III contribution to the Fifth assessment report of the Intergovernmental Panel on Climate Change*. New York, NY: Cambridge University Press, 2014.

[8] A. Hosa, M. Esentia, J. Stewart, and S. Haszeldine, 'Injection of CO2 into saline formations: Benchmarking worldwide projects', *Chemical Engineering Research and Design*, vol. 89, no. 9, pp. 1855–1864, Sep. 2011.

[9] K. Wallmann, M. Haeckel, P. Linke, L. Haffert, M. Schmidt, S. Buenz, R. James, C. Hauton, M. Tsimplis, S. Widdicombe, J. Blackford, A. M. Queiros, D. Connelly, A. Lichtschlag, M. Dewar, B. Chen, T. Baumberger, S. Beaubin, S. Vercelli, A. Proelss, T. Wildenborg, T. Mikunda, M. Nepveu, C. Maynard, S. Finnerty, T. Flach, N. Ahmed, A. Ulfsnes, L. Brooks, T. Moskeland, and M. Purcell, 'Best Practice Guidance for Environmental Risk Assessment for offshore CO2 geological storage', ECO2 Deliverable, D14.1 ., May 2015.

[10] Y. Shirayama and H. Thornton, 'Effect of increased atmospheric CO2 on shallow water marine benthos', *J. Geophys. Res.*, vol. 110, no. C9, p. C09S08, Sep. 2005.

[11] W. Thuiller, 'Biodiversity: Climate change and the ecologist', *Nature*, vol. 448, no. 7153, pp. 550–552, Aug. 2007.

[12] 'IPCC - Intergovernmental Panel on Climate Change'. [Online]. Available: http://www.ipcc.ch/organization/organization.shtml. [Accessed: 04-Jul-2015].

[13] A. Arguez and R. S. Vose, 'The Definition of the Standard WMO Climate Normal: The Key to Deriving Alternative Climate Normals', *Bulletin of the American Meteorological Society*, vol. 92, no. 6, pp. 699–704, Jun. 2011.

[14] P. W. Thorne, D. E. Parker, S. F. B. Tett, P. D. Jones, M. McCarthy, H. Coleman, and P. Brohan, 'Revisiting radiosonde upper air temperatures from 1958 to 2002', *J. Geophys. Res.*, vol. 110, no. D18, p. D18105, Sep. 2005.

[15] S. C. Sherwood, C. L. Meyer, R. J. Allen, and H. A. Titchner, 'Robust Tropospheric Warming Revealed by Iteratively Homogenized Radiosonde Data', *J. Climate*, vol. 21, no. 20, pp. 5336–5352, Oct. 2008.

[16] M. Free, D. J. Seidel, J. K. Angell, J. Lanzante, I. Durre, and T. C. Peterson, 'Radiosonde Atmospheric Temperature Products for Assessing Climate (RATPAC): A new data set of large-area anomaly time series', *J. Geophys. Res.*, vol. 110, no. D22, p. D22101, Nov. 2005.

[17] L. Haimberger, ‘Homogenization of Radiosonde Temperature Time Series Using Innovation Statistics’, *J. Climate*, vol. 20, no. 7, pp. 1377–1403, Apr. 2007.

[18] L. Haimberger, C. Tavolato, and S. Sperka, ‘Toward Elimination of the Warm Bias in Historic Radiosonde Temperature Records—Some New Results from a Comprehensive Intercomparison of Upper-Air Data’, *J. Climate*, vol. 21, no. 18, pp. 4587–4606, Sep. 2008.

[19] C. A. Mears and F. J. Wentz, ‘Construction of the RSS V3.2 Lower-Tropospheric Temperature Dataset from the MSU and AMSU Microwave Sounders’, *J. Atmos. Oceanic Technol.*, vol. 26, no. 8, pp. 1493–1509, Aug. 2009.

[20] C. A. Mears and F. J. Wentz, ‘Construction of the Remote Sensing Systems V3.2 Atmospheric Temperature Records from the MSU and AMSU Microwave Sounders’, *J. Atmos. Oceanic Technol.*, vol. 26, no. 6, pp. 1040–1056, Jun. 2009.

[21] J. R. Christy, R. W. Spencer, W. B. Norris, W. D. Braswell, and D. E. Parker, ‘Error Estimates of Version 5.0 of MSU–AMSU Bulk Atmospheric Temperatures’, *J. Atmos. Oceanic Technol.*, vol. 20, no. 5, pp. 613–629, May 2003.

[22] P. Brohan, J. J. Kennedy, I. Harris, S. F. B. Tett, and P. D. Jones, ‘Uncertainty estimates in regional and global observed temperature changes: A new data set from 1850’, *J. Geophys. Res.*, vol. 111, no. D12, p. D12106, Jun. 2006.

[23] J. Hansen, R. Ruedy, M. Sato, M. Imhoff, W. Lawrence, D. Easterling, T. Peterson, and T. Karl, ‘A closer look at United States and global surface temperature change’, *J. Geophys. Res.*, vol. 106, no. D20, pp. 23947–23963, Oct. 2001.

[24] K. M. Lugina, P. Y. Groisman, K. Y. Vinnikov, V. V. Koknaeva, and N. A. Speranskaya, ‘Monthly Surface Air Temperature Time Series Area-Averaged Over the 30-Degree Latitudinal Belts of the Globe’, Sep. 2006.

[25] T. M. Smith, R. W. Reynolds, T. C. Peterson, and J. Lawrimore, ‘Improvements to NOAA’s Historical Merged Land–Ocean Surface Temperature Analysis (1880–2006)’, *J. Climate*, vol. 21, no. 10, pp. 2283–2296, May 2008.

[26] T. Stocker, Ed., *Climate change 2013: the physical science basis: Working Group I contribution to the Fifth assessment report of the Intergovernmental Panel on Climate Change*. New York: Cambridge University Press, 2014.

[27] N. US Department of Commerce, ‘NOAA ESRL Global Monitoring Division’. [Online]. Available: http://www.esrl.noaa.gov/gmd/. [Accessed: 09-Jul-2015].

[28] J. T. Kiehl and K. E. Trenberth, ‘Earth’s Annual Global Mean Energy Budget’, *Bull. Amer. Meteor. Soc.*, vol. 78, no. 2, pp. 197–208, Feb. 1997.

[29] R. A. Feely, C. L. Sabine, K. Lee, W. Berelson, J. Kleypas, V. J. Fabry, and F. J. Millero, ‘Impact of Anthropogenic CO2 on the CaCO3 System in the Oceans’, *Science*, vol. 305, no. 5682, pp. 362–366, Jul. 2004.

[30] D. A. Robinson and A. Frei, ‘Seasonal Variability of Northern Hemisphere Snow Extent Using Visible Satellite Data’, *The Professional Geographer*, vol. 52, no. 2, pp. 307–315, May 2000.

[31] R. D. Brown, ‘Northern Hemisphere Snow Cover Variability and Change, 1915–97’, *J. Climate*, vol. 13, no. 13, pp. 2339–2355, Jul. 2000.

[32] A. Trupin and J. Wahr, ‘Spectroscopic Analysis of Global Tide Gauge Sea Level Data’, *Geophys. J. Int.*, vol. 100, no. 3, pp. 441–453, Mar. 1990.

[33] Leuliette, ‘Calibration of TOPEX/Poseidon and Jason Altimeter Data to Construct a Continuous Record of Mean Sea Level Change’, *Marine Geodesy*, vol. 27, no. 1, p. 79, 2004.

[34] S. Jevrejeva, A. Grinsted, J. C. Moore, and S. Holgate, ‘Nonlinear trends and multiyear cycles in sea level records’, *J. Geophys. Res.*, vol. 111, no. C9, p. C09012, Sep. 2006.

[35] S. J. Holgate and P. L. Woodworth, ‘Evidence for enhanced coastal sea level rise during the 1990s’, *Geophys. Res. Lett.*, vol. 31, no. 7, p. L07305, Apr. 2004.

[36] V. Gornitz, ‘Global Sea-Level Changes During the Past Century’, 1987.

[37] P. L. Woodworth, N. J. White, S. Jevrejeva, S. J. Holgate, J. A. Church, and W. R. Gehrels, ‘Evidence for the accelerations of sea level on multi-decade and century timescales’, *Int. J. Climatol.*, vol. 29, no. 6, pp. 777–789, May 2009.

[38] J. A. Church and N. J. White, ‘A 20th century acceleration in global sea-level rise’, *Geophys. Res. Lett.*, vol. 33, no. 1, p. L01602, Jan. 2006.

[39] J. G. Canadell, C. L. Quéré, M. R. Raupach, C. B. Field, E. T. Buitenhuis, P. Ciais, T. J. Conway, N. P. Gillett, R. A. Houghton, and G. Marland, ‘Contributions to accelerating atmospheric CO2 growth from economic activity, carbon intensity, and efficiency of natural sinks’, *PNAS*, vol. 104, no. 47, pp. 18866–18870, Nov. 2007.

[40] IEA Greenhouse Gas R&D Programme (IEA GHG), ‘Assesment of Sub Sea Ecosystem Impacts’, 2008/8, Aug. 2008.

[41] C. A. Katsman, W. Hazeleger, S. S. Drijfhout, G. J. van Oldenborgh, and G. Burgers, ‘Climate scenarios of sea level rise for the northeast Atlantic Ocean: a study including the effects of ocean dynamics and gravity changes induced by ice melt’, *Climatic Change*, vol. 91, no. 3–4, pp. 351–374, Aug. 2008.

[42] D. Stammer, ‘Response of the global ocean to Greenland and Antarctic ice melting’, *J. Geophys. Res.*, vol. 113, no. C6, p. C06022, Jun. 2008.

[43] I. Stirling and A. E. Derocher, ‘Possible Impacts of Climatic Warming on Polar Bears’, *Arctic*, vol. 46, no. 3, pp. 240–245, Sep. 1993.

[44] C. B. Field, V. R. Barros, and Intergovernmental Panel on Climate Change, Eds., *Climate change 2014: impacts, adaptation, and vulnerability: Working Group II contribution to the fifth assessment report of the Intergovernmental Panel on Climate Change*. New York, NY: Cambridge University Press, 2014.

[45] S. Fischer and O. Geden, 'The Changing Role of International Negotiations in EU Climate Policy', *The International Spectator*, vol. 50, no. 1, pp. 1–7, Jan. 2015.

[46] L. Clarke, P. Kyle, M. Wise, K. Calvin, J. Edmonds, S. Kim, M. Placet, and S. Smith, 'CO2 emissions mitigation and technological advance: An updated analysis of advanced technology scenarios', *PNNL Report Pacific Northwest National Laboratory, Richmond*, 2008.

[47] K. Calvin, J. Edmonds, B. Bond-Lamberty, L. Clarke, S. H. Kim, P. Kyle, S. J. Smith, A. Thomson, and M. Wise, '2.6: Limiting climate change to 450 ppm CO2 equivalent in the 21st century', *Energy Economics*, vol. 31, Supplement 2, pp. S107–S120, Dec. 2009.

[48] 'IEA - ETP 2015'. [Online]. Available: http://www.iea.org/etp/etp2015/. [Accessed: 13-Jul-2015].

[49] International Energy Agency, *Energy Technology Perspectives 2015 - Mobilising Innovation to Accelerate Climate Action*. 2015.

[50] T. Dietz, G. T. Gardner, J. Gilligan, P. C. Stern, and M. P. Vandenbergh, 'Household actions can provide a behavioral wedge to rapidly reduce US carbon emissions', *Proceedings of the National Academy of Sciences*, vol. 106, no. 44, pp. 18452–18456, 2009.

[51] J. FUJINO, G. HIBINO, T. EHARA, Y. MATSUOKA, T. MASUI, and M. KAINUMA, 'Back-casting analysis for 70% emission reduction in Japan by 2050', *Climate Policy*, vol. 8, no. sup1, pp. S108–S124, Jan. 2008.

[52] N. Eyre, ‘Policing carbon: design and enforcement options for personal carbon trading’, *Climate Policy*, vol. 10, no. 4, pp. 432–446, Jan. 2010.

[53] R. Kannan and N. Strachan, ‘Modelling the UK residential energy sector under long-term decarbonisation scenarios: Comparison between energy systems and sectoral modelling approaches’, *Applied Energy*, vol. 86, no. 4, pp. 416–428, Apr. 2009.

[54] H. Lund, ‘Renewable energy strategies for sustainable development’, *Energy*, vol. 32, no. 6, pp. 912–919, Jun. 2007.

[55] S. Allen, ‘Carbon Footprint of Electricity Generation’, Houses of Parliament, Parlimentary Office of Science and Technology, POSTNOTE 383, Jun. 2011.

[56] N. Hawkes, G. Lean, D. Leigh, R. McKie, P. Pringle, and A. Wilson, ‘The worst accident in the world’, 1986.

[57] ‘BP Statistical Review of World Energy June 2015 - Nuclear Energy’. [Online]. Available: http://www.bp.com/content/dam/bp/pdf/Energy-economics/statistical-review-2015/bp-statistical-review-of-world-energy-2015-nuclear-energy-section.pdf.

[58] ‘Japan’s Nuclear Power Sector Awakens After Long Sleep’, *Forbes*, Aug-2015. [Online]. Available: http://www.forbes.com/sites/jamesconca/2015/08/11/japans-nuclear-power-awakens-after-long-sleep/. [Accessed: 13-Aug-2015].

[59] J. Cowie, *Climate Change: Biological and Human Aspects*. Cambridge University Press, 2013.

[60] W. S. Broecker, T. Peng, and Z. Beng, *Tracers in the sea*. Lamont-Doherty Geological Observatory, Columbia University, 1982.

[61] U. Riebesell, K. G. Schulz, R. G. J. Bellerby, M. Botros, P. Fritsche, M. Meyerhöfer, C. Neill, G. Nondal, A. Oschlies, J. Wohlers, and E. Zöllner,

‘Enhanced biological carbon consumption in a high CO2 ocean’, *Nature*, vol. 450, no. 7169, pp. 545–548, Nov. 2007.

[62] J. C. Orr, V. J. Fabry, O. Aumont, L. Bopp, S. C. Doney, R. A. Feely, A. Gnanadesikan, N. Gruber, A. Ishida, F. Joos, R. M. Key, K. Lindsay, E. Maier-Reimer, R. Matear, P. Monfray, A. Mouchet, R. G. Najjar, G.-K. Plattner, K. B. Rodgers, C. L. Sabine, J. L. Sarmiento, R. Schlitzer, R. D. Slater, I. J. Totterdell, M.-F. Weirig, Y. Yamanaka, and A. Yool, ‘Anthropogenic ocean acidification over the twenty-first century and its impact on calcifying organisms’, *Nature*, vol. 437, no. 7059, pp. 681–686, Sep. 2005.

[63] P. Freund and W. G. Ormerod, ‘Progress toward storage of carbon dioxide’, *Energy Conversion and Management*, vol. 38, Supplement, pp. S199–S204, 1997.

[64] Statoil, ‘Statoil Annual Report 2010’, 2010.

[65] Global CCS Institute, ‘The Global Status of CCS: 2014’, Global CCS Institute, Technical Report, May 2014.

[66] J. J. Dooley, S. H. Kim, J. A. Edmonds, S. J. Friedman, and M. A. Wise, ‘A first order global geological CO2 storage potential supply curve and its application in a global integrated assessment model’, *Joint Global Change Research Institute University of Maryland*, 2003.

[67] ‘Scottish Carbon Capture & Storage | SCCS’. [Online]. Available: http://www.sccs.org.uk/. [Accessed: 14-Jul-2015].

[68] M. A. Latham, ‘BP Deepwater Horizon: A Cautionary Tale for CCS, Hydrofracking, Geoengineering and Other Emerging Technologies with Environmental and Human Health Risks, The’, *Wm. & Mary Envtl. L. & Pol’y Rev.*, vol. 36, p. 31, 2012 2011.

[69] M. Kanniche, R. Gros-Bonnivard, P. Jaud, J. Valle-Marcos, J.-M. Amann, and C. Bouallou, ‘Pre-combustion, post-combustion and oxy-combustion in thermal

power plant for CO2 capture', *Applied Thermal Engineering*, vol. 30, no. 1, pp. 53–62, Jan. 2010.

[70] S. Wong and R. Bioletti, 'Carbon dioxide separation technologies', *Alberta Research Council*, 2002.

[71] J. Gale, J. C. Abanades, S. Bachu, and C. Jenkins, 'Special Issue commemorating the 10th year anniversary of the publication of the Intergovernmental Panel on Climate Change Special Report on CO2 Capture and Storage', *International Journal of Greenhouse Gas Control*, vol. 40, pp. 1–5, Sep. 2015.

[72] R. Idem, T. Supap, H. Shi, D. Gelowitz, M. Ball, C. Campbell, and P. Tontiwachwuthikul, 'Practical experience in post-combustion CO2 capture using reactive solvents in large pilot and demonstration plants', *International Journal of Greenhouse Gas Control*, vol. 40, pp. 6–25, Sep. 2015.

[73] Z. (Henry) Liang, W. Rongwong, H. Liu, K. Fu, H. Gao, F. Cao, R. Zhang, T. Sema, A. Henni, K. Sumon, D. Nath, D. Gelowitz, W. Srisang, C. Saiwan, A. Benamor, M. Al-Marri, H. Shi, T. Supap, C. Chan, Q. Zhou, M. Abu-Zahra, M. Wilson, W. Olson, R. Idem, and P. (PT) Tontiwachwuthikul, 'Recent progress and new developments in post-combustion carbon-capture technology with amine based solvents', *International Journal of Greenhouse Gas Control*, vol. 40, pp. 26–54, Sep. 2015.

[74] D. Jansen, M. Gazzani, G. Manzolini, E. van Dijk, and M. Carbo, 'Pre-combustion CO2 capture', *International Journal of Greenhouse Gas Control*, vol. 40, pp. 167–187, Sep. 2015.

[75] R. Stanger, T. Wall, R. Spörl, M. Paneru, S. Grathwohl, M. Weidmann, G. Scheffknecht, D. McDonald, K. Myöhänen, J. Ritvanen, S. Rahiala, T. Hyppänen, J. Mletzko, A. Kather, and S. Santos, 'Oxyfuel combustion for CO2 capture in power plants', *International Journal of Greenhouse Gas Control*, vol. 40, pp. 55–125, Sep. 2015.

[76] P. W. Parfomak and P. Folger, ‘Carbon dioxide (CO2) pipelines for carbon sequestration: Emerging policy issues’, 2007.

[77] R. Svensson, M. Odenberger, F. Johnsson, and L. Strömberg, ‘Transportation infrastructure for CCS - Experiences and expected development’, in *Chalmers Publication Library (CPL)*, 2004, vol. Poster 350.

[78] H. J. Herzog, ‘“Ocean Sequestration of CO2 - An Overview’, presented at the Fourth International Conference on Greenhouse Gas Control Technologies, Interlaken, Switzerland, 1998.

[79] J. Heinrich, *Legal implications of CO2 ocean storage*. Laboratory for Energy and the Environment, MIT, 2002.

[80] J. Bradshaw and T. Dance, ‘Mapping geological storage prospectivity of CO_2 for the world’s sedimentary basins and regional source to sink matching’, 2005.

[81] F. M. Orr, ‘Onshore geologic storage of CO2’, *Science*, vol. 325, no. 5948, pp. 1656–1658, 2009.

[82] D. P. Schrag, ‘Storage of Carbon Dioxide in Offshore Sediments’, *Science*, vol. 325, no. 5948, pp. 1658–1659, Sep. 2009.

[83] J. Gibbins and H. Chalmers, ‘Carbon capture and storage’, *Energy Policy*, vol. 36, no. 12, pp. 4317–4322, Dec. 2008.

[84] A. W. Woods, *Flow in Porous Rocks*. Cambridge University Press, 2014.

[85] R. Shukla, P. Ranjith, A. Haque, and X. Choi, ‘A review of studies on CO2 sequestration and caprock integrity’, *Fuel*, vol. 89, no. 10, pp. 2651–2664, Oct. 2010.

[86] M. Mazzotti, R. Pini, and G. Storti, ‘Enhanced coalbed methane recovery’, *The Journal of Supercritical Fluids*, vol. 47, no. 3, pp. 619–627, Jan. 2009.

[87] S. Taku Ide, K. Jessen, and F. M. Orr Jr., ‘Storage of CO2 in saline aquifers: Effects of gravity, viscous, and capillary forces on amount and timing of trapping’, *International Journal of Greenhouse Gas Control*, vol. 1, no. 4, pp. 481–491, Oct. 2007.

[88] S. Krevor, M. J. Blunt, S. M. Benson, C. H. Pentland, C. Reynolds, A. Al-Menhali, and B. Niu, ‘Capillary trapping for geologic carbon dioxide storage – From pore scale physics to field scale implications’, *International Journal of Greenhouse Gas Control*, vol. 40, pp. 221–237, Sep. 2015.

[89] T. Suekane, T. Nobuso, S. Hirai, and M. Kiyota, ‘Geological storage of carbon dioxide by residual gas and solubility trapping’, *International Journal of Greenhouse Gas Control*, vol. 2, no. 1, pp. 58–64, Jan. 2008.

[90] H. Emami-Meybodi, H. Hassanzadeh, C. P. Green, and J. Ennis-King, ‘Convective dissolution of CO2 in saline aquifers: Progress in modeling and experiments’, *International Journal of Greenhouse Gas Control*, vol. 40, pp. 238–266, Sep. 2015.

[91] B. Hitchon and A. R. Council, *Aquifer disposal of carbon dioxide: hydrodynamic and mineral trapping : proof of concept*. Geoscience Pub., 1996.

[92] Y. Song, Y. Zhan, Y. Zhang, S. Liu, W. Jian, Y. Liu, and D. Wang, ‘Measurements of CO2–H2O–NaCl Solution Densities over a Wide Range of Temperatures, Pressures, and NaCl Concentrations’, *J. Chem. Eng. Data*, vol. 58, no. 12, pp. 3342–3350, Dec. 2013.

[93] X. Liu and P. B. Flemings, ‘Dynamic multiphase flow model of hydrate formation in marine sediments’, *Journal of Geophysical Research (Solid Earth)*, vol. 112, p. B03101, Mar. 2007.

[94] Y.-S. Choi, S. Nesic, and D. Young, ‘Effect of Impurities on the Corrosion Behavior of CO2 Transmission Pipeline Steel in Supercritical CO2−Water

Environments', *Environ. Sci. Technol.*, vol. 44, no. 23, pp. 9233–9238, Dec. 2010.

[95] J. Gale and J. Davison, 'Transmission of CO2—safety and economic considerations', *Energy*, vol. 29, no. 9–10, pp. 1319–1328, Jul. 2004.

[96] S. Bassi, R. Boyd, S. Buckle, P. Fennell, N. Mac Dowell, Z. Makuch, and I. Staffell, 'Bridging the gap: improving the economic and policy framework for carbon capture and storage in the European Union', 2015.

[97] S. M. Benson, R. Hepple, J. Apps, C.-F. Tsang, and M. Lippmann, 'Lessons learned from natural and industrial analogues for storage of carbon dioxide in deep geological formations', *Lawrence Berkeley National Laboratory*, 2002.

[98] P. Holland, *Offshore Blowouts: Causes and Control*, 1 edition. Houston, Tex: Gulf Professional Publishing, 1997.

[99] S. Holloway, 'An overview of the underground disposal of carbon dioxide', *Energy Conversion and Management*, vol. 38, Supplement, pp. S193–S198, 1997.

[100] I. J. Duncan, J.-P. Nicot, and J.-W. Choi, 'Risk Assessment for future CO2 Sequestration Projects Based CO2 Enhanced Oil Recovery in the U.S.', *Energy Procedia*, vol. 1, no. 1, pp. 2037–2042, Feb. 2009.

[101] E. Fleming, L. Brown, R. Cook, and others, 'Overview of production engineering aspects of operating the Denver Unit CO2 flood', in *SPE/DOE Enhanced Oil Recovery Symposium*, 1992.

[102] S. Holloway, 'Underground sequestration of carbon dioxide—a viable greenhouse gas mitigation option', *Energy*, vol. 30, no. 11–12, pp. 2318–2333, Aug. 2005.

[103] K. Ellison, ‘Risks Posed to Drinking Water Aquifers Due to Leakage of Dissolve’, Master of Science (MS) Thesis, Clemson University, South Carolina, 2011.

[104] IEAGHG, ‘Criteria of Fault Geomechanical Stability during Pressure Build-up’. Apr-2015.

[105] J. Blackford, H. Stahl, J. M. Bull, B. J. P. Bergès, M. Cevatoglu, A. Lichtschlag, D. Connelly, R. H. James, J. Kita, D. Long, M. Naylor, K. Shitashima, D. Smith, P. Taylor, I. Wright, M. Akhurst, B. Chen, T. M. Gernon, C. Hauton, M. Hayashi, H. Kaieda, T. G. Leighton, T. Sato, M. D. J. Sayer, M. Suzumura, K. Tait, M. E. Vardy, P. R. White, and S. Widdicombe, ‘Detection and impacts of leakage from sub-seafloor deep geological carbon dioxide storage’, *Nature Clim. Change*, vol. 4, no. 11, pp. 1011–1016, Nov. 2014.

[106] J. M. West, J. Pearce, M. Bentham, and P. Maul, ‘Issue profile: environmental issues and the geological storage of CO2’, *Eur. Env.*, vol. 15, no. 4, pp. 250–259, Jul. 2005.

[107] ‘ECO2 - ECO2’. [Online]. Available: http://www.eco2-project.eu/. [Accessed: 20-Jul-2015].

[108] ‘QICS’. [Online]. Available: http://www.bgs.ac.uk/qics/. [Accessed: 20-Jul-2015].

[109] N. M. Burnside and M. Naylor, ‘Review and implications of relative permeability of CO2/brine systems and residual trapping of CO2’, *International Journal of Greenhouse Gas Control*, vol. 23, pp. 1–11, Apr. 2014.

[110] A. M. Queirós, P. Taylor, A. Cowles, A. Reynolds, S. Widdicombe, and H. Stahl, ‘Optical assessment of impact and recovery of sedimentary pH profiles in ocean acidification and carbon capture and storage research’, *International Journal of Greenhouse Gas Control*, vol. 38, pp. 110–120, Jul. 2015.

[111] P. Taylor, A. Lichtschlag, M. Toberman, M. D. J. Sayer, A. Reynolds, T. Sato, and H. Stahl, ‘Impact and recovery of pH in marine sediments subject to a temporary carbon dioxide leak’, *International Journal of Greenhouse Gas Control*, vol. 38, pp. 93–101, Jul. 2015.

[112] A. Lichtschlag, R. H. James, H. Stahl, and D. Connelly, ‘Effect of a controlled sub-seabed release of CO2 on the biogeochemistry of shallow marine sediments, their pore waters, and the overlying water column’, *International Journal of Greenhouse Gas Control*, vol. 38, pp. 80–92, Jul. 2015.

[113] N. Sellami, M. Dewar, H. Stahl, and B. Chen, ‘Dynamics of rising CO2 bubble plumes in the QICS field experiment: Part 1 – The experiment’, *International Journal of Greenhouse Gas Control*, vol. 38, pp. 44–51, Jul. 2015.

[114] M. Cevatoglu, J. M. Bull, M. E. Vardy, T. M. Gernon, I. C. Wright, and D. Long, ‘Gas migration pathways, controlling mechanisms and changes in sediment acoustic properties observed in a controlled sub-seabed CO2 release experiment’, *International Journal of Greenhouse Gas Control*, vol. 38, pp. 26–43, Jul. 2015.

[115] P. Taylor, H. Stahl, M. E. Vardy, J. M. Bull, M. Akhurst, C. Hauton, R. H. James, A. Lichtschlag, D. Long, D. Aleynik, M. Toberman, M. Naylor, D. Connelly, D. Smith, M. D. J. Sayer, S. Widdicombe, I. C. Wright, and J. Blackford, ‘A novel sub-seabed CO2 release experiment informing monitoring and impact assessment for geological carbon storage’, *International Journal of Greenhouse Gas Control*, vol. 38, pp. 3–17, Jul. 2015.

[116] M. D. J. Sayer, P. Taylor, and H. Stahl, ‘The use of scientific diving in support of a novel carbon dioxide release experiment’, in *Proceedings of the American Academy for Underwater Sciences 33rd Symposium*, AAUS: Dauphin Island, AL, 2014, pp. 50–54.

[117] C. Mori, T. Sato, Y. Kano, H. Oyama, D. Aleynik, D. Tsumune, and Y. Maeda, ‘Numerical study of the fate of CO2 purposefully injected into the sediment and

seeping from seafloor in Ardmucknish Bay', *International Journal of Greenhouse Gas Control*, vol. 38, pp. 153–161, Jul. 2015.

[118] M. Dewar, N. Sellami, and B. Chen, 'Dynamics of rising CO2 bubble plumes in the QICS field experiment: Part 2 – Modelling', *International Journal of Greenhouse Gas Control*, vol. 38, pp. 52–63, Jul. 2015.

[119] M. Dewar, W. Wei, D. McNeil, and B. Chen, 'Small-scale modelling of the physiochemical impacts of CO2 leaked from sub-seabed reservoirs or pipelines within the North Sea and surrounding waters', *Marine Pollution Bulletin*, vol. 73, no. 2, pp. 504–515, Aug. 2013.

[120] M. Dewar, W. Wei, D. McNeil, and B. Chen, 'Simulation of the Near Field Physiochemical Impact of CO2 Leakage into Shallow Water in the North Sea', *Energy Procedia*, vol. 37, pp. 3413–3423, 2013.

[121] H. K. Hvidevold, G. Alendal, T. Johannessen, and T. Mannseth, 'Assessing model parameter uncertainties for rising velocity of CO2 droplets through experimental design', *International Journal of Greenhouse Gas Control*, vol. 11, pp. 283–289, Nov. 2012.

[122] H. K. Hvidevold, G. Alendal, T. Johannessen, and T. Mannseth, 'Assessing Model Uncertainties Through Proper Experimental Design', *Energy Procedia*, vol. 37, pp. 3439–3446, 2013.

[123] J. Kita, H. Stahl, M. Hayashi, T. Green, Y. Watanabe, and S. Widdicombe, 'Benthic megafauna and CO2 bubble dynamics observed by underwater photography during a controlled sub-seabed release of CO2', *International Journal of Greenhouse Gas Control*, vol. 38, pp. 202–209, Jul. 2015.

[124] Y. Maeda, K. Shitashima, and A. Sakamoto, 'Mapping observations using AUV and numerical simulations of leaked CO2 diffusion in sub-seabed CO2 release experiment at Ardmucknish Bay', *International Journal of Greenhouse Gas Control*, vol. 38, pp. 143–152, Jul. 2015.

[125] K. Shitashima, Y. Maeda, and A. Sakamoto, ‘Detection and monitoring of leaked CO2 through sediment, water column and atmosphere in a sub-seabed CCS experiment’, *International Journal of Greenhouse Gas Control*, vol. 38, pp. 135–142, Jul. 2015.

[126] B. J. P. Bergès, T. G. Leighton, and P. R. White, ‘Passive acoustic quantification of gas fluxes during controlled gas release experiments’, *International Journal of Greenhouse Gas Control*, vol. 38, pp. 64–79, Jul. 2015.

[127] H. A. Botnen, A. M. Omar, I. Thorseth, T. Johannessen, and G. Alendal, ‘The effect of submarine CO2 vents on seawater: Implications for detection of subsea carbon sequestration leakage’, *Limnol. Oceanogr.*, vol. 60, no. 2, pp. 402–410, Mar. 2015.

[128] M. Schmidt, P. Linke, S. Sommer, D. Esser, and S. Cherednichenko, ‘Natural CO2 Seeps Offshore Panarea: A Test Site for Subsea CO2 Leak Detection Technology’, *Marine Technology Society Journal*, vol. 49, no. 1, pp. 19–30, Jan. 2015.

[129] S. E. Beaubien, C. De Vittor, D. F. McGinnis, S. Bigi, C. Comici, G. Ingrosso, S. Lombardi, and L. Ruggiero, ‘Preliminary Experiments and Modelling of the Fate of CO2 Bubbles in the Water Column Near Panarea Island (Italy)’, *Energy Procedia*, vol. 59, pp. 397–403, 2014.

[130] S. E. Beaubien, S. Graziani, A. Annunziatellis, S. Bigi, L. Ruggiero, M. C. Tartarello, and S. Lombardi, ‘Spatial-temporal water column monitoring using multiple, low-cost GasPro-pCO2 sensors: implications for monitoring, modelling, and potential impact’, *Energy Procedia*, vol. 63, pp. 3840–3847, 2014.

[131] S. Graziani, S. E. Beaubien, S. Bigi, and S. Lombardi, ‘Spatial and Temporal pCO2 Marine Monitoring Near Panarea Island (Italy) Using Multiple Low-Cost GasPro Sensors’, *Environ. Sci. Technol.*, vol. 48, no. 20, pp. 12126–12133, Oct. 2014.

[132] D. de Beer, M. Haeckel, J. Neumann, G. Wegener, F. Inagaki, and A. Boetius, ‘Saturated CO2 inhibits microbial processes in CO2-vented deep-sea sediments’, *Biogeosciences*, vol. 10, no. 8, pp. 5639–5649, Aug. 2013.

[133] J. Schneider von Deimling and C. Papenberg, ‘Technical Note: Detection of gas bubble leakage via correlation of water column multibeam images’, *Ocean Science*, vol. 8, no. 2, pp. 175–181, Mar. 2012.

[134] J. J. C. Phelps, J. C. Blackford, J. T. Holt, and J. A. Polton, ‘Modelling large-scale CO2 leakages in the North Sea’, *International Journal of Greenhouse Gas Control*, vol. 38, pp. 210–220, Jul. 2015.

[135] H. K. Hvidevold, G. Alendal, T. Johannessen, A. Ali, T. Mannseth, and H. Avlesen, ‘Layout of CCS monitoring infrastructure with highest probability of detecting a footprint of a CO2 leak in a varying marine environment’, *International Journal of Greenhouse Gas Control*, vol. 37, pp. 274–279, Jun. 2015.

[136] L. Vielstädte, P. Linke, D. McGinnis, S. Sommer, K. J. G. Wallmann, D. McGinnis, and M. Haeckel, ‘The footprint of CO2 leakage in the water column: Insights from numerical modeling based on a North Sea gas release experiment’, in *[Talk] In: AGU Fall Meeting 2013, 09.-13.12.2013, San Francisco, USA .*, San Francisco, USA, 2013.

[137] J. Blackford, J. M. Bull, M. Cevatoglu, D. Connelly, C. Hauton, R. H. James, A. Lichtschlag, H. Stahl, S. Widdicombe, and I. C. Wright, ‘Marine baseline and monitoring strategies for carbon dioxide capture and storage (CCS)’, *International Journal of Greenhouse Gas Control*, vol. 38, pp. 221–229, Jul. 2015.

[138] D. Atamanchuk, A. Tengberg, D. Aleynik, P. Fietzek, K. Shitashima, A. Lichtschlag, P. O. J. Hall, and H. Stahl, ‘Detection of CO2 leakage from a simulated sub-seabed storage site using three different types of pCO2 sensors’,

International Journal of Greenhouse Gas Control, vol. 38, pp. 121–134, Jul. 2015.

[139] P. Linke, M. Schmidt, M. Rohleder, A. Al-Barakati, and R. Al-Farawati, 'Novel Online Digital Video and High-Speed Data Broadcasting via Standard Coaxial Cable Onboard Marine Operating Vessels', *Marine Technology Society Journal*, vol. 49, no. 1, pp. 7–18, Jan. 2015.

[140] S. Schutting, T. Jokic, M. Strobl, S. M. Borisov, D. de Beer, and I. Klimant, 'NIR optical carbon dioxide sensors based on highly photostable dihydroxy-aza-BODIPY dyes', *J. Mater. Chem. C*, vol. 3, no. 21, pp. 5474–5483, May 2015.

[141] S. Schutting, I. Klimant, D. de Beer, and S. M. Borisov, 'New highly fluorescent pH indicator for ratiometric RGB imaging of pCO2', *Methods Appl. Fluoresc.*, vol. 2, no. 2, p. 024001, Jun. 2014.

[142] J. Schneider von Deimling, W. Weinrebe, Z. Tóth, H. Fossing, R. Endler, G. Rehder, and V. Spieß, 'A low frequency multibeam assessment: Spatial mapping of shallow gas by enhanced penetration and angular response anomaly', *Marine and Petroleum Geology*, vol. 44, pp. 217–222, Jun. 2013.

[143] S. Schutting, S. M. Borisov, and I. Klimant, 'Diketo-Pyrrolo-Pyrrole Dyes as New Colorimetric and Fluorescent pH Indicators for Optical Carbon Dioxide Sensors', *Anal. Chem.*, vol. 85, no. 6, pp. 3271–3279, Mar. 2013.

[144] C. Jenkins, A. Chadwick, and S. D. Hovorka, 'The state of the art in monitoring and verification—Ten years on', *International Journal of Greenhouse Gas Control*, vol. 40, pp. 312–349, Sep. 2015.

[145] N. Pratt, B. J. Ciotti, E. A. Morgan, P. Taylor, H. Stahl, and C. Hauton, 'No evidence for impacts to the molecular ecophysiology of ion or CO2 regulation in tissues of selected surface-dwelling bivalves in the vicinity of a sub-seabed CO2 release', *International Journal of Greenhouse Gas Control*, vol. 38, pp. 193–201, Jul. 2015.

[146] S. Widdicombe, C. L. McNeill, H. Stahl, P. Taylor, A. M. Queirós, J. Nunes, and K. Tait, 'Impact of sub-seabed CO2 leakage on macrobenthic community structure and diversity', *International Journal of Greenhouse Gas Control*, vol. 38, pp. 182–192, Jul. 2015.

[147] K. Tait, H. Stahl, P. Taylor, and S. Widdicombe, 'Rapid response of the active microbial community to CO2 exposure from a controlled sub-seabed CO2 leak in Ardmucknish Bay (Oban, Scotland)', *International Journal of Greenhouse Gas Control*, vol. 38, pp. 171–181, Jul. 2015.

[148] Y. Watanabe, K. Tait, S. Gregory, M. Hayashi, A. Shimamoto, P. Taylor, H. Stahl, K. Green, I. Yoshinaga, Y. Suwa, and J. Kita, 'Response of the ammonia oxidation activity of microorganisms in surface sediment to a controlled sub-seabed release of CO2', *International Journal of Greenhouse Gas Control*, vol. 38, pp. 162–170, Jul. 2015.

[149] A. Tsukasaki, M. Suzumura, A. Lichtschlag, H. Stahl, and R. H. James, 'Phosphorus behavior in sediments during a sub-seabed CO2 controlled release experiment', *International Journal of Greenhouse Gas Control*, vol. 38, pp. 102–109, Jul. 2015.

[150] N. Dorey, P. Lançon, M. Thorndyke, and S. Dupont, 'Assessing physiological tipping point of sea urchin larvae exposed to a broad range of pH', *Glob Change Biol*, vol. 19, no. 11, pp. 3355–3367, Nov. 2013.

[151] M. Stumpp, M. Hu, I. Casties, R. Saborowski, M. Bleich, F. Melzner, and S. Dupont, 'Digestion in sea urchin larvae impaired under ocean acidification', *Nature Clim. Change*, vol. 3, no. 12, pp. 1044–1049, Dec. 2013.

[152] S. Widdicombe, A. Beesley, J. A. Berge, S. L. Dashfield, C. L. McNeill, H. R. Needham, and S. Øxnevad, 'Impact of elevated levels of CO2 on animal mediated ecosystem function: The modification of sediment nutrient fluxes by burrowing urchins', *Marine Pollution Bulletin*, vol. 73, no. 2, pp. 416–427, Aug. 2013.

[153] K. Yanagawa, Y. Morono, D. de Beer, M. Haeckel, M. Sunamura, T. Futagami, T. Hoshino, T. Terada, K. Nakamura, T. Urabe, G. Rehder, A. Boetius, and F. Inagaki, 'Metabolically active microbial communities in marine sediment under high-CO2 and low-pH extremes', *ISME J*, vol. 7, no. 3, pp. 555–567, Mar. 2013.

[154] K. Y. K. Chan, D. Grünbaum, M. Arnberg, M. Thorndyke, and S. T. Dupont, 'Ocean acidification induces budding in larval sea urchins', *Mar Biol*, vol. 160, no. 8, pp. 2129–2135, Nov. 2012.

[155] Y. S. Appelhans, J. Thomsen, S. Opitz, C. Pansch, F. Melzner, and M. Wahl, 'Juvenile sea stars exposed to acidification decrease feeding and growth with no acclimation potential', *Mar Ecol Prog Ser*, vol. 509, pp. 227–239, Aug. 2014.

[156] M. Y. Hu, I. Casties, M. Stumpp, O. Ortega-Martinez, and S. Dupont, 'Energy metabolism and regeneration are impaired by seawater acidification in the infaunal brittlestar Amphiura filiformis', *J Exp Biol*, vol. 217, no. 13, pp. 2411–2421, Jul. 2014.

[157] S. Dupont, A. Moya, and X. Bailly, 'Stable Photosymbiotic Relationship under CO2-Induced Acidification in the Acoel Worm Symsagittifera Roscoffensis', *PLoS ONE*, vol. 7, no. 1, p. e29568, Jan. 2012.

[158] M. Stumpp, K. Trübenbach, D. Brennecke, M. Y. Hu, and F. Melzner, 'Resource allocation and extracellular acid–base status in the sea urchin Strongylocentrotus droebachiensis in response to CO2 induced seawater acidification', *Aquatic Toxicology*, vol. 110–111, pp. 194–207, Apr. 2012.

[159] D. G. Jones, S. E. Beaubien, J. C. Blackford, E. M. Foekema, J. Lions, C. De Vittor, J. M. West, S. Widdicombe, C. Hauton, and A. M. Queirós, 'Developments since 2005 in understanding potential environmental impacts of CO2 leakage from geological storage', *International Journal of Greenhouse Gas Control*.

[160] S. Widdicombe, J. C. Blackford, and J. I. Spicer, ‘Assessing the environmental consequences of CO2 leakage from geological CCS: Generating evidence to support environmental risk assessment’, *Marine Pollution Bulletin*, vol. 73, no. 2, pp. 399–401, Aug. 2013.

[161] R. Gerlagh and B. van der Zwaan, ‘Evaluating Uncertain CO2 Abatement over the Very Long Term’, *Environ Model Assess*, vol. 17, no. 1–2, pp. 137–148, Jul. 2011.

[162] S. Shackley and E. Dütschke, ‘Introduction to the Special Issue on CCS Carbon Dioxide Capture and Storage - Not a Silver Bullet to Climate Change, But a Feasible Option?’, *Energy & Environment*, vol. 23, no. 2–3, pp. 209–226, May 2012.

[163] R. J. Pawar, G. S. Bromhal, J. W. Carey, W. Foxall, A. Korre, P. S. Ringrose, O. Tucker, M. N. Watson, and J. A. White, ‘Recent advances in risk assessment and risk management of geologic CO2 storage’, *International Journal of Greenhouse Gas Control*, vol. 40, pp. 292–311, Sep. 2015.

[164] B. Chen, Y. Song, M. Nishio, and M. Akai, ‘A Eulerian-Eulerian physical-biological impact model of zooplankton injury due to CO2 ocean sequestration’, *Journal of oceanography*, vol. 60, no. 4, pp. 797–805, 2004.

[165] S. Bachu, ‘Review of CO2 storage efficiency in deep saline aquifers’, *International Journal of Greenhouse Gas Control*, vol. 40, pp. 188–202, Sep. 2015.

[166] J. T. Birkholzer, C. M. Oldenburg, and Q. Zhou, ‘CO2 migration and pressure evolution in deep saline aquifers’, *International Journal of Greenhouse Gas Control*, vol. 40, pp. 203–220, Sep. 2015.

[167] R. James, D. Connelly, A. Lichtschlag, T. Baumberger, R. B. Pedersen, S. Beaubien, D. de Beer, B. Chen, P. Linke, M. Haeckel, and others, ‘Report

summarizing all information from WP2 relevant for the creation of an Environmental Best Practice for offshore CCS sites', 2014.

[168] R. Heggland, 'Detection of gas migration from a deep source by the use of exploration 3D seismic data', *Marine Geology*, vol. 137, no. 1–2, pp. 41–47, Feb. 1997.

[169] B. Chen, Y. Song, M. Nishio, S. Someya, and M. Akai, 'Modeling near-field dispersion from direct injection of carbon dioxide into the ocean', *J. Geophys. Res.*, vol. 110, no. C9, p. C09S15, Sep. 2005.

[170] G. Alendal and H. Drange, 'Two-phase, near-field modeling of purposefully released CO2 in the ocean', *J. Geophys. Res.*, vol. 106, no. C1, pp. 1085–1096, Jan. 2001.

[171] R. Eid, A. Ziolkowski, M. Naylor, and G. Pickup, 'Seismic monitoring of CO2 plume growth, evolution and migration in a heterogeneous reservoir: Role, impact and importance of patchy saturation', *International Journal of Greenhouse Gas Control*, vol. 43, pp. 70–81, Dec. 2015.

[172] A. Chadwick, G. Williams, N. Delepine, V. Clochard, K. Labat, S. Sturton, M.-L. Buddensiek, M. Dillen, M. Nickel, A. L. Lima, R. Arts, F. Neele, and G. Rossi, 'Quantitative analysis of time-lapse seismic monitoring data at the Sleipner CO2 storage operation', *The Leading Edge*, vol. 29, no. 2, pp. 170–177, Feb. 2010.

[173] D. L. Meadows and S. E. Rowell, 'Core sample test method and apparatus', US5325723 A, 05-Jul-1994.

[174] B. Bennion and S. Bachu, 'Relative Permeability Characteristics for Supercritical CO2 Displacing Water in a Variety of Potential Sequestration Zones', 2005.

[175] D. B. Bennion and S. Bachu, ‘Permeability and Relative Permeability Measurements at Reservoir Conditions for CO2-Water Systems in Ultra Low Permeability Confining Caprocks’, 2007.

[176] S. Bachu and D. B. Bennion, ‘Experimental assessment of brine and/or CO2 leakage through well cements at reservoir conditions’, *International Journal of Greenhouse Gas Control*, vol. 3, no. 4, pp. 494–501, Jul. 2009.

[177] E. Wilhelm, R. Battino, and R. J. Wilcock, ‘Low-pressure solubility of gases in liquid water’, *Chem. Rev.*, vol. 77, no. 2, pp. 219–262, Apr. 1977.

[178] D. Topham, ‘Hydrodynamics of an Oilwell Blowout’, Technical Report No. 33, 1975.

[179] Ø. Johansen, H. Rye, and C. Cooper, ‘DeepSpill—Field Study of a Simulated Oil and Gas Blowout in Deep Water’, *Spill Science & Technology Bulletin*, vol. 8, no. 5–6, pp. 433–443, 2003.

[180] M. Motarjemi and G. J. Jameson, ‘Mass transfer from very small bubbles—the optimum bubble size for aeration’, *Chemical Engineering Science*, vol. 33, no. 11, pp. 1415–1423, 1978.

[181] W. G. Davenport, F. D. Richardson, and A. V. Bradshaw, ‘Spherical cap bubbles in low density liquids’, *Chemical Engineering Science*, vol. 22, no. 9, pp. 1221–1235, Sep. 1967.

[182] R. I. L. Guthrie and A. V. Bradshaw, ‘Spherical capped gas bubbles rising in aqueous media’, *Chemical Engineering Science*, vol. 28, no. 1, pp. 191–203, Jan. 1973.

[183] A. I. Johnson, F. Besik, and A. E. Hamielec, ‘Mass transfer from a single rising bubble’, *Can. J. Chem. Eng.*, vol. 47, no. 6, pp. 559–564, Dec. 1969.

[184] R. Clift, J. R. Grace, and M. E. Weber, *Bubbles, Drops, and Particles*. Academic Press, 1978.

[185] W. L. Haberman and R. K. Morton, ‘An Experimental Study of Bubbles Moving in Liquids’, *Transactions of the American Society of Civil Engineers*, vol. 121, no. 1, pp. 227–250, 1956.

[186] M. H. I. Baird and J. F. Davidson, ‘Gas absorption by large rising bubbles’, *Chemical Engineering Science*, vol. 17, no. 2, pp. 87–93, Feb. 1962.

[187] D. F. McGinnis, J. Greinert, Y. Artemov, S. E. Beaubien, and A. Wüest, ‘Fate of rising methane bubbles in stratified waters: How much methane reaches the atmosphere?’, *J. Geophys. Res.*, vol. 111, no. C9, p. C09007, Sep. 2006.

[188] N. K. Bigalke, G. Rehder, and G. Gust, ‘Experimental Investigation of the Rising Behavior of CO2 Droplets in Seawater under Hydrate-Forming Conditions’, *Environ. Sci. Technol.*, vol. 42, no. 14, pp. 5241–5246, Jul. 2008.

[189] N. K. Bigalke, L. I. Enstad, G. Rehder, and G. Alendal, ‘Terminal velocities of pure and hydrate coated CO2 droplets and CH4 bubbles rising in a simulated oceanic environment’, *Deep Sea Research Part I: Oceanographic Research Papers*, vol. 57, no. 9, pp. 1102–1110, Sep. 2010.

[190] P. H. Calderbank, D. S. L. Johnson, and J. Loudon, ‘Mechanics and mass transfer of single bubbles in free rise through some Newtonian and non-Newtonian liquids’, *Chemical Engineering Science*, vol. 25, no. 2, pp. 235–256, Feb. 1970.

[191] P. B. Stewart and P. K. Munjal, ‘Solubility of carbon dioxide in pure water, synthetic sea water, and synthetic sea water concentrates at -5.deg. to 25.deg. and 10- to 45-atm. pressure’, *J. Chem. Eng. Data*, vol. 15, no. 1, pp. 67–71, Jan. 1970.

[192] M. Ozaki, ‘Annual Report of RITE (in Japanese)’, pp. 286–307, 1999.

[193] H. Kimuro, T. Kusayanagi, F. Yamaguchi, K. (Ishikawajima-H. H. I. C. Ohtsubo, and M. (Tokyo E. P. C. (Japan)) Morishita, ‘Basic Experimental Results of Liquid CO2 Injection into the Deep Ocean’, *IEEE Transactions on*

Energy Conversion (Institute of Electrical and Electronics Engineers); (United States), vol. 9:4, Dec. 1994.

[194] S. S. Alves, S. P. Orvalho, and J. M. T. Vasconcelos, 'Effect of bubble contamination on rise velocity and mass transfer', *Chemical Engineering Science*, vol. 60, no. 1, pp. 1–9, Jan. 2005.

[195] S. Hirai, K. Okazaki, N. Araki, H. Yazawa, H. Ito, and K. Hijikata, 'Transport phenomena of liquid CO2 in pressurized water flow with clathrate-hydrate at the interface', *Energy Conversion and Management*, vol. 37, no. 6–8, pp. 1073–1078, Jun. 1996.

[196] F. N. Peebles and H. J. Garber, 'Studies on the motion of gas bubbles in liquids', *Chemical Engineering Progress*, vol. 49, no. 2, pp. 88–97, 1953.

[197] G. Rehder, P. W. Brewer, E. T. Peltzer, and G. Friederich, 'Enhanced lifetime of methane bubble streams within the deep ocean', *Geophys. Res. Lett.*, vol. 29, no. 15, pp. 21–1, Aug. 2002.

[198] Y. Song, B. Chen, M. Nishio, and M. Akai, 'The study on density change of carbon dioxide seawater solution at high pressure and low temperature', *Energy*, vol. 30, no. 11–12, pp. 2298–2307, Aug. 2005.

[199] Y. Song, M. Nishio, B. Chen, S. Someya, T. Uchida, and M. Akai, 'Measurement of the Density of CO2 Solution by Mach-Zehnder Interferometry', *Annals of the New York Academy of Sciences*, vol. 972, no. 1, pp. 206–212, Oct. 2002.

[200] S. Someya, S. Bando, Y. Song, B. Chen, and M. Nishio, 'DeLIF measurement of pH distribution around dissolving CO2 droplet in high pressure vessel', *International Journal of Heat and Mass Transfer*, vol. 48, no. 12, pp. 2508–2515, Jun. 2005.

[201] Q. Wu, S. Kim, M. Ishii, and S. G. Beus, ‘One-group interfacial area transport in vertical bubbly flow’, *International Journal of Heat and Mass Transfer*, vol. 41, no. 8–9, pp. 1103–1112, Apr. 1998.

[202] T. Hibiki and M. Ishii, ‘Two-group interfacial area transport equations at bubbly-to-slug flow transition’, *Nuclear Engineering and Design*, vol. 202, no. 1, pp. 39–76, Nov. 2000.

[203] T. Hibiki and M. Ishii, ‘One-group interfacial area transport of bubbly flows in vertical round tubes’, *International Journal of Heat and Mass Transfer*, vol. 43, no. 15, pp. 2711–2726, Aug. 2000.

[204] T. Hibiki and M. Ishii, ‘Development of one-group interfacial area transport equation in bubbly flow systems’, *International Journal of Heat and Mass Transfer*, vol. 45, no. 11, pp. 2351–2372, May 2002.

[205] V. T. Nguyen, C.-H. Song, B.-U. Bae, and D.-J. Euh, ‘Modeling of bubble coalescence and break-up considering turbulent suppression phenomena in bubbly two-phase flow’, *International Journal of Multiphase Flow*, vol. 54, pp. 31–42, Sep. 2013.

[206] M. Ishii and S. Kim, ‘Micro four-sensor probe measurement of interfacial area transport for bubbly flow in round pipes’, *Nuclear Engineering and Design*, vol. 205, no. 1–2, pp. 123–131, Mar. 2001.

[207] X. Y. Fu and M. Ishii, ‘Two-group interfacial area transport in vertical air–water flow -II. Model evaluation’, *Nuclear Engineering and Design*, vol. 219, no. 2, pp. 169–190, Feb. 2003.

[208] X. Sun, S. Kim, M. Ishii, and S. G. Beus, ‘Modeling of bubble coalescence and disintegration in confined upward two-phase flow’, *Nuclear Engineering and Design*, vol. 230, no. 1–3, pp. 3–26, May 2004.

[209] W. Yao and C. Morel, ‘Volumetric interfacial area prediction in upward bubbly two-phase flow’, *International Journal of Heat and Mass Transfer*, vol. 47, no. 2, pp. 307–328, Jan. 2004.

[210] H. Drange, G. Alendal, and O. M. Johannessen, ‘Ocean release of fossil fuel CO2: A case study’, *Geophys. Res. Lett.*, vol. 28, no. 13, pp. 2637–2640, Jul. 2001.

[211] K. Caldeira and M. E. Wickett, ‘Ocean model predictions of chemistry changes from carbon dioxide emissions to the atmosphere and ocean’, *J. Geophys. Res.*, vol. 110, no. C9, p. C09S04, Sep. 2005.

[212] P. G. Brewer, E. T. Peltzer, G. Friederich, and G. Rehder, ‘Experimental Determination of the Fate of Rising CO2 Droplets in Seawater’, *Environ. Sci. Technol.*, vol. 36, no. 24, pp. 5441–5446, Dec. 2002.

[213] L. Vielstädte, M. Haeckel, P. Linke, D. McGinnis, M. Schmidt, S. Sommer, and K. J. G. Wallmann, ‘Footprint of CO2 leaking from the seabed: insights from a gas release experiment’, in *[Talk] In: International Workshop on Leakage effects from natural analogues, 13.05.2013, Bergen, Norway* ., Bergen, Norway, 2013.

[214] P. G. Brewer, E. T. Peltzer, G. Friederich, I. Aya, and K. Yamane, ‘Experiments on the ocean sequestration of fossil fuel CO2: pH measurements and hydrate formation’, *Marine Chemistry*, vol. 72, no. 2–4, pp. 83–93, Dec. 2000.

[215] M. G. Domingos and S. S. S. Cardoso, ‘Turbulent two-phase plumes with bubble-size reduction owing to dissolution or chemical reaction’, *Journal of Fluid Mechanics*, vol. 716, pp. 120–136, Feb. 2013.

[216] A. Esposito, G. Giordano, and M. Anzidei, ‘The 2002–2003 submarine gas eruption at Panarea volcano (Aeolian Islands, Italy): Volcanology of the seafloor and implications for the hazard scenario’, *Marine Geology*, vol. 227, no. 1–2, pp. 119–134, Mar. 2006.

[217] C. Caudron, A. Mazot, and A. Bernard, ‘Carbon dioxide dynamics in Kelud volcanic lake’, *J. Geophys. Res.*, vol. 117, no. B5, p. B05102, May 2012.

[218] D. F. McGinnis, M. Schmidt, T. DelSontro, S. Themann, L. Rovelli, A. Reitz, and P. Linke, ‘Discovery of a natural CO2 seep in the German North Sea: Implications for shallow dissolved gas and seep detection’, *J. Geophys. Res.*, vol. 116, no. C3, p. C03013, Mar. 2011.

[219] ‘RISCS’. [Online]. Available: http://www.riscs-co2.eu/. [Accessed: 29-Jul-2015].

[220] G. T. Eigestad, H. K. Dahle, B. Hellevang, F. Riis, W. T. Johansen, and E. Øian, ‘Geological modeling and simulation of CO2 injection in the Johansen formation’, *Comput Geosci*, vol. 13, no. 4, pp. 435–450, Aug. 2009.

[221] R. S. Middleton, G. N. Keating, P. H. Stauffer, A. B. Jordan, H. S. Viswanathan, Q. J. Kang, J. W. Carey, M. L. Mulkey, E. J. Sullivan, S. P. Chu, R. Esposito, and T. A. Meckel, ‘The cross-scale science of CO2 capture and storage: from pore scale to regional scale’, *Energy Environ. Sci.*, vol. 5, no. 6, pp. 7328–7345, May 2012.

[222] M. Majumder, *Impact of Urbanization on Water Shortage in Face of Climatic Aberrations*. Springer, 2015.

[223] C. on G. Change, *Research Strategies for the U.S. Global Change Research Program*. National Academies, 1990.

[224] B. Chen, M. Nishio, Y. Song, and M. Akai, ‘The fate of CO2 bubble leaked from seabed’, *Energy Procedia*, vol. 1, no. 1, pp. 4969–4976, Feb. 2009.

[225] B. Chen, Y. Song, M. Nishio, and M. Akai, ‘Large-eddy simulation of double-plume formation induced by CO2 dissolution in the ocean’, *Tellus B*, vol. 55, no. 2, pp. 723–730, Apr. 2003.

[226] T. Sato and K. Sato, ‘Numerical prediction of the dilution process and its biological impacts in CO2 ocean sequestration’, *J Mar Sci Technol*, vol. 6, no. 4, pp. 169–180, May 2002.

[227] P. G. Brewer, B. Chen, R. Warzinki, A. Baggeroer, E. T. Peltzer, R. M. Dunk, and P. Walz, ‘Three-dimensional acoustic monitoring and modeling of a deep-sea CO2 droplet cloud’, *Geophysical Research Letters*, vol. 33, no. 23, Dec. 2006.

[228] S. Jeong, T. Sato, B. Chen, and S. Tabeta, ‘Numerical simulation on multi-scale diffusion of CO2 injected in the deep ocean in a practical scenario’, *International Journal of Greenhouse Gas Control*, vol. 4, no. 1, pp. 64–72, Jan. 2010.

[229] ‘Enhanced Carbon Sequestration in Oceans: Principles, Strategies, Impacts, and Future Perspectives’, in *Carbon Capture and Storage*, American Society of Civil Engineers, 2015, pp. 455–474.

[230] C. Tsouris, P. Szymcek, P. Taboada-Serrano, S. D. McCallum, P. Brewer, E. Peltzer, P. Walz, E. Adams, A. Chow, W. K. Johnson, and J. Summers, ‘Scaled-Up Ocean Injection of CO2–Hydrate Composite Particles†’, *Energy Fuels*, vol. 21, no. 6, pp. 3300–3309, Nov. 2007.

[231] Y. H. Mori and T. Mochizuki, ‘Dissolution of liquid CO2 into water at high pressures: A search for the mechanism of dissolution being retarded through hydrate-film formation’, *Energy Conversion and Management*, vol. 39, no. 7, pp. 567–578, May 1998.

[232] I. Aya, K. Yamane, and H. Nariai, ‘Solubility of CO2 and density of CO2 hydrate at 30 MPa’, *Energy*, vol. 22, no. 2–3, pp. 263–271, Feb. 1997.

[233] L. Zheng and P. D. Yapa, ‘Modeling gas dissolution in deepwater oil/gas spills’, *Journal of Marine Systems*, vol. 31, no. 4, pp. 299–309, Jan. 2002.

[234] R. F. Weiss, ‘Carbon dioxide in water and seawater: the solubility of a non-ideal gas’, *Marine Chemistry*, vol. 2, no. 3, pp. 203–215, Nov. 1974.

[235] M. Schmid, ‘How hazardous is the gas accumulation in Lake Kivu? Arguments for a risk assessment in light of the Nyiragongo Volcano eruption of 2002’, *Acta vulcanologica*, vol. 15, pp. 115–120, 2003.

[236] M. B. King, *Phase equilibrium in mixtures*. Pergamon Press, 1969.

[237] M. Jamialahmadi, C. Branch, and H. Müller-Steinhagen, ‘Terminal bubble rise velocity in liquids’, *Chemical engineering research & design*, vol. 72, no. 1, pp. 119–122, 1994.

[238] L. Zhao, M. C. Boufadel, S. A. Socolofsky, E. Adams, T. King, and K. Lee, ‘Evolution of droplets in subsea oil and gas blowouts: Development and validation of the numerical model VDROP-J’, *Marine Pollution Bulletin*, vol. 83, no. 1, pp. 58–69, Jun. 2014.

[239] M. Ishii and T. Hibiki, *Thermo-Fluid Dynamics of Two-Phase Flow*. New York, NY: Springer New York, 2011.

[240] R. Bhaskaran and L. Collins, ‘Introduction to CFD basics’, *Cornell University-Sibley School of Mechanical and Aerospace Engineering*, 2002.

[241] V. J. Katz, ‘The history of Stokes’ theorem’, *Mathematics Magazine*, pp. 146–156, 1979.

[242] L. B. Okuň, *Energy and Mass in Relativity Theory*. World Scientific, 2009.

[243] I. Newton, *Philosophiae naturalis principia mathematica*. sumptibus Societatis, 1723.

[244] G. Biswas, *Introduction to Fluid Mechanics and Fluid Machines,2e*. Tata McGraw-Hill Education, 2003.

[245] R. H. Nunn, *Intermediate fluid mechanics*. CRC Press, 1989.

[246] D. S. Viswanath, T. Ghosh, D. H. L. Prasad, N. V. K. Dutt, and K. Y. Rani, *Viscosity of Liquids: Theory, Estimation, Experiment, and Data*. Springer Science & Business Media, 2007.

[247] C. L. M. H. Navier, *Mémoire sur les lois du mouvement des fluides*. 1827.

[248] G. Stokes, 'On the theories of internal friction of fluids in motion', *Transactions of the Cambridge Philosophical Society*, vol. 8, p. 287, 1845.

[249] L. Euler, 'Principes généraux du mouvement des fluides', *Opera Ser. II*, vol. 12, pp. 274–315, 1755.

[250] J. B. J. Fourier, *Théorie analytique de la chaleur*. Chez Firmin Didot, père et fils ..., 1822.

[251] L. Prandtl, 'Über Flüssigkeitsbewegung bei sehr kleiner Reibung. Heidelberg', presented at the Verh. d. 3. Intern. Math. Kongr., Heidelberg, Germany, 1904, vol. 2, pp. 575–584.

[252] H. Schlichting and K. Gersten, *Boundary-Layer Theory*. Springer Science & Business Media, 2003.

[253] O. Reynolds, 'An Experimental Investigation of the Circumstances Which Determine Whether the Motion of Water Shall Be Direct or Sinuous, and of the Law of Resistance in Parallel Channels', *Philosophical Transactions of the Royal Society of London*, vol. 174, pp. 935–982, Jan. 1883.

[254] L. Prandtl, 'Der luftwiderstand von Kugeln', *Nachrichten der Gesellschaft der Wissenschaften zu Göttingen, Mathematisch-physikalische Klasse*, vol. 91, pp. 177–190, 1914.

[255] N. Rott, 'Note on the history of the Reynolds number', *Annual review of fluid mechanics*, vol. 22, no. 1, pp. 1–12, 1990.

[256] H. L. Dryden, ‘Air flow in the boundary layer near a plate’, Report, Jan. 1937.

[257] Bloomer, *Practical Fluid Mechanics for Engineering Applications*. CRC Press, 1999.

[258] M. Dhainaut and S. T. Johansen, ‘Literature study on observations and experiments on coalescence and breakup of bubbles and drops’, *SINTEF Report*, vol. 24, pp. 1–64, 2002.

[259] C. W. Hall, *Laws and Models: Science, Engineering, and Technology*. CRC Press, 1999.

[260] S. B. Hall, M. S. Bermel, Y. T. Ko, H. J. Palmer, G. Enhorning, and R. H. Notter, ‘Approximations in the measurement of surface tension on the oscillating bubble surfactometer’, *J. Appl. Physiol.*, vol. 75, no. 1, pp. 468–477, Jul. 1993.

[261] L. A. Glasgow, *Transport Phenomena: An Introduction to Advanced Topics*. John Wiley & Sons, 2010.

[262] M. Ozaki, J. Minamiura, Y. Kitajima, S. Mizokami, K. Takeuchi, and K. Hatakenaka, ‘CO2 ocean sequestration by moving ships’, *J Mar Sci Technol*, vol. 6, no. 2, pp. 51–58, Dec. 2001.

[263] G. G. Stokes, *On the effect of the internal friction of fluids on the motion of pendulums*, vol. 9. Pitt Press, 1851.

[264] M. Tek and J. Wilkes, ‘Fluid flow and heat transfer’, *Ann Arbor: University of Michigan*, 1974.

[265] D. W. Moore, ‘The velocity of rise of distorted gas bubbles in a liquid of small viscosity’, *Journal of Fluid Mechanics*, vol. 23, no. 04, pp. 749–766, Dec. 1965.

[266] G. Bozzano and M. Dente, ‘Shape and terminal velocity of single bubble motion: a novel approach’, *Computers & Chemical Engineering*, vol. 25, no. 4–6, pp. 571–576, May 2001.

[267] Y. Kano, T. Sato, J. Kita, S. Hirabayashi, and S. Tabeta, ‘Model prediction on the rise of pCO2 in uniform flows by leakage of CO2 purposefully stored under the seabed’, *International Journal of Greenhouse Gas Control*, vol. 3, no. 5, pp. 617–625, Sep. 2009.

[268] Y. Kano, T. Sato, J. Kita, S. Hirabayashi, and S. Tabeta, ‘Multi-scale modeling of CO2 dispersion leaked from seafloor off the Japanese coast’, *Marine Pollution Bulletin*, vol. 60, no. 2, pp. 215–224, Feb. 2010.

[269] R. Gangstø, P. M. Haugan, and G. Alendal, ‘Parameterization of drag and dissolution of rising CO2 drops in seawater’, *Geophys. Res. Lett.*, vol. 32, no. 10, p. L10612, May 2005.

[270] A. Faghri, Y. Zhang, and J. Howell, *Advanced Heat and Mass Transfer*. Global Digital Press, 2010.

[271] T. K. Sherwood, *Absorption and extraction*, First Edition edition. New York, 1937.

[272] T. K. Sherwood, R. L. Pigford, and C. R. Wilke, *Mass Transfer*. New York: McGraw-Hill Inc.,US, 1975.

[273] J. Gabitto and C. Tsouris, ‘Dissolution mechanisms of CO2 hydrate droplets in deep seawaters’, *Energy Conversion and Management*, vol. 47, no. 5, pp. 494–508, Mar. 2006.

[274] R.-T. Jung and T. Sato, ‘Numerical simulation of high Schmidt number flow over a droplet by using moving unstructured mesh’, *Journal of Computational Physics*, vol. 203, no. 1, pp. 221–249, Feb. 2005.

[275] W. E. Ranz and W. R. J. Marshall, ‘Evaporation from drops Part I’, *Chem. Eng. Prog.*, vol. 48, pp. 141–146, 1952.

[276] W. E. Ranz and W. R. J. Marshall, ‘Evaporation from drops Part II’, *Chem. Eng. Prog.*, vol. 48, pp. 173–180, 1952.

[277] F. P. Incropera, D. P. DeWitt, T. L. Bergman, and A. S. Lavine, *Fundamentals of Heat and Mass Transfer*, 6th Edition edition. Hoboken, NJ: John Wiley & Sons, 2006.

[278] R. B. Bird, W. E. Stewart, and E. N. Lightfoot, *Transport phenomena*. Wiley, 1960.

[279] N. Froessling, 'Über die verdunstung fallender tropfen', *Gerlands Beiträge zur Geophysik*, vol. 52, pp. 170–215, 1938.

[280] A. A. Kulkarni and J. B. Joshi, 'Bubble Formation and Bubble Rise Velocity in Gas−Liquid Systems: A Review', *Ind. Eng. Chem. Res.*, vol. 44, no. 16, pp. 5873–5931, Aug. 2005.

[281] L. Zhang, C. Yang, and Z.-S. Mao, 'An Empirical Correlation of Drag Coefficient for a Single Bubble Rising in Non-Newtonian Liquids', *Ind. Eng. Chem. Res.*, vol. 47, no. 23, pp. 9767–9772, Dec. 2008.

[282] S. Bando and F. Takemura, 'Rise speed of supercritical carbon dioxide spheres in aqueous surfactant solutions', *Journal of Fluid Mechanics*, vol. 548, pp. 133–140, Feb. 2006.

[283] F. Takemura and A. Yabe, 'Rising speed and dissolution rate of a carbon dioxide bubble in slightly contaminated water', *Journal of Fluid Mechanics*, vol. 378, pp. 319–334, Jan. 1999.

[284] A. Zaruba, E. Krepper, H.-M. Prasser, and B. N. Reddy Vanga, 'Experimental study on bubble motion in a rectangular bubble column using high-speed video observations', *Flow Measurement and Instrumentation*, vol. 16, no. 5, pp. 277–287, Oct. 2005.

[285] X. Zhang, H. Dong, Y. Huang, C. Li, and X. Zhang, 'Experimental study on gas holdup and bubble behavior in carbon capture systems with ionic liquid', *Chemical Engineering Journal*, vol. 209, pp. 607–615, Oct. 2012.

[286] R. Hain, C. J. Kähler, and C. Tropea, ‘Comparison of CCD, CMOS and intensified cameras’, *Exp Fluids*, vol. 42, no. 3, pp. 403–411, Jan. 2007.

[287] T. R. Oakley, E. Loth, and R. J. Adrian, ‘A Two-Phase Cinematic PIV Method for Bubbly Flows’, *J. Fluids Eng*, vol. 119, no. 3, pp. 707–712, Sep. 1997.

[288] D. A. Johnson, ‘Laser Doppler anemometry’, *NASA STI/Recon Technical Report N*, vol. 88, p. 23187, Jun. 1988.

[289] N. Yoshida, ‘Laser doppler velocimeter’, in *Handbook of Signal Processing in Acoustics*, Springer, 2008, pp. 1329–1338.

[290] T. G. Leighton, *The Acoustic Bubble*. Academic Press, 1994.

[291] M. Minnaert, ‘XVI. On musical air-bubbles and the sounds of running water’, *The London, Edinburgh, and Dublin Philosophical Magazine and Journal of Science*, vol. 16, no. 104, pp. 235–248, Aug. 1933.

[292] C. A. Greene and P. S. Wilson, ‘Laboratory investigation of a passive acoustic method for measurement of underwater gas seep ebullition’, *The Journal of the Acoustical Society of America*, vol. 131, no. 1, pp. EL61–EL66, Jan. 2012.

[293] B. McLernon, *Canon EOS 5D Mark II Digital Field Guide*. John Wiley & Sons, 2012.

[294] ‘Solstice Side Scan Sonar [8200]’. [Online]. Available: http://www.sonardyne.com/products/sonar/solstice.html. [Accessed: 03-Sep-2015].

[295] C.-C. Wang, Y.-H. Hsiao, and M.-C. Huang, ‘Development of MSP430-based ultra-low power expandable underwater acoustic recorder’, *Ocean Engineering*, vol. 36, no. 6–7, pp. 446–455, May 2009.

[296] I. Leifer and D. Tang, ‘The acoustic signature of marine seep bubbles’, *The Journal of the Acoustical Society of America*, vol. 121, no. 1, pp. EL35–EL40, Jan. 2007.

[297] T. G. Leighton and P. R. White, ‘Quantification of undersea gas leaks from carbon capture and storage facilities, from pipelines and from methane seeps, by their acoustic emissions’, *Proceedings of the Royal Society A: Mathematical, Physical and Engineering Sciences*, vol. 468, no. 2138, pp. 485–510, Feb. 2012.

[298] A. E. Gill, *Atmosphere-Ocean Dynamics*. Academic Press, 1982.

[299] E. Halley, ‘An Historical Account of the Trade Winds, and Monsoons, Observable in the Seas between and Near the Tropicks, with an Attempt to Assign the Phisical Cause of the Said Winds, By E. Halley’, *Philosophical Transactions (1683-1775)*, vol. 16, pp. 153–168, Jan. 1686.

[300] G. Hadley, ‘Concerning the Cause of the General Trade-Winds: By Geo. Hadley, Esq; F. R. S.’, *Phil. Trans.*, vol. 39, no. 436–444, pp. 58–62, Jan. 1735.

[301] P. Linke and L. Vielstädte, ‘ADCP current measurements during Celtic Explorer cruise CE12010 at station OCE1’, Unpublished dataset #833751, 2014.

[302] A. Tsinober, *An Informal Introduction to Turbulence*. Springer Science & Business Media, 2001.

[303] A. Kolmogorov, ‘The local Structure of turbulence in incompressible viscous fluid for very large Reynolds numbers’, *Dokl. Akad. Nauk SSSR*, vol. 30, pp. 299–303, 1941.

[304] T. Pang, *An Introduction to Computational Physics*. Cambridge University Press, 1997.

[305] P. Bradshaw, Ed., *Turbulence*, vol. 12. Berlin, Heidelberg: Springer Berlin Heidelberg, 1976.

[306] J. JIMÉNEZ, ‘Oceanic turbulence at millimeter scales’, *Oceanographic Literature Review*, vol. 3, no. 45, p. 598, 1998.

[307] O. Reynolds, ‘On the dynamical theory of incompressible viscous fluids and the determination of the criterion’, *Philosophical Transactions of the Royal Society of London. A*, pp. 123–164, 1895.

[308] J. Boussinesq, *Essai sur la théorie des eaux courantes / par J. Boussinesq*. Impr. nationale (Paris), 1877.

[309] L. Prandtl and K. Wieghardt, *Über ein neues Formelsystem für die ausgebildete Turbulenz*. Vandenhoeck & Ruprecht, 1947.

[310] A. N. Kolmogorov, ‘Equations of turbulent motion in an incompressible fluid’, *Dokl. Akad. Nauk SSSR*, 1941. [Online]. Available: http://cds.cern.ch/record/739754. [Accessed: 23-Nov-2015].

[311] J. Rotta, ‘Statistische Theorie nichthomogener Turbulenz’, *Z. Physik*, vol. 129, no. 6, pp. 547–572, Nov. 1951.

[312] S. A. Orszag and G. S. Patterson, ‘Numerical Simulation of Three-Dimensional Homogeneous Isotropic Turbulence’, *Phys. Rev. Lett.*, vol. 28, no. 2, pp. 76–79, Jan. 1972.

[313] G. N. Coleman and R. D. Sandberg, ‘A primer on direct numerical simulation of turbulence-methods, procedures and guidelines’, 2010.

[314] B. Galperin, *Large Eddy Simulation of Complex Engineering and Geophysical Flows*. Cambridge University Press, 1993.

[315] A. Leonard, ‘Energy cascade in large-eddy simulations of turbulent fluid flows’, presented at the Turbulent Diffusion in Environmental Pollution, 1974, pp. 237–248.

[316] A. N. Kolmogorov, ‘Dissipation of Energy in the Locally Isotropic Turbulence’, *Proceedings: Mathematical and Physical Sciences*, vol. 434, no. 1890, pp. 15–17, Jul. 1991.

[317] K. Hanjalić and B. Launder, *Modelling Turbulence in Engineering and the Environment: Second-Moment Routes to Closure*. Cambridge University Press, 2011.

[318] S. A. Thorpe, *An introduction to ocean turbulence*. Cambridge; New York: Cambridge University Press, 2007.

[319] J. Meyers, B. Geurts, and P. Sagaut, *Quality and Reliability of Large-Eddy Simulations*. Springer Science & Business Media, 2008.

[320] I. B. Celik, Z. N. Cehreli, and I. Yavuz, ‘Index of Resolution Quality for Large Eddy Simulations’, *Journal of Fluids Engineering*, vol. 127, no. 5, p. 949, 2005.

[321] C. Speziale, ‘Turbulence Modeling for Time-Dependent RANS and VLES: A Review’, *AIAA Journal*, vol. 36, no. 2, pp. 173–184, 1998.

[322] R. Sun and Z. Duan, ‘Prediction of CH4 and CO2 hydrate phase equilibrium and cage occupancy from ab initio intermolecular potentials’, *Geochimica et Cosmochimica Acta*, vol. 69, no. 18, pp. 4411–4424, Sep. 2005.

[323] C. A. Schneider, W. S. Rasband, and K. W. Eliceiri, ‘NIH Image to ImageJ: 25 years of image analysis’, *Nat Meth*, vol. 9, no. 7, pp. 671–675, Jul. 2012.

[324] C. Song, P. Wang, and H. A. Makse, ‘A phase diagram for jammed matter’, *Nature*, vol. 453, no. 7195, pp. 629–632, May 2008.

[325] GZSPTU Campus Bathinda, M. Singh, and E. N. Kumar Garg, ‘Audio Noise Reduction Using Butter Worth Filter’, *International Journal of Computer & Organization Trends*, vol. 6, no. 1, pp. 20–23, Mar. 2014.

[326] S. Butterworth, ‘On the theory of filter amplifiers’, *Wireless Engineer*, vol. 7, no. 6, pp. 536–541, 1930.

[327] Y. Liao and D. Lucas, ‘A literature review of theoretical models for drop and bubble breakup in turbulent dispersions’, *Chemical Engineering Science*, vol. 64, no. 15, pp. 3389–3406, Aug. 2009.

[328] R. Manasseh, R. F. LaFontaine, J. Davy, I. Shepherd, and Y.-G. Zhu, ‘Passive acoustic bubble sizing in sparged systems’, *Experiments in Fluids*, vol. 30, no. 6, pp. 672–682, Jun. 2001.

[329] S. H. Lamb, *Hydrodynamics*. Cambridge [Eng.]: University Press, 1895.

[330] B. Jähne, K. O. Münnich, R. Bösinger, A. Dutzi, W. Huber, and P. Libner, ‘On the parameters influencing air-water gas exchange’, *J. Geophys. Res.*, vol. 92, no. C2, pp. 1937–1949, Feb. 1987.

[331] I. Leifer and R. K. Patro, ‘The bubble mechanism for methane transport from the shallow sea bed to the surface: A review and sensitivity study’, *Continental Shelf Research*, vol. 22, no. 16, pp. 2409–2428, Nov. 2002.

[332] M. Nishio, S. M. Masutani, J. Minamiura, and M. Ozaki, ‘Study of liquid CO2 droplet formation under simulated mid-depth ocean conditions’, *Energy*, vol. 30, no. 11–12, pp. 2284–2297, Aug. 2005.

[333] C. A. Coulaloglou and L. L. Tavlarides, ‘Description of interaction processes in agitated liquid-liquid dispersions’, *Chemical Engineering Science*, vol. 32, no. 11, pp. 1289–1297, 1977.

[334] T. O. Oolman and H. W. Blanch, ‘Bubble coalescence in air-sparged bioreactors’, *Biotechnol. Bioeng.*, vol. 28, no. 4, pp. 578–584, Apr. 1986.

[335] T. O. Oolman and H. W. Blanch, ‘Bubble Coalescence in Stagnant Liquids’, *Chemical Engineering Communications*, vol. 43, no. 4–6, pp. 237–261, May 1986.

[336] M. J. Prince and H. W. Blanch, ‘Bubble coalescence and break-up in air-sparged bubble columns’, *AIChE J.*, vol. 36, no. 10, pp. 1485–1499, Oct. 1990.

[337] V. Levich, *Physicochemical Hydrodynamics*. Englewood Cliffs, N. J: Prentice Hall, 1962.

[338] M. S. Johnson, M. S. Johnson, J. Lehmann, and E. G. Couto, ‘A Simple, Direct Method to Measure Dissolved CO2 Using Soda Lime’, *Oecologia Brasileira*, vol. 12, pp. 85–91, 2008.

[339] A. G. Dickson, ‘An exact definition of total alkalinity and a procedure for the estimation of alkalinity and total inorganic carbon from titration data’, *Deep Sea Research Part A. Oceanographic Research Papers*, vol. 28, no. 6, pp. 609–623, Jun. 1981.

[340] A. G. Dickson and C. Goyet, ‘Handbook of Methods for the Analysis of the Various Parameters of the Carbon Dioxide System in Sea Water. Version 2’, Oak Ridge National Lab., TN (United States), ORNL/CDIAC--74, Sep. 1994.

[341] F. J. Millero, ‘Thermodynamics of the carbon dioxide system in the oceans’, *Geochimica et Cosmochimica Acta*, vol. 59, no. 4, pp. 661–677, Feb. 1995.

[342] R. N. Roy, L. N. Roy, K. M. Vogel, C. Porter-Moore, T. Pearson, C. E. Good, F. J. Millero, and D. M. Campbell, ‘The dissociation constants of carbonic acid in seawater at salinities 5 to 45 and temperatures 0 to 45°C’, *Marine Chemistry*, vol. 44, no. 2–4, pp. 249–267, Dec. 1993.

[343] A. G. Dickson and J. P. Riley, ‘The estimation of acid dissociation constants in seawater media from potentionmetric titrations with strong base. I. The ionic product of water — Kw’, *Marine Chemistry*, vol. 7, no. 2, pp. 89–99, Feb. 1979.

[344] A. G. Dickson, ‘Standard potential of the reaction: AgCl(s) + 12H2(g) = Ag(s) + HCl(aq), and and the standard acidity constant of the ion HSO4− in synthetic sea water from 273.15 to 318.15 K’, *The Journal of Chemical Thermodynamics*, vol. 22, no. 2, pp. 113–127, Feb. 1990.

[345] F. J. Millero, ‘The thermodynamics of the carbonate system in seawater’, *Geochimica et Cosmochimica Acta*, vol. 43, no. 10, pp. 1651–1661, Oct. 1979.

[346] L. R. Uppström, ‘The boron/chlorinity ratio of deep-sea water from the Pacific Ocean’, *Deep Sea Research and Oceanographic Abstracts*, vol. 21, no. 2, pp. 161–162, Feb. 1974.

[347] A. W. Morris and J. P. Riley, ‘The bromide/chlorinity and sulphate/chlorinity ratio in sea water’, *Deep Sea Research and Oceanographic Abstracts*, vol. 13, no. 4, pp. 699–705, Aug. 1966.

[348] J. P. Riley, ‘The occurrence of anomalously high fluoride concentrations in the North Atlantic’, *Deep Sea Research and Oceanographic Abstracts*, vol. 12, no. 2, pp. 219–220, Apr. 1965.

[349] E. A. Guggenheim, *Thermodynamics: An Advanced Treatment for Chemists and Physicists*. North-Holland Publishing Company, 1967.

[350] J. O. Hirschfelder, C. F. Curtiss, R. B. Bird, and U. of W. T. C. Laboratory, *Molecular theory of gases and liquids*. Wiley, 1954.

[351] J. M. H. L. Sengers, M. Klein, and J. S. Gallagher, ‘Pressure-Volume-Temperature Relationships of Gases Virial Coefficients’, Mar. 1971.

[352] M. Ito, *Kagaku Binran II (Chemistry Handbook)*, 3rd ed. The Chemical Society Japan: Maruzen, Tokyo, 1984.

[353] D. G. Friend, J. F. Ely, and H. Ingham, ‘Thermophysical Properties of Methane’, *Journal of Physical and Chemical Reference Data*, vol. 18, no. 2, pp. 583–638, Apr. 1989.

[354] J. P. on O. T. and Standards, Unesco, I. C. for the E. of the Sea, I. C. of S. U. S. C. on O. Research, and I. A. for the P. S. of the Ocean, *Tenth report of the Joint Panel on Oceanographic Tables and Standards, Sidney, B.C., Canada, 1-5 September 1980*. Unesco, 1981.

[355] A. Bradshaw, ‘The Effect of Carbon Dioxide on the Specific Volume of Seawater1’, *Limnol. Oceanogr.*, vol. 18, no. 1, pp. 95–105, Jan. 1973.

[356] P. M. Haugan and H. Drange, ‘Sequestration of C02 in the deep ocean by shallow injection’, *Nature*, vol. 357, no. 6376, pp. 318–320, May 1992.

[357] Z. Duan and S. Mao, ‘A thermodynamic model for calculating methane solubility, density and gas phase composition of methane-bearing aqueous fluids from 273 to 523K and from 1 to 2000bar’, *Geochimica et Cosmochimica Acta*, vol. 70, no. 13, pp. 3369–3386, Jul. 2006.

[358] P. Tishchenko, C. Hensen, K. Wallmann, and C. S. Wong, ‘Calculation of the stability and solubility of methane hydrate in seawater’, *Chemical Geology*, vol. 219, no. 1–4, pp. 37–52, Jun. 2005.

[359] E. Kossel, N. K. Bigalke, E. Pinero, and M. Haeckel, ‘The SUGAR Toolbox: a library of numerical algorithms and data for modelling of gas hydrate systems and marine environments’, 2013.

[360] B. Jähne, G. Heinz, and W. Dietrich, ‘Measurement of the diffusion coefficients of sparingly soluble gases in water’, *J. Geophys. Res.*, vol. 92, no. C10, pp. 10767–10776, Sep. 1987.

[361] D. N. Espinoza and J. C. Santamarina, ‘Water-CO2-mineral systems: Interfacial tension, contact angle, and diffusion—Implications to CO2 geological storage’, *Water Resour. Res.*, vol. 46, no. 7, p. W07537, Jul. 2010.

[362] W. Sachs and V. Meyn, ‘Pressure and temperature dependence of the surface tension in the system natural gas/water principles of investigation and the first precise experimental data for pure methane/water at 25°C up to 46.8 MPa’, *Colloids and Surfaces A: Physicochemical and Engineering Aspects*, vol. 94, no. 2–3, pp. 291–301, Jan. 1995.

[363] J. F. Wendt, J. D. Anderson, and Von Karman Institute for Fluid Dynamics, Eds., *Computational fluid dynamics: an introduction*, 3rd ed. Berlin ; [London]: Springer, 2008.

[364] S. Patankar, *Numerical Heat Transfer and Fluid Flow*. CRC Press, 1980.

[365] E. Madenci and I. Guven, *The Finite Element Method and Applications in Engineering Using ANSYS®*. Springer Science & Business Media, 2007.

[366] J. H. Ferziger, *Computational Methods for Fluid Dynamics*. Springer, 1996.

[367] J.-L. Puebe, *Fluid Mechanics*. John Wiley & Sons, 2013.

[368] S. Chen and G. D. Doolen, 'Lattice Boltzmann Method for Fluid Flows', *Annual Review of Fluid Mechanics*, vol. 30, no. 1, pp. 329–364, 1998.

[369] W. Zhang, Z. Chen, C. C. Douglas, and W. Tong, *High Performance Computing and Applications: Second International Conference, HPCA 2009, Shanghai, China, August 10-12, 2009, Revised Selected Papers*. Springer, 2010.

[370] S. De, F. Guilak, and M. Mofrad, *Computational Modeling in Biomechanics*. Springer Science & Business Media, 2010.

[371] J. J. Monaghan, 'Smoothed particle hydrodynamics', *Rep. Prog. Phys.*, vol. 68, no. 8, p. 1703, 2005.

[372] J. J. Monaghan, 'Smoothed particle hydrodynamics', *Annual Review of Astronomy and Astrophysics*, vol. 30, pp. 543–574, 1992.

[373] P. Bodenheimer, G. P. Laughlin, M. Rozyczka, T. Plewa, H. W. Yorke, and H. W. Yorke, *Numerical Methods in Astrophysics: An Introduction*. CRC Press, 2006.

[374] S. Bhojwani, *Smoothed Particle Hydrodynamics Modeling of the Friction Stir Welding Process*. ProQuest, 2007.

[375] R. Courant, E. Isaacson, and M. Rees, ‘On the solution of nonlinear hyperbolic differential equations by finite differences’, *Comm. Pure Appl. Math.*, vol. 5, no. 3, pp. 243–255, Aug. 1952.

[376] D. B. Spalding, ‘A novel finite difference formulation for differential expressions involving both first and second derivatives’, *Int. J. Numer. Meth. Engng.*, vol. 4, no. 4, pp. 551–559, Jul. 1972.

[377] S. V. Patankar and D. B. Spalding, *Heat and Mass Transfer in Boundary Layers: A General Calculation Procedure*. Intertext, 1970.

[378] S. V. Patankar, ‘A Calculation Procedure for Two-Dimensional Elliptic Situations’, *Numerical Heat Transfer*, vol. 4, no. 4, pp. 409–425, Oct. 1981.

[379] F. H. Harlow and J. E. Welch, ‘Numerical Calculation of Time-Dependent Viscous Incompressible Flow of Fluid with Free Surface’, *Physics of Fluids (1958-1988)*, vol. 8, no. 12, pp. 2182–2189, Dec. 1965.

[380] S. Kubacki, J. Rokicki, and E. Dick, ‘Hybrid RANS/LES computation of plane impinging jet flow’, *Archives of Mechanics*, vol. 63, no. 2, pp. 117–136, 2011.

[381] R. N. Gibson, R. J. A. Atkinson, and J. D. M. Gordon, Eds., *Oceanography and Marine Biology: An Annual Review, Volume 49*, Annual edition. Boca Raton, Fla.: CRC Press, 2011.

[382] E. Adams, D. Golomb, X. Zhang, and H. Herzog, ‘Confined release of CO2 into shallow seawater’, pp. 153–164, 1995.

[383] P. Chen, J. Sanyal, and M. P. Duduković, ‘Numerical simulation of bubble columns flows: effect of different breakup and coalescence closures’, *Chemical Engineering Science*, vol. 60, no. 4, pp. 1085–1101, Feb. 2005.

[384] A. Wüest, N. H. Brooks, and D. M. Imboden, ‘Bubble plume modeling for lake restoration’, *Water Resour. Res.*, vol. 28, no. 12, pp. 3235–3250, Dec. 1992.

[385] J. Smagorinsky, ‘General circulation experiments with the primitive equations’, *Mon. Wea. Rev.*, vol. 91, no. 3, pp. 99–164, Mar. 1963.

[386] M. Germano, U. Piomelli, P. Moin, and W. H. Cabot, ‘A dynamic subgrid-scale eddy viscosity model’, *Physics of Fluids A: Fluid Dynamics (1989-1993)*, vol. 3, no. 7, pp. 1760–1765, Jul. 1991.

[387] W.-W. Kim and S. Menon, ‘A new dynamic one-equation subgrid-scale model for large eddy simulations’, in *33rd Aerospace Sciences Meeting and Exhibit*, American Institute of Aeronautics and Astronautics, 1995.

[388] F. F. Grinstein, L. G. Margolin, and W. J. Rider, *Implicit Large Eddy Simulation: Computing Turbulent Fluid Dynamics*. Cambridge University Press, 2007.

[389] C. Brun, R. Friedrich, C. B. D. Silva, and O. Métais, ‘A New Mixed Model Based on the Velocity Structure Function’, in *Advances in LES of Complex Flows*, R. Friedrich and W. Rodi, Eds. Springer Netherlands, 2002, pp. 49–64.

[390] O. Métais and M. Lesieur, ‘Spectral large-eddy simulation of isotropic and stably stratified turbulence’, *Journal of Fluid Mechanics*, vol. 239, pp. 157–194, Jun. 1992.

[391] F. Ducros, P. Comte, and M. Lesieur, ‘Large-eddy simulation of transition to turbulence in a boundary layer developing spatially over a flat plate’, *Journal of Fluid Mechanics*, vol. 326, pp. 1–36, Nov. 1996.

[392] J.-P. Chollet and M. Lesieur, ‘Parameterization of Small Scales of Three-Dimensional Isotropic Turbulence Utilizing Spectral Closures’, *J. Atmos. Sci.*, vol. 38, no. 12, pp. 2747–2757, Dec. 1981.

[393] G. K. Batchelor, *The Theory of Homogeneous Turbulence*. Cambridge University Press, 1953.

[394] S. A. Orszag, *Lectures on the Statistical Theory of Turbulence*. MIT, 1977.

[395] S. B. Pope, *Turbulent flows*. Cambridge university press, 2000.

[396] M. H. Zhang, *Wind Resource Assessment and Micro-siting: Science and Engineering*. John Wiley & Sons, 2015.

[397] S. T. Johansen, J. Wu, and W. Shyy, 'Filter-based unsteady RANS computations', *International Journal of Heat and Fluid Flow*, vol. 25, no. 1, pp. 10–21, Feb. 2004.

[398] S. Ghosal, 'An analysis of numerical errors in large-eddy simulations of turbulence', *Journal of Computational Physics*, vol. 125, no. 1, pp. 187–206, 1996.

[399] E. Garnier, N. Adams, and P. Sagaut, *Large eddy simulation for compressible flows*. Springer Science & Business Media, 2009.

[400] R. Ferrari and C. Wunsch, 'Ocean circulation kinetic energy: Reservoirs, sources, and sinks', *Annual Review of Fluid Mechanics*, vol. 41, no. 1, p. 253, 2008.

[401] *These data were collected and made freely available by the Coriolis project and programmes that contribute to it (http://www.coriolis.eu.org)*. 2015.

[402] I. Mann, M. Akhurst, and Scottish Carbon Capture & Storage (Research team), Eds., *Unlocking North Sea CO_2 storage for Europe: practical actions for the next five years : SCCS recommendations and conference 2013 report*. 2013.

[403] H.-R. Buser, M. D. Müller, and N. Theobald, 'Occurrence of the Pharmaceutical Drug Clofibric Acid and the Herbicide Mecoprop in Various Swiss Lakes and in the North Sea', *Environ. Sci. Technol.*, vol. 32, no. 1, pp. 188–192, Jan. 1998.

[404] H. Thomas, Y. Bozec, H. J. De Baar, K. Elkalay, M. Frankignoulle, L.-S. Schiettecatte, G. Kattner, and A. V. Borges, 'The carbon budget of the North Sea', *Biogeosciences*, vol. 2, no. 1, pp. 87–96, 2005.

[405] J. C. Blackford and F. J. Gilbert, ‘pH variability and CO2 induced acidification in the North Sea’, *Journal of Marine Systems*, vol. 64, no. 1–4, pp. 229–241, Jan. 2007.

[406] D. J. Ellett, C. R. Griffiths, D. T. Meldrum, and G. Britain, *Near-Surface Current Measurements in the North Sea*. London: Stationery Office Books, 1991.

[407] L. Pan, C. M. Oldenburg, K. Pruess, and Y.-S. Wu, ‘Transient CO2 leakage and injection in wellbore-reservoir systems for geologic carbon sequestration’, *Greenhouse Gases: Science and Technology*, vol. 1, no. 4, pp. 335–350, Dec. 2011.

[408] J. C. Blackford, et al., ‘ETI report Technical Report Tr 1.3 hydrodynamic modelling’, Fugro Reference Number: 8559, Sep. 2014.

[409] T. R. Kelley, ‘Environmental Health Insights into the 2010 Deepwater Horizon (BP) Oil Blowout’, *Environ Health Insights*, vol. 4, pp. 61–63, Aug. 2010.

[410] S. Socolofsky and E. Adams, ‘Role of Slip Velocity in the Behavior of Stratified Multiphase Plumes’, *J. Hydraul. Eng.*, vol. 131, no. 4, pp. 273–282, Apr. 2005.

[411] J. C. Blackford, N. Jones, R. Proctor, and J. Holt, ‘Regional scale impacts of distinct CO2 additions in the North Sea’, *Marine Pollution Bulletin*, vol. 56, no. 8, pp. 1461–1468, Aug. 2008.

[412] Y. Bozec, H. Thomas, K. Elkalay, and H. J. W. de Baar, ‘The continental shelf pump for CO2 in the North Sea—evidence from summer observation’, *Marine Chemistry*, vol. 93, no. 2–4, pp. 131–147, Jan. 2005.

[413] H. Thomas, A. E. Friederike Prowe, S. van Heuven, Y. Bozec, H. J. W. de Baar, L.-S. Schiettecatte, K. Suykens, M. Koné, A. V. Borges, I. D. Lima, and S. C. Doney, ‘Rapid decline of the CO2 buffering capacity in the North Sea and implications for the North Atlantic Ocean’, *Global Biogeochem. Cycles*, vol. 21, no. 4, p. GB4001, Dec. 2007.